

STAVEBNÍ OBZOR

ČÍSLO 4/2018

Obsah čísla:

STUDY ON THE SETTLEMENT OF TUNNEL BOTTOM AND PRESSURE OF ROCK MASS BASED ON CURVED BEAM ON ELASTIC FOUNDATION THEORY

Haobo Fan, Siyue He, Dongping Zhao, Xiuling Wang, Hao Wang, Hao Ding

APPLICATION OF GEOSTATISTICS IN THE ESTIMATION OF SUJISHAN GRAPHITE DEPOSITS, MONGOLIA

Huang Song, Huaming An

EXAMINATION OF THE USABILITY OF BASALT AGGREGATE IN SIFCON

Metin İpek

APPLICATION OF MACHINE VISION TECHNOLOGY IN ROAD DETECTION

Qingzhe Zhang, Zhi Qin

PARAMETRIC ANALYSIS OF THE DYNAMIC BEHAVIOUR OF RC COLUMNS WITH THE CONFINEMENT EFFECT OF OVERLAPPING HOOPS SUBJECTED TO LATERAL RAPID LOADINGS

Xiang Zeng, Bin Xu

INVESTIGATING OF SEISMIC PARAMETERS OF RC FRAMES REHABILITATED BY ECCENTRICALLY BRACING WITH VERTICAL LINK

Faramarz Noruzi , Heydar Dashti Naserabadi , Hosein Nematian Jelodar, Hosein Dorvar

NUMERICAL STUDY OF THE WIND TURBINE WAKE FLOW AND EFFECTS OF THE INFLOW TURBULENCE

Xiaoyu Luo, Shengyu Lu

INFLUENCE OF PVD-ENHANCING SOFT SOIL GROUND ON THE ADJACENT BRIDGE PILES – A 3D FEM ANALYSIS

Hong-quan Li, Li-min Wei, Sheng-yang Feng, Zhi Chen

NUMERICAL INVESTIGATION OF THE PERFORMANCE OF INSULATED FRP-STRENGTHENED REINFORCED CONCRETE BEAMS IN FIRE

Osama El-Mahdy, Gehan Hamdy Moustafa Abdullah

INFLUENCE OF VIBRATION ON PERFORMANCE OF RECYCLED CONCRETE

Ergang Xiong, Tian Li, Sheliang Wang, Yujiang Fan

DIFFUSION CHARACTERISTICS OF GROUT IN LAYERED FAULT MEDIUM

Li Peng, Zhang Xiao, Wang Qian, Zhang Qingsong

3D DYNAMIC TIME-HISTORY RESPONSE ANALYSIS OF AN ISLAND PLATFORM METRO STATION IN LOESS AREA

Wang Ke, Siyue He, Guanglong Zhang

STUDY ON THE SETTLEMENT OF TUNNEL BOTTOM AND PRESSURE OF ROCK MASS BASED ON CURVED BEAM ON ELASTIC FOUNDATION THEORY

*Haobo Fan^{1,2}, Siyue He^{*2}, Dongping Zhao¹, Xiuling Wang², Hao Wang³, Hao Ding²*

1. *China Railway Eryuan Engineering Group Co.Ltd, Chengdu 610031, China*
2. *School of Highway, Chang'an University, Xi'an 710064, China; hesiyue@chd.edu.cn, 408423231@qq.com*
3. *School of Civil & Construction Engineering, Oregon State University, 101 Kearney Hall, Corvallis, OR 97331 USA*

ABSTRACT

Tunnel invert is a weak section of curved beam on tunnel foundation, and it is easy to break down. Based on the curved beam theory on elastic foundation, the curved beam model of tunnel invert was established, the displacement equation of tunnel invert under external load was deduced, and the formula of settlement of tunnel bottom and the pressure of rock mass was presented. By means of the calculating formula, the distribution law of settlement of tunnel bottom and pressure of rock mass were obtained when tunnel bottom was strengthened and not strengthened by high pressure jet grouting pile. The final formula in the paper is precise to predict the settlement of tunnel bottom and pressure of rock mass, so it is of great value for tunnel design and construction.

KEYWORDS

Tunnel invert, Curved beam, Elastic foundation, Displacement equation, Pressure of rock mass

INTRODUCTION

There are many problems in the construction of curved beams, such as embankment culvert, underground pipeline and tunnel lining, and the curved beam model can be used to solve them [1-3]. At present, the research of curved beams is mostly concentrated on the study of the basic theory [4-5]. Pagano et al. [6-7], Chien et al. [8], Shen et al. [9], and Tornabene et al. [10] used the linear elastic theory to study laminated composite plates under the condition of column bending and gave the exact solutions. Lekhnitskii et al. [11] gave the general solution of anisotropic bending beam under moment load. This method was also adopted to calculate the interlaminar tensile stress for four point bending experiment of curved beam (ASTMD6415/D6415M-06a) [12]. Shenoj et al. [13], Arici et al. [14] established the model for bending behaviour of elastically curved beams and obtained the elastic solution of the anisotropic beam. Higher-order shear deformation theory can accurately calculate in-plane deformation and stress for shell structure with span to thickness ratio than four, but cannot calculate the interlaminar stresses for composite plates and shells [15, 16]. Aköz et al. [17] used the finite element method to analyse circular beam with variable cross section

on elastic foundation under arbitrary load. Banan et al. [18] found the general finite element formula for spatial curved beams and arches on elastic foundation. Çalim et al. [19, 20] presented an effective method for analysing the dynamic performance of straight beams and curved beams on elastic foundation. Wang et al. [21], Öz et al. [22], Chen et al. [23], Malekzadeh et al. [24], and Wei et al. [25] studied the vibration problem of curved beam on elastic foundation. Based on Euler beam theory, Zhong et al. [26], Adineh et al. [27], Cong et al. [28], Duc et al. [29, 30], and Dung et al. [31] studied the nonlinear transient thermal response for FGM beam with unstable heat conduction and revealed the mechanical characteristics of FGM beams on the basis of tension free. The academic research on the curved beam on elastic foundation has made a wealth of research results, but there is little research in practical engineering applications.

In tunnelling engineering, the tunnel lining is closely contacted with rock mass, the tunnel lining can be regarded as curved beam on elastic foundation. Dai et al. [32] put forward the calculation model of tunnel lining deformation and internal force on the basis of the Qingdao overlapping tunnel on the beam theory on elastic foundation. Based on principle of initial parameter method, Sun et al. [33] established the initial parameter matrix equation for solving the internal force and deformation of concrete lining on curved beam on elastic foundation. Through on-site monitoring of steel arch stress and pressure of rock mass, Wen et al. [34] deduced an analytical formula for internal force of the primary support of tunnel on curved beam on elastic foundation. Based on the beam model on double elastic foundation and influence of uneven settlement of soft soil, Li et al. [35] established a plane numerical model and analysed the arrange of settlement joint and the longitudinal stress and deformation of the tunnel. In summary, more emphasis focuses on the analysis of the internal force and the uneven settlement in the longitudinal range of the superstructure of the tunnel, while the analysis of the tunnel invert is relatively rare.

In this paper, the curved beam model of the tunnel invert was established and the displacement equation of curved beam on elastic foundation under external load was deduced based on the differential equation of beam on elastic foundation. The displacement equation was used to calculate the settlement of tunnel bottom and the pressure of rock mass when the tunnel foundation of soft loess was strengthened and not strengthened by high pressure jet grouting pile.

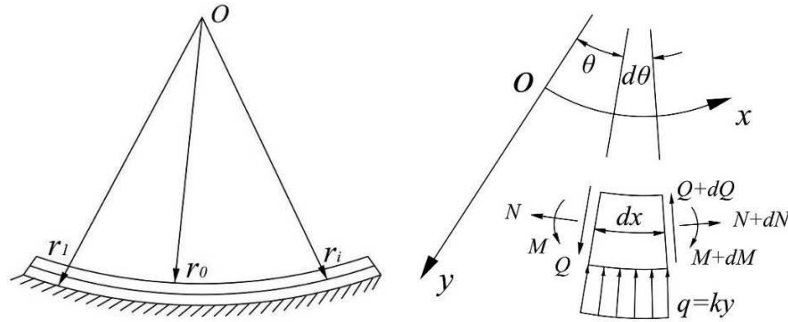
DIFFERENTIAL EQUATION OF CURVED BEAM ON ELASTIC FOUNDATION

The Winkler Foundation assumes that the settlement at any point on the surface of the foundation is proportional to the pressure on the unit area of the point. This assumption is the foundation for series of independent spring simulation on rigid base. When a point on the foundation surface is subjected to pressure p , because the springs are independent of each other, only the local settlement y is generated at this point, and no settlement occurs in other places. The foundation model is also called the local elastic foundation model. The formula is expressed in Equation 1.

$$p=Ky \quad (1)$$

Where K is the coefficient of foundation reaction which represents the pressure intensity required to produce the unit deformation at a point on the foundation (kN/m^3); p is the pressure intensity at any point on the foundation (kPa) and y is the deformation of the foundation at the point of pressure (m).

The local elastic foundation model is still applicable in the derivation of curved beam on elastic foundation. There is a constant cross-section beam on the Winkler Foundation (Figure 1(a)). The inner and outer radius of curved beam is r_0 and r_1 respectively, and the thickness of curved beam is $h=r_1-r_0$, the sectional area is A , the sectional inertia moment is I , and the centre radius is $r_i = (r_1+r_0)/2$. Assuming that there is no friction effect, the resistance of the foundation is proportional to the radial displacement of the curved beam.



(a) Curved beam with constant cross section (b) The force of element

Fig. 1 - Schematic diagram of curved beam on elastic foundation

We selected an arbitrary element $r_i d\theta$ from the beam as the object of analysis, as shown in Figure 1(b). $y(\theta)$ is the radial displacement; K is the coefficient of foundation reaction; $M(\theta)$ is the bending moment of initial section; $Q(\theta)$ is the shear force and $N(\theta)$ is the axial force. All the forces are positive in the direction of the Figure 1.

According to the force state of the element, as shown in Figure 1(b), the radial, tangential and centre moment balance equations of the infinitesimal element are established, as shown in Equations 2 to 4.

$$N(\theta)d\theta + Ky(\theta)r_i d\theta + dQ(\theta) = 0 \tag{2}$$

$$Q(\theta)d\theta - dN(\theta) = 0 \tag{3}$$

$$dM(\theta) - Qr_i d\theta = 0 \tag{4}$$

The radial displacement $y(\theta)$ of the curved beam has following relationship with internal force [34]:

$$\frac{d^2 y(\theta)}{d\theta^2} + y(\theta) = \frac{M(\theta)r_i^2}{EI} + \frac{N(\theta)r_i}{EA} \tag{5}$$

Where E is the elastic modulus of the curved beam.

To derive θ in the Equation 5 once and three times, we can get the following equation:

$$\frac{d^3 y(\theta)}{d\theta^3} + \frac{dy(\theta)}{d\theta} = \frac{r_i^2 dM(\theta)}{EId\theta} + \frac{r_i dN(\theta)}{EAd\theta} \tag{6}$$

$$\frac{d^5 y(\theta)}{d\theta^5} + \frac{d^3 y(\theta)}{d\theta^3} = \frac{r_i^2 d^3 M(\theta)}{EId\theta^3} + \frac{r_i d^3 N(\theta)}{EAd\theta^3} \tag{7}$$

Then we can obtain the Equation 8 by adding equation 6 and 7:

$$\frac{d^5 y(\theta)}{d\theta^5} + 2\frac{d^3 y(\theta)}{d\theta^3} + \frac{dy(\theta)}{d\theta} = \frac{r_i^2 d^3 M(\theta)}{EId\theta^3} + \frac{r_i d^3 N(\theta)}{EAd\theta^3} + \frac{r_i^2 dM(\theta)}{EId\theta} + \frac{r_i dN(\theta)}{EAd\theta} \tag{8}$$

We can get a five order radial displacement $y(\theta)$ differential equation with constant coefficients

based on simultaneous Equation 2, 4 and 8:

$$\frac{d^5 y(\theta)}{d\theta^5} + 2 \frac{d^3 y(\theta)}{d\theta^3} + n^2 \frac{dy(\theta)}{d\theta} = 0 \quad (9)$$

where: $n^2 = 1 + Kr_1 \left(\frac{r_i^3}{EI} + \frac{r_i}{EA} \right)$

The characteristic equation of the general solution of Equation 9 is as follows:

$$\lambda^5 + 2\lambda^3 + n^2\lambda = 0$$

The solution of the characteristic equation is:

$$\lambda_1 = 0, \lambda_{2,3} = \alpha \pm i\beta, \lambda_{4,5} = -(\alpha \pm i\beta)$$

where: $\alpha = \sqrt{\frac{n-1}{2}}$; $\beta = \sqrt{\frac{n+1}{2}}$; $i = \sqrt{-1}$.

So the general solution of the Equation 9 is:

$$y(\theta) = C_0 + C_1 \chi \alpha \theta \cos \beta \theta + C_2 \text{sh} \alpha \theta \cos \beta \theta + C_3 \chi \alpha \theta \sin \beta \theta + C_4 \text{sh} \alpha \theta \sin \beta \theta \quad (10)$$

The Equation 11 can be obtained by simultaneous Equation 3, 4 and 6:

$$Q(\theta) = \left(\frac{r_i^3}{EI} + \frac{r_i}{EA} \right)^{-1} \left[\frac{d^3 y(\theta)}{d\theta^3} + \frac{dy(\theta)}{d\theta} \right] \quad (11)$$

The Equation 12 can be got by simultaneous Equation 2 and 11:

$$N(\theta) = - \left(\frac{r_i^3}{EI} + \frac{r_i}{EA} \right)^{-1} \left[\frac{d^4 y(\theta)}{d\theta^4} + \frac{d^2 y(\theta)}{d\theta^2} \right] - Kr_1 y(\theta) \quad (12)$$

And the Equation 13 can be obtained by simultaneous Equation 5 and 12:

$$M(\theta) = \frac{EI}{r_i^2} \left\{ \frac{d^2 y(\theta)}{d\theta^2} + y(\theta) + \left(\frac{r_i^2 A}{I} + 1 \right)^{-1} \left[\frac{d^4 y(\theta)}{d\theta^4} + \frac{d^2 y(\theta)}{d\theta^2} \right] + \frac{r_i}{EA} Kr_1 y(\theta) \right\} \quad (13)$$

Finally, we can get analytical equation of internal force of curved beam by simultaneous Equation 2 to 6 and Equation 10:

$$Q(\theta) = T [C_1 (A_1 \text{sh} \alpha \theta \cos \beta \theta + A_2 \chi \alpha \theta \sin \beta \theta) + C_2 (A_1 \chi \alpha \theta \cos \beta \theta + A_2 \text{sh} \alpha \theta \sin \beta \theta) + C_3 (A_1 \text{sh} \alpha \theta \sin \beta \theta - A_2 \chi \alpha \theta \cos \beta \theta) + C_4 (A_1 \chi \alpha \theta \sin \beta \theta - A_2 \text{sh} \alpha \theta \cos \beta \theta)] \quad (14)$$

$$N(\theta) = -Kr_1 C_0 - C_1 (2\alpha \beta T \text{sh} \alpha \theta \sin \beta \theta) - C_2 (2\alpha \beta T \chi \alpha \theta \sin \beta \theta) + C_3 (2\alpha \beta T \text{sh} \alpha \theta \cos \beta \theta) + C_4 (2\alpha \beta T \chi \alpha \theta \cos \beta \theta) \quad (15)$$

$$M(\theta) = [(Kr_1 B_1 + 1)C_0 + C_1 (2\alpha \beta)(B_1 T - 1) \text{sh} \alpha \theta \sin \beta \theta + C_2 (2\alpha \beta)(B_1 T - 1) \chi \alpha \theta \sin \beta \theta - C_3 (2\alpha \beta)(B_1 T - 1) \text{sh} \alpha \theta \cos \beta \theta - C_4 (2\alpha \beta)(B_1 T - 1) \chi \alpha \theta \cos \beta \theta] / B_2 \quad (16)$$

Where: $A_1 = -2\alpha \beta^2$; $A_2 = -2\alpha^2 \beta$; $B_1 = r_i / (EA)$; $B_2 = r_i^2 / (EI)$; $T = \left(\frac{r_i^3}{EI} + \frac{r_i}{EA} \right)^{-1}$

THE DIFFERENTIAL EQUATION OF CURVED BEAM ON ELASTIC FOUNDATION UNDER SYMMETRIC LOAD

Section forms of the highway tunnel are generally symmetrical about the vertical axis, and no asymmetric loading tunnel, so it can be assumed that the load of tunnel rock mass is also symmetrical about vertical axis. The section where the tunnel centre is located is taken as the initial

section, the symmetry of structure and load can be used.

$$\left[\frac{dy(\theta)}{d(\theta)} \right]_{\theta=0} = 0,$$

$$[Q(\theta)]_{\theta=0} = 0$$

That is:

$$\alpha C_2 + \beta C_3 = 0$$

$$\beta C_2 - \alpha C_3 = 0$$

So we can get $C_2 = C_3 = 0$.

Then, Equations 10 and 14 to 16 can be simplified as follows:

$$y(\theta) = C_0 + C_1 \chi \alpha \theta \cos \beta \theta + C_4 \operatorname{sh} \alpha \theta \sin \beta \theta \quad (17)$$

$$-Q_0 = T[C_1(A_1 \operatorname{sh} \alpha \theta_0 \cos \beta \theta_0 + A_2 \chi \alpha \theta_0 \sin \beta \theta_0) + C_4(A_1 \chi \alpha \theta_0 \sin \beta \theta_0 - A_2 \operatorname{sh} \alpha \theta_0 \cos \beta \theta_0)] \quad (18)$$

$$-Q_0 = T[C_1(A_1 \operatorname{sh} \alpha \theta_0 \cos \beta \theta_0 + A_2 \chi \alpha \theta_0 \sin \beta \theta_0) + C_4(A_1 \chi \alpha \theta_0 \sin \beta \theta_0 - A_2 \operatorname{sh} \alpha \theta_0 \cos \beta \theta_0)] \quad (19)$$

$$-Q_0 = T[C_1(A_1 \operatorname{sh} \alpha \theta_0 \cos \beta \theta_0 + A_2 \chi \alpha \theta_0 \sin \beta \theta_0) + C_4(A_1 \chi \alpha \theta_0 \sin \beta \theta_0 - A_2 \operatorname{sh} \alpha \theta_0 \cos \beta \theta_0)] \quad (20)$$

In Equations 17 - 20, the internal force analytical equation of curved beam on elastic foundation can be obtained after the integral constants C_0 , C_1 and C_4 are calculated. And the integral constants C_0 , C_1 and C_4 can be obtained by the boundary conditions at both ends of the curved beam.

ESTABLISHMENT OF CURVED BEAM MODEL ON ELASTIC FOUNDATION OF TUNNEL INVERT

When the tunnel invert was completed, it would be affected by the weight of the lining and the load of the rock mass. The settlement of tunnel bottom would produce pressure on the foundation; similarly, the tunnel foundation would also produce the counterforce to the tunnel invert. Therefore, the tunnel invert could be regarded as a curved beam on the elastic foundation. The self-weight of tunnel lining and the pressure of rock mass could be equivalent to the load acting on both ends of tunnel invert, and the boundary conditions at the ends of the tunnel invert could be obtained by the equivalent load. Assuming that the tunnel invert was rigidly connected with the secondary lining of the tunnel, the equivalent load could be simplified as shear Q_0 , axial force N_0 and bending moment M_0 , as shown in Figure 2.

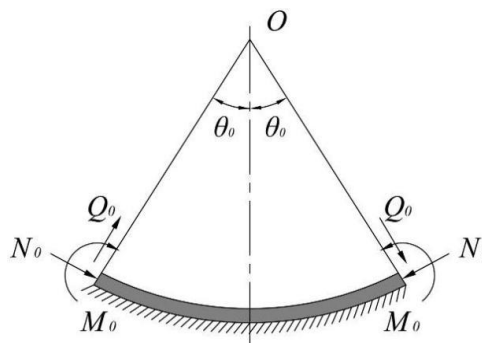


Fig. 2- Simplified calculation model of tunnel invert

Then the boundary condition of the beam end was:

$$\begin{aligned} Q(\theta_0) &= -Q_0 \\ N(\theta_0) &= -N_0 \\ M(\theta_0) &= -M_0 \end{aligned} \quad (21)$$

So we could establish a three-variable linear equation by simultaneous Equations 18 - 20, 21, as shown in Equation 22 - 24:

$$-Q_0 = T[C_1(A_1 sh\alpha\theta_0 \cos\beta\theta_0 + A_2 ch\alpha\theta_0 \sin\beta\theta_0) + C_4(A_1 ch\alpha\theta_0 \sin\beta\theta_0 - A_2 sh\alpha\theta_0 \cos\beta\theta_0)] \quad (22)$$

$$-N_0 = -Kr_1 C_0 - C_1(2\alpha\beta T sh\alpha\theta_0 \sin\beta\theta_0) + C_4(2\alpha\beta T ch\alpha\theta_0 \cos\beta\theta_0) \quad (23)$$

$$-M_0 = [(Kr_1 B_1 + 1)C_0 + C_1(2\alpha\beta)(B_1 T - 1)sh\alpha\theta_0 \sin\beta\theta_0 - C_4(2\alpha\beta)(B_1 T - 1)ch\alpha\theta_0 \cos\beta\theta_0] / B_2 \quad (24)$$

The pressure of rock mass of tunnel invert could be calculated according to literature (JTGD70-2004). The internal force of the corner of tunnel invert could be obtained according to the elastic centre method in Structural Mechanics. Then the shear force Q_0 , axial force N_0 and bending moment M_0 acting on both ends of tunnel invert could be obtained.

CALCULATION EXAMPLES OF THE SETTLEMENT OF TUNNEL BOTTOM AND PRESSURE OF ROCK MASS IN THE DAYOUSHAN TUNNEL

The foundation reinforcement section of the Dayoushan tunnel was selected as the typical section, and the above theoretical formula was tested by the engineering case. Firstly, the settlement of the tunnel bottom and pressure of rock mass were calculated when the foundation was not strengthened, and the law of the force and settlement of the tunnel bottom was explored. Then the settlement and pressure of rock mass of foundation reinforcement by high pressure jet grouting pile were calculated.

The composite lining was adopted in the Dayoushan tunnel, the excavation radius was 6.41m, and the excavation was constructed by bench method. The primary support of shallow section was sprayed with C25 concrete, and its thickness was 26cm; the secondary lining used C25 reinforced concrete, and its thickness was 50cm. The analysis of unit length of tunnel invert in shallow section was carried out. The geometric parameters and calculation parameters of tunnel invert were shown in Table 1 and Table 2 respectively.

Tab.1 - Geometric parameters of tunnel invert

Thickness h (m)	External radius r_1 (m)	Inner radius r_0 (m)	Central angle θ_0 ($^\circ$)	Cross-sectional area A (m^2)
50	12.561	12.061	26.9	5.87

Tab.2 - Calculation parameters of tunnel invert

Parameters	Value	Material
Elastic modulus of concrete E_c (GPa)	29.5	C25 concrete
Elastic modulus of reinforcement E_s (GPa)	200	Φ8 double layer steel mesh
Sectional area of tunnel invert steel bar (m^2)	5.03×10^{-5}	Φ8 double layer steel mesh
Coefficient of foundation reaction K_1 (kN/m^3)	8000	Soft foundation
Coefficient of foundation reaction K_2 (kN/m^3)	60000	Foundation reinforcement by high pressure jet grouting pile

The composite elastic modulus of reinforced concrete could be calculated according to formula (25):

$$EA = E_c A_c + E_s A_s \quad (25)$$

Where E_c and E_s is the elastic modulus of concrete and steel bars of curved beam on foundation reinforcement, respectively; A_c and A_s is the sectional area of concrete and steel bars.

$$E = (E_c A_c + E_s A_s) / A = 29.54 \text{ (GPa)}$$

The section ZK3+160 of Dayoushan tunnel was selected for the study. The depth of this section was 30m, and the rock mass was 13m collapsible loess and 17m non collapsible loess. The lateral pressure coefficient was calculated according to the lateral pressure and vertical pressure obtained from the previous monitoring, and $\lambda = 0.5$. The pressure of rock mass of shallow tunnel was calculated according to the literature (JTGD70-2004), the vertical pressure $q = 348 kN/m$ and horizontal lateral pressure $e = 174 kN/m$ were calculated, after the load was reduced by 60% (The pressure of rock mass acting on secondary lining accounted for about 60%), so $q_1 = 208 kN/m$ and $e_1 = 104 kN/m$. The internal force at the corner of tunnel invert could be obtained according to the elastic centre method in Structural Mechanics. The shear force $Q_1 = 342 kN$, the axial force $N_1 = 1233 kN$ and the bending moment $M_0 = 591 kN \cdot m$ were obtained.

Considering the influence of the weight of secondary lining, the cross section area of secondary lining was $11.52 m^2$, and the bulk density was $25 kN/m^3$. So the weight of unit length of the secondary lining was $281.25 kN$. The force produced by the weight of secondary lining acting on the tunnel invert could be calculated by the following formula:

$$\text{Shear force: } Q_2 = (281.25/2) \times \cos \theta_0 = 125 \text{ (kN)}$$

$$\text{Axial force: } N_2 = (281.25/2) \times \sin \theta_0 = 63 \text{ (kN)}$$

Therefore, the total force acting on both ends of the tunnel invert were:

$$\text{Shear force: } Q_0 = Q_1 + Q_2 = 467 \text{ (kN)}$$

$$\text{Axial force: } N_0 = N_1 + N_2 = 1296 \text{ (kN)}$$

$$\text{Bending moment: } M_0 = 591 \text{ (kN} \cdot \text{m)}$$

Settlement of tunnel bottom and pressure of rock mass when tunnel foundation was not strengthened

When the tunnel foundation was not reinforced, the tunnel foundation was soft soil, and the foundation stiffness was small, and the coefficient of foundation reaction was selected according to the empirical value [1], $K_f=8000 \text{ kN/m}^3$. The MATLAB program was compiled to solve the Equations 22 - 24, and the integral constant C_0, C_1 and C_4 in differential equations could be obtained.

$$C_0=12.39 \times 10^{-3}, C_1=4.16 \times 10^{-3}, C_4=7.95 \times 10^{-3}$$

We could get the Equation 26 - 29 when we substitute C_0, C_1 and C_4 into Equation 17 - 20:

$$y(\theta) = [12.39 + 4.16c\alpha\theta\cos\beta\theta + 7.95sh\alpha\theta\sin\beta\theta] \times 10^{-3} \tag{26}$$

$$Q(\theta) = T[4.16(A_1sh\alpha\theta\cos\beta\theta + A_2c\alpha\theta\sin\beta\theta) + 7.95(A_1c\alpha\theta\sin\beta\theta - A_2sh\alpha\theta\cos\beta\theta)] \times 10^{-3} \tag{27}$$

$$N(\theta) = [-12.39Kr_1 - 4.16(2\alpha\beta Tsh\alpha\theta\sin\beta\theta) + 7.95(2\alpha\beta Tc\alpha\theta\cos\beta\theta)] \times 10^{-3} \tag{28}$$

$$M(\theta) = [12.39(Kr_1B_1 + 1) + 4.16(2\alpha\beta)(B_1T - 1)sh\alpha\theta\sin\beta\theta - 7.95(2\alpha\beta)(B_1T - 1)c\alpha\theta\cos\beta\theta] \times 10^{-3} / B_2 \tag{29}$$

From Equations 26 to 29, the deflection, shear force, axial force and bending moment of any section of the tunnel invert can be obtained.

Internal force of tunnel invert

We calculated the internal force of any section of tunnel invert by Equation 27 - 29. Considering the symmetry of tunnel invert, half of the tunnel structure was calculated. The internal force diagrams were shown in Figure 3 - 5.

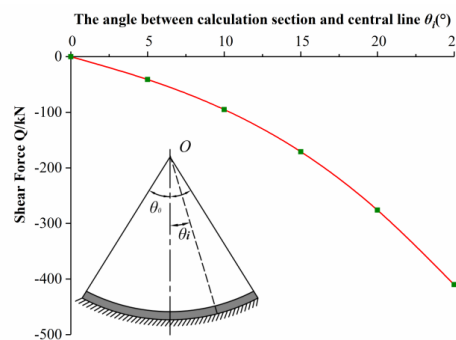


Fig.3 - The shear force of tunnel invert (kN)

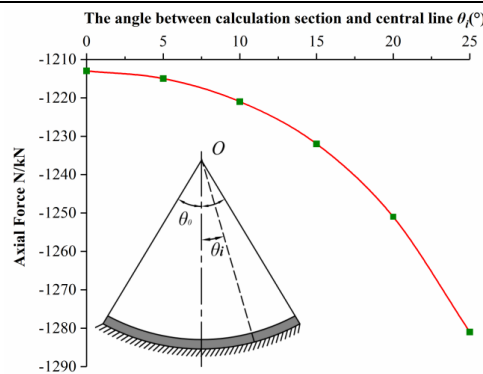


Fig.4 - The axial force of tunnel invert (kN)

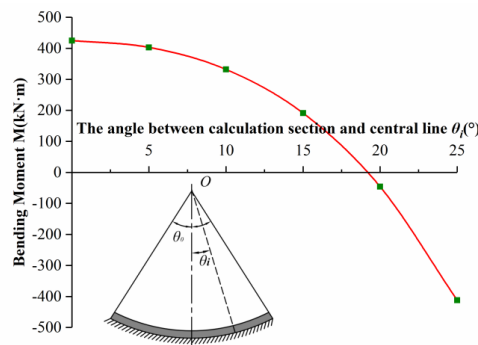


Fig.5 - The bending moment of tunnel invert (kN· m)

As shown in Figure 3 - 5, the centre and the waist of tunnel invert bore the tension stress, and the lateral bore compressive stress. However, the outer sides bore tension stress and the inner sides bore compressive stress at the corner of tunnel invert. The internal force at the corner of tunnel invert was greater, and there was stress concentration phenomenon.

The axial force of the tunnel invert was relatively large, and the maximum axial force was located at the corner of tunnel invert, which was $-1282kN$, and the direction was pointing to the inside of the tunnel. The shear force of the tunnel invert was relatively small, and the maximum shear force was located at the corner of tunnel invert, which was $-410kN$. The bending moment was relatively large, and the positive moment $425kN \cdot m$ was located at the centre of the tunnel invert. The force form was not conducive to the stability of the tunnel invert, and the inside of the tunnel invert was easy to be pulled to crack.

Settlement of tunnel bottom

The radial displacement of any section of tunnel invert could be calculated by Equation 26, the vertical displacement of different sections of tunnel invert could be obtained by formula $S_i = y_i \cos \theta_i$, the calculated results are shown in Table 3.

Tab.3 - Settlement of tunnel bottom (mm)

The angle between the calculation section and central line $\theta_i(^{\circ})$	Horizontal distance between calculation section and tunnel invert center L (m)	Radial displacement y (mm)	Settlement of tunnel bottom S (mm)
0	0	16.6	16.6
5	1.1	17.3	17.2
10	2.1	19.4	19.1
15	3.2	22.5	21.8
20	4.2	26.2	24.6
25	5.2	29.4	26.7

As shown in Table 3, the settlement of tunnel bottom was generally large when the tunnel foundation of soft loess was not reinforced. The settlement reached 26.7mm at the corner of the tunnel bottom, and the settlement at the centre of the tunnel bottom reached 16.6mm. The maximum differential settlement within the cross-section of tunnel bottom was as follow:

$$\Delta S_{\max} = 26.7 - 16.6 = 10.1(\text{mm})$$

The horizontal distance between the centre and corner point of tunnel bottom was 5.2m, therefore, the differential settlement of unit length was as follows:

$$\Delta S'_{\max} = \Delta S_{\max} / L = 1.94(\text{mm/m})$$

There is a big difference between the centre and corner point of tunnel bottom, so the tunnel invert was easy to crack. According to the distribution of the bending moment of the tunnel invert, the risk of cracking at the centre of tunnel invert was the biggest.

Pressure of rock mass of tunnel bottom

After calculating the radial displacement y of the tunnel invert, the elastic resistance of the tunnel foundation to the tunnel invert could be obtained by the formula (1). The normal elastic resistance was approximately equal to the pressure of rock mass of the tunnel bottom, assuming that the frictional force was not taken into account. The calculation results of pressure of rock mass were shown in Figure 6.

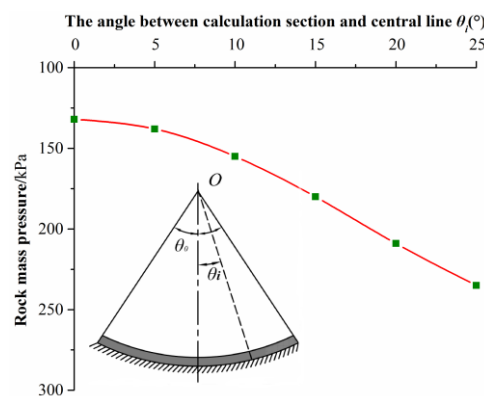


Fig.6 - pressure of rock mass of tunnel bottom (kPa)

As shown in Figure 6, rock mass at the tunnel bottom was mainly subjected to compressive stress. The compressive stress at the centre of tunnel invert centre was the minimum, $132kPa$. The pressure of rock mass increased uniformly from the centre to the corner of tunnel invert, and the maximum compressive stress was reached $235kPa$ at the corner of tunnel invert. The stress concentration was easy to occur due to the structural reasons at the corner of tunnel invert. The weight of secondary lining and the pressure of rock mass acted at the corner of tunnel invert, and the corner of tunnel invert bore the large load. There should be smooth transition between side wall and the corner of tunnel invert, and the section size at the corner of tunnel invert could be increased appropriately to improve the force situation in the process of tunnel construction.

Settlement and pressure of rock mass of foundation reinforcement by high pressure jet grouting pile

When the tunnel foundation was reinforced by high pressure jet grouting pile, the bearing capacity and the stiffness of the tunnel foundation was greatly improved. The coefficient of foundation reaction was determined by field loading test, $K_2=60000 kN/m^3$. The MATLAB program was compiled to solve the Equations 22 - 24, and the integral constant C_0 , C_1 and C_4 in differential equations could be obtained.

$$C_0=16.6 \times 10^{-4}, C_1=-1.4 \times 10^{-4}, C_4=6.8 \times 10^{-4}$$

We can get the Equation 30 - 33 when substitute C_0 , C_1 and C_4 into Equation 17 - 20:

$$y(\theta) = [16.6 - 1.4c\alpha\theta\cos\beta\theta + 6.8s\alpha\theta\sin\beta\theta] \times 10^{-4} \quad (30)$$

$$Q(\theta) = T[-1.4(A_1s\alpha\theta\cos\beta\theta + A_2c\alpha\theta\sin\beta\theta) + 6.8(A_1c\alpha\theta\sin\beta\theta - A_2s\alpha\theta\cos\beta\theta)] \times 10^{-4} \quad (31)$$

$$N(\theta) = [-16.6Kr_1 + 1.4(2\alpha\beta T s\alpha\theta\sin\beta\theta) + 6.8(2\alpha\beta T c\alpha\theta\cos\beta\theta)] \times 10^{-4} \quad (32)$$

$$M(\theta) = [16.6(Kr_1B_1 + 1) - 1.4(2\alpha\beta)(B_1T - 1)s\alpha\theta\sin\beta\theta - 6.8(2\alpha\beta)(B_1T - 1)c\alpha\theta\cos\beta\theta] \times 10^{-4} / B_2 \quad (33)$$

From Equations 30 - 33, the deflection, shear force, axial force and bending moment of any section of the tunnel invert could be obtained.

Internal force of tunnel invert

We calculated the internal force of any section of tunnel invert by Equation 31 - 33. Considering the symmetry of tunnel invert, half of the tunnel structure was calculated. The internal force diagram was shown in Figure 7 - 9.

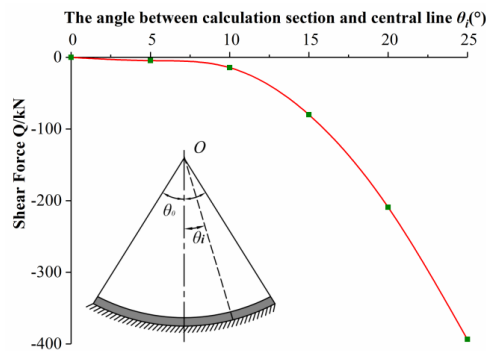


Fig.7 - The shear force of tunnel invert (kN)

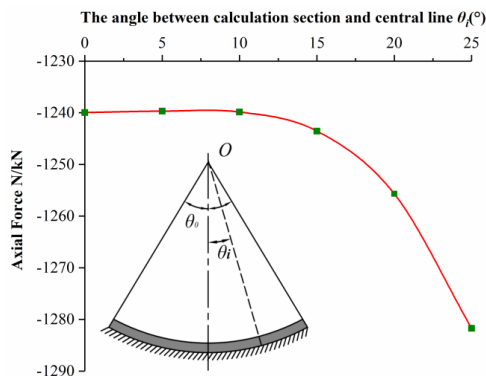


Fig.8 - The axial force of tunnel invert (kN)

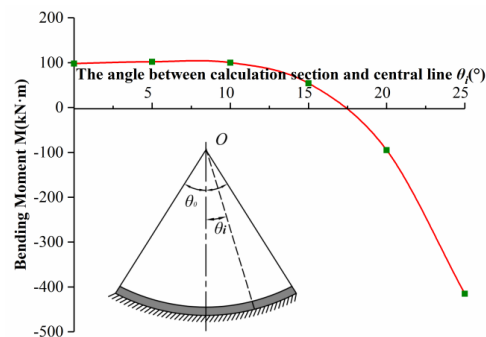


Fig. 9 The bending moment of tunnel invert (kN.m)

As shown in Figure 7 - 9, after the reinforcement of the tunnel foundation, the internal force of the tunnel invert was similar to that without reinforcement. The inside at the centre and the waist of tunnel bottom bore the tension stress, and the lateral bore compressive stress. The outer side at the corner of tunnel invert bore tension stress, and the inner side bore compressive stress. However, the stress condition of the tunnel invert had been improved. The axial force at the centre the tunnel invert increased slightly and the shear force and bending moment decreased. The maximum positive bending moment at the centre of the tunnel invert decreased to $98\text{kN}\cdot\text{m}$, which greatly improved the stress state of the tunnel invert.

Settlement of tunnel bottom

The radial displacement of any section of tunnel invert could be calculated by Equation 30, the

vertical displacement of different sections of tunnel invert could be obtained by formula $S_i = y_i \cos \theta_i$, the calculation results were shown in Table 4.

Tab.- 4 Settlement of tunnel bottom (mm)

The angle between the calculation section and central line $\theta_i(^{\circ})$	Horizontal distance between calculation section and tunnel invert center L (m)	Radial displacement y (mm)	Settlement of tunnel invert S (mm)
0	0	1.5	1.5
5	1.1	1.7	1.7
10	2.1	2.2	2.2
15	3.2	3.1	3.0
20	4.2	4.1	3.9
25	5.2	4.7	4.3

As shown in Table 3 and Table 4, the settlement of the tunnel bottom was greatly reduced when the tunnel foundation was reinforced by jet grouting pile. The settlement at the corner of the tunnel invert decreased to 4.3mm, and the differential settlement of unit length was as follows:

$$\Delta S_{\max}' = \Delta S_{\max} / L = 0.54(\text{mm/m})$$

The settlement of the tunnel invert was smaller and the overall settlement was more harmonious, which met the requirements of the standard. Thus, the bearing capacity and stiffness of tunnel foundation was greatly improved after the jet grouting pile was used to reinforce the tunnel foundation, and the reinforcement effect was good.

Pressure of rock mass of tunnel bottom

The calculation results of pressure of rock mass were shown in Figure 10.

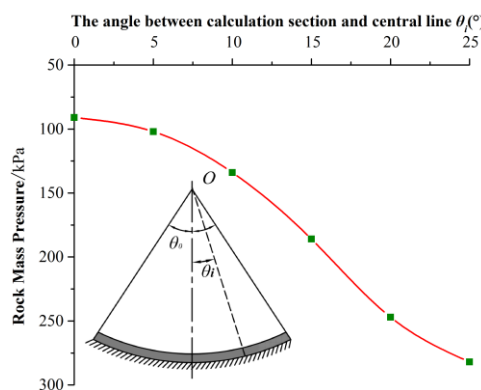


Fig.10 - pressure of rock mass of tunnel bottom (kPa)

As shown in Figure 10, the pressure of rock mass at tunnel bottom was similar to that without reinforcement, the compressive stress at the centre of tunnel invert was the smallest, and the

maximum compressive stress at the corner of tunnel invert, after foundation reinforcement, the compressive stress at the corner of tunnel invert increased more obviously, and increased from $235kPa$ to $282kPa$. The stress concentration phenomenon at the corner of tunnel invert was more obvious, which was related to the substantial increase of the bearing capacity of the tunnel foundation after the foundation reinforcement.

CONCLUSIONS

(1) When the tunnel foundation was not strengthened, the inside at the centre and the waist of tunnel invert bore the tension stress, and the lateral bore compressive stress; the outside at the foot of the tunnel invert bore tension stress and the inside bore compressive stress; the internal force at the foot of tunnel invert was greater, the axial force and bending moment of the tunnel invert were relatively large, and the greater positive moment was inside the centre of the tunnel invert. The maximum positive bending moment at the centre of the tunnel invert decreased greatly after the reinforcement of the tunnel foundation.

(2) When the tunnel foundation was not strengthened, the settlement of tunnel bottom was generally large; the settlement at the corner of tunnel invert reached $26.7mm$, and the maximum differential settlement within the range of tunnel invert reached $10.1mm$; the risk of tension crack at the centre of tunnel invert was larger. After tunnel foundation was strengthened, the settlement of tunnel bottom decreased greatly, and the overall settlement was more coordinated, and the reinforcement effect was good.

(3) When the tunnel foundation was not strengthened, theoretical calculation results showed that the rock mass at tunnel bottom was mainly subjected to compressive stress; the compressive stress at the centre of the tunnel invert was minimum, and it was large at the corner of tunnel invert. After the tunnel foundation was strengthened, the pressure of rock mass at tunnel bottom was similar to that without reinforcement; the compressive stress at the corner of tunnel invert increased obviously and the stress concentration phenomenon was more obvious.

COMPETING INTERESTS

The authors declare that there is no conflict of interests regarding the publication of this paper.

ACKNOWLEDGEMENTS

This work is financially supported by the Brainstorm Project on Social Development of Shaanxi Provincial Science and Technology Department (No. 2016SF-412) and the Special Fund for Basic Scientific Research of Central Colleges of Chang'an University (No. 310821172004, No. 310821153312, No. 310821165011) and the National Key R&D problem of China (No. 2017YFC0805306). We also acknowledge the editor for the valuable suggestion.

REFERENCES

- [1] S. Chakraborty, S. K. Sarkar, "Analysis of a curved beam on uncertain elastic foundation", *Finite Elements in Analysis and Design*, vol. 36, no. 1, pp. 73-82, 2000.
- [2] A. M. Talmon, A. Bezuijen, "Analytical model for the beam action of a tunnel lining during construction", *International Journal for Numerical & Analytical Methods in Geomechanics*, vol. 37, no. 2, pp. 181-200, 2013.

- [3] L. Zhang, M. H. Zhao, C. J. Shi, H. Zhao, "Settlement Calculation of Composite Foundation Reinforced with Stone Columns", *International Journal of Geomechanics*, vol. 13, no. 3, pp. 248-256, 2013.
- [4] W. Wang, R. A. Shenoi, "Delamination modelling of a curved composite beam subjected to an opening bending moment", *Journal of Strain Analysis for Engineering Design*, vol. 38, no. 5, pp. 453-457, 2003.
- [5] E. L. Tan, B. Uy, "Experimental study on straight composite beams subjected to combined flexure and torsion", *Journal of Constructional Steel Research*, vol. 65, no. 8, pp. 1855-1863, 2009.
- [6] N. J. Pagano, "Analysis of The Flexure Test of Bidirectional Composites", *Journal of Composite Materials*, vol. 1, no. 4, pp. 336-342, 1967.
- [7] N. J. Pagano NJ, "Exact solution for composite laminates in cylindrical bending", *Solid Mechanics & Its Applications*, vol. 3, no. 3, pp. 398-411, 1969.
- [8] R. D. Chien, C. S. Chen, "Nonlinear vibration of laminated plates on a nonlinear elastic foundation", *Composite Structures*, vol. 70, no. 1, pp. 606-615, 2005.
- [9] H. S. Shen, F. Lin, Y. Xiang, "Nonlinear vibration of functionally graded graphene-reinforced composite laminated beams resting on elastic foundations in thermal environments", *Nonlinear Dynamics*, vol. 90, no. 2, pp. 899-914, 2017.
- [10] F. Tornabene, N. Fantuzzi, M. Baccocchi, J. N. Reddy, "A posteriori stress and strain recovery procedure for the static analysis of laminated shells resting on nonlinear elastic foundation", *Composites Part B-Engineering*, vol. 126, pp. 162-191, 2017.
- [11] S. G. Lekhnitskii, "Bending of a curved rod by moments and a force applied at the ends, theory of elasticity of an anisotropic body", *Moscow: Mir. Pub*, 1981.
- [12] ASTM D6415/D6415M-06a, "Standard test method for measuring the curved beam strength of a fiber-reinforced polymermatrix composite", *West Conshohocken: American Society for Testing and Materials*, 2013.
- [13] R. A. Shenoi, W. Wang, "Flexural behaviour of a curved orthotropic beam on an elastic foundation", *Journal of Strain Analysis for Engineering Design*, vol. 36, no. 1, pp. 1-15, 2001.
- [14] M. Arici, M. F. Granata, "Generalized curved beam on elastic foundation solved by transfer matrix method", *Structural Engineering and Mechanics*, vol. 40, no. 2, pp. 279-295, 2011.
- [15] K. H. Lo, R. M. Christensen, E. M. Wu, "Stress solution determination for high order plate theory", *International Journal of Solids & Structures*, vol. 14, no. 8, pp. 655-662, 1978.
- [16] J. N. Reddy, "A Simple Higher-Order Theory for Laminated Composite Plates", *Journal of Applied Mechanics*, vol. 51, no. 4, pp. 745-752, 1984.
- [17] A. Y. Aköz, F. Kadioğlu, "The mixed finite element solution of circular beam on elastic foundation", *Computers & Structures*, vol. 60, no. 4, pp. 643-651, 1996.
- [18] M. R. Banan, G. Karami, M. Farshad, "Finite element analysis of curved beams on elastic foundations", *Computers & Structures*, vol. 32, no. 1, pp. 45-53, 1989.
- [19] F. F. Çalım, F. G. Akkurt, "Static and free vibration analysis of straight and circular beams on elastic foundation", *Mechanics Research Communications*, vol. 38, no. 2, pp. 89-94, 2011.
- [20] F. F. Çalım, "Forced vibration of curved beams on two-parameter elastic foundation", *Applied Mathematical Modelling*, vol. 36, no. 3, pp. 964-973, 2012.
- [21] T. M. Wang, W. F. Brannen, "Natural frequencies for out-of-plane vibrations of curved beams on elastic foundations", *Journal of Sound & Vibration*, vol. 84, no. 2, pp. 241-246, 1982.
- [22] H.R.Öz, M. Pakdemirli, E. Özkaya, "Non-linear vibrations of a slightly curved beam resting on a non-linear elastic foundation", *Journal of Sound & Vibration*, vol. 212, no. 2, pp. 295-309, 1998.

- [23] C. S. Chen, A. H. Tan, R. D. Chien, "Non-linear oscillations of orthotropic plates on a non-linear elastic foundation", *Journal of Reinforced Plastics and Composites*, vol. 28, no. 7, pp. 851-867, 2009.
- [24] P. Malekzadeh, M. R. G. Haghghi, M. M. Atashi, "Out-of-plane free vibration of functionally graded circular curved beams in thermal environment", *International Journal of Applied Mechanics*, vol. 2, no. 3, pp. 635-652, 2010.
- [25] C. L. Wei, C. S. Chen, C. S. Shih, Y. C. Chang, Nonlinear vibration of initially stressed hybrid composite plates on elastic foundations, *Mechanics of Composite Materials*, vol. 48, no. 4, pp. 467-482, 2012.
- [26] J. Zhong, Y. Fu, Y. Chen, Y. Li, "Analysis of nonlinear dynamic responses for functionally graded beams resting on tensionless elastic foundation under thermal shock", *Composite Structures*, vol. 142, pp. 272-277, 2016.
- [27] M. Adineh, M. Kadkhodayan, "Three-dimensional thermo-elastic analysis and dynamic response of a multi-directional functionally graded skew plate on elastic foundation", *Composites Part B-Engineering*, vol. 125, pp. 227-240, 2017.
- [28] P. H. Cong, P. T. N. An, N. D. Duc, "Nonlinear stability of shear deformable eccentrically stiffened functionally graded plates on elastic foundations with temperature-dependent properties", *Science and Engineering of Composite Materials*, vol. 24, no. 3, pp. 455-469, 2017.
- [29] N. D. Duc, P. D. Nguyen, N. D. Khoa, "Nonlinear dynamic analysis and vibration of eccentrically stiffened S-FGM elliptical cylindrical shells surrounded on elastic foundations in thermal environments", *Thin-walled structures*, vol. 117, pp. 178-189, 2017.
- [30] N. D. Duc, V. D. Quang, V. T. T. Anh, "The nonlinear dynamic and vibration of the S-FGM shallow spherical shells resting on an elastic foundations including temperature effects", *International Journal of Mechanical Sciences*, vol. 123, pp. 54-63, 2017.
- [31] D. V. Dung, P. M. Vuong, "Analytical investigation on buckling and postbuckling of FGM toroidal shell segment surrounded by elastic foundation in thermal environment and under external pressure using TSDT", *Acta Mechanica*, vol. 228, no. 10, pp. 3511-3531, 2017.
- [32] C. Q. Dai, L. Wang, Y. J. Wang, "Deformation study of Lining on Overlap Tunnels Based on Elastic Foundation Beam", *Applied Mechanics & Materials*, vol. 94, no. 10, pp. 1875-1878, 2011.
- [33] F. X. Sun, X. H. Cai, Y. H. Zhu, "Analytical solution of internal force and displacement in multi-center circular arc tunnel lining based on initial parameter method", *Rock & Soil Mechanics*, vol. 30, no. 4, pp. 1127-1130, 2009. (in Chinese)
- [34] J. Z. Wen, Y. X. Zhang, C. Wang, "Back analysis of internal force of initial support in tunnel based on touch stress", *Rock & Soil Mechanics*, vol. 32, no. 8, pp. 2467-2472, 2011. (in Chinese)
- [35] Z. Li, S. Y. Chen, "Calculation and analysis of longitudinal settlement joint of shield tunnel based on dual elastic foundation beam", *World Automation Congress. IEEE*, pp. 1-6, 2012.

APPLICATION OF GEOSTATISTICS IN THE ESTIMATION OF SUJISHAN GRAPHITE DEPOSITS, MONGOLIA

Huang Song^{1 3}, Huaming An²

- 1. Beijing University of Technology and Science, Civil and Resource Engineering College, China;*
- 2. Kunming University of Science and Technology, Faculty of Public Security and Emergency Management; Huaming.an@yahoo.com*
- 3. Australian RPMGlobal Mining Consultant Company.*

ABSTRACT

In this paper, the author used mine 3D software to establish the 3D geological model of Sujishan Graphite deposit, and applied geostatistics to estimate the resource, offered references for next exploration and mining. Surpac was used to set up geological database of Sujishan Graphite deposit, topographical DTM, ore body model and grade model, 3D of drilling database, also analysis the spatial grade distribution in reality. Based on geostatistics, drilling samples are composited and statistically analysed and eliminate the impact of outliers. Experimental variograms were constructed for the striking, dipping and vertical directions. Grade and resource are estimated by ordinary kriging. Comparing to the traditional estimation methods, this 3D software gives reliable estimation, which provides references for dynamic management of mine's resource.

KEYWORDS

Surpac software, 3D model, Geostatistics, Ordinary kriging, Resource estimation

INTRODUCTION

Geostatistics is based on regionalized variables and uses variability as a tool for research. It is a science that studies natural phenomena that are both random and structural, or spatially related and dependent. Any research related to the structural and random nature of spatial data, or spatial correlation and dependence, and any optimal unbiased interpolation estimation of these data, or simulation of the discreteness and volatility of these data can be researched based on geostatistics. The famous French statistician Georges Matheron first proposed the concept of geostatistics in the article *Traité de géostatistique appliquée* [1]. Professor Matheron proposed the concept of regionalized variable based on his own research results, and finally created geostatistics subject. According to geostatistical theory, geological features can be represented by the spatial distribution characteristics of regionalized variables. In the process of studying the spatial distribution characteristics of regionalized variables, Variogram is often used as the main research tool for analysis. The similarity between geostatistics and classical statistics is that they all need enough samples first, and then determined by analysing the relationship between the frequency distribution of the sample attribute values or the mean, maximum and minimum, variance, standard deviation and their corresponding relationship, spatial distribution characteristics and correlation. The differences between geostatistics and classical statistics include: classical statistical research subjects are mainly pure random variables, while geostatistical research subjects are mainly

regionalized variables; classical statistical requirements can be used for repeated sampling and observation experiments, etc., and the variables studied by geostatistics are generally not capable of repeated sampling and observational experiments; the data of classical statistical studies is independent of each other and the data of geostatistical studies is spatially correlated; classical statistics are studied by frequency distribution maps. And geostatistics is based on spatial distribution characteristics [2, 3].

The three-dimensional geological modelling can reflect the results and characteristics of the ore body, which enables the geologists to have a more intuitive and clear understanding of the ore body. Since the 1990s, a large number of 3D geological software based on geostatistical theory has been developed globally. The theory of geostatistics has been continuously supplemented and improved. At the same time, geostatistical analysis and commercial software have sprung up. IDRISI, GEO-EAS, GS+, Surfer, GeoDA, Surpac, Datamine, Vulcan, CGES, 3Dmine, DIMINE and other pieces of software are representative development software. [4, 5] With the continuous development of geostatistical theory, new geostatistical algorithms are gradually integrated into geostatistical software. Stanford University's GSLIB and SGEMS are the two most representative of the software, a large number of random simulation algorithms and other application modules are integrated into two pieces of software.

In this study, the Surpac mining software was used to construct a three-dimensional model of the Sujishan graphite deposit in Mongolia, and the grade distribution of the Sujishan graphite deposit was statistically analysed. The Ordinary Kriging method based on geostatistical theory was adopted, and the grade original data was used. The ore body parameters were estimated and finally the distribution of mine resource quantity is obtained, which provides technical support for the optimization of mine resource quantity control and the establishment of "digital mine" [6-8].

Geological characteristics of the mining area

1) Formation: The project area is located in the Xingmeng orogenic belt between the North China and Siberian land masses and forms the eastern part of the Ural-Mongolian metallogenic belt. The sedimentary strata in the mining area are mainly the Upper Proterozoic - Cretaceous strata. The Permian - Cretaceous strata are mainly distributed in the southeast of the mining area. Both strata are unconformity contact relationships which are controlled by the structure. Graphite - bearing shale is controlled by structural alteration zones.

There is a small number of metamorphic rocks of the Upper Proterozoic and sedimentary rocks of the Lower Cretaceous in the mining area. The earliest metamorphic rocks are part of the green schist in the combination of Delong (NP2-3 do), and the overlying rock Sujishan (NP3-su) is a combination of natural graphite schist, Chaganwula (NP3 cu) combined limestone, etc. The youngest rock is the relatively loose sediment of the Lower Cretaceous Ulande (K1-ud) combination.

2) Structure: The fractured structures in the mining area are developed in the NE - NEE and near SN faults, both of which are post-mineral faults. In the mining area, there is a monoclinic structure that is gently inclined to the southeast. The meridional structure is formed only at the northeast end of the mining area, so that the ore belt is divided into two parts with a fault contact in the middle. In the direction of the fold hub, the lithology of the core at 32° northeast is limestone. The obliquely turned end and the west wing are cut by F3 fracture, and the main ore belt on the west side is divided into two parts.

3) The magmatic rocks: Magmatic rock are widely distributed, mainly intrusive rocks, which belong to the Caledonian and Early Hercynian, respectively. It is mainly composed of gabbro, diorite, quartz diorite, biotite granite and a small amount of alkaline white granite in the Devonian invasion. The eruptive rocks are mainly Yinggan, Andesite, and Liu Rocks and tuffs. The formation of graphite

ore in the area is closely related to frequent magmatism and regional metamorphism. The intrusive activity after mineralization is only limited quartz vein, which has little effect on the deposit.

4) Characteristics of ore bodies: The graphite ore body in the mining area is located in the upper part of the Upper Proterozoic Sujishan combination metamorphic rock series. It is a set of graphite schist layer containing sericite schist. Through the surface geological and drilling verification work, the different sized graphite ore bodies are exposed in the mining area whose number is about 20. The elevation of the ore body is in the range of 1271~1286m above sea level. The ore body is layered and undulated along the stratum. The clusters are arranged in parallel, the ore bodies are about 30~50m apart, and the ore body overall striking is 40~42°, dipping to the south, gently inclined, and the dip degree is 5~47°.

5) Ore composition: The ore structure is a fine-grained Granitic metamorphic texture. The ore structure is a schistose structure, banded structure, dense massive structure. The ore mineral in the ore is graphite, and the gangue minerals main include quartz (5~49%), sericite, biotite, lithium mica (10~15%), goethite, limonite, chlorite, and pyroxene, copper ore, etc.

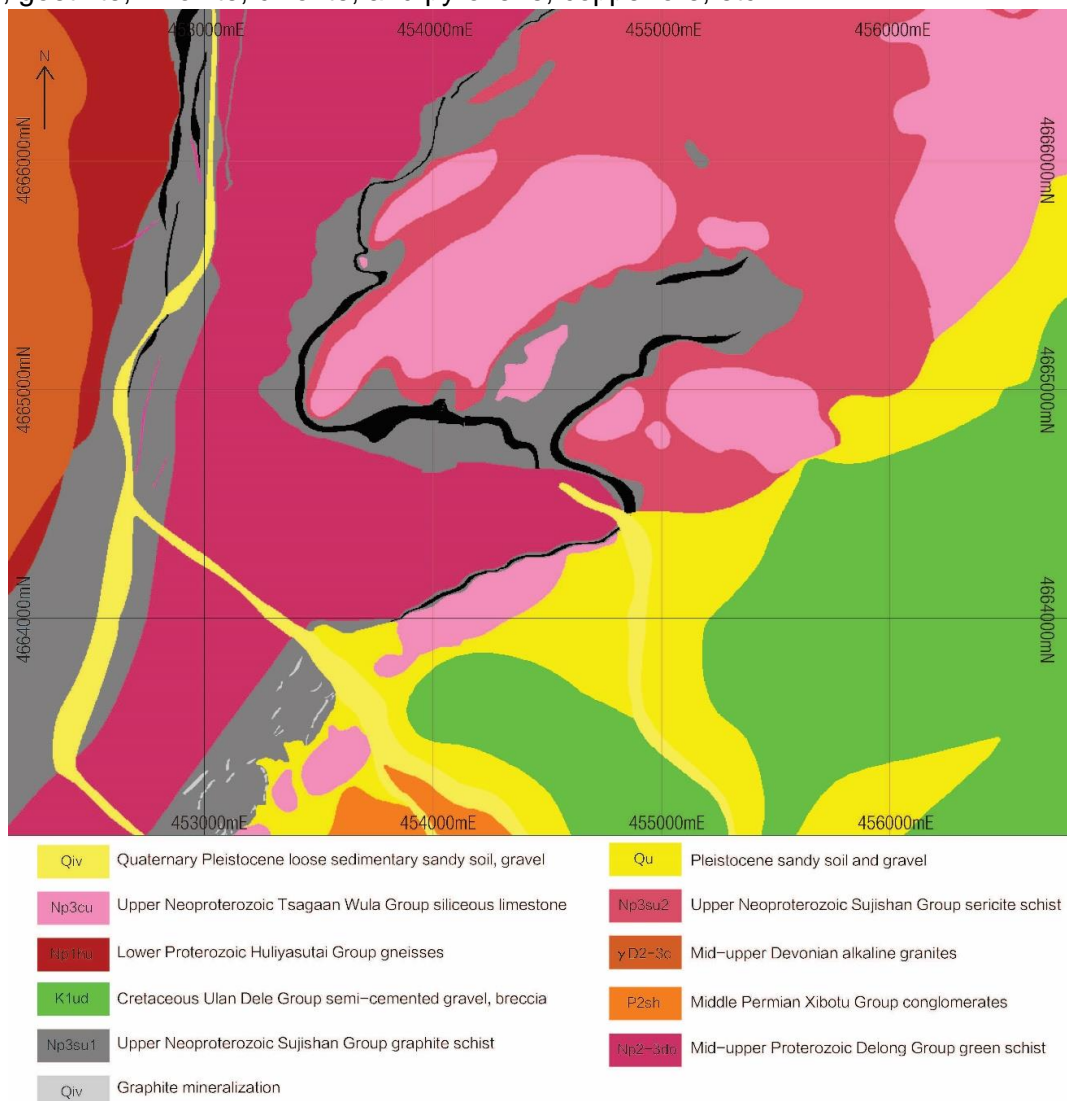


Fig. 1 - Geological map of the Sujishan graphite deposit in Mongolia

Model construction and resource estimation

Database construction

The database establishment procedure mainly includes collecting all exploration data in the mining area. The geological data includes trenching, drilling and pit exploration results which can be used for recording the distribution of lithology and faults through geological logging, and then importing the data into Surpac to establish a 3D geological database with proper format. The use of geological databases to store geologically relevant information can establish a three-dimensional geological model of the mining area more accurately and completely and construct the foundation for subsequent resource estimation. In this paper, the relevant geological information of 85 boreholes and trenches in the mining area were collected, and four basic tables such as collar, survey, assay and lithology tables were established. Among them, the collar table mainly includes the collar coordinates of the borehole, drilling depth, drilling type, drilling time and hole path; the survey table mainly includes the azimuth and dip of the drilling and the depth of the inclination; the assay table mainly includes the sample assay results (mainly including grade information of total carbon, graphite carbon and other elements); the lithology table mainly includes information of rock types, strata, minerals, alterations and so on. Finally, the established geological database is verified in 3D software, and the digital terrain model (DTM) and the 3 digital model (3DM) are created by Surpac software as we can see in the Figure 2 below.

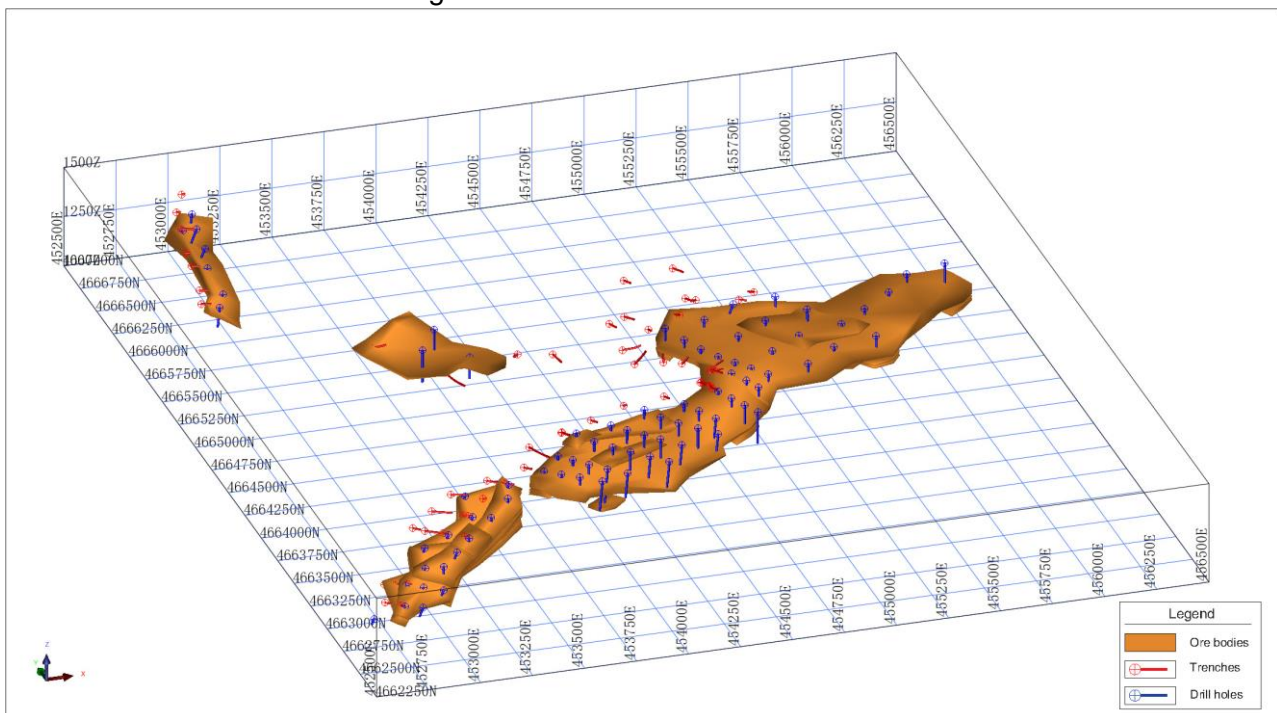


Fig. 2 - 3D view of the ore body and borehole

Composite sample and variogram analysis

Geostatistical analysis of the database data, and the estimation of the block model with using the sample grade or body weight value, both require that each sample has the same weight, the sample length of each sample is consistent. Thus, we can ensure that the analytical calculation results are in reasonable estimation process. Therefore, it is essential to perform a composition of samples before performing basic statistical analysis and variogram analysis of the samples. There are various methods for compositing samples, such as compositing along drilling direction, compositing by bench, compositing by geology domain, and internal compositing in the ore bodies. At this time, the combination of compositing along drilling direction and compositing by geology

domain method was applied. In the process of sample compositing, various factors that may affect the determination of the length of the compositing sample were considered, such as the average length of the original samples, the exploration spacing, the minimum mining unit, the block model block size, and so on.

A graphite mineralization wireframe ("domain") was used to encode the assay database to allow identification of resource intersections. The length of the sample is then checked to determine the optimal composite length. The most common sample length inside the mineralized wireframe is 2 meters, so this length is chosen as the sample composite length and Surpac is used to extract the composite sample. After the sample compositing, the graphite carbon data was statistically analyzed by statistical software of Supervisors. The analysis results showed that the composite samples still follow the lognormal distribution (Figure 3a, Figure 3b), indicating that the grade of graphite carbon is still a continuous random variable after the sample compositing. This provides a prerequisite for experimental semivariogram analysis. Although simple statistical analysis can reflect the global characteristics of the geological body, it still cannot reflect the changes of the sample in the local range and specific direction (striking, dipping, and vertical). Compositing the samples, and then analyzing the semivariogram of the composited results is a good solution to the problem of analyzing local geological features.

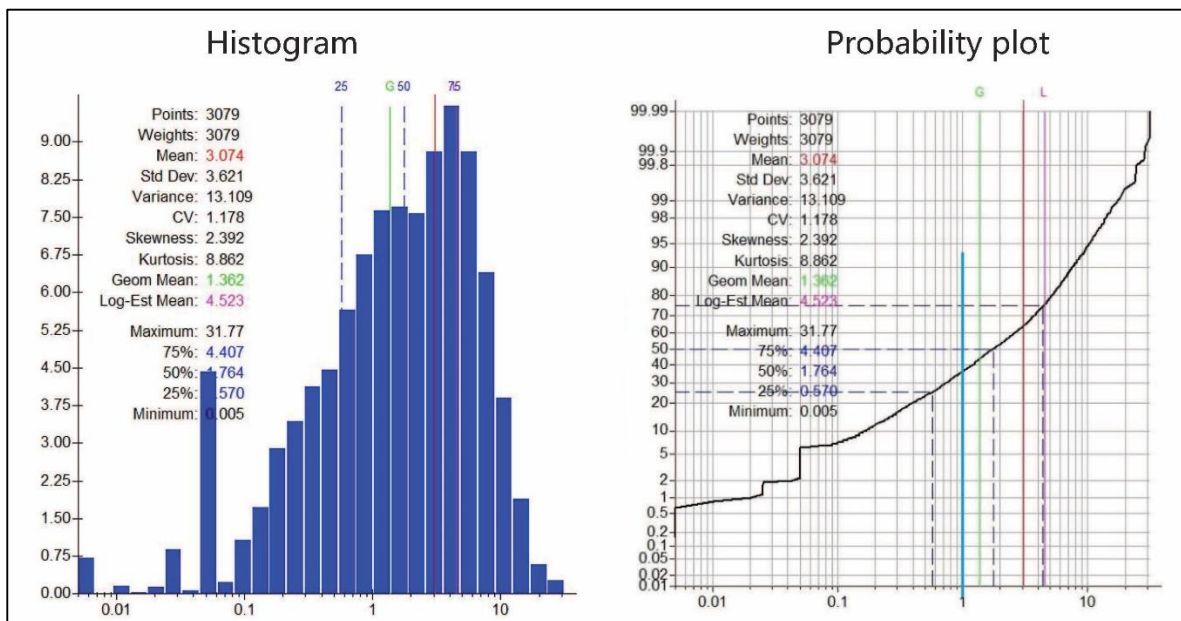


Fig. 3 - sample histogram and probability distribution

Variogram analysis

In order to describe the variability of the ore grade distribution in the deposit, we often use the mean, maximum value, variance, standard deviation and other parameters of the sample as analytical tools for common statistics, and these statistics can only summarize the characteristics of the samples. The global characteristics of the values do not simply reflect changes in the sample and in a particular direction. The introduction of experimental variograms into geostatistics can accurately reflect the correlation and randomness of regionalized variables, especially the stochasticity of grades to reflect the structurality of regionalized variables. As the spatial distribution of the ore body is often not exactly the same in different directions, the so-called spatial anisotropy, the regionalization variable can be used to characterize the mine that changes continuously according to different directions. In the analysis and calculation of the experimental semi-variogram,

the main mineralization extension direction, the secondary mineralization extension direction and the third mineralization extension direction will be analysed. Hypothetical regionalization variable $Z(x)$ satisfy the second-order stationary hypothesis and the eigen hypothesis, whose mathematical expectation is m , covariance function and variogram $c(h)$ exists, according to the basic concept of geostatistics, the variogram formula is as follows:

$$\gamma(h) = \frac{1}{2N(h)} \sum_{i=1}^{N(h)} [Z(x_i) - Z(x_i + h)]^2 \quad (1)$$

In formula (1), $N(h)$ is the step size, h is the number of pairs of data; $Z(x_i)$ with $Z(x_i + h)$ is a two-point sample value that is separated by h . Because the variogram is a statistical method, the more samples are taken at a certain step size, the more reliable the variogram estimate is.

When performing a simple Kriging estimate, we assume that the average of the entire region is known, but in fact the overall mean is difficult to be found directly, unless the mean of the known sample points is used to represent the overall sentence. The ordinary Kriging estimation method does not depend on the mathematical expectation that the random variable $Z(x)$ is known for all x . The ordinary Kriging interpolation formula is:

$$Z^*(x) = \sum_{i=1}^n \lambda_i Z(x_i) \quad (2)$$

In formula (2) $Z(x_i)$ is the sample value, $Z^*(x)$ is the estimated value, λ_i is the weight coefficient, indicating the extent of contribution of sample value $Z(x_i)$ to estimated value $Z^*(x)$ at a spatial sample point x_i .

In order to calculate the weight coefficient λ_i under the condition that the two conditions of unbiased estimation and optimal estimation are satisfied, the calculation is based on the Lagrangian principle, and the Kriging equation (3) is obtained:

$$\begin{cases} \sum_{j=1}^n \lambda_j c(x_i, x_j) - \mu = c(x_i, x) \\ \sum_{i=1}^n \lambda_i = 1 \end{cases} \quad (3)$$

In formula (3) $c(x_i, x_j)$, $c(x_i, x)$ are the covariances, μ is the Lagrange multiplier.

Find the weight coefficient by solving the above linear equations λ_i and Lagrangian coefficient μ , substituting to the following formula (4) we can obtain the Kriging estimated variance

$$\sigma_E^2 = c(x, x) - \sum_{i=1}^n \lambda_i c(x_i, x) + \mu \quad (4)$$

In formula (4), $c(x_i, x_j)$, $c(x_i, x)$ are the covariances, μ is the Lagrange multiplier.

For the project we used a spherical model as a variogram model to analyse all data. The standard form of the spherical model is as below:

$$\gamma(h) = \begin{cases} \frac{3}{2} \frac{h}{a} - \frac{1}{2} \left(\frac{h}{a}\right)^3 & h \leq a \\ 1 & h > a \end{cases} \quad (5)$$

In equation (5), a is the range and h is the distance between the two samples.

In this analysis, the ore-dominated ore body 10 was selected as the main research object for variogram analysis and parameter extraction. According to the principle of geostatistics, the sample logarithm can be selected to find the maximum number of down hole directions within a certain search radius, and then the nugget value data is obtained (Figure 4a). The direction of the down hole is substantially perpendicular to the plane determined by the first and second mineralization directions (depending on the rationality of the initial exploration engineering design). Geostatistics uses the variogram as the most important research tool. Whether it is used for structural analysis of regionalized variables or for interpolation of other samples, the variogram obtained in the previous direction must be in several main directions. The fitting was performed (Figure 4b, Figure 4c, Figure 4d). According to the theoretical variogram model, the variogram model which is actually used for valuation calculation in all directions of the ore body is determined, and its parameters (variable range, base value, nugget value, etc.) are obtained [9-10].

In this paper, according to the striking, dipping and vertical direction, the variogram of the graphite carbon grade is fitted and calculated. The calculation results are shown in Table 1.

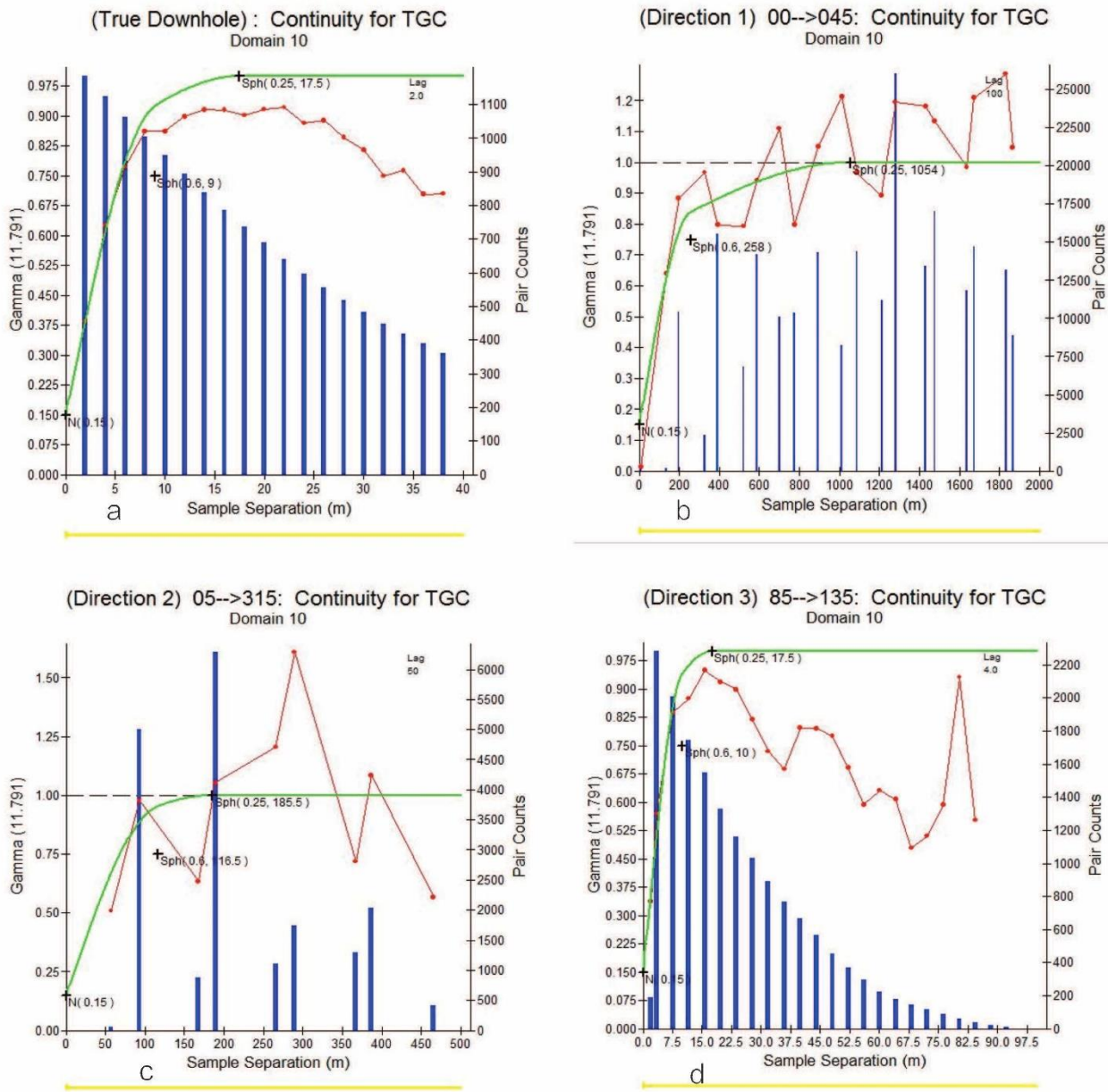


Fig. 4 - Variation function distribution map

Tab.1 - variogram analysis results table

ingredient	direction	Axis direction	Block gold value	Structure 1				Structure 2			
				Abutment value	Range	Primary and secondary axis ratio	Main short axis ratio	Abutment value	Range	Primary and secondary axis ratio	Main short axis ratio
Total graphitic carbon	Spindle direction	00-->045	0.15	0.6	100	2.2	25.8	0.25	100	5.7	60.2
	Secondary axis direction	05-->315	0.15	0.6	50			0.25	50		
	Short axis direction	85-->135	0.15	0.6	4			0.25	4		

Variogram validation

The rationality verification procedure is used to test the rationality and correctness of the grade estimation results based on the parameters obtained by the variogram curve fitting. Firstly, the estimation results of each ore body are compared with the historical inverse distance method and the average grade of the composited samples. The comparison results are shown in the following Table 2. According to the statistical results, the estimation results are stable, for all primary and secondary ore bodies, the actual estimation errors of the ore bodies are within 5%.

Tab.2 - Sujishan Resource Block Model Verification Table

Area	Wireframe	Block model				Composited sample		Data deviation		
	Wireframe volume	Resource model total volume	Resource model estimation volume	Graphit e carbon IDW	Graphite Carbon OK	Number of composites	Graphit e carbon	Volum e Invers e ratio Ordinar y krig		
				%	%		%			
1	5,283,216	5,270,703	5,202,734	4.18	4.26	152	4.28	-0.24	-2.33	-0.46
2	2,310,000	2,298,828	2,230,469	3.52	3.50	78	3.37	-0.48	4.35	3.68
3	2,905,220	2,889,844	2,889,844	4.68	4.60	66	4.56	-0.53	2.53	0.76
4	529,299	532,813	514,063	2.50	2.65	16	2.31	0.66	8.41	14.85
5	160,201	162,500	161,719	2.89	2.90	4	3.30	1.44	-12.41	-12.12
6	156,857	158,984	136,328	2.53	2.44	4	2.46	1.36	2.75	-0.76
7	306,096	304,297	304,297	2.86	2.81	7	2.83	-0.59	1.08	-0.71
8	132,021	130,469	130,469	2.71	2.57	4	2.48	-1.18	9.21	3.64
9	3,921,001	3,915,234	3,793,750	3.62	3.21	52	4.12	-0.15	-12.20	-22.09
10	64,484,474	64,084,766	64,048,828	5.20	5.22	1249	4.63	-0.62	12.35	12.71
11	738,644	730,469	730,469	4.55	5.10	11	4.38	-1.11	3.77	16.49
12	274,754	268,750	268,750	3.24	3.60	4	3.22	-2.19	0.61	11.71
13	378,390	372,266	372,266	2.13	2.15	6	2.26	-1.62	-5.54	-4.65
14	317,343	320,313	320,313	1.08	1.12	5	1.11	0.94	-2.37	0.94
15	677,822	679,297	679,297	1.46	1.36	8	1.50	0.22	-2.84	-9.08
16	2,894,215	2,889,453	2,889,453	2.85	2.88	50	2.89	-0.16	-1.28	-0.42
17	155,569	160,547	160,547	4.98	5.38	3	4.99	3.20	-0.29	7.90
18	294,667	291,797	291,797	4.03	4.89	10	3.76	-0.97	7.09	29.96
19	16,234	15,625	15,625	7.30	7.30	1	7.30	-3.75	0.00	0.00
20	149,091	150,391	150,391	3.09	2.96	5	2.70	0.87	14.50	9.56
21	23,439	23,828	23,828	10.38	10.38	1	10.38	1.66	0.00	0.00
22	260,535	250,391	250,391	2.39	2.36	9	2.33	-3.89	2.76	1.43
23	37,652	35,547	35,547	2.28	2.30	2	2.27	-5.59	0.52	1.21
24	35,276	32,031	32,031	4.46	4.46	2	4.46	-9.20	0.00	0.00
25	44,805	42,578	42,578	4.60	4.79	3	5.00	-4.97	-7.97	-4.25
26	9,190,205	9,192,188	9,190,234	5.73	5.53	180	5.45	0.02	5.14	1.38
28	364,902	360,938	360,938	5.26	5.12	13	5.69	-1.09	-7.51	-10.03
29	109,361	109,766	109,766	5.03	5.11	6	5.20	0.37	-3.20	-1.74
Total	96,151,289	95,988,285	95,336,722	4.90	4.88	1,951	4.49	-0.17	9.08	8.75

At the same time, after completing the macroscopic comparison of the estimation results of each ore body, the deviation between the graded values and the true values in each section of the ore body are plotted, and the difference and change are statistically analyzed as Figure 5 (X and Y directions). Through the analysis of the block model swats plots, we can see that the estimation result curve and the original data curve have a high degree of fitting in each ore body segment, which confirm the high correlation between the estimation results and the original composited results. Meanwhile, some high-grade sections are processed by the Ordinary Kriging estimation method, the smoothing effect leads to a more reasonable grade distribution. Each segment-related block is combined with a reasonable number of original samples for estimation, and the reliable estimation results are obtained as well.

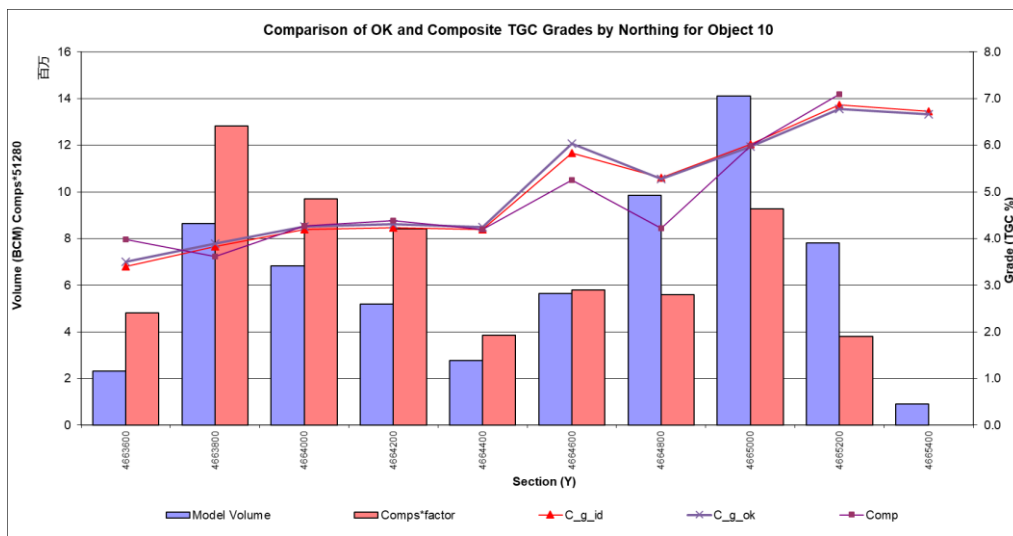


Fig.5 - Resource quantity estimation result segmentation chart verification result (X, Y direction)

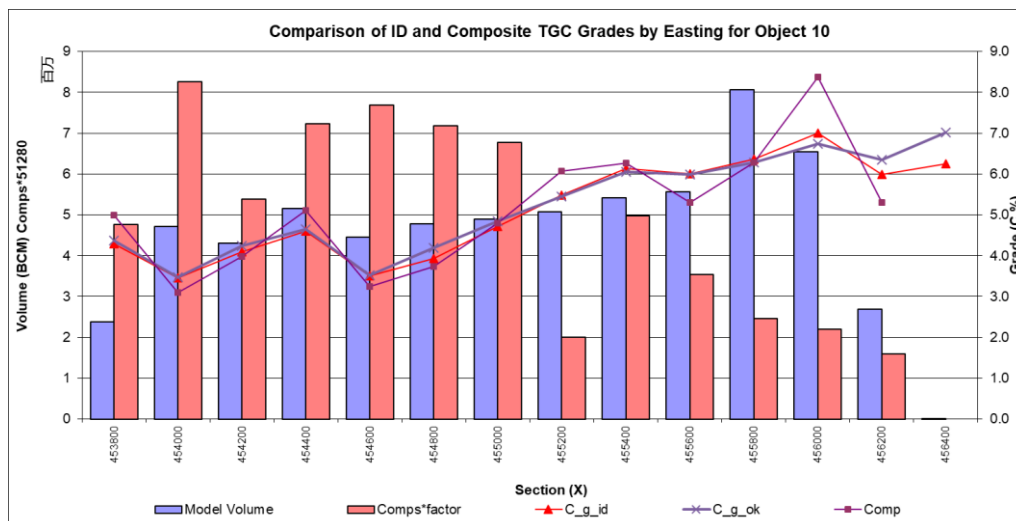


Fig.5 - Resource quantity estimation result segmentation chart verification result (X, Y direction)

Fig.5 - Resource quantity estimation result segmentation chart verification result (X, Y direction)

Resource estimation

In this study, a block model was created in the mining area, covering the mineralization range of the whole ore body, and constrained by the ore body solid model. The block size of the block model selected for this resource estimation is 50m×100m×5m. The sub block size is 12.5 m x 25 m x 1.25 m. The composited sample string files were obtained by sample compositing, and the string file data was extracted to perform the grade estimation of the remaining unknown blocks in the block model. The estimation method selected was the ordinary Kriging method, and the relevant parameters such as nugget and the sill and range obtained by fitting the variogram model were obtained and imported into the 3D geological software to estimate all relevant blocks in the block model (Figure 6). The calculation formula is as follows.

$$Q_m = C_i \times V_i \times \rho \tag{6}$$

In formula (6), Q_m is the amount of metal, V_i is the bulk volume, C_i is the average grade of the block, ρ is the ore weight.

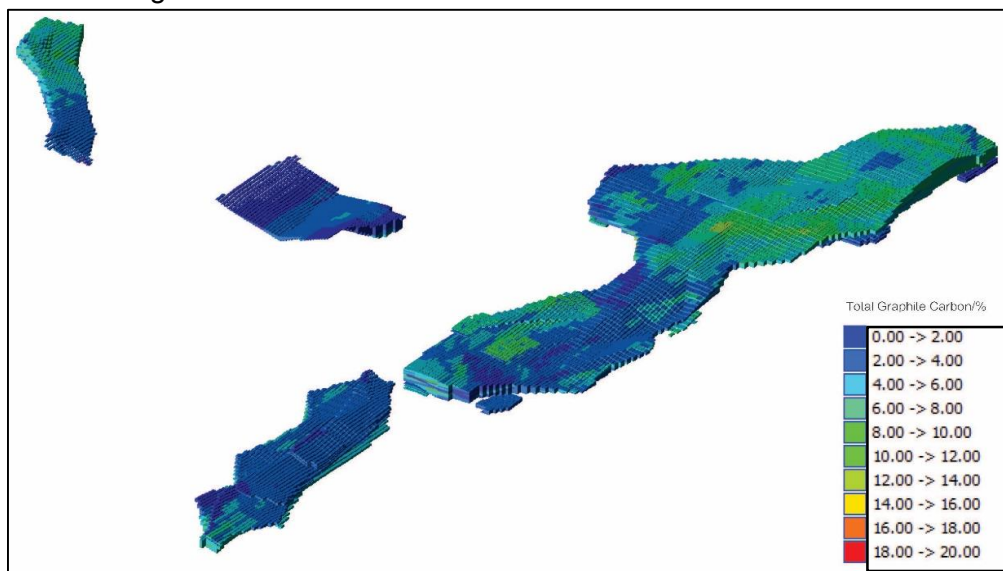


Fig.6 - Ore body model (colored by grade distribution)

Surpac software was used for resource estimation, the total amount of graphite ore was calculated to be 178 million tons and the total amount of graphite carbon was 10 million tons at the lowest industry grade of 3.5%. At the same time, according to the calculation results of the resource, the Surpac software was used for statistics to obtain the tonnage and grade curves as below (Figure 7).

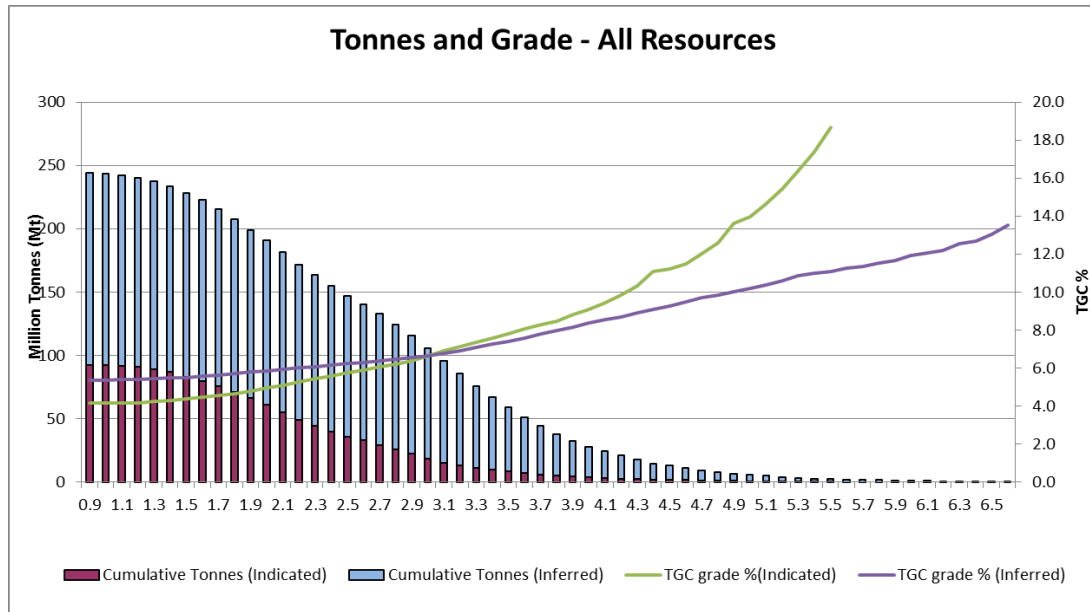


Fig.7 - Sujishan graphite ore grade tonnage map

It is noted that based on Figure 7 the total carbon ore and total graphite carbon ore are inversely related to the grades. According to the current market price and production operation cost, we can adjust the current indicators such as the ore grade and the selected grade in real time. Under different product market price conditions, the minimum mining industrial grade can be adjusted according to the tonnage-grade comparison chart to ensure the reasonability and orderly mining activity.

Comparing with the procedures of traditional resource estimation method which is normally called polygon method and direct geological interpolation are applied for all areas between sections, the geostatistical estimation of the resource process is more intuitive and reliable. Because of more delicate consideration of extension rules and local geological variability, the geostatistical estimation method can reflect the actual occurrence status of the deposit, and can effectively guide the production and exploration of the mine as well.

CONCLUSION

With using the theory of geostatistics, the author established the three-dimensional geological model of the Sujishan graphite mine by using Surpac software, and estimated the grade distribution of the ore body. At the same time, the experimental semi-variogram of the ore body striking, dipping and vertical directions were studied. The theoretical curve was fitted and the relevant estimation parameters were extracted. Finally, the total ore volume of the deposit was calculated to be 178 million tons and the total amount of graphite minerals is 10 million tons. Comparing with the traditional polygon estimation method, it is noted that the mine resource estimation by using the 3D geological software on the basis of the Kriging estimation method is more reasonable for the distribution of different grades of samples, and are closer to the actual mining situation of the mine. Meanwhile, the volume grade comparison table and the block model swats plots are applied to the block model validation, which verifies the rationality of the estimation method and results. Furthermore, in this paper, we analysed the grade tonnage curve of the mine, which provides further theoretical guidance for the selection of different minimum industry grades in the future exploration and production of the mine.

REFERENCES

- [1] Matheron, G. 1962. *Traité de géostatistique appliquée*, Vol. 1. Editions Technip, Paris, France.
- [2] Hou J R, Huang J X. *Practical geostatistics*[M]. Beijing: Geological Publishing Press, 1998.
- [3] Hou J R. Review and Prospect of the development of China's geostatistics (Spatial Information Statistics)[J]. *Geology and Prospecting*, 1997(1):53-58
- [4] Shao Y J, Rao Y F, He K B. Complicated ore body 3D modelling and estimation based on 3Dmine[J]. *Non-ferrous metal science and engineering*, 2016,7(04):98-102.
- [5] Liu X M, Xiao H Z, Chen H, et al. Practical of application of Dimine software in geostatistics research[J]. *China geology education*, 2015,24(01):99-102.
- [6] Luo Z Q, Liu X M, Wu Y B, et al. Application of geostatistics in the calculation of resource of polymetallic deposits[J]. *Geology and Prospecting*, 2007, 43(3): 83-87
- [7] Liu H Y. Application of multiple Kriging methods in the estimation of solid reources[D], 2010
- [8] Yang L R. Research on 3D Modeling and resource estimation method of complex ore body structure[D]. Chengdu: Chengdu University of Technology, 2013:9-10
- [9] Zhu X J, Ge Y B. Ordinary Kriging Study on resource estimation of Sicomines copper-cobalt deposit in Congo[J]. *World Nonferrous Metals*, 2016, 3:28-31
- [10] Tang P, Tang J X, Lin B, et al. Comparative analysis of traditional geometric methods and geostatistics in the estimation of mineral resources [J]. *Journal of Geology Technology*, 2016, 35(1):156-160

EXAMINATION OF THE USABILITY OF BASALT AGGREGATE IN SIFCON

Metin Ipek

Sakarya University of Applied Sciences, Technology Faculty, Civil Engineering Department, 54187 Sakarya, Turkey; e-mail: metini@sakarya.edu.tr

ABSTRACT

In this study, the usability of the quartz and basalt rocks as aggregate in Slurry Infiltrated Fiber Concrete (SIFCON) has been examined. In the study, quartz aggregate has been taken as reference and basalt aggregate has been used as a substitute and separately. The aggregates have been ground and classified in the dimensions of 0-0.1 mm (powder) and 0.1-0.6 mm (sand). The physical properties of the aggregates have been determined and SIFCON slurry has been prepared. The samples produced by this slurry have been conducted to Compressive Strength, Flexural Tensile Strength, Fracture Toughness, Ultrasonic Pulse Velocity, Schmidt Hammer tests. Moreover, unit cost has been examined with the different aggregate usages. Consequently; the highest compressive and flexural strength being respectively 99.75 MPa and 32.01 MPa have been reached with the use of quartz aggregate. The compressive strength of the basalt aggregate is 14% lower than that of the quartz aggregate where, its flexural strength almost remained in the same value. It has been observed that basalt aggregate is more economical in terms of unit strength cost. It is suggested that basalt aggregate could also be used in SIFCON as an alternative to the quartz aggregate.

KEYWORDS

SIFCON, fiber, quartz, basalt

INTRODUCTION

Steel, polypropylene, and glass fibers are added into the concrete to develop its mechanical properties such as tensile strength, crack strength, abrasion, impact strength and toughness. The fibers used in the concretes decrease the shrinkage fractures and increase tensile and flexural strength [1]. As the fiber ratio increases, important workability problems occur in the concrete, therefore high ratios of fibers were not able to be incorporated into mixtures. Due to this problem, the idea of the addition of concrete to the fiber has occurred and SIFCON (Slurry Infiltrated Fiber Concrete) has been produced. SIFCON being in the fiber reinforced concrete class was firstly developed in 1983 by Lankard in New Mexico Engineering Research Institute (NMERI) [2, 3].

SIFCON is the new cement based composite material which is reinforced with 5-20% steel wire in high ratios in terms of volume in a matrix occurring from the hardening of a slurry consisting of cement, water, superplasticizer, silica fume, and very fine sand. Besides, its engineering properties are quite high [4].

SIFCON is a new material containing steel wire up to the ratios of 20% in volume with its characteristics of low permeability, high durability, strength, and ductility. One of the most important properties of SIFCON, different from the high strength concretes, is that it shows ductile behavior

during the fracture [1]. SIFCON provides an opportunity for using high ratios of fibers with the advantage of the production technique of filling the fiber into the mold and injecting the slurry in the fibers [5,6,7,8].

SIFCON is used in various applications such as industrial elastic ground and thin-walled elements where ductility is a problem. Thanks to superior performance against disintegration, it is also used in structures which are exposed to impact loads and built to store explosive materials [9,10].

The mixture ratios of the SIFCON slurry, the aspect ratio of steel fibers and embedding lengths were studied by Tuyana and Yazıcı. Improvement of sludge strength, fiber diameter and geometry has increased the adherence of the fiber [9].

Impact experiments were made in concrete plates by Rao et al. They compared SIFCON and reinforced concrete plates' behaviors in terms of the impact load. The highest impact strength was obtained from SIFCON plate which has 12% steel fiber [11].

When the literature is reviewed, it could be seen that the studies conducted related to SIFCON are limited and no studies examining the impact of the aggregates generally in different types on SIFCON have been encountered. Therefore; this study examined the issue of using basalt as aggregate in SIFCON concrete.

EXPERIMENT

Material

The largest one of the main components of SIFCON is cement in terms of amount. For this reason; cement type has a great importance. CEM I 42.5 R type cement produced by Bolu Cement Factory has been used in all of the conducted experimental studies. Chemical, physical and mechanical properties of the cement are given in Table 1. Silica fume with high pozzolanic properties and space filling performance has been used as pozzolana. Silica fume is a mineral consisting of shapeless, transparent silicium dioxide (SiO_2) spheres occurring as waste during the production of silicone or iron silicium [12,13]. In the experiments, Polycar 300 being a new generation polycarboxylate based, highly water reducer and superplasticizer have been used.

Quartz and basalt aggregates are the ones occurring as a result of the fracture of the rocks and they take their properties from the bedrock. The chemical and physical properties belonging to these aggregates are given in Table 1. Quartz rock is much harder and stronger than other rocks and because it is a very hard aggregate, its abrasion strength is known to be high. Generally, quartz aggregates are used in SIFCON concrete [6,14,15]. However; quartz aggregates are hard to attain and very valuable in terms of the reserve. Basalt is the rock which is equal to very dark colored gabbro and dolerite and consists of pyroxene and olivine crystals [16]. Basalt aggregates are the ones having great reserves in many places of the world and therefore, they are widely used in the concrete and asphalt production. The basalt aggregate to be used in the experiment has been ground via mill, sieved and brought to the dimensions of powder and sand. Because the quartz aggregate is widely used in the repair mortars, it has been supplied from the market in the desired dimensions and its gradation curve is as in Figure 1. The gradation curves of the granular materials used in the experiments are given in Figure 1.

Tab. 1 - Properties of cement, silica fume, quartz and basalt

Component	Chemical Composition (% by mass)			
	Cement	Silica fume	Quartz powder	Basalt powder
CaO	64.47	0.5	-	11.75
SiO ₂	20.09	96	99.50	50.40
Al ₂ O ₃	5.01	0.7	0.01	16.7
Fe ₂ O ₃	2.73	0.25	0.01	2.34
MgO	1.95	0.60	-	7.56
FeO	-	-	-	5.8
C	-	1.5	-	-
Na ₂ O+K ₂ O	0.87	1.10	0.37	4.95
SO ₃	2.65			
TiO ₂			0.07	-
LOI				
A.Z.				
Loss on ignition	2.34	1.50	0.40	0.35
Specific gravity	3.16	2.26	2.71	2.68
Physical Properties				
Blaine specify surface (cm ² /gr)	3830	200000	2142	2101
Moisture content (%)	-	-	0.08	0.16
Initial setting time (minute)	156			
Final setting time (minute)	198			
Volume expansion (mm)	1.1			
Compressive Strength of Cement (MPa)				
2 days compressive strength (MPa)	27.3			
28 days compressive strength (MPa)	55.3			

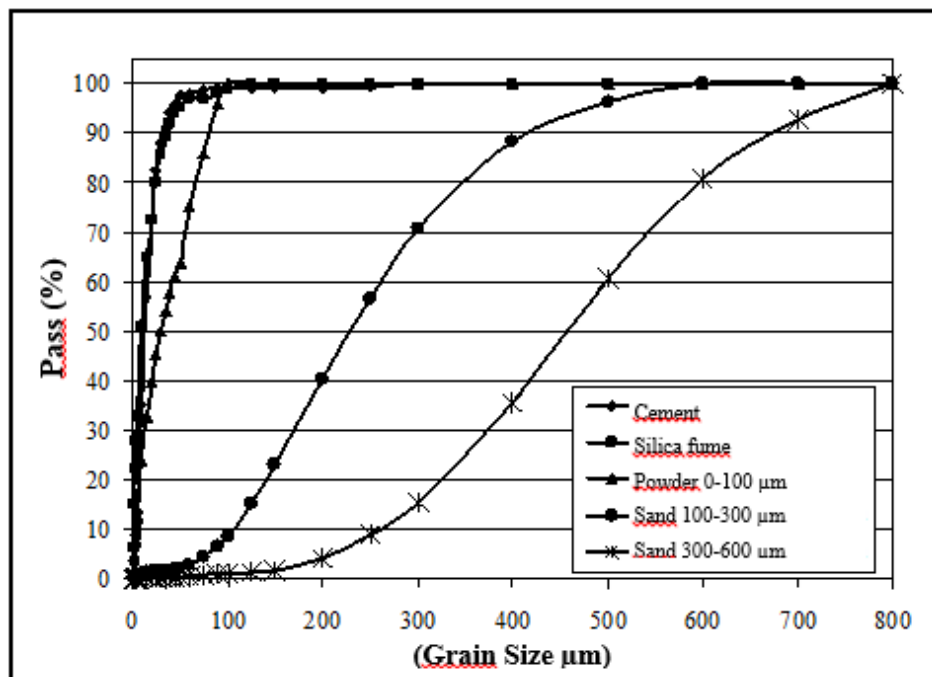


Fig. 1 – The gradation curves of the granular materials

Experimental procedures

Mixtures have been prepared by benefiting from the previous studies for SIFCON mixture and the one with the highest compressive strength has been selected and given in Table 3 [3,4,7,8]. The mixture ratios have been kept constant and the aggregates have been changed. Firstly; the quartz sand has been kept constant and the powder of basalt aggregate has been used instead of the quartz powder. At the second stage, Quartz powder has been kept constant and the sands of basalt aggregate have been used instead of the quartz sand. The third and last stage, the powder and sands of basalt aggregate have been used instead of the powder and sand of Quartz. Codes of the samples are given in Table 2.

Tab. 2 - Aggregate mixtures and sample codes

Aggregate mixture	Sample Code	Steps
Reference	REF	-
Basalt Powder+Quartz Sand	BPQS	First
Quartz Powder+Basalt Sand	QPBS	Second
Basalt Powder and Sand	B	Third

Tab. 3 - The mix proportion of SIFCON (kg/m³)

Materials	REF	BPQS	QPBS	B
Cement	900	900	900	900
Silica Fume	270	270	270	270
Quartz Powder	278	-	278	-
Basalt Powder	-	282	-	282
Quartz Sand	504	504	-	-
Basalt Sand	-	-	507	507
Water	270	270	270	270
Super plasticizer	36	36	36	36

The mixture process has been carried out by respectively filling the cement, silica fume, water additive, and aggregates in the mixer. Molds with the dimensions of 15 cubic centimeters have been used for the compressive strength and molds with the dimensions of 4x8x40 cm in rectangular prism shape have been used for the flexural strength. Fibers have been randomly filled in these molds and slurry has been injected on the vibratory table (Figure 2). Samples have been taken out of the molds after keeping for 24 hours in them and they have been subjected to the hot steam cure at 90 °C for 3 days. Following that, they have been kept in the curing pool at 20°C for 28 days.

Compressive strength tests have been conducted in the concrete tester with the capacity of 3000 kN and whose loading speed could be adjusted in accordance with TSE standards (Turkish standard) [17,18]. Test results have been assessed according to the standard and the mechanical properties belonging to the samples have been found.

Flexural tests have been conducted in the computerized bending test device that could draw the load-deflection graphs automatically (Figure 3). As specified in TS 10515, the loading speed of the test device has been adjusted in a way that it will make a deflection of 0.05-0.10 mm/min. in the middle point of the beam. 360 mm is the space between two supports has been divided into three equal parts and the beam sample has been loaded from two points [19,20]. As a

result of the test, load-deflection graphs have been drawn and the values of fracture toughness have been calculated [21].

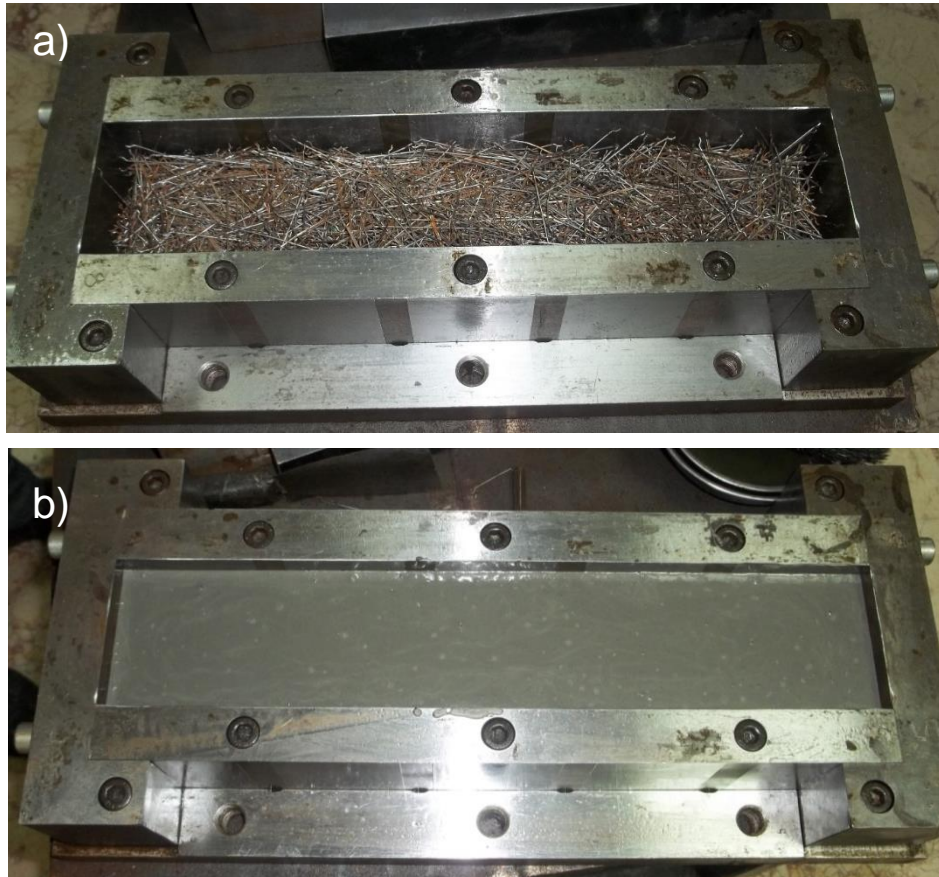


Fig. 2 - a) Filling the fibers into the mold, b) the fresh SIFCON



Fig. 3 - Flexural test apparatus

Ultrasonic pulse velocity test is one of the non-destructive experiments conducted to attain information about the quality of the concrete according to the speed of the sound transmission by taking the space amount in the concrete as the basis. Schmidt hammer test is a method developed to estimate the compressive strength of the sample by benefiting from the surface hardness. Ultrasonic pulse velocities of the samples and Schmidt hammer test reaction number are detected and the changes in other mechanical and physical properties of the samples are tried to be explained. For the test, ASTM C597-09 has been conveniently conducted in the cubic samples with the dimension of 15x15x15 cm (Figure 4) [22]. Sound transition period (t , μs) has been read from the screen and the proportioning to the distance between the probes (l , mm) and sound pulse velocity (V , mm/ μs) have been attained [6]. Schmidt Hammer Test has been conducted by fixing the concrete samples with the help of the concrete apparatus (Figure 5).



Fig. 4 - Sound pulse velocity experimental setup



Fig. 5 - Schmidt Hammer test setup

RESULTS AND DISCUSSION

The results attained from the test are given in Table 4 and Figure 6. The use of basalt aggregate instead of quartz powder has negatively affected the compressive strength and strength has decreased when compared to the REF sample. The compressive strength of the sample whose powder and sand aggregates consist of basalt is 14% lower than that of REF sample. This ratio has increased up to 30% on average with the use of basalt aggregate together with the quartz aggregate. Basalt aggregate has been ground from the rock and classification has been conducted only according to the minimum and maximum granular magnitude during the grinding. The distribution of the minimum and maximum grain interval has been checked and the gradation graphs in Figure 7 has been drawn. These graphs have been formed as a result of mixing the basalt aggregate in a certain ratio (35% powder+65% sand) as a result of its grinding as powder and sand. When Figure 7 is examined, quartz aggregate has been seen to be the closest one to the Fuller curve (assuming a Fuller exponential number of 0.50) accepted as the ideal curve [23,24]. Therefore, it is the aggregate with the highest composition. The highness of the composition has a positive impact on the increase in the compressive strength. The gradation curve of the basalt aggregate is different the gradation curve of Fuller and has an irregular curve. For this reason; the compressive strength of the basalt aggregate is lower. Schmidt hammer test results of the samples with high compressive strength are also high and show a little decrease in the REF sample. Because Schmidt hammer test conducts measurements depending on the surface hardness of the sample, it is possible for it to contain errors according to the real strength. No meaningful change has been observed in the ultrasonic pulse velocity values.

Tab. 4 - Mechanical properties of the sample

Sample Types	Compressive Strength (MPa)	Ultrasonic Velocity (km/sn)	Schmidt Test Hammer	Flexural Strength (MPa)	Fracture Toughness (Nm)
REF	98.89	3.42	61	32.44	70.61
BPQS	70.13	3.45	53	28.33	55.3
QPBS	71.87	3.47	52	29.21	59.62
B	88.40	3.41	62	32.05	69.77

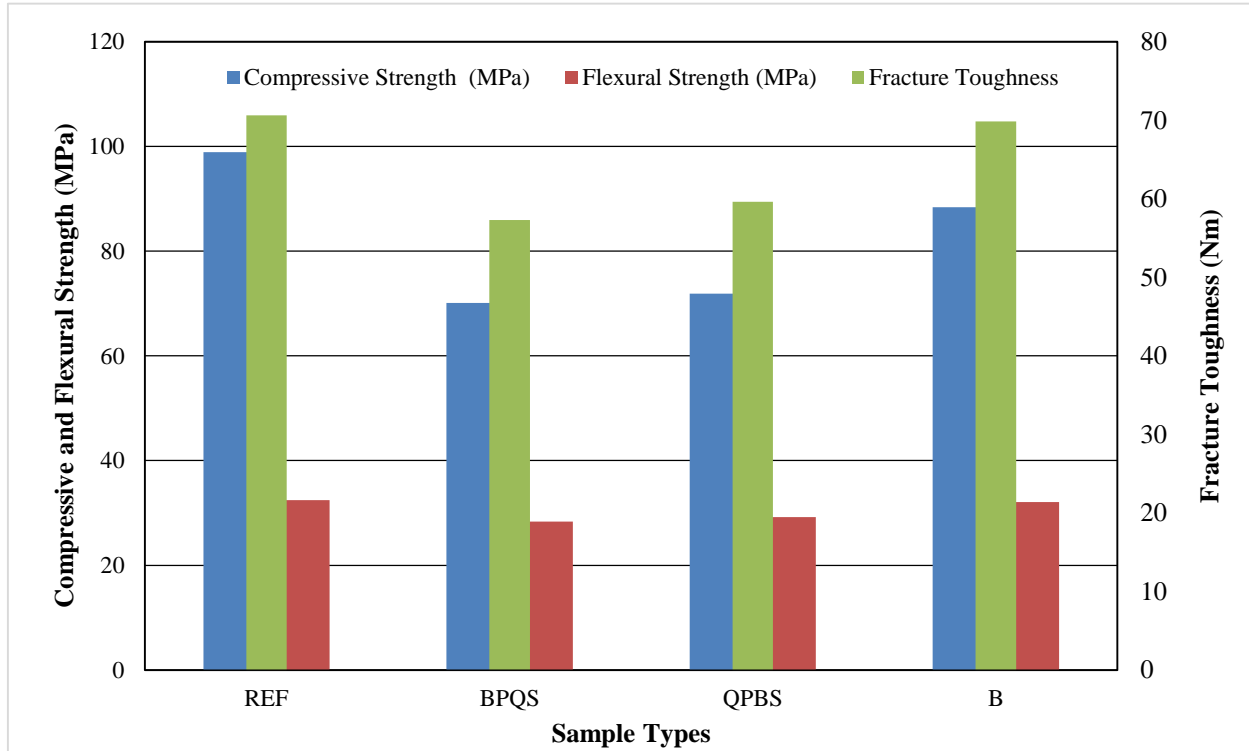


Fig. 6 - Compressive and Flexural Strength and Fracture Toughness graphics

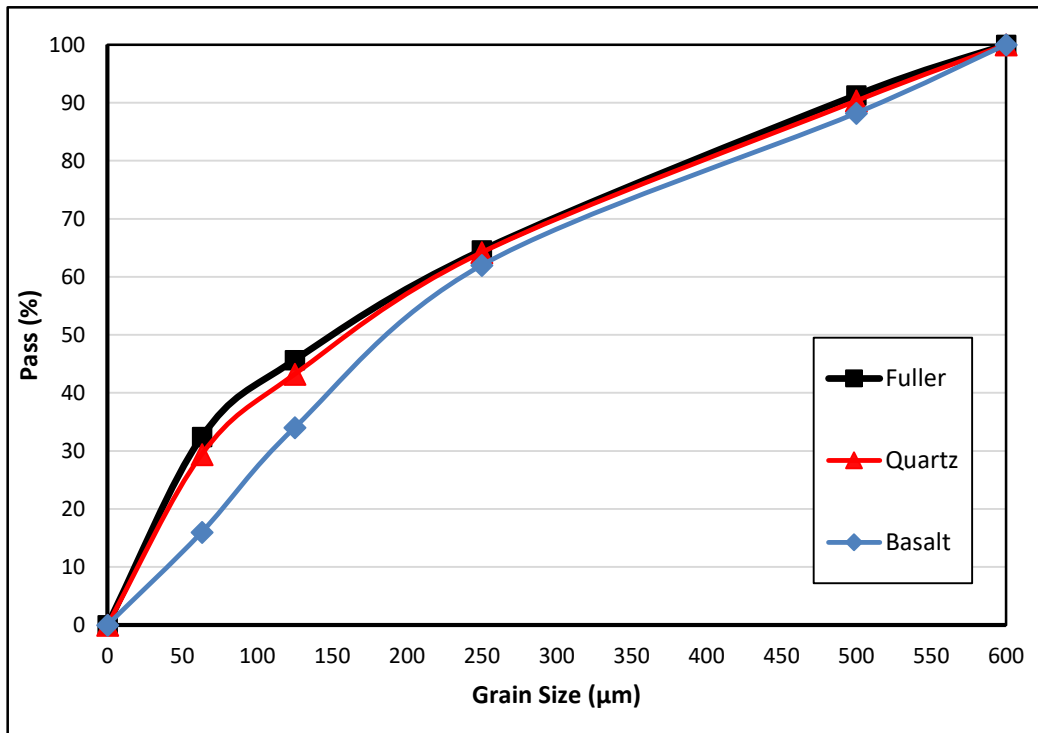


Fig. 7 – The gradation curves of the aggregate mixtures

It has been observed during the flexural test that the load has reached the peak point in a linear way and the fibers have started to debond after the maximum load. It has been seen that the sample has been broken by fracturing from almost the middle point (Fig. 8). It has also been observed that because the fibers are hooked, they break parts from the concrete during the debonding. Load-deflection graphs belonging to SIFCON samples as a result of the bending test is given in Figure 9-11. The strength and toughness results attained from the graphs are given in Table 4. While the flexural strength and fracture toughness values of the samples containing basalt aggregate have decreased when compared to REF sample, it has been seen that there has been a much higher decrease in the sample containing basalt powder (BPQS). A similarity is seen to be existent between the flexural strength and compressive strength. It is observed that the important factor decreasing the strength is basalt powder. When the aggregate gradation curves (Fig. 7) are examined, it is seen that basalt is 15% and quartz is 30% under 63 μm . The excessiveness of the fine material amount in quartz powder is very important in filling the spaces in micro dimensions and in cement paste. Filling the spaces in micro dimensions both affects the compressive and flexural strength.



Fig. 8 - Fracture sample as a result of the flexural test

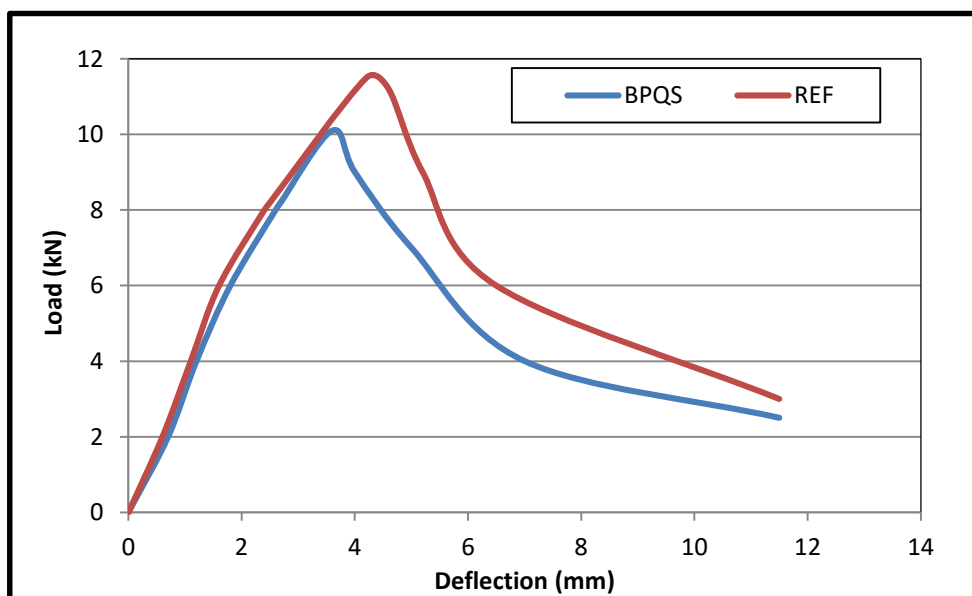


Fig. 9 - Load-deflection graphics of REF and BPQS sample

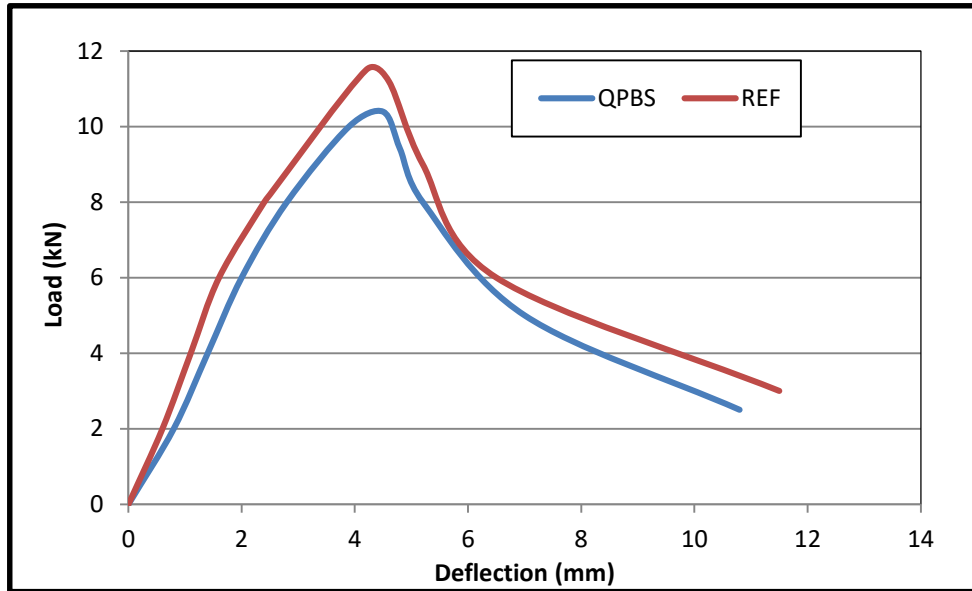


Fig. 10 - Load-deflection graphics of REF and QPBS sample

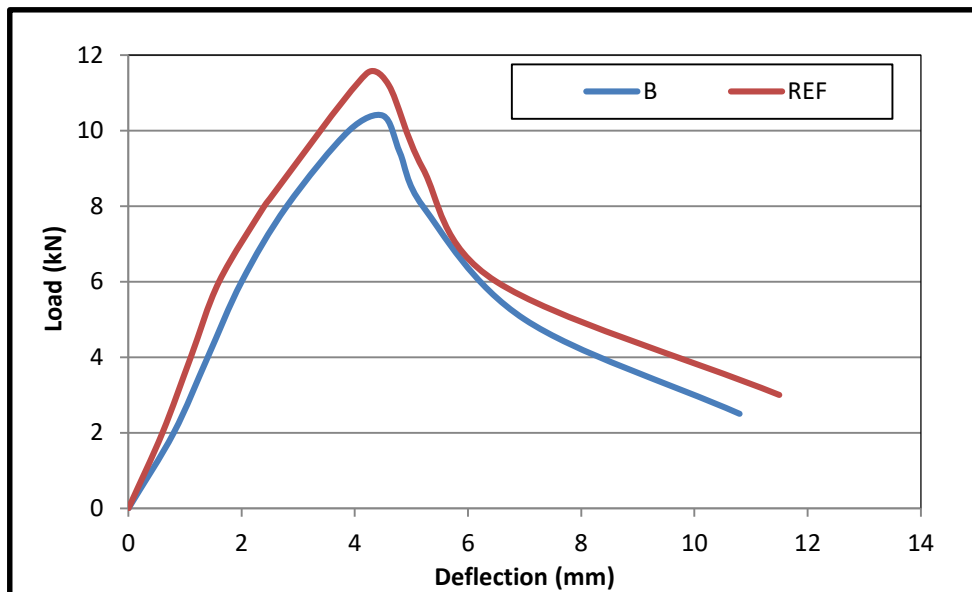


Fig. 11 - Load-deflection graphics of REF and basalt sample

Unit cost graphs of compressive and flexural strength are given in Fig. 11. The unit price of basalt aggregate in Turkey is approximately 75% cheaper than the unit price of quartz aggregate. Unit strength costs have been calculated by dividing the unit cost of SIFCON into strength. When Fig. 12 is examined, it is observed that the combined usage of quartz aggregate and basalt aggregate has increased the unit costs of compressive and flexural strength. However; there has not been any clear change in the compressive unit strength costs of the samples in which only basalt or quartz aggregates have been used and the unit cost of the flexural strength of the sample in which basalt aggregate has been used is approximately 7% lower.

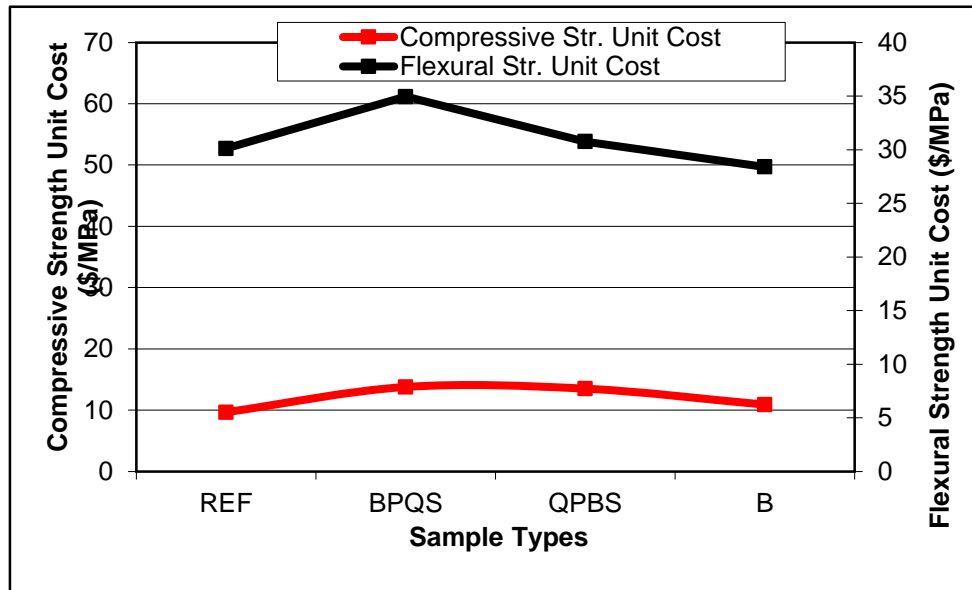


Fig. 12 - Unit cost graphics of the compressive and flexural strength of the samples

CONCLUSIONS

In the conducted study, the usability of the different rock types instead of the quartz powder used in SIFCON production and being in powder dimension has been examined.

The use of basalt aggregate instead of quartz powder has negatively affected the compressive strength and the strength has decreased when compared to that of REF sample. The decrease ratio in the compressive strength has increased by 30% together with the combined usage of the quartz and basalt aggregates. The gradation curve of the basalt aggregate is different from Fuller curve and it is irregular. Therefore; this may be the reason for the low compressive strength of the basalt aggregate. Schmidt hammer test results of the samples with high compressive strength are also high. However; no meaningful change has been observed in the values of ultrasonic pulse velocity.

According to the flexural test results, the flexural strength and fracture toughness values of the samples containing basalt aggregate have decreased slightly when compared to the values of the REF sample. The flexural strength and fracture toughness values of the sample in which quartz and basalt aggregates have been used in combination (BPQS) have decreased significantly. It has been observed that there is a similarity between the flexural strength and compressive strength results.

When the aggregate The gradation curves (Fig. 7) have been examined, it has been seen that the important factor decreasing the strength is basalt powder due to the fact that basalt is 15% and quartz is 30% under 63 μm .

The unit cost of SIFCON has been more economical because of the fact that the unit price of basalt aggregate in Turkey is as much as $\frac{1}{4}$ of the price of the quartz aggregate. Flexural strength unit cost has decreased by %8. However; no clear change has occurred in the unit compressive strength costs. It is suggested that the basalt aggregate could also be used as an alternative to the quartz aggregate in SIFCON.

ACKNOWLEDGMENTS

This work was supported by Sakarya University Scientific Research Foundation (Project number: 2012-05-08-008, 2010-05-08-005). The author would like to thank Sakarya University.

REFERENCES

- [1] Çivici F., 2006. Çelik lif donatılı betonun eğilme tokluğu. Pamukkale Üniversitesi Mühendislik Fakültesi Mühendislik Bilimleri Dergisi, Vol. 12, No. 2: 183-188,
- [2] Lankard D.R., 1984. Properties, Applications: Slurry infiltrated fiber concrete (SIFCON). Concrete International Journal, ACI, Vol. 6, No. 12: 287-306.
- [3] Lankard D.R., Newell J.K., 1984. Preparation of highly reinforced steel fiber reinforced concrete composites. Fiber Reinforced Concrete-International Symposium, ACI SP-81, American Concrete Institute, Detroit, 287-306
- [4] Taşdemir M.A., Bayramov F., 2002. Yüksek performanslı çimento esaslı kompozitlerin mekanik davranışı. İTÜ Dergisi, Vol. 1, No. 2: 125-144
- [5] Beglarigale A., Yalçınkaya Ç., Yiğiter H., Yazıcı H., 2016. Flexural performance of SIFCON composites subjected to high temperature. Construction and Building Materials, Vol. 104: 99-108
- [6] Canbay M., 2014. Çelik ve polipropilen liflerin yalın ve kombinasyonlu olarak SIFCON'da kullanılması. Yüksek Lisans Tezi, Sakarya Üniversitesi, Fen Bilimleri Enstitüsü, 20-60
- [7] Ipek M., Aksu M., Yılmaz K., Uysal M., 2014. The effect of pre-setting pressure on the flexural strength and fracture toughness of SIFCON during the setting phase. Constr Build Mater, Vol. 66: 515–521.
- [8] Ipek M., Aksu M., Uysal M., Yılmaz K., Vural I., 2015. Effect of pre-setting pressure applied flexure strength and fracture toughness of new SIFCON + RPC composite during setting phase. Constr Build Mater, Vol. 79: 90-96
- [9] Tuyan M., Yazıcı H., 2012. Pull-Out behavior of single steel fiber from SIFCON matrix. Constr Build Mater. Vol.;1: 571-577
- [10] <http://sifcon.quinting.com>.
- [11] Raoa H.S., Ghorpade V.G., Ramanac N.V., Gnaneward K., 2010. Response of SIFCON two-way slabs under impact loading. International Journal of Impact Engineering, Vol. 37: 452-458
- [12] Yeğınobalı A., 2002. Silis Dumanı ve Çimento ile Betonda Kullanımı, 18-46 (Türkiye Çimento Müstahsilileri Birliği/AR-GE Enstitüsü 80 pp.
- [13] <http://www.materials.elkem.com>, 07.03.2013
- [14] Korkanç M., Tuğrul A., 2004. Beton agregası olarak kullanılacak bazaltların alkali-silis reaksiyonu yönünden incelenmesi. İstanbul Üniv. Müh. Fak. Yerbilimleri Dergisi, Vol. 17, No. 2: 161-169
- [15] Aitcin P.C., 2004. High performance concrete, 400-422 (Taylor & Francis e-Library) 624 pp.
- [16] Kozak M., 2014. Bazalt agregası ile üretilen beton travers de çelik lifin kullanılabilirliğinin araştırılması. Afyonkarahisar Fen Bilimleri Enstitüsü Dergisi, Vol.11: 17-30
- [17] ASTM C 469, 1996. Standard Test Method for Static Modulus of Elasticity and Poisson's Ratio of Concrete in Compression (American Society for Testing and Materials) 10 pp.
- [18] TS 10513, 1992. Çelik Teller - Beton Takviyesinde Kullanılan (Türk Standartları Enstitüsü) 15 pp.
- [19] TS 10514, 1992. Beton-Çelik Tel Takviyeli-Çelik Telleri Betona Karıştırma ve Kontrol Kuralları, (Türk Standartları Enstitüsü) 18 pp.
- [20] Nataraja M.C., Dhang N., Gupta A.P., 2000. Toughness characterization of steel fiber-reinforced concrete by JSCE Approach. Cement and Concrete Research Vol. 30, No. 4: 593-597
- [21] Özalp F., 2006. Ultra Yüksek Performanslı Betonların Mekanik Davranışı. Yüksek Lisans Tezi, İstanbul Teknik Üniversitesi Fen Bilimleri Enstitüsü, 36-40
- [22] ASTM C597, 2016. Standard Test Method for Pulse Velocity Through Concrete (American Society for Testing and Materials) 8 pp.
- [23] Fuller W., Thompson S., 1907. The laws of proportioning concrete. Trans. Am. Soc. Civ. Eng. Vol. 57, No: 2: 67–143

- [24] Santos A.R., Veiga M.R., Silva A.S., Brito J., Álvarez J.I., 2018. Evolution of the microstructure of lime based mortars and influence on the mechanical behaviour: The role of the aggregates. *Constr Build Mater.*, Vol. 187: 907–922

APPLICATION OF MACHINE VISION TECHNOLOGY IN ROAD DETECTION

Qingzhe Zhang, Zhi Qin

Chang'an University, Key Laboratory of Road Construction Technology and Equipment, Ministry of Education of China, Xi'an, China; zqzh@chd.edu.cn

ABSTRACT

Machine vision was first applied in industrial manufacturing field, and now it is also used in road detection, with the rapid development and continuous innovation of computer technology and digital image processing technology. This study provides a detailed description of the application of machine vision technology in detection of pavement crack, such as crack image acquisition, preprocessing (image de-noising and enhancement), segmentation, and recognition technology. Further the application of machine vision technology in pavement compactness and evenness was introduced. Finally, based on the application of machine vision in other aspects of road detection, hopefully, this study can provide a reference for method of road detection.

KEYWORDS

Machine vision, Road detection, Crack, Compactness, Evenness

INTRODUCTION

Since the end of 20th century, with the rapid development and continuous innovation of computer technology and digital image processing technology, machine vision technology has been progressively applied to highway pavement detection. In this period, the United States, Japan, France and other developed countries have devoted extensive research efforts and development work on the main contents of the road automatic testing equipment and pavement management system, and published a number of related research results [1]. Although the application of machine vision technology in the automatic detection of pavement in China has started later, it is developing rapidly, and gradually narrowing the gap with the world's advanced level [2]. This study reviews the application of machine vision technology in detection of pavement cracks, pavement compaction, and pavement roughness, with primary focus on the application of machine vision in pavement crack detection. Finally, based on the application of machine vision in other aspects of road detection, hopefully, this study can provide a reference for method of road detection.

THE DEVELOPMENT HISTORY OF MACHINE VISION TECHNOLOGY

A machine vision system refers to the capturing of images through a machine vision device (i.e. image capture device). Then the image is transferred to the processing unit through digital processing. Based on the pixel distribution and brightness, colour, and other information, it can discriminate the size, shape, colour, and other parameters, and then according to the results it controls the operation of the field equipment. The study of machine vision began with the pattern recognition in two-dimensional images in 1950s. In 1960s American scholar Roberts put forward the concept of building blocks of polyhedron [3], preprocessing, edge detection, and object modelling which are still used in the field of machine vision. In 70s the visual computing theory

proposed by David Marr provided an unified theoretical framework for machine vision research [4]. At the same time, machine vision was incorporated in several important research branches such as target guided image processing, parallel algorithms for image processing and analysis, knowledge base of vision system, and so on. In 80s with the rapid development of machine vision technology, new technology and new knowledge were continuing without end, for example, the theoretical framework of object recognition based on perceptual feature group, the framework of active vision theory, and the framework of visual integration theory, etc. By the middle of the 90s, machine vision has entered a period of deep development and wide range of application and by now, machine vision has become a very active research field. This section should describe in detail the study material, procedures and methods used.

APPLICATION OF MACHINE VISION IN DETECTION OF PAVEMENT CRACK The composition of machine vision system for detection of pavement crack

The machine vision system for detection of pavement crack is mainly composed of two parts: hardware system and software system. The hardware system mainly includes power supply system, image acquisition system, and image lighting system. The software system mainly includes image preprocessing system, image segmentation and recognition system, and so on, as shown in Figure 1.

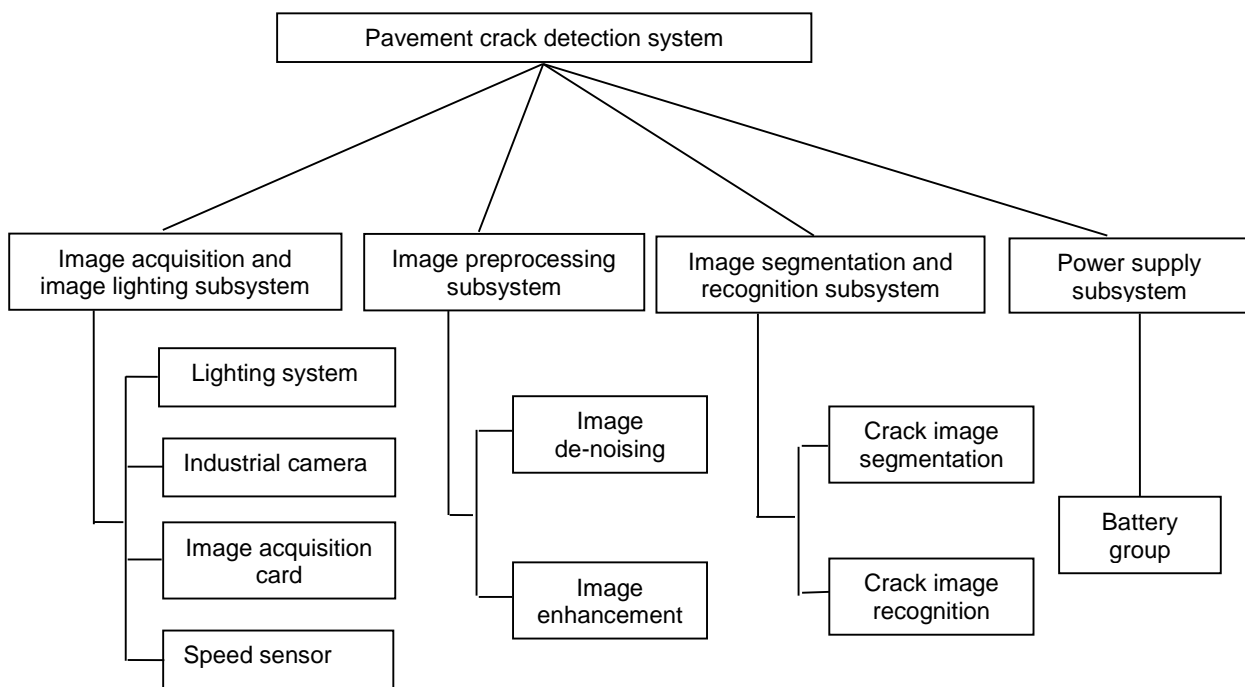


Fig.1 - The system composition diagram

Pavement image acquisition

Pavement image acquisition system is the foundation and key of the entire machine vision system, which determines the accuracy and precision of image analysis. The pavement image acquisition system is mainly composed of industrial camera, lens, lighting device, speed sensor, and digital image capture card. At present, the pavement image acquisition is mainly acquired using the industrial camera. Based on the type of sensor, the industrial camera can be divided into charge-coupled device (CCD) camera and complementary metal oxide semiconductor (CMOS)

image sensor camera, as shown in Figure 2. Owing to the high imaging quality of CCD camera, it is usually used in pavement detection. The linear array CCD camera can only obtain one line of information at a time. It has fast speed and high resolution, which can realize continuous detection of moving objects; therefore, the linear array CCD camera is especially suitable for image acquisition for pavement detection.



(a) CCD camera



(b) CMOS camera

Fig.2 - Industrial cameras

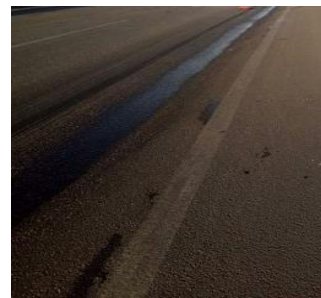
At the same time, the change of the ambient light plays a very important role in the image acquisition; therefore, the selection of light source in the image acquisition system is also important. The light emitting diode is widely used as a lighting device in pavement acquisition system because of its small size, low power, fast response, high reliability, and long service life.

Pavement image preprocessing

Uneven traffic signs, road line spilled materials, oil, shadow, and other interference, as shown in Figure 3, leads to strong noise in the pavement image, which increases the difficulty of identification of pavement crack. Therefore, it is necessary to eliminate or weaken these interferences and preprocess the pavement image. Although there are various methods of image preprocessing, they can be divided into two categories according to different emphasis: image de-noising and image enhancement.



(a) traffic signs line



(b) greasy dirt and inclusion

Fig.3 - Pavement image

Image de-noising

The noise in pavement image mainly comes from two aspects: one is the interference from the external environment, such as uneven illumination, shadow, etc. The other is road itself, due to the heterogeneity of the road surface, in particular, the size of the road material, particles, and the different roughness of the road. According to the actual situation of road noise, the noise can be divided into two types: random noise and interference noise. Random noise is commonly referred to as image noise; however, the interference noise is referred to the source information of the

images that interfere with the detection of cracks, such as the line of traffic signs in the road surface image.

At present, the representative methods of image de-noising include mean filtering, median filtering, Wiener filtering, low-pass filtering, high-pass filtering, and morphological filtering. The pavement image mainly contains salt-and-pepper noise and particle noise, and median filtering and mean filtering methods are simple; therefore, they are widely used in pavement image de-noising.

Median filtering is a nonlinear signal processing technology based on the sequencing theory, which can effectively suppress noise. In 1D situation, 1D median filter contains odd number of slide template, the template data is in the order from small to large, and the data in the middle position is considered as the final result. The core of the median filter aids in sorting the data in the template; thus, if a bright spot (dark spot) is noise, it is ranked in the sequencing process in the right (left) side of the data sequence. Therefore, the final value of the data sequence in the middle position is generally not the value of the noise point, which can achieve the purpose of noise suppression, as shown in Figure 4.

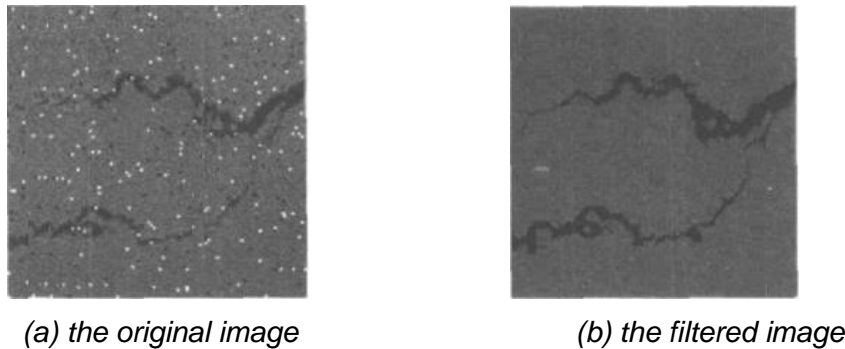


Fig. 4 - Median filtering of pavement image

Mean filtering uses the average pixel value to replace each pixel value of the original image. Assuming that the signal contaminated by noise is $h(t)$, the original signal is $\omega(t)$, and the noise is $\gamma(t)$, then $h(t) = \omega(t) + \gamma(t)$. The mean filter formula is as follows:

$$\overline{h(t)} = \frac{1}{n} [h(t-n) + \dots + h(t+m)] \quad (1)$$

Taking mathematical expectations on both sides of the equation, $\overline{h(t)} = \overline{\omega(t)} + \overline{\gamma(t)}$ is obtained. We considered the noise to be the salt-and-pepper noise, thus $\overline{\gamma(t)} \neq 0$. According to the above mentioned definition, for the salt-and-pepper noise, amplitude basically remains the same. However, there are some points in the data without noise, so that the output noise can be equated to the point that the noise is 0, so $\overline{\gamma(t)} < \gamma(t)$. As a result of average filtering, the noise intensity value of $\overline{\gamma(t)}$ is lower than $\gamma(t)$, as shown in Figure 5.

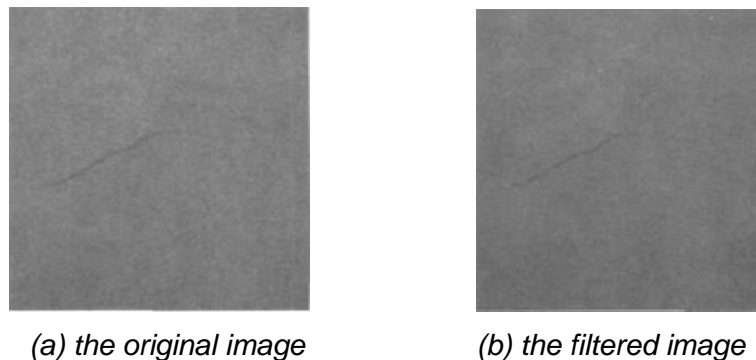


Fig.5 - Mean filtering of pavement image

The median filter and mean filter also have common defects, they cannot effectively filter various noises superimposed on the pavement image. Thus, in order to overcome this shortcoming, the scholars continue to improve. Combined with the advantages of the existing de-noising algorithms and characteristics of the noise and crack information of pavement image, a novel multilevel de-noising model based on the detection of pavement crack was presented by Wang et al [5]. In order to remove the isolated noises in pavement crack images and protect the fine features of cracking edges, a de-noising algorithm based on the connectivity checking of pixel level and cracking subimage level was designed by Peng et al [6]. The traditional image de-noising algorithm suffers from difficulty in maintaining the edge and texture features, which seriously interrupts the reliability of the detection system. To overcome this issue, an algorithm for image de-noising with line-type texture based on gradient enhanced diffusion was proposed by Zhang Yongqiang [7]. The noise spectrum often superposes with the signal spectrum, and the threshold de-noising losses part of the information while de-noising image; therefore, a novel image de-noising algorithm based on the statistical model in contourlet transform domain was proposed by Wang et al [8]. A novel pavement image de-noising method based on shearlet transform was proposed by Wu et al [9], which could smooth most of the noisy spot, but well maintain the cracks details. Owing to without regard of the noise statistical distribution, and only using Fast Fourier Transform and wavelet transform to image noise reduction bringing an image distortion, Han et al. [10] offered a method of image de-noising based on the transform domain and noise estimation. This method could completely consider the advantages of wavelet transform and Fourier Transform. Considering the image characteristics on different scales, a new image de-noising method based on ContourBougie elements morphology was proposed by Huang et al [11]. Based on the non-local means filter, an improved de-noising algorithm for synthetic aperture radar images was proposed by Zheng et al [12].

Image enhancement

At present, the enhancement technology of pavement crack image includes the histogram equalization, the image subtraction method, and the image enhancement method based on prior knowledge. In order to make the pavement crack image feature better protection and more obvious crack, Cui Hua [13] adopted the Partial Differential Equation (PDE) method for preprocessing the pavement images, and improved the P-M diffusion coefficient and fused it with coherence enhancing diffusion, thus forming the new PDE model. Aiming at overcoming the shortcoming of Retinex algorithm, an improved image enhancement algorithm based on improved Retinex algorithm combined with fuzzy algorithm was proposed by Luo Rui [14], as shown in Figure 6. With the objective of improving the traditional fuzzy enhancement algorithm, a fuzzy enhancement algorithm for pavement image based on gray relational order threshold judgment was proposed by Li Ziqiang [15]. To improve the uneven illumination of the background in the pavement image, Liu Yuchen [16] used a fuzzy relation method to eliminate the non-uniform background illumination. An adaptive multiplicative factor removal method of non-uniform background was proposed by Wang

Xiaoming [17]. Liu Yiling [18] proposed an algorithm based on gray level correction algorithm of multiplicative models with some modifications. Chen Xianqiao [19] introduced an algorithm based on difference threshold to remove the shadow from the pavement images. In order to overcome the shortcomings of the traditional image fuzzy enhancement algorithm such as small enhanced intensity and poor gray level changes in the rich image processing effect, difficult to set control parameters and other problems, a new image enhancement algorithm was proposed by Tang Lei [20]. Changxia Ma [21] offered a new approach for the detection of pavement cracks based on fractional differential and wavelet transform, and experimental results proved that the proposed detection was a valid method for the different road crack image even if any noise existed.

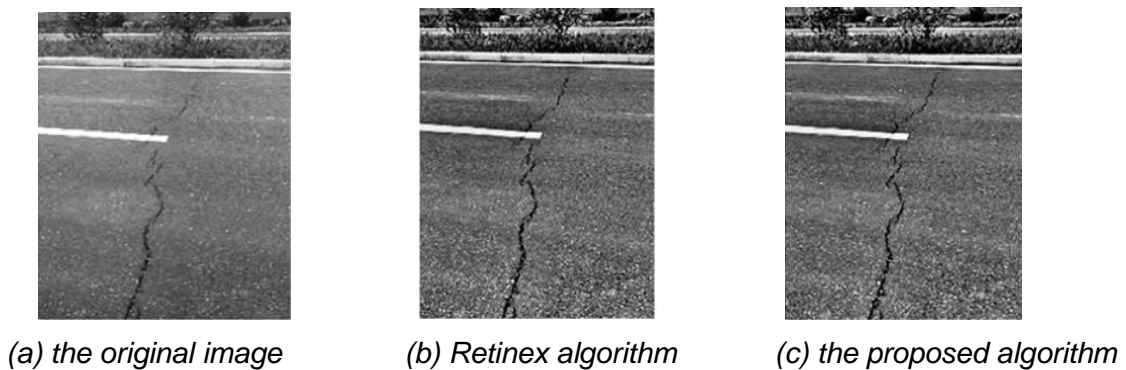


Fig.6 - Retinex algorithm combined with fuzzy algorithm

Segmentation and recognition of pavement crack image

Pavement crack image segmentation algorithm mainly includes three methods: threshold segmentation, region segmentation, and edge detection.

Threshold segmentation is one of the earliest research and application method. The basic principle is as follows: a gray level image size is set as $M \times N$, the gray level is L , and $f(x, y)$ represents the gray level of the pixel in coordinates of (x, y) , where $x \in [1, M]$, $y \in [1, N]$. The purpose of single threshold segmentation is to determine a threshold value, and the gray level of all pixels is mapped as follows:

$$f(x, y) = \begin{cases} 0, & 0 \leq f(x, y) \leq t \\ L-1, & t < f(x, y) \leq L-1 \end{cases} \quad (2)$$

The segmented image contains only two types of pixel: 0 and $L-1$, also known as “binaryzation”, which is suitable for the situation that the distribution of target and background pixels in the two different gray level ranges, for example, the global threshold method.

For the multi-threshold segmentation, it is assumed that the threshold number is n , then the gray level of pixels is mapped as follows:

$$f(x, y) = \begin{cases} l_0, & 0 \leq f(x, y) \leq t_1 \\ l_1, & t_1 \leq f(x, y) \leq t_2 \\ \dots & \dots \\ l_n, & t_n < f(x, y) \leq L-1 \end{cases} \quad (3)$$

where l_0, l_1, \dots, l_n are $n + 1$ gray levels of the segmented image. Multi-threshold segmentation method is suitable for the situation when many targets are needed to be extracted, and distributed

in different gray level intervals, for example, local threshold method. For the classic example, in 1979, OTSU proposed a threshold segmentation algorithm based on gray histogram that was used widely, which divided the image into the target area and background area. A maximum entropy image segmentation method was proposed by Liu Na [22], and the adaptive threshold segmentation was proposed by Zhang Lei [23]. In order to overcome the deficiency of OSTU threshold method and maximum entropy method, a threshold segmentation method based on histogram estimation and shape analysis was proposed by Xu Zhigang [24]. Moreover, the experimental results showed that the performance was better than the minimum error method, the OSTU threshold method, and the maximum entropy method.

The 1986 Canny algorithm is the classic algorithm based on edge detection. Based on these classical segmentation algorithms, the later researchers constructed their own segmentation algorithms, such as Sobel, Prewitt, Kirsch, Roberts, LOG, gradient operator, and Laplasse operator were studied based on edge detection, as shown in Figure 7. According to the crack edge, a gradient may exist at various angles. Li Jinhui [25] proposed the detection of image by Sobel edge detection on templates in eight directions, combined with the noise filtering algorithm of neighbourhood weighted averaging and OSTU segmentation algorithm to segment the crack images.

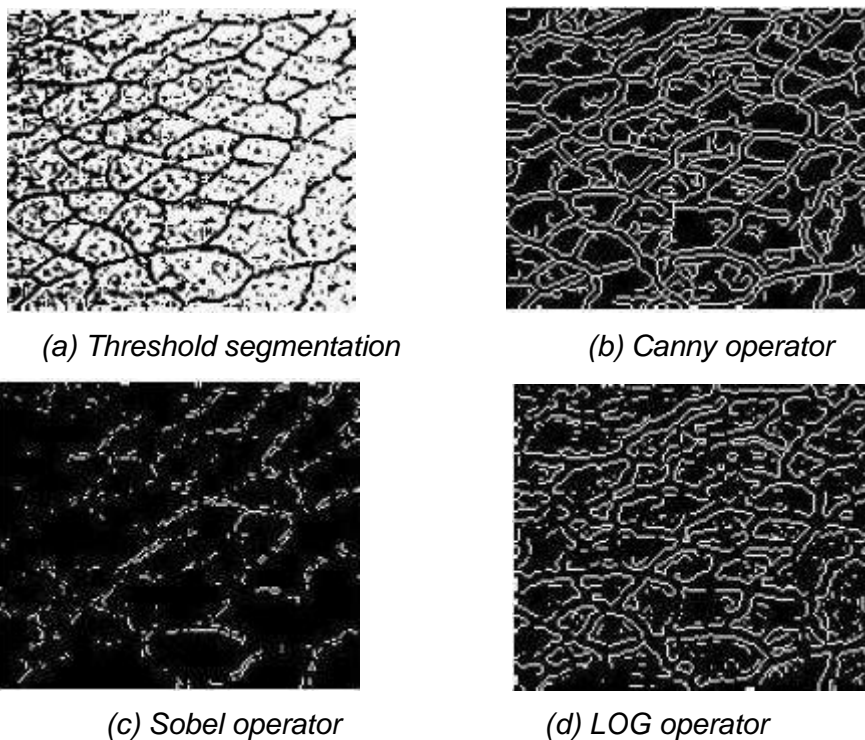


Fig.7 - Segmentation algorithms for pavement cracks image

In recent years, some new algorithms have been developed in the field of pavement crack image recognition, which do not belong to the above mentioned three types of crack identification algorithms. For example, an asphalt pavement cracks extraction method using Fuzzy C-Means clustering (FCM) segmentation and morphology was proposed by Song Beibei [26]. Xiao Xiaoming [27] presented an improved method based on cluster analysis and region growing for road detection. An automatic detection method based on binocular vision and digital image processing was proposed by Li Zhun [28]. Xu Wei [29] presented a novel pavement crack detection method through integrating multi-features fusion and Gestalt principles. According to the data characteristics of 3D pavement cracks combined with the digital image processing technology, Yuan Mengxia [30] presented a new method for 3D pavement crack identification based on the

background subtraction method. The existing algorithms exhibit lack of stability, reliability, and timeliness in large-scale applications, in particular, in wide geographical areas and varying road conditions. Therefore, in order to overcome these drawbacks, Zhang Dejin [31] proposed a new algorithm for pavement crack detection based on spatial clustering characteristics. Moreover, Li Wei [32] proposed a pavement crack detection algorithm based on 3D data and double scale clustering algorithm. Inspired by recent success on applying deep learning to computer vision and medical problems, a deep-learning based method for crack detection was proposed by Lei Zhang [33]. Wang Xiaoming [34] presented a pavement crack detection method based on multi-image and multi-resolution treatment. The application of 3D imaging technique for the detection of pavement cracks was proposed by Hu Kebo [35] and Senthan Mathavan [36]. Roberto Medina [37] presented a pavement crack detection method combining 2D/3D image processing techniques.

THE APPLICATION OF MACHINE VISION TECHNOLOGY IN PAVEMENT EVENNESS

At the end of last century, measuring equipment for road surface roughness in China mainly included the spirit level, the 3m ruler, continuum flatness instrument, and so on. These equipment sets have many disadvantages, such as low efficiency and slow speed. At present, road surface roughness measuring equipment used in China mainly consists of direct contact type mechanical device and intelligent road inspection vehicle. The direct contact mechanical device has the disadvantages of low detection accuracy, low detection efficiency, and bulky instrument. Intelligent road inspection vehicle has complex structure and high price, thus it is difficult to popularize it in practice. In recent years, with the development of machine vision technology, some researchers began to apply machine vision technology to road surface evenness detection, and achieved good results. For example, a method of pavement surface evenness detection based on image moire method was proposed by Ou Yangaiguo [38], as shown in Figure 8. Jiang Xin [39] presented a method of pavement surface evenness detection based on photogrammetry. For the cement concrete pavement, Ma Yukun [40] presented a laser vision measuring system for pavement evenness. Xie Jian [41] presented the method of pavement evenness detection based on machine vision, as shown in Figure 9. Zhang Xuelian [42] reported an on-line measurement method of road evenness based on weak calibration laser structured light.

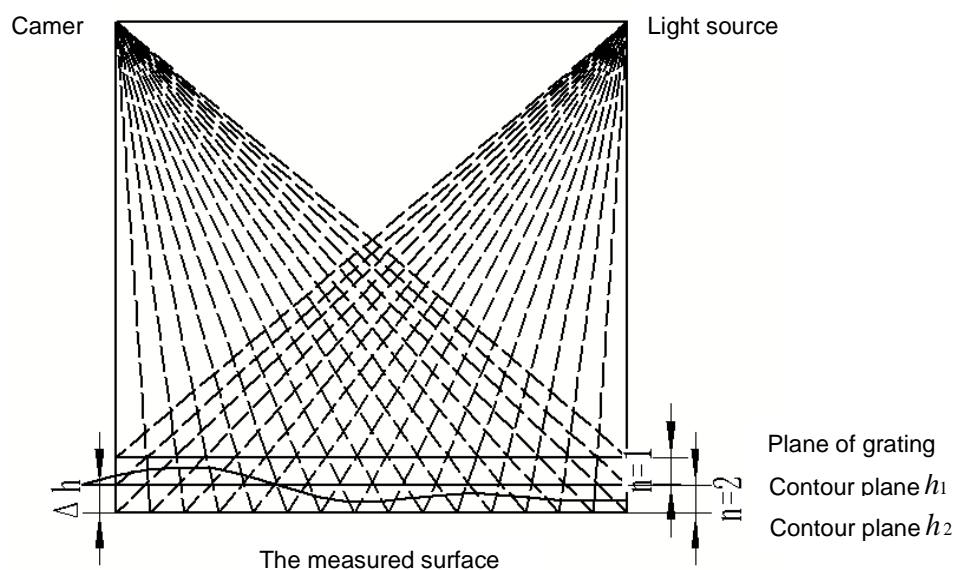
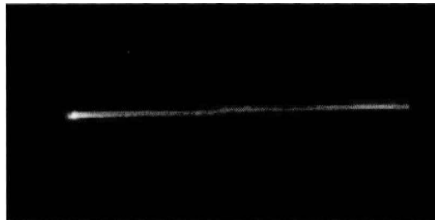
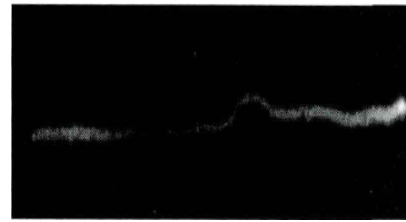


Fig.8 - The principle of shadow moire method



(a) Laser irradiation on even pavement



(b) Laser irradiation on uneven pavement

Fig.9 - The image of laser irradiation on even pavement and uneven pavement

THE APPLICATION OF MACHINE VISION TECHNOLOGY IN PAVEMENT COMPACTNESS

With the rapid development of China's transportation industry, the construction standards for the construction of the traffic line are getting higher and higher. The compaction quality of highway pavement is related to the quality of entire project, thus it is very important to detect the compactness of pavement. At present, the methods for detection of pavement compaction are divided into destructive and non-destructive testing methods. The destructive testing method includes cutting ring method, wax sealing method, sand replacement method, and water-filling method, etc. Non-destructive testing methods include vibration acceleration method, Rayleigh wave, the nuclear density instrument, and the vehicular compactness method, etc. However, research on application of machine vision technology on pavement compaction has rarely been reported yet. According to the Monte Carlo model, Li Xirong [43] offered a method of laser image processing of compacted soil based on Matlab Gui, as shown in Figure 10.

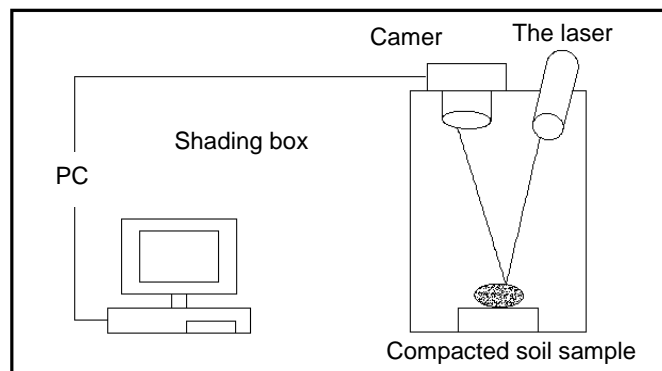


Fig.10 - Machine vision detecting system for compactness

OUTLOOK

With the emergence of new machine vision theory and new measurement theory, digital image acquisition equipment with higher resolution, faster acquisition, better image quality, and lower cost has become more popular. In this case, machine vision technology will be more widely used in other aspects of road pavement detection, such as road marking damage of intelligent detection and detection of road congestion. Some scholars have reported the use of the machine vision technology in highway construction machinery. Moreover, based on machine vision technology, some application systems, such as road construction machinery navigation and automatic levelling, construction machinery condition monitoring, and fault diagnosis, etc. have been designed. Undeniably, the application of machine vision technology in road detection will become a signature technology.

ACKNOWLEDGEMENTS

This study was financially supported by Natural Science Basic Research Plan in Shaanxi Province of China (Program No. 2018JM5049).

REFERENCES

- [1] Zhang Hong, Ying Hong., 2009. Research progress of the recognition technology of asphalt pavement crack image[J]. East China Highway, 4(178), 81-84.
- [2] Liu Wanyu, Xie Kai, Pu Zhaobang., 2007. Review of development of automatic detection system for highway pavement[J]. Journal of China & Foreign Highway, 27(2),30-33.
- [3] Qin Yahang, Su Jianhuan, Yu Rongchuan., 2016. Development of machine vision and applications[J]. Science & Technology Vision, 153-154.
- [4] Yao Guozheng, Wang Yunjiu., 1984. D.Marr and visual computing theory[J]. Automation abroad, 6,55-57.
- [5] Wang Xingjian, Qin Guofeng, Zhao Huili., 2010. Pavement crack detection method of basing on the multilevel denoising model[J]. Journal of Computer Applications, 30(6),1606-1612.
- [6] Peng Bo, Luo Nanxin, Jiang Yangsheng, Chen Cheng, K C P WANG., 2015. A denoising algorithm for pavement cracking images based on Bi-layer connectivity checking[J]. Journal of Highway and Transportation Research and Development, 32(11),7-13.
- [7] Zhang Yongqiang., 2013. Algorithm for pavement distress image denoising based on gradient enhanced diffusion[J]. Computer Science, 40(6),288-290.
- [8] Wang Gang, Wang Juan, Wang Dehua, Zhang Zhifeng, Xiao Liang, He Anzhi., 2009. The denoising algorithm for pavement images based on the statistical model in contourlet transform domain[J]. Journal of Optoelectronics·Laser, 20(10),1394-1398.
- [9] Chengdong Wu, Baihua Lu, Dongyue Chen, Li Wang., 2011. Pavement image denoising based on shearlet transform. 2011 International Conference on Electronics and Optoelectronics, 262-265.
- [10] Han Lina, Gong Guohua, Zhou Mingquan., 2012. Research on pavement image denoising using transform do-main and noise estimation[J]. Computer Engineering and Applications, 48(19),1-3.
- [11] Huang Baogui, Ma Chunmei, Lu Zhentai., 2011. New image denoising approach based on morphology[J]. Journal of Computer Applications, 31(3),757-759.
- [12] Zheng Yongheng, Cheng Jian, Cao Zongjie., 2012. SAR image denoising via improved non-local means filter[J]. Journal of Image and Graphics, 17(7),886-891.
- [13] Cui Hua, Zhou Tingjie, Guo Lu, Yuan Chao, Song Huansheng., 2014. Image enhancement using the improved partial differential equation[J]. Journal of Xidian University, 41(6),195-198.
- [14] Luo Rui, Qu Chengming., 2016. Research on image enhancement of pavement cracks based on improved Retinex algorithm[J]. Journal of Nanyang Institute of Technology, 8(6),14-18.
- [15] Li Ziqiang, Li Gang., 2011. Fuzzy enhancement algorithm of road image based on grey relational order threshold judging[J]. Journal of Hubei University of Technology, 26(3),103-109.
- [16] Liu Yuchen, Wang Guoqiang, Lin Jianrong., 2006. Image enhancement for pavement crack image based on fuzzy theory[J]. Maintenance Machinery & Construction Technology, 2,35-37.
- [17] Wang Xiaoming, Feng Xin, Dang Jianwu., 2012. Algorithm of background processing and break-point connection for pavement distress detection[J]. Journal of Lanzhou University of Technology, 38(2),63-67.
- [18] Liu Yiling, Xie Shutong., 2014. Pavement cracks detection technology based on fuzzy mathematics[J]. Journal of Jimei University(Natural Science), 19(3),224-229.
- [19] Chen Xianqiao, Yan Xinping, Chu Xiumin., 2008. Enhancement method for pavement images with shadow based on difference threshold[J]. Computer Engineering and Applications, 44(33),188-190.
- [20] Tang Lei, Zhao Chunxia, Wang Hongnan, Shao Wenze., 2007. An self-adaption fuzzy enhancement algorithm for pavement images[J]. ACTA PHOTONICA SINICA, 36(10),1943-1948.

- [21] Changxia Ma, Wengming Wang, Chunxia Zhao, Feng Di, Zhengli Zhu., 2009. Pavement cracks detection based on FDWT. IEEE International Conference on Computational Intelligence and Software Engineering, 1-4.
- [22] Liu Na, Song Weidong, Zhao Quanhua., 2015. Morphology and maximum entropy image segmentation based urban pavement cracks detection[J]. Journal of Liaoning Technical University(Natural Science), 34(1),57-61.
- [23] Zhang Lei, Ma Jian, Song Hongxun., 2009. Pavement distress detection algorithm based on tiles in wavelet domain [J]. Journal of Zhengzhou University (Engineering Science), 30(3),48-51.
- [24] Xu Zhigang, Zhao Xiangmo, Song Huansheng, Lei Tao, Wei Na., 2010. Asphalt pavement crack recognition algorithm based on histogram estimation and shape analysis[J]. Chinese Journal of Scientific Instrument, 31(10),2260-2266.
- [25] Li Jinhui., 2003. Image processing algorithm for detecting the pavement crack diseases[J]. Computer Engineering and Applications, 35,212-232.
- [26] Song Beibei, Wei Na., 2013. FCM segmentation and morphology based asphalt pavement image cracks extraction[J]. Computer Engineering and Applications, 49(4),31-34.
- [27] Xiao Xiaoming, Ma Zhi, Cai Zixing, Tang Jin., 2011. Road image segmentation based on an adaptive region growing[J]. Control Engineering, 18(3),364-368.
- [28] Li Zhun, Xu Mingming., 2016. Application of binocular vision technology in pavement crack detection of urban road[J]. Subgrade Engineering, 4,227-229.
- [29] Xu Wei, Tang Zhenmin, Xu Dan, Wu Guoxing., 2015. Integrating multi-features fusion and gestalt principles for pavement crack detection[J]. Journal of Computer-Aided Design & Computer Graphics, 27(1),147-156.
- [30] Yuan Mengxia, Sun Zhaoyun., 2015. A method of 3D surface crack identification based on target background subtraction[J]. Journal of China & Foreign Highway, 35(5),88-93.
- [31] Zhang Dejin, Li Qingquan, Chen Ying, Cao Min, He Li., 2016. Asphalt Pavement Crack Detection Based on Spatial Clustering Feature[J]. ACTA AUTOMATICA SINICA, 42(3),443-454.
- [32] Li Wei, Hu Yanju, Sha Aimin, Sun Chaoyun, Hao Xueli., 2015. Pavement crack detection based on 3D data and dual scale clustering algorithm [J]. Journal of South China University of Technology(Natural Science Edition), 43(8),99-105.
- [33] Lei Zhang, Fan Yang, Yimin Daniel Zhang, Ying Julie Zhu., 2016. Road crack detection using deep convolutional neural network. 2016 IEEE International Conference on Image Processing, IEEE.
- [34] Wang Xiaoming, Feng Xin, Dang Jianwu., 2013. Pavement crack detection method of based on multi-image and multi-resolution[J]. Journal of Lanzhou University of Technology, 39(1),76-82.
- [35] Hu Kebo, Bai Xiuqin, Xie Lei, Cao Ping., 2008. Research on surface microcosmic detection technology of asphalt pavement based on machine vision[J]. Journal of Transport Information ang Safety, 26(4),99-102.
- [36] Senthana Mathavan, Khurram Kamal, Mujib Rahman., 2015. A review of three-dimensional imaging technologies for pavement distress detection and measurements. IEEE TRANSACTIONS ON INTELLIGENT TRANSPORTATION SYSTEMS(C), 16(5),2353-2362.
- [37] Roberto Medina, José Llamas, Eduardo Zalama, Jaime Gómez-García-Bermejo., 2014. Enhanced automatic detection of road surface cracks by combining 2D/3D image processing techniques. IEEE International Conference on Image Processing, IEEE,778-782.
- [38] Ou Yangaiguo, Luo Chagen, Wang Yaping., 2011. Pavement roughness detection based on shadow moire method[J]. Highway, 55(6),185-188.
- [39] Jiang Xin., 2008. The research on pavement roughness detecting and the intelligent vision for hoisting equipment base on videogrammetry[D]. Changsha: National University of defense technology.
- [40] Ma Yukun., 2013. Laser vision method measurement system for pavement evenness[D]. Tianjin: Tianjin University.
- [41] Xie Jian., 2014. Study of surface flatness detection method based on machine vision[D]. Changsha: Central South University.
- [42] Zhang Xuelian., 2016. Realtime pavement roughness measurement via weakly calibrated laser triangulation[D]. Shenyang: Shenyang University.



- [43] Li Xirong., 2015. Process method for laser image of the compacted soil based on Matlab Gui[J]. Journal of Heilongjiang Bayi Agricultural University, 27(1),85-87.

PARAMETRIC ANALYSIS OF THE DYNAMIC BEHAVIOUR OF RC COLUMNS WITH THE CONFINEMENT EFFECT OF OVERLAPPING HOOPS SUBJECTED TO LATERAL RAPID LOADINGS

Xiang Zeng¹, Bin Xu^{2,3}

1. *College of Civil Engineering and Architecture, Hainan University, No.58, Renmin Ave., Haikou 570228, China; zengxce@hainu.edu.cn*
2. *College of Civil Engineering, Huaqiao University, Xiamen 361021, China; binxu@hqu.edu.cn*
3. *Key Laboratory for Structural Engineering and Disaster Prevention of Fujian Province (Huaqiao University), Xiamen 361021, China*

ABSTRACT

To further examine the effect of the strain rate on the behaviour of hoop-confined reinforced concrete (RC) columns, the dynamic behaviour of overlapping hoop-confined RC columns subjected to lateral rapid loadings is investigated by applying finite element analysis. Based on the verified finite element model, the effect of the following five parameters on the dynamic behaviour of RC columns were discussed considering both strain rate effect and confinement effect: the loading rate, axial load ratio, volume ratio of stirrups, shear span ratio and configuration of hoops. The following conclusions were made. The lateral-load-carrying capacity increases and the ductility decreases because of the rapid loadings, but the increase in volume ratio of the stirrups weakens the effect of the loading rate on the ductility. The axial load ratio and volumetric ratio of the stirrups affect the dynamic increasing factor (*DIF*) of the lateral-load-carrying capacity, but the effect of the shear span ratio on the *DIF* can be neglected. The increase in flexural-load-carrying capacity due to the increase in volume ratio of the stirrups under static loadings is higher than that under rapid loadings. The difference in effect of the two configurations of overlapping hoops on the dynamic behaviour of RC columns is notably small.

KEYWORDS

RC columns, Dynamic behaviour, Lateral rapid loadings, Confinement effect of overlapping hoops, Strain rate effect, Finite element analysis

INTRODUCTION

Many studies have demonstrated that the strain rate sensitivity of concrete and reinforcing steel significantly affect the RC members and structures [1-19]. The strain rate sensitivity indicates the change in properties of these materials with the increase in strain rate of concrete and reinforcing steel. Commonly, RC members can acquire the strength gain with increasing strain rate. The increase in strength is not necessarily beneficial to the dynamic response of the structure because it may result in a critical redistribution of forces in the structures or brittle types of failure with less hysteretic energy absorption capacities in some elements [19]. Bad abnormal phenomena have been found in the rapid loading tests. Some tests on RC beams show that the final failure mode shifts from the flexural failure mode at the quasi-static strain rate to the shear failure mode at the high strain rate [12-13], or the opposite transition occurs [14]. Under cyclic loadings, the damage level, stiffness degradation and strength degradation are significantly higher in the RC

columns subjected to rapid loadings compared to quasi-static loadings [5-6]. It is believed that code provisions may be non-conservative for long-duration seismic loadings with significant cyclic damage [6]. To appreciate the effect of the strain rate sensitivity of concrete and reinforcing steel on the global seismic response of RC frame structures, Asprone et al. conducted an earthquake evaluation analysis, and the result shows that considering the updated material properties, to account for the earthquake-induced strain rate, a strength reserve of the structural system is experienced when only ductile failure mechanisms are considered; however, the structural capacity decreases when the brittle failure mechanisms are included [7]. Generally, the strain rate of materials in RC structures under earthquake loadings is approximately 10^{-4} - 10^{-1} /sec. Thus, it may be more rational to consider the strain rate effect of concrete and steel when one evaluates the dynamic behaviour of RC structures under earthquake action.

For the dynamic behaviour of RC column considering the strain rate effect, until now, many experimental studies focus on the lightly confined RC columns [2,5-6,15-16]. Fewer experimental studies [17-18] have been conducted on confined RC columns under concentric compressive rapid loadings. To make up for the lack of experimental studies, the finite element analysis method was used to analyse the dynamic compressive behaviour of confined RC columns [1,3,8], but there is no study on the confined RC columns subjected to lateral rapid loadings. Because of the high requirement on loading instrument for the rapid loading test, the FEA modelling becomes a good choice for parametric studies.

In this paper, the objective is to investigate the strain rate effect on the dynamic behaviour of reinforced concrete columns confined by overlapping hoops under lateral rapid loadings using finite element analysis. The finite element model developed by the author [1] is used, which considers the confining effect of the overlapping hoops and strain rate effect of concrete and steel. The effect of the parameters, including the lateral loading rate, axial load ratio, volumetric ratios of transverse reinforcement, shear span ratio and configuration of hoops (type A and type B in Figure 1), on the dynamic behaviour of confined RC columns were investigated.

COLUMN MODEL FOR PARAMETRIC ANALYSIS

The designed column model for the parametric analysis is presented in Figure 1. The center region in the column is 950 mm or 1680 mm, which corresponds to the shear span ratio of 2.7 or 4.5. The columns have a fixed boundary condition at the bottom with 300 mm in length and loading end at the top with 300 mm in length. The spacing of transverse hoops was reduced by one-half at each end of the columns to provide extra confinement and ensure that failure occurred in the central region. All columns have identical cross sections of 450 mm × 450 mm, and the core size measured from the center of the perimeter hoop was maintained constant at 400 mm × 400 mm. Two configurations of hoops (type A and type B in Figure 1) were used. These arrangements are typical for 8-bar and 12-bar columns. The center-to-center spacing of longitudinal bars across the section for type-A and type-B arrangements was 183 mm and 123 mm, respectively. More details of the cross sections in the test regions of different columns are shown in Table 1. All specimens with identical longitudinal reinforcement ratios of 2.65% had identical yielding strength (400 MPa) of longitudinal steel and strength (300 MPa) of the transverse hoops. The concrete compressive cylinder strength f_c was 30 MPa.

Various key parameters in Table 1 were considered, including the lateral loading rate (0.1 mm/s (quasi-static loadings) and 100 mm/s), axial load ratio n (0, 0.2, 0.4, 0.6, 0.8), volumetric ratios of transverse reinforcement ρ_{sv} (1.5% and 3.0%), shear span ratio λ (2.7, 4.5) and configuration of hoops (type A and type B). Table 1 summarizes the specimen characteristics of the simulation matrix. The titles of the specimens in Table 3 describe the varying parameters and have the following meaning. The first letter (A or B) in the titles represents the reinforcement arrangement of type A or type B. The numbers after the first letter indicates the shear span ratio λ ($\lambda=2.7$ or $\lambda=4.5$). The numbers behind the middle hyphen represent the volumetric ratio ρ_{sv} of the

transverse reinforcement. Numbers 3.0 and 1.5 indicate $\rho_{sv}=3\%$ and $\rho_{sv}=1.5\%$, respectively. The last character n represents the axial load ratio of 0-0.8.

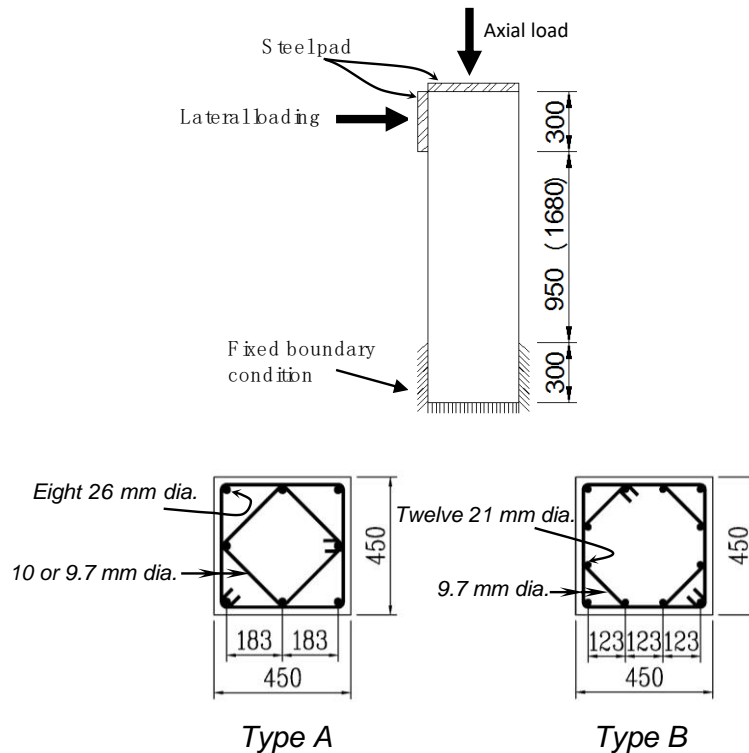


Fig. 1 - Details of the column model for the parameter analysis

Tab. 1 - Columns for the parameter analysis

Specimen	Longitudinal reinforcement diameter (mm)	Transverse reinforcement			Axial load ratio n	Lateral loading rate
		Diameter (mm)	Spacing (mm)	Volumetric ratio ρ_{sv}		
A2.7-1.5-n	26	10	86	1.5%		
A2.7-3.0-n	26	10	43	3.0%	0,0.2,0.4,	0.1 mm/s (Quasi-static), 100 mm/s
A4.5-3.0-n	26	9.7	43	3.0%	0.6,0.8	
B2.7-3.0-n	21.2	9.7	43	3.0%		

EXPLICIT DYNAMIC FEA MODELLING

The finite element model was developed by the author [1], which has been verified by the experiment on axial compression RC column confined by type-A and type-B overlapping hoops at low and high strain rates, was used to investigate the strain rate effect on the behaviour of the RC column under lateral rapid loadings. As shown in Figure 2, a half model with symmetric boundaries on the Y-Z plane was used based on the symmetry, which reduced the computation cost. A fixed boundary condition was applied at the bottom of the columns with 300 mm in length. The steel plates in Figure 1 were modelled with analytical rigid plates, which is reasonable to save the computing cost. The motion of the rigid plate was constrained to the motion of the reference point, which implies that the translational and rotary motions of the rigid plate are consistent with the

corresponding reference point. Thus, the axial load was applied to the top reference point RP with an allowable translational motion in direction Z and an allowable rotational motion around the X-axis, and the lateral load was applied to the side reference point RP-1 with an allowable translational motion in direction Y and an allowable rotational motion around the X-axis.

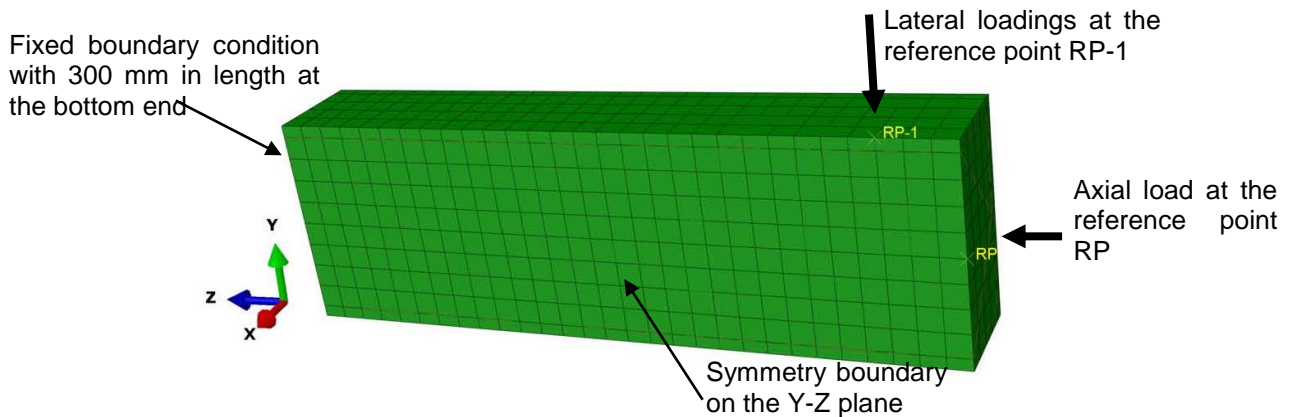


Fig. 2 - Illustration of the finite element model

INFLUENCE ANALYSIS OF INVESTIGATED PARAMETERS

Effect of loading rate

At the loading rate of 100 mm/s, the strain rates reach to the order of magnitude of $10^{-1}/s$ and $10^{-2}/s$ for columns with shear span ratio 2.7 and 4.5, respectively, which is in the range of strain rate of RC structures under earthquake action. As shown in Figure 3, the loading rate has an obvious effect on the lateral load F versus displacement Δ curves. The lateral bearing capacity increases with the increase in loading rate. The dynamic increasing factor (DIF) of the lateral bearing capacity, namely, the ratio of dynamic bearing capacity to quasi-static bearing capacity at a loading rate of 0.1 mm/sec, is commonly used to describe the effect of the loading rate on the bearing capacity. In these cases, the maximum DIF is 1.2 when the loading rate reaches to 100 mm/s. Figure 3(a) shows the descending branches of $F-\Delta$ curves become obviously steeper with the loading rate increasing when the axial load ratio is 0.8. However, increasing the volumetric ratio of stirrups the effect of loading rate on the slope of the descending branches of $F-\Delta$ curves becomes weaker, which is shown in Figure 3(b).

Influence of axial load ratio and volumetric ratio of stirrups

(1) Lateral load F versus displacement Δ curves

Figure 4 shows the similar influence of the axial load ratio n and volumetric ratio of stirrups ρ_{sv} on $F-\Delta$ curves for quasi-static and rapid loadings. When the axial load ratio n is between 0.0 and 0.6, the lateral bearing capacity of columns increases as the axial load ratio increases, but the ductility decreases. When the axial load ratio is in the low range of 0.0 to 0.2, the columns behave with good ductility and increasing the volumetric ratio of stirrups from 1.5% to 3.0% has little influence on the $F-\Delta$ curves. As the axial load ratio increases to 0.6, the ductility decreases obviously. However, increasing the volumetric ratio of stirrups is able to enhance the lateral bearing capacity and obviously improve the ductility in the range of axial load ratio from 0.4 to 0.6. The reason is that the compressive area of the core concrete confined by the overlapping hoops increases as the axial load ratio increases, and then the confining effect of overlapping hoops on

the core concrete becomes stronger, which enhances the strength and ductility of the core concrete.

When the axial load ratio n reaches to 0.8, the descending branches of $F-\Delta$ curves drop more remarkable for the columns with volumetric ratio of stirrups 1.5%. In addition, the lateral bearing capacity drops obviously for the columns under quasi-static loading. However, the lateral bearing capacity for the columns under rapid loading drops a little. That is because the strain rate effects increase the strength of concrete and steel. As the axial load ratio increases, that the lateral bearing capacity falls down means the failure model of the RC sections changes from a tension failure to a compression failure. When raising the volumetric ratio of stirrups to 3.0% at $n=0.8$, the lateral bearing capacity drops slightly under quasi-static loading or increases slightly under rapid loading.

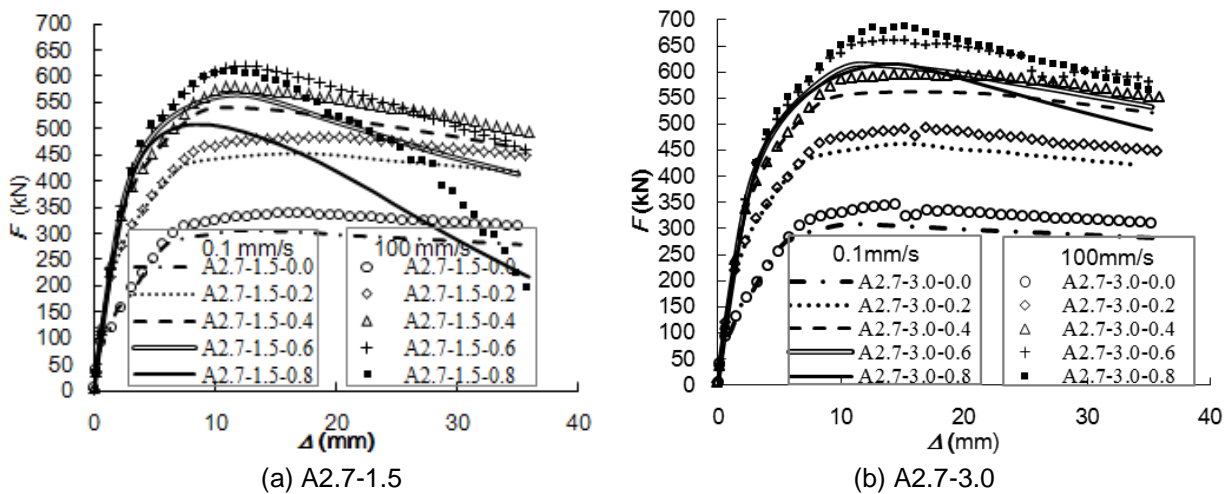


Fig. 3 - Effect of the loading rate on the $F-\Delta$ curves

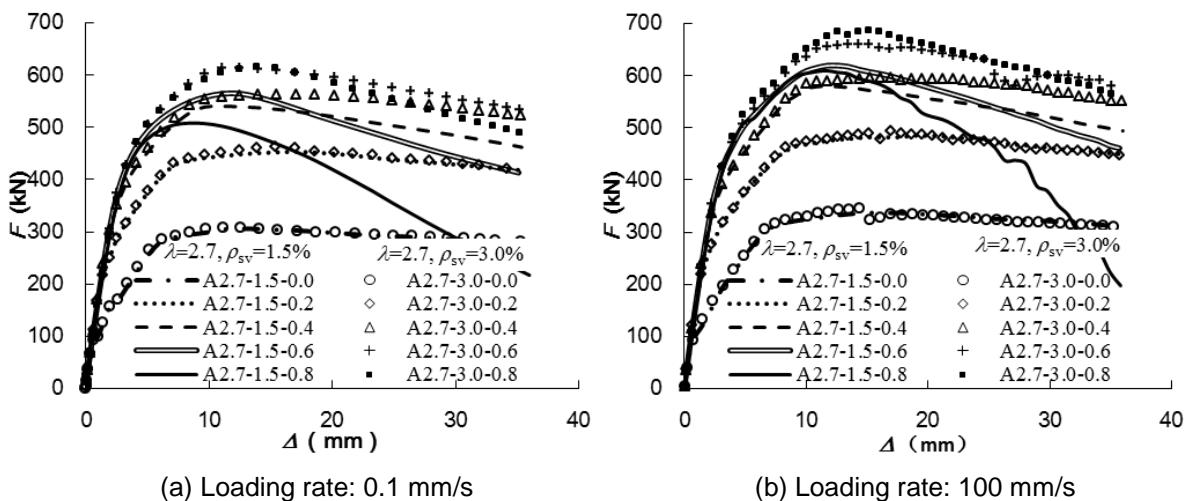


Fig. 4 - Influence of axial load ratio and volumetric ratio of stirrups on $F-\Delta$ curves

(2) Dynamic increasing factor (DIF) of the lateral bearing capacity

As shown in Figure 5, the DIF decreases with the axial load ratio n increasing at first, and then inversely ascends with n increasing. Figure 6 depicts the influence of volumetric ratio of

stirrups ρ_{sv} on *DIF*. In Figure 6, $R_{DIF,sv}$ means the ratio of the *DFI* with ρ_{sv} of 3.0% to the *DFI* with ρ_{sv} of 1.5% for the columns with shear span ratio of 2.7 at the same axial load ratio. It can be seen that increasing the volumetric ratio of stirrups reduces the *DIF*, and $R_{DIF,sv}$ becomes smaller with the axial load ratio increasing. Raising the volumetric ratio of stirrups from 1.5% to 3.0% makes the *DFI* reduce 7% at an axial load ratio of 0.8. After the axial load ratio increasing, the compression area of the section broadens, which is beneficial to the confining effect. The phenomenon of *DIF* reducing has been explained by the researches [20-21] that as the confining effect of stirrups on concrete strengthens, the increase in strength of concrete due to strain rate effect reduces.

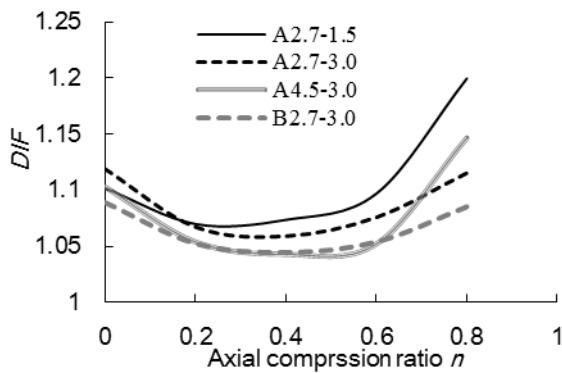


Fig 5 - Influence of axial load ratio n on *DIF*

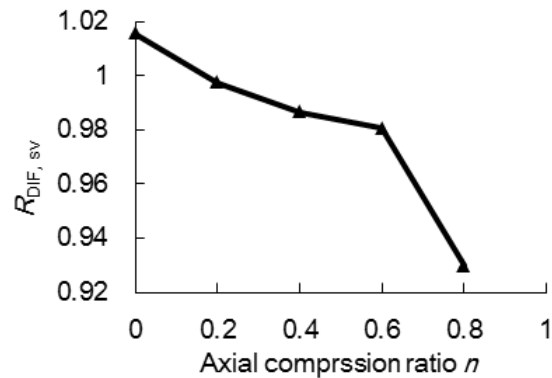


Fig. 6 - Influence of volumetric ratio of stirrups on *DIF*

(3) Moment (*M*)-Axial load (*N*) interaction diagram for RC column section

Figure 7 shows the similar influence of volumetric ratio of stirrups ρ_{sv} on *M-N* interaction diagrams of RC columns section for quasi-static and rapid loading. Increasing the ρ_{sv} makes the axial load at balance failure increase. The ρ_{sv} has little influence on the interaction diagrams when the axial load ratio n is in low range. As the n rises, the increase in ρ_{sv} enhances the flexural capacity. It seems that Figure 8 shows the influence of ρ_{sv} on flexural capacity at a certain n for different loading rate. There $M_{3.0}/M_{1.5}$ means the ratio of flexural capacity with $\rho_{sv}=3.0\%$ to flexural capacity with $\rho_{sv}=1.5\%$ at the same loading rate and axial load ratio. It is seen that increasing the ρ_{sv} makes the percentage of increase in flexural capacity larger with the axial load ratio increases and the effect is stronger under quasi-static loading than under rapid loading.

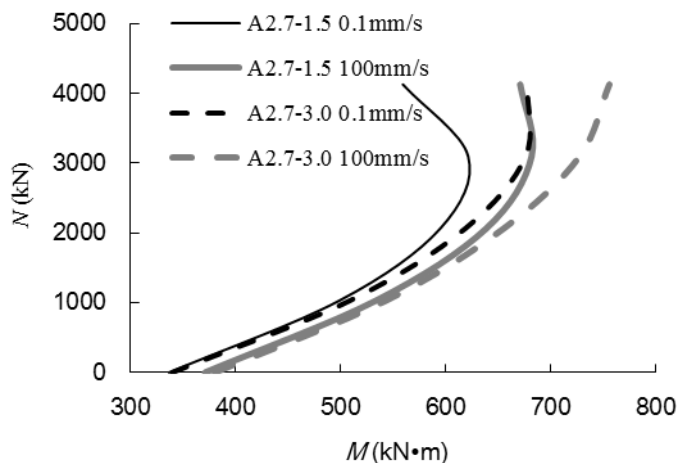


Fig. 7 - Influence of volumetric ratio of stirrups and loading rate on *M-N* interaction diagrams

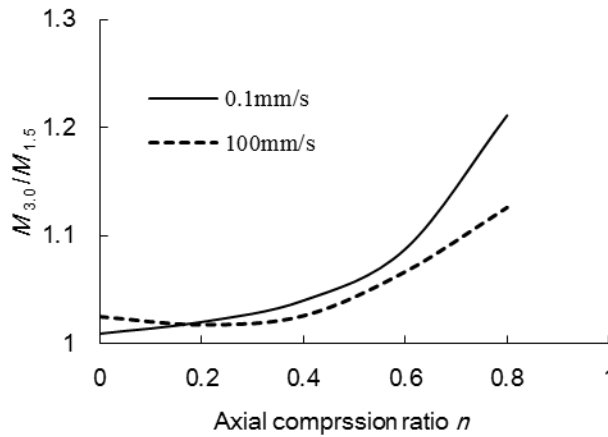


Fig. 8 - Influence of volumetric ratio of stirrups on flexural capacity for column with shear span ratio of 2.7

Influence of shear span ratio

Figure 9 shows the similar influence of shear span ratio λ on $F-\Delta$ curves for quasi-static and rapid loading. As the shear span ratio increases, the lateral stiffness and lateral bearing capacity fall obviously, but the ductility becomes better. Figure 10 shows the influence of shear span ratio λ on the DIF of lateral bearing capacity. In the figure, $R_{DIF, \lambda}$ means the ratio of the DFI with λ of 4.5 to the DFI with λ of 2.7 for the columns with the same axial ratio and volumetric ratio of stirrups. It seems that the influence of shear span ratio on the DIF , which is less than 3%, can be negligible.

Influence of configuration of stirrups

When investigating the influence of configuration of stirrups, the longitudinal reinforcement ratio, the volumetric ratio of stirrups and the spacing of overlapping hoops keep the same for the contrast columns, only the configuration of stirrups is different from each other. From Figure 11, it is seen that the type A and type B reinforcement arrangements have little different influence on the $F-\Delta$ curves for different loading rate.

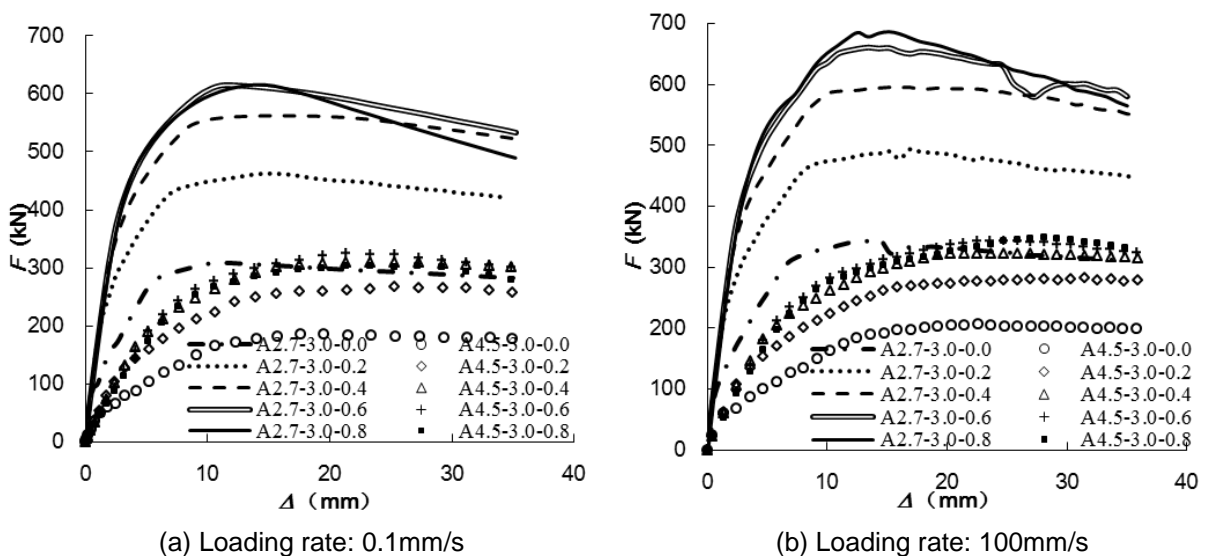


Fig. 9 - Influence of shear span ratio on $F-\Delta$ curves

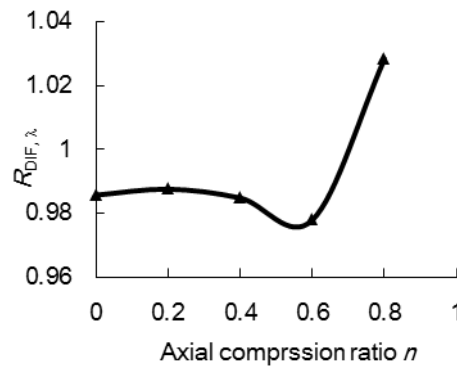


Fig. 10 - Influence of shear span ratio on DIF

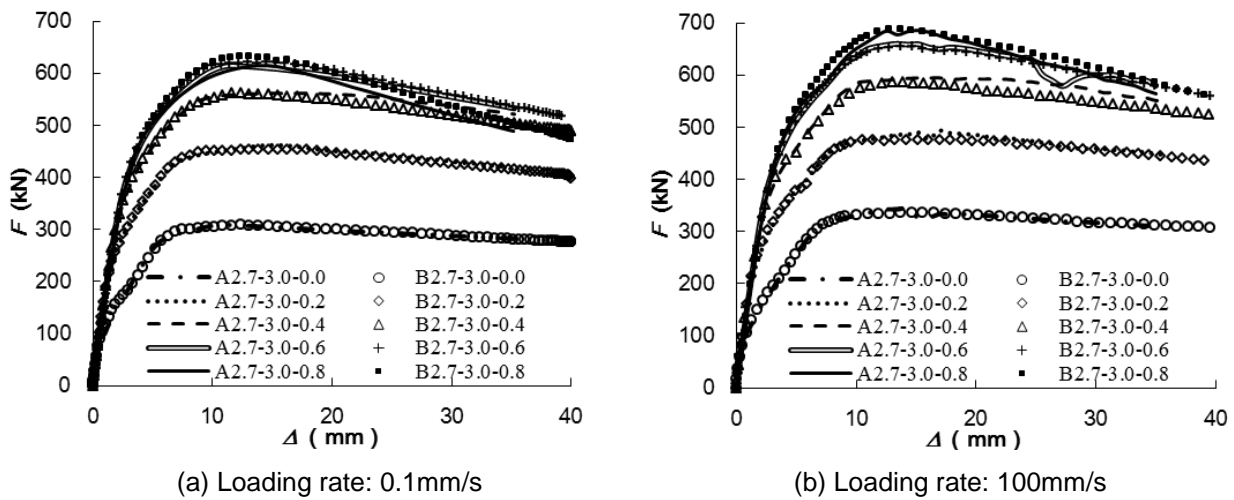


Fig. 11 - Influence of configuration of stirrups on $F-\Delta$ curves

CONCLUSION

Based on the three-dimensional nonlinear finite element analysis model, a parametric analysis of dynamic behaviour of RC columns with confinement effect of overlapping hoops subjected to lateral rapid loading in this paper. The following conclusions were drawn.

- (1) Increasing the lateral loading rate increases the lateral bearing capacity, but decreases the ductility and makes the descending branches of $F-\Delta$ curves become steeper. However, increasing the volumetric ratio of stirrups is able to weaken the effect of loading rate on the slope of the descending branches of $F-\Delta$ curves. Raising the axial load ratio makes the descending branches of $F-\Delta$ curves become steeper for different loading rate.
- (2) The influence of axial load ratio, volumetric ratio of stirrups and shear span ratio on the behaviour of RC columns is similar for different lateral loading rate.
- (3) The dynamic increasing factor (DIF) of lateral loading carrying capacity decreases with the axial load ratio increasing and then inversely develops. Increasing the volumetric ratio of stirrups reduces the DIF and the larger the axial load ratio is, the more the DIF reduces. The influence of shear span ratio and configuration of hoops on the DIF can be negligible.
- (4) The volumetric ratio of stirrups has similar influence on the interaction diagram of RC column section for different lateral loading rate. However, the increase in volumetric ratio of stirrups enhances flexural capacity larger under quasi-static loading than under rapid loading and that is influenced by the axial load ratio.

- (5) With the identical longitudinal reinforcement ratio, volumetric ratio of stirrups and spacing of overlapping hoops, the change of configuration of hoops between type A and type B slightly affects the behaviour of RC columns for different lateral loading rate.

ACKNOWLEDGEMENTS

The research reported in the paper is supported by the National Natural Science Foundation of China (No. 51608156) and the Project of the Natural Science Foundation of Hainan Province (No. 20165208). These sources of financial support are highly appreciated.

REFERENCES

- [1] Zeng X., 2017. Finite element analysis of behavior of reinforced concrete columns confined by overlapping hoops subjected to concentric rapid loading. *Civil Engineering Journal*, 26(4): 530-543.
- [2] Xu B., Zeng X., 2014. Experimental study and finite element analysis on the dynamic behavior of slender RC columns under concentric compressive rapid loadings. *Engineering Mechanics*, 31(4): 210-217. (in Chinese)
- [3] Zeng X., Xu B., 2014. Numerical simulation on the dynamic behavior of short RC columns subjected to concentric rapid loading considering confinement effect of stirrups. *Engineering Mechanics*, 31: 190-197. (in Chinese)
- [4] Adhikary S.D., Li B., Fujikake K., 2013. Strength and behavior in shear of reinforced concrete deep beams under dynamic loading conditions. *Nuclear Engineering and Design*, 259: 14-23.
- [5] Wang D., Li H.N., Li G., 2013. Experimental tests on reinforced concrete columns under multi-dimensional dynamic loadings. *Construction and Building Materials*, 47: 1167-1181.
- [6] Ghannoum W., Saouma V., Haussmann G., et al., 2012. Experimental investigations of loading rate effects in reinforced Concrete Columns. *Journal of Structural Engineering*, 138(8):1032-1041.
- [7] Asprone D., Frascadore R., Ludovico M.D., et al., 2012. Influence of strain rate on the seismic response of RC structures. *Engineering Structures*, 35: 29-36.
- [8] Song Z., Lu Y., 2011. Numerical simulation of concrete confined by transverse reinforcement. *Computers & Concrete*, 8(1): 757-760.
- [9] Adhikary S.D., Li B., Fujikake K., 2012. Dynamic behavior of reinforced concrete beams under varying rates of concentrated loading. *International Journal of Impact Engineering*, 47: 24-38.
- [10] Mizuno J., Matsuo I., Suzuki A., et al., 2001. Effects of loading rate on reinforced concrete shear walls- Part 3: High speed loading tests of reinforced concrete shear walls and FE simulation analyses. In: *International Conference on Earthquake Resistant Engineering Structures*, 63-72.
- [11] Ogawa T., Nakanishi M., Adachi H., 2006. Study on the mechanical properties of reinforced concrete exterior beam-column joints under dynamic loading. *Journal of Structural & Construction Engineering (Transactions of AIJ)*, 71(600): 155-162.
- [12] Takeda J., Tachikawa H., Fujimoto K., 1977. Effects of straining rate on deformation and fracture of reinforced concrete members. In: *Proceeding of Sixth World Conference on Earthquake Engineering*. New Delhi, 32-56.
- [13] Mutsuyoshi H., Machida A., 1984. Properties and failure of reinforced concrete members subjected to dynamic loading. *Transactions of the Japan Concrete Institute*, 6: 521-528.
- [14] Kulkarni S.M., Shah S.P., 1998. Response of reinforced concrete beams at high strain rates. *ACI Structural Journal*, 95(6): 705-715.
- [15] Iwai S., Minami K., Wakabayashi M., 1988. Stability of slender reinforced concrete members subjected to static and dynamic loads. In: *Proceedings of Ninth World Conference on Earthquake Engineering*, Vol. VIII 901-906.
- [16] Reinschmidt K.F., Hansen R.J., Yang C.Y., 1964. Dynamic tests of reinforced concrete columns. *ACI Journal Proceedings*, 61(3): 317-334.
- [17] Scott B.D., Park R., Priestley M.J.N., 1982. Stress-strain behavior of concrete confined by overlapping hoops at low and high strain rates. *ACI Journal Proceedings*, 79(1): 13-27.
- [18] Li B., Park R., Tanaka H., 2000. Constitutive behavior of high-strength concrete under dynamic loads. *ACI Structural Journal*, 97(4): 619-629.

- [19] Soroushian P., Obaseki K., 1986. Strain rate-dependent interaction diagrams for reinforced concrete sections. *Journal of the American Concrete Institute*, 83(1): 108-116.
- [20] Fujikake K., Mori K., Uebayashi K., et al., 2000. Dynamic properties of concrete materials with high rates of triaxial compressive loads. In: *International Conference on Structures under Shock & Impact VI* Cambridge, 511-522.
- [21] Yan D.M., Lin G., Chen G., 2009. Dynamic properties of plain concrete in triaxial stress state. *ACI Material Journal*, 106(1): 89-94.

INVESTIGATING OF SEISMIC PARAMETERS OF RC FRAMES REHABILITATED BY ECCENTRICALLY BRACING WITH VERTICAL LINK

Faramarz Noruzi¹, Heydar Dashti Naserabadi¹, Hosein Nematian Jelodar¹, Hosein Dorvar²

- 1. Islamic Azad University, Faculty of Civil Engineering, Department of Civil Engineering, Chalus, Iran; faramarz.noruzi46@gmail.com, dashti@iauc.ac.ir, hnematian@gmail.com*
- 2. Iran University of Science & Technology, Faculty of Civil Engineering, Department of Civil Engineering, Tehran, Iran; hoseindorvar@yahoo.com*

ABSTRACT

Most of existing concrete structures do not have suitable seismic performance due to various reasons, therefore they need seismic rehabilitation. One of the seismic rehabilitation method in structural level is using of steel bracing. New investigation of steel bracing can be referred to eccentrically bracing with single vertical link. This method of rehabilitation provides many advantages such as increasing in ductility, stiffness, lateral resistance, architectural compatibility, low weight, and the fewest changes in primary structural system. In this paper, two existing 3- and 9-story RC frames are assessed on the basis of FEMA356. Eccentrically bracing with single vertical link is used for seismic rehabilitation of these frames. The results of nonlinear time history analysis based on the maximum inter-story drift, maximum roof displacement and plastic rotation in critical elements of original and rehabilitated frames for two performance levels of Life safety (LS) and Collapse Prevention (CP) are presented. The results indicate that single vertical link can lead structures to the desired performance level with minimum cost and braced span number.

KEYWORDS

Seismic rehabilitation, RC frames, eccentrically bracing, Time history, Shear link

INTRODUCTION

The possibilities of severe earthquakes due to natural geology conditions of structure site on one hand and the design and construction of many RC (Reinforced Concrete) buildings that seismic loading criteria are not observed or due to changes of these criteria, their seismic loading are underestimated on the other hand, make the seismic evaluation and rehabilitation essential for these buildings. Recent earthquakes around the world have shown that non-ductile (gravity load-designed) RC structures are so vulnerable to the earthquake that it causes severe damage or complete collapse. Various methods have been proposed for the seismic rehabilitation of RC structures, that each of them has their own advantages and disadvantages. One of the common methods among researchers is applying of new structural members as steel braces to RC structures [1-8]. Steel bracing are often used for seismic retrofitting of RC buildings, in contrast, while they are subjected to strong ground motions, the buckling of the braces leads to loss of lateral stiffness and strength of the structural system [9]. Thus, seismic retrofitting of RC buildings

with steel bracing that may lead buckling cannot be a reliable retrofitting solution. Using of eccentrically bracing with vertical link, not only eliminates the probable buckling, but also leads to reduction of large inelastic deformations of RC members. Accordingly, this study is motivated to a seismic rehabilitation system that is capable of dissipating the earthquake input energy without buckling of braces. In recent years, seismic rehabilitation method of using the eccentrically bracing with vertical link as an additional energy dissipation element has been widely used. Ghobarah and Abou Elfath (2001) examined the distribution effect of eccentrically bracing along the height of the RC frames in cases of stories drift and damage indexes [10]. Seismic assessment of RC structures that were rehabilitated by eccentrically bracing with single vertical link was studied by Durucan and Dicleli (2010) [11]. Results show that plastic deformations of structural components were less, compared to conventional approaches. According to the research carried out by Sahoo and Rai (2010), the effect of changing the vertical link material from steel to aluminium is discussed and the results showed a significant increase in the energy absorption capability of seismic rehabilitated non-ductile RC frames using eccentrically bracing with single vertical link [12]. The failure modes of the connections between vertical link with slab, and the braces with RC columns and the beams by a series of full-scale experiments on RC building rehabilitated by eccentrically braces with vertical link were assessed by Mazzolani (2008) [13]. This method also provides many advantages such as increasing in ductility, stiffness, lateral resistance, architectural compatibility, low weight, and the fewest change in primary structural system. Since, the approach of seismic rehabilitation by usage of eccentrically bracing with vertical link has not been done before, more studies about this system are required. The Proposed Seismic Rehabilitation System (PSRM), as it is shown in Figure 1, can be applied in various configurations which including: (a) link and braces are directly connected to the RC members through steel plates by bolts and epoxy grouting, (b) the link is connected to steel beam collector, which is attached to the concrete beam, and the rest of the members are connected to the RC members via steel plates or (c) link and braces are housed in a rectangular steel frame (housing frame) where the steel frame is connected to the RC members by bolts and epoxy grouting.

Research Outline

In this paper, the basis of seismic rehabilitation method by usage of eccentrically bracing with single vertical link is studied. In order to evaluate the seismic performance of PSRM, two existing non-ductile RC frames, 3 and 9 stories are selected according to Ref. [14] and they will be seismically evaluated according to FEMA 356 [15] after numerical modelling in OpenSees software [16]. The PSRM is determined after the seismic evaluation of frames and then the frames are designed based on the desired performance level. A performance based approach that includes nonlinear static analysis and response spectrum analysis is used for the seismic rehabilitation design of the frames which is considered in this study. Then, numerical modelling of single vertical link is done in OpenSees according to the respective experimental results. After that, Nonlinear Time History (NLTH) analysis are conducted to assess the maximum inter-story drifts, maximum roof displacement, plastic rotations of critical members and deformed shapes of frame at the instant of maximum stories drifts in two different seismic performance levels (Life Safety and Collapse Prevention PLs). Then, the results are compared with restrictions of FEMA 356.

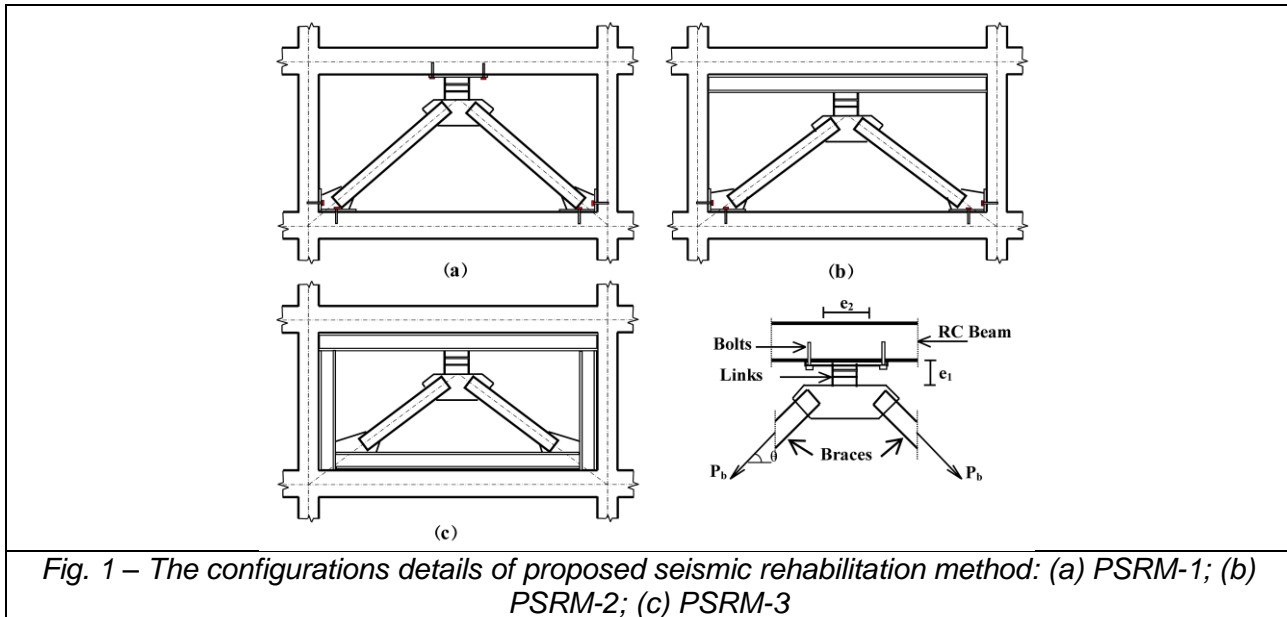


Fig. 1 – The configurations details of proposed seismic rehabilitation method: (a) PSRM-1; (b) PSRM-2; (c) PSRM-3

Details of the Considered Frames

Analytical models to evaluate PSRM are two 2D frames of non-ductile RC office buildings, 3 and 9 stories that are designed according to the ACI code [17] by considering only the gravity loads. The design concrete strength is 21 MPa and the design steel strength is 300 MPa and the modulus of elasticity is 200000 MPa. The design dead load and live load for the frames are taken as 35 kN/m and 12 kN/m respectively. The building mass due to the weight of all structural and nonstructural elements is equal to 945kN/floor. The frame elevations are shown in Figure 2 and the structural details of frames are given in Table 1.

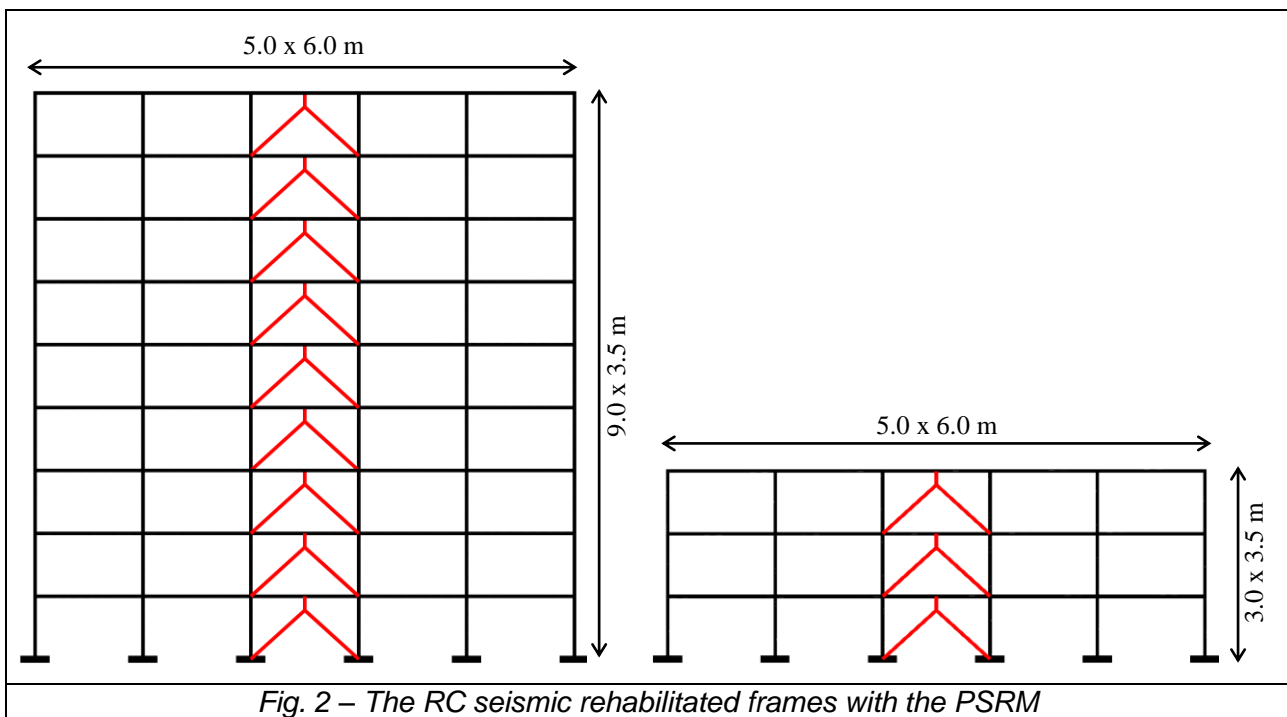


Fig. 2 – The RC seismic rehabilitated frames with the PSRM

Tab. 1 - Structural details of 3 and 9 story RC frames

Story		exterior column		interior column		interior beam		
		Size	Steel	Size	Steel	Size	Top Steel	Bottom Steel
3 Story	1-3	300x300	4Φ19	400x500	8Φ19	250x600	5Φ19	2Φ19
9 Story	1-3	500x500	8Φ22	600x600	8Φ25	250x600	5Φ19	2Φ19
	4-6	400x400	8Φ19	500x500	8Φ22	250x600	5Φ19	2Φ19
	7-9	300x300	4Φ19	400x500	8Φ19	250x600	5Φ19	2Φ19

Design of Proposed Seismic Rehabilitation System

Seismic rehabilitation objectives which are used in this paper consist of basic and optimal objectives. In basic and optimal objectives, the frames should achieve the Performance Levels (PLs) of Life Safety (LS) and Collapse Prevention (CP). In LS PL, low or repairable structural and non-structural damage is expected for moderate earthquake excitations (10% possibility of exceedance in 50-year). In CP PL, irreparable or hardly repairable structural and nonstructural damage will be happened but collapse is not expected for major earthquake excitations (2% possibility of exceedance in 50-year). In FEMA 356, the allowable criteria of PLs are mainly defined by plastic rotation limits for the RC members.

In order to design the rehabilitation details of the frames; a performance based approach is used, that is mainly based on the equal energy dissipation principle. In this method, the monotonic energy dissipation capacities of the frames based on the roof displacement are calculated and compared in two regions of linear elastic region which is obtained from Response Spectrum (RS) analyses and nonlinear inelastic region which is obtained from Nonlinear Static Pushover (NLSP) analyses. The difference in area between the two regions of elastic and inelastic of base shear force versus roof displacement curve is equal to the required additional energy that should be absorbed by the PSRM [11].

The steel characteristics which are used for the design process of PSRM have yield strength of 250 MPa and the modulus of elasticity of 200000 MPa. Braces and shear links details of PSRM for frames are available in Table 2.

Tab. 2 - Details of PSRM for 3 and 9 story RC frames

Story		Braces	Frame	Single -VL	
		Section	Section	Section	e_1 (mm)
3 Story	1	2UNP140	IPE240	IPE400	820
	2	2UNP120	IPE220	IPE360	760
	3	2UNP120	IPE220	IPE330	700
9 Story	1-3	2UNP140	IPE270	IPE450	860
	4-6	2UNP140	IPE240	IPE400	760
	7-9	2UNP120	IPE220	IPE360	700

PSRM Details Design

At first, the number of brace-link system and the shear strength that is required at each floor, Q_{Li} , is calculated based on seismic rehabilitation design procedure. In order to prevent lateral strength and stiffness degradation that is associated with braces buckling, the shear link is designed in such a way that yields before brace buckling. Shear yielding provides more effective energy dissipation than flexural yielding [18] and hence, it is appropriate for the design of vertical link in the PSRM. The shear yield strength, V_y , of I section according to AISC 2010 [19] is given by:

$$V_y = 0.6F_y A_w \tag{1}$$

Where F_y is the yield strength of steel, and A_w is the cross-section area of the web of the link. Setting $V_y = Q_{Li}$, the cross-section area of the web at i story is obtained by $A_{wi} = \frac{Q_{Li}}{0.6F_y}$. Then an I section with the calculated web area, A_w , is chosen. The middle stiffeners for the link web are designed based on AISC 2010. For vertical shear link that its moment diagram is shown in Figure 3, in order to obtain the conditions of shear plastic hinge formation before flexural plastic hinge formation due to the unequal moments at both ends of the link, the Equation 2 for determining the length of shear link, (h_s) is proposed by Eurocode 8 [20].

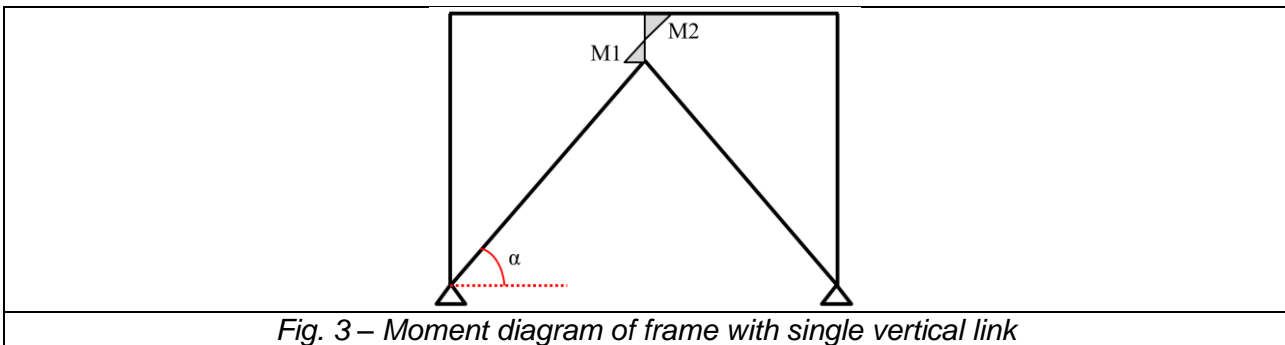


Fig. 3 – Moment diagram of frame with single vertical link

$$h_s \leq \frac{0.8 \times (1 + k)M_p}{Q_{Li}} \quad ; \quad k = \frac{M_2}{M_1} \quad ; \quad M_2 \leq M_1 \tag{2}$$

Where, M_1 and M_2 are the unequal moments at both ends of the shear link and M_p is the plastic moment of shear link. According to proposed details in the region of the compression bracing buckling, the axial tensile and compressive forces of the both tension and compression braces are equal to the buckling load, P_b . Consequently, in order to prevent the buckling of the compression braces, the sum of the horizontal components of the buckling loads of the two braces must be larger than the yielding strength of the link multiplied by the over-strength factor (φ_s). Thus:

$$2P_b \cos\alpha \geq \varphi_s Q_{Li} \tag{3}$$

In Equation 3, α is the angle that the braces make with horizontal line. By solving P_b from the above equation, the required buckling strength of the brace can be obtained as:

$$P_b = \frac{\varphi_s Q_{Li}}{2 \cos\alpha} \tag{4}$$

The braces are selected in order to have a minimum buckling capacity (P_b).

Verification of Single Vertical Link

According to Ref. [21], the shear link was modelled as a linear element with six nonlinear rotational and translational springs at each end. So that, 3 rotational bilinear springs and 3 translational bilinear springs were used to represent the inelastic flexural behavior of plastic hinge and inelastic shear behaviour of the link web located at the end of the link that is represented by the multilinear functions shown in *Figure 4*. For numerical modeling of vertical link in this paper, the model of Ref. [22] is chosen; this model is same as the model of Ref. [20], but with different stiffness values for shear springs. The values of M_y and V_y are considered equal to M_P and $0.9V_P$, respectively. The relations between the moment-rotation and the shear-displacement of shear link with the stiffness values are shown in *Figure 4*. The values of K_{1M} and K_{1V} are respectively equal to $\frac{3EI}{e}$ and $\frac{GA_{web}}{e}$. In which, E is Young's modulus of steel, I is the moment of inertia of the link cross section, G is the modulus of rigidity of steel, and A_{web} is the area of the web of the link section.

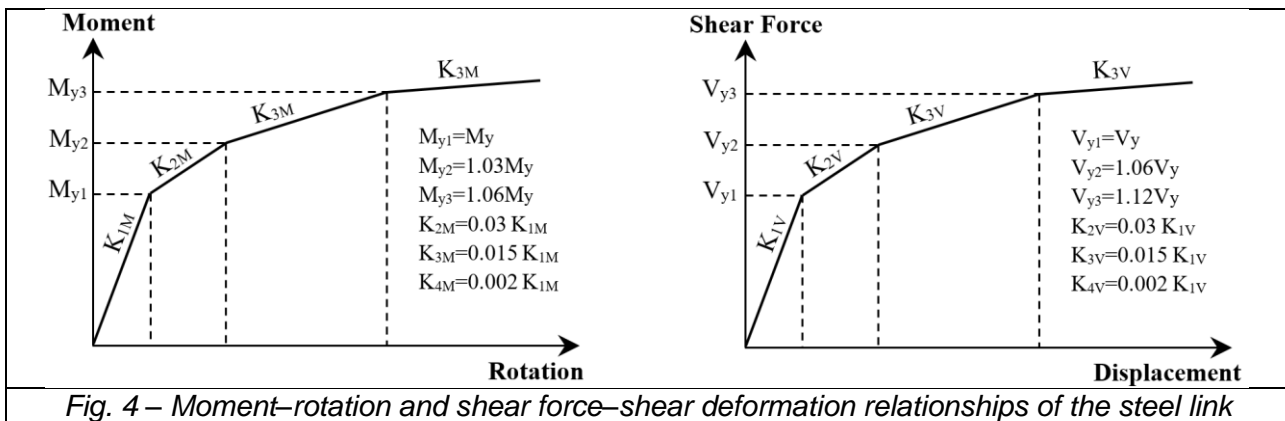


Fig. 4 – Moment–rotation and shear force–shear deformation relationships of the steel link

For comparing the results of numerical modelling of single vertical link with experimental results, the experimental model of Ref. [23] is chosen. The experimental model is a single story, single span frame with eccentrically braces with single vertical link. The design steel is ST37 with yield strength of 240 MPa, ultimate strength of 420 MPa and the modulus of elasticity of 200000 MPa as it is shown in *Figure 5*. The connections of beam to column, the braces to column and the columns to the floor is simple. The connection of single vertical link to beam and braces is welded on the basis of fix connection type. After the numerical analysis of considered frame under the loading according to the *Figure 6*, the hysteretic curve is formed as it is shown in *Figure 7*. By comparing this curve with hysteretic curve of experimental study, appropriate compatibility is observed that result in accuracy of modelling approach of single vertical link with behavioural model of Ref. [22].

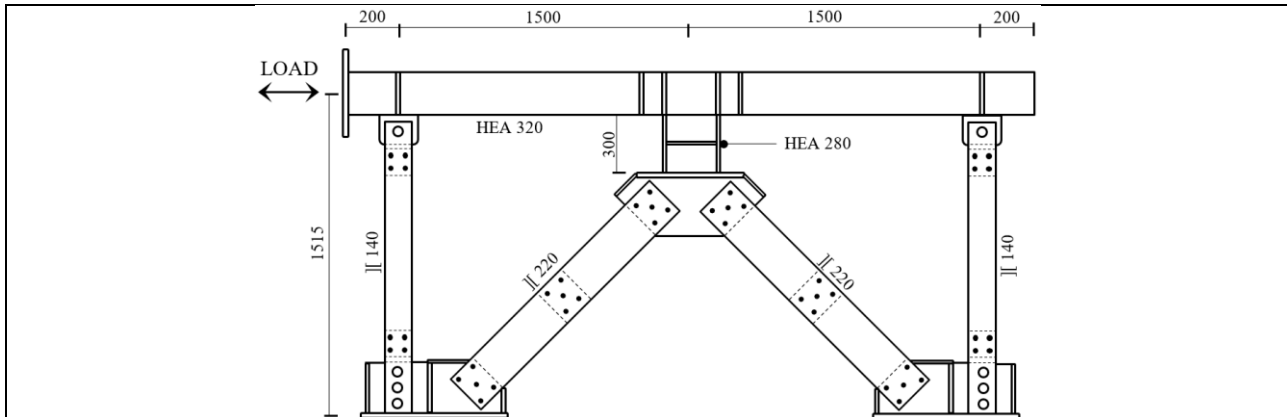


Fig. 5 - Details and configuration of eccentrically braced frame with single vertical link in the laboratory

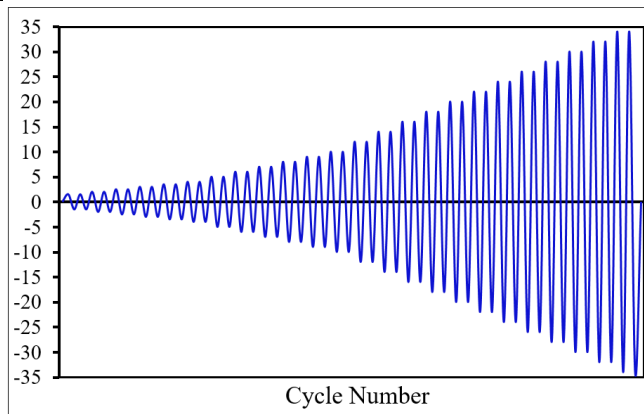


Fig. 6 - Loading protocol of eccentrically braced frame with single vertical link in the laboratory

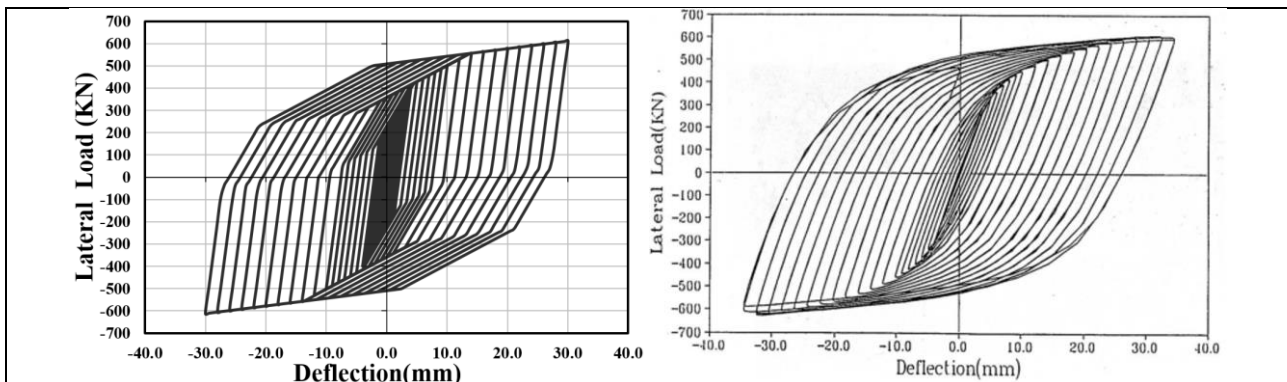


Fig. 7 - Hysteresis curves: (a) obtained from experimental work (b) obtained from modelling in OpenSees

Nonlinear Dynamic Analysis (Time History)

In this section, the seismic behaviour of the original frames and seismic rehabilitated frames (configuration of PSRM-3) under the ground motions is discussed. The main objectives of this study are the assessment of the maximum drifts, the changes of ductility and the energy dissipation. Behaviour of all beams and columns of frames are controlled by bending and shear forces, respectively. The allowable value of beam's plastic rotation to form nonlinear hinge at LS

and CP PLs are equal to 0.02 and 0.025, and these amounts for column are equal to 0.005 and 0.01, respectively, also the allowable amount of shear link's plastic rotation are 0.11 and 0.14 radian for LS and CP PLs. The gravity load combination for combining with the seismic load is equal to $Q_G = 1.1(Q_D + Q_L)$, where Q_D is the dead load and Q_L is equal to 25% of the non-reduced design live load.

In order to calculate the plastic rotation of nonlinear hinges of RC members, firstly, the amount of ultimate curvature of each fiber section of the elements must be determined by results of moment-curvature, which are obtained via NLSP analysis and then the Equation 5 is used:

$$\theta_p = (\phi_U - \phi_y) \times L_p \tag{5}$$

Where θ_p is the plastic rotation, ϕ_U is the ultimate curvature, ϕ_y is the yield curvature that is defined according to Ref. [24]:

$$\phi_y = \frac{M_y}{E_c I_{cr}} \tag{6}$$

for Beams : $M_y = 0.5f_c B kd \left(\frac{kd}{3} - d'\right) + f_y B d (d - d')\rho$ (7)

for Columns : $M_y = \frac{f_y B kd}{2n_{sc}} \left(\frac{D}{2} - \frac{kd}{3}\right) \frac{k^2}{1 - k}$ (8)

$$k = \sqrt{(\rho + \rho')^2 n_{sc}^2 + \left(\rho + \rho' \frac{d'}{d}\right) n_{sc}} - (\rho + \rho') n_{sc} \tag{9}$$

Where M_y is the yield moment, E_c is the modulus of elasticity of concrete, I_{cr} is the critical moment of inertia, that is equal to $0.5I_g$ where I_g is the moment of inertia of RC section without crack, ρ is the tensile steel ratio, ρ' is the compression steel ratio and also $n_{sc} = \frac{E_s}{E_c}$ is the proportion of the modulus of elasticity of steel to the modulus of elasticity of concrete. f_y is the yield strength of the tension steel and d is the effective depth, which is equal to the distance from the extreme compression fiber to the centroid of the tension steel, d' is equal to the distance from the extreme compression fiber to the centroid of the compression steel, B is section width. k is the neutral axis depth factor at the first yield and $n_{sc} = E_s/E_c$ where E_c and E_s are the moduli of elasticity of the concrete and the steel, respectively.

The assumption length of plastic hinge (L_p) is defined according to Ref. [25]:

$$L_p = 0.08L + 0.022 f_{ya} d_{bl} \tag{10}$$

Where, L is the considered element length in mm, f_{ya} is the yield strength of bars in MPa, d_{bl} is the diameter of bar in mm.

Tab. 3 - Details of selected earthquakes

EQ. NO	Year	Earthquake	Recording Station	PGA (g)	Vp (m/s)	EQ. Scale Factor			
						3St. BSE-1	3St. BSE-2	9St. BSE-1	9St. BSE-2
1	1987	Whittier Narrows	90079 Downey-Birchdale/180	0.299	0.378	1.34	1.89	1.48	2.18
2	1989	Loma Prieta WVC	CDMG 58235 Saratoga-W Valley Coll.	0.332	0.625	2.02	2.84	2.09	3.07
3	1990	Manjil, Iran	BHRC 99999 Abhar	0.496	0.4378	1.01	1.42	1.04	1.54
4	1987	New Zealand A-MAT	99999 Matahina Dam	0.293	0.2107	1.68	2.36	2.18	3.2
5	1981	Westmorland	5169Westmorland Fire Sta/90	0.496	0.344	1.57	2.21	1.83	2.69
6	1966	Park FieldTMB	CDMG 1438 Temblor pre-1969	0.357	0.215	2.24	3.15	2.61	3.84
7	1987	Tabas DAY	9102 Dayhook	0.406	0.265	1.68	2.36	2.00	2.94

The selected earthquakes have similar characteristics such as: magnitudes from 4.5 to 8 Richter scale, and the shear wave velocity according to the site soil type is classified as type D and this velocity is equal to 182.88 to 365.76 m/s and the selected range of the maximum acceleration

is between 0.2g-2g. The elastic acceleration response spectrum with the damping of 5% for each ground motion and the average of 7 ground motions are shown in Figure 8.

Design Spectrum (DS) for two earthquake hazard levels, BSE-1 and BSE-2 (Basic Safety Earthquake), is calculated according to ASCE 2010 [26]. At first, each of these ground motions are scaled for the two earthquake hazard levels (BSE-1 and BSE-2). Following ASCE 2010, the maximum difference in the range of 0.2T-1.5T between the average value of the seven ground motions with the 1.4 times of the DS should be equal to 10%. Details of 7 earthquakes and their scale factors for earthquake hazard levels are shown in Table 3. Also, the calculated DS for the two earthquake hazard levels including: BSE-1 and BSE-2 and the acceleration response spectra for the 7 ground motions for both frames of 3 and 9 story are shown in Figure 9.

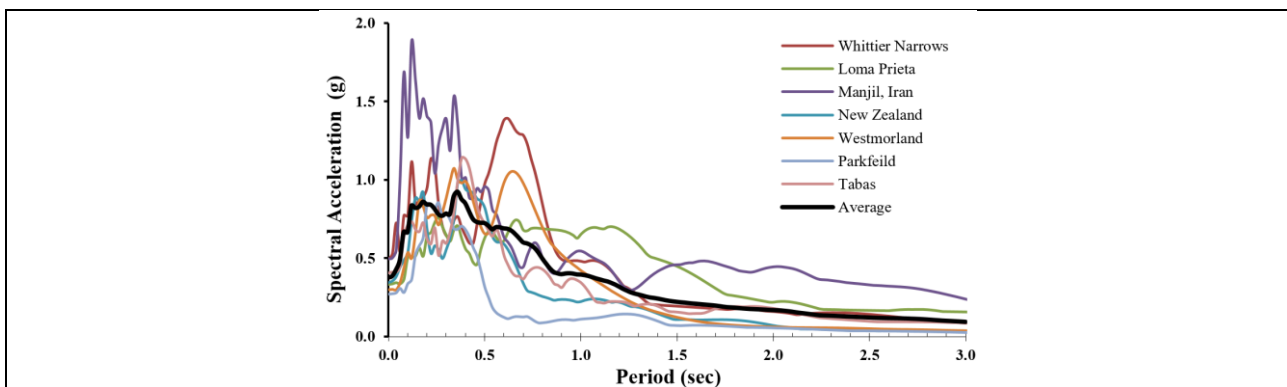


Fig. 8 - The acceleration spectrum for the selected earthquakes

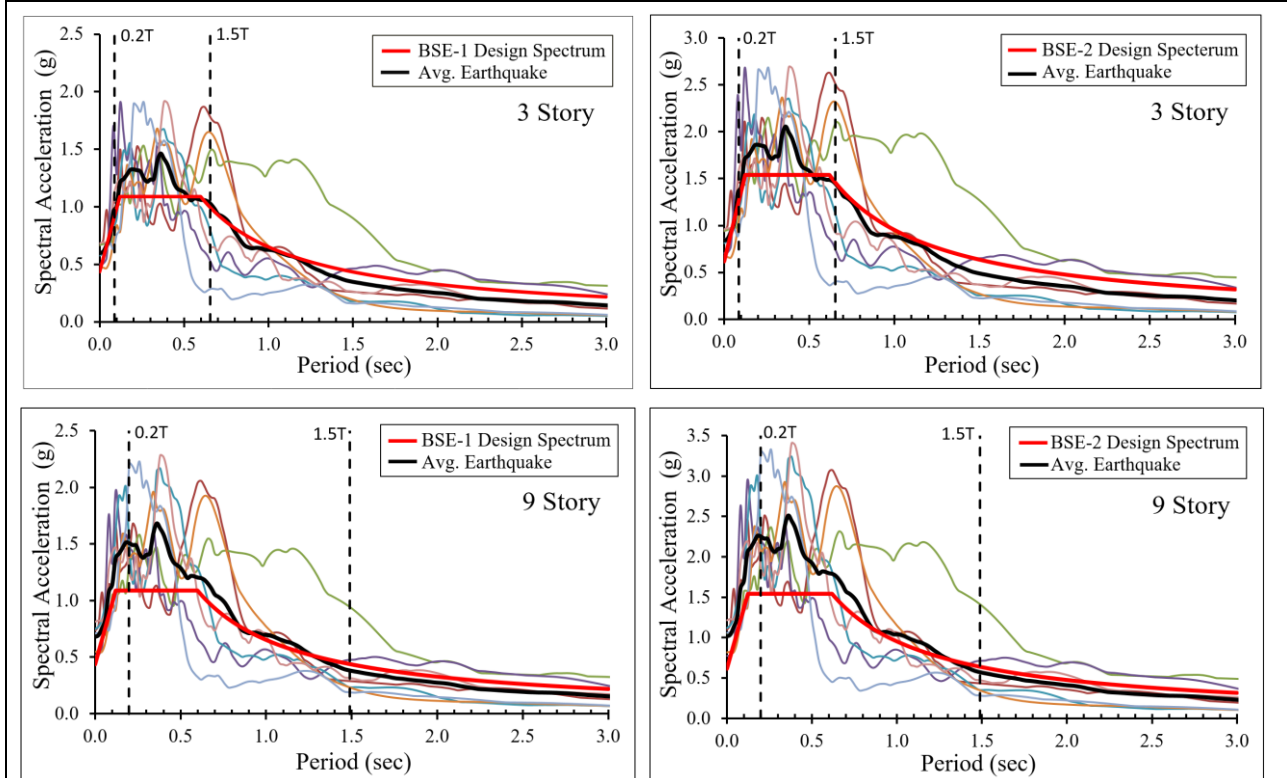
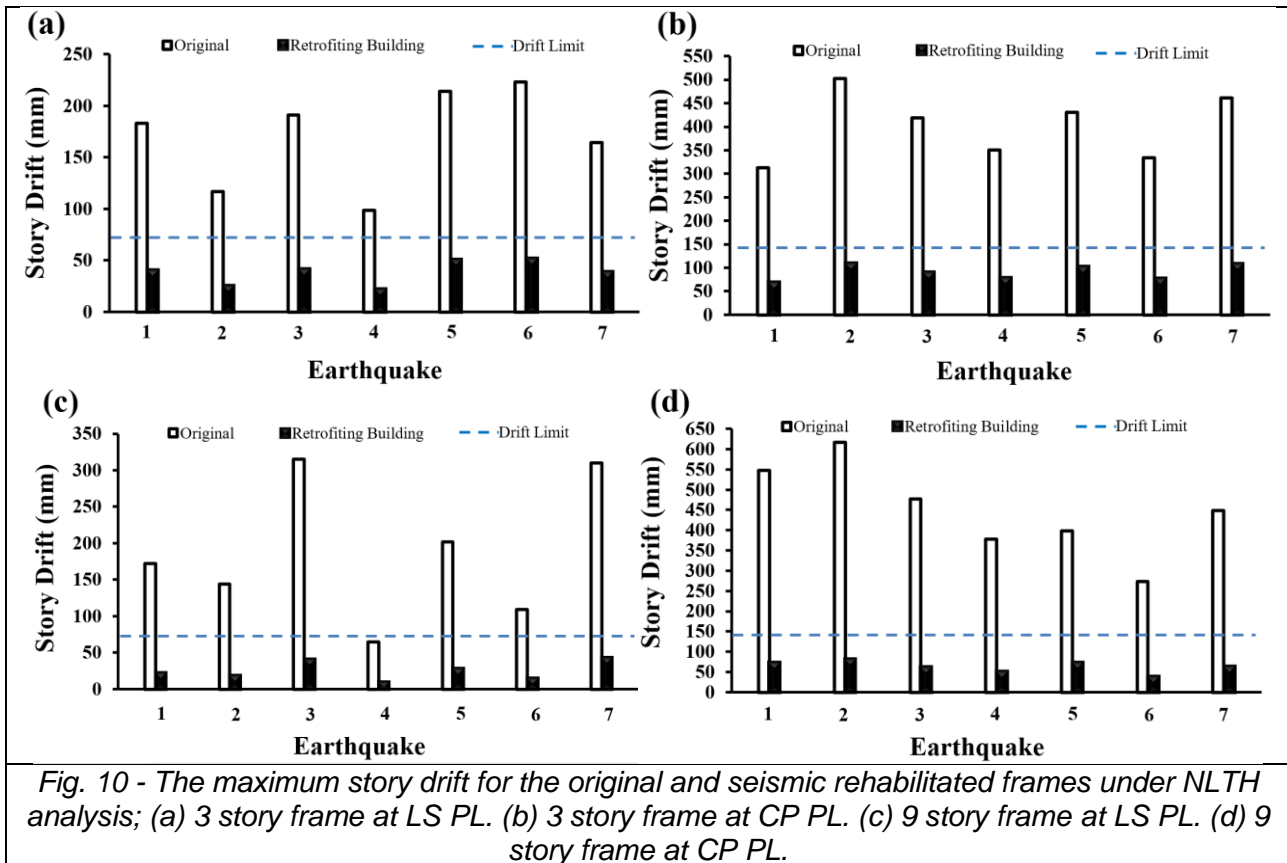


Fig. 9 - The site special acceleration spectrum and the selected earthquakes acceleration spectrum scaled to the site special acceleration spectrum

The maximum drifts of the original and seismic rehabilitated frames which are obtained from NLTH analysis for each performance levels, are shown in Figure 10. The frames rehabilitated with PSRM indicate more appropriate response than the original frames at the both performance levels. Moreover, regardless of the earthquakes characteristic (Such as frequency content) that is used in the analysis, the PSRM indicates more stable response. It means that the PSRM presents more uniform or similar response for all selected earthquakes.



In order to evaluate the performance of the seismic rehabilitated frames with PSRM in comparison with the original frames, the maximum inter-story displacement in the frame's height is shown in Figure 11. The deformations of frames are obtained at the time of the maximum stories drift. The reduction amount of the average maximum stories drift under seven selected earthquakes for the seismic rehabilitated frames of 3 and 9 story in comparison with the original frames, in case of the LS PL are equal to 77% and 86%, in case of the CP PL are equal to 72% and 81% respectively. This indicates the relatively uniform behaviour of the PSRM in decreasing the story drift in various performance levels. Consequently, damages which are created by probable earthquake are severely reduced. Moreover, the frames equipped with the PSRM have the uniform lateral deformation pattern. So, the amount of energy dissipation will have a better distribution at the height of frames.

In order to assess the ductility improvement of RC members in the frames with PSRM, the critical beam and column of the first story (the critical beam and column at both frames) are selected and analysed under nonlinear time history method by the earthquake number 5, to compare the formed plastic hinge rotation to the elastic one (θ/θ_y) in the original case with the

rehabilitation case. As it is shown in Figure 12, the reduction of the maximum ratio of (θ/θ_y) for 3 and 9 story rehabilitated frames in comparison with the original frames for beam are equal to 6.47, 9.25 and for column are equal to 5.17, 7.03 respectively, that indicates the significant improvement in ductility behaviour.

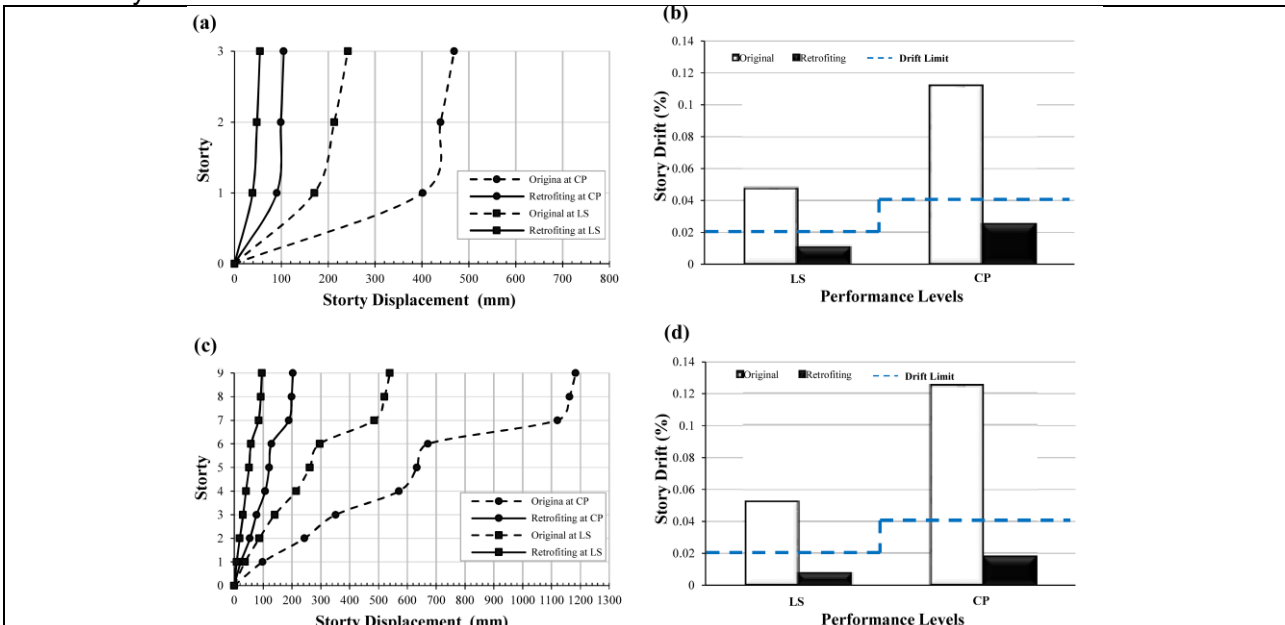


Fig. 11 - (a) The maximum inter-story drifts along the height of the 3 story frame, (b) the average inter-story drift for the 3 story frame, (c) The maximum inter-story drifts along the height of the 9 story frame, (d) the average of inter-story drift for the 9 story frame

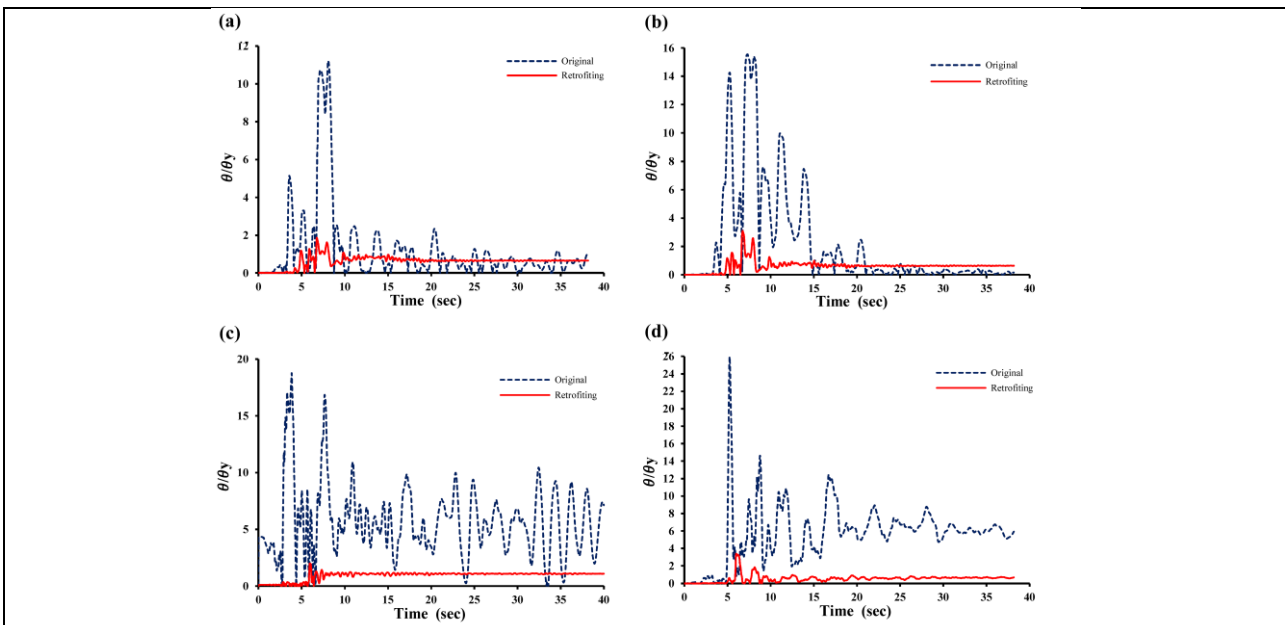


Fig. 12 - The ratio comparison of the ultimate rotation to the yield rotation for the critical elements of original and seismic rehabilitated frames under NLTH analysis for CP PL, (a) critical beam for 3 story frame, (b) critical column for 3 story frame, (c) critical beam for 9 story frame, (d) critical column for 9 story frame

RESULTS

In this paper, a new seismic rehabilitation method based on the performance is used for the seismic rehabilitation design of frames to ensure the satisfactory performance of the rehabilitated structures with the PSRM. The efficiency of this method was evaluated by performing the nonlinear time history analysis on two 3 and 9 story RC frames according to FEMA356. The results of NLTH have shown that the distribution of inter-story drift in the height of frames have more non-uniform behaviour by increasing the story level and it is because of the gravity loads that is governed in design of low rise frames in comparison with high rise frames. So the application of PSRM in low rise frames not only have no significant effect in the uniform distribution of inter-story drift but also decrease the inter-story drift. It is observed that in case of using the PSRM, a significant increase in ductility of RC components is achieved during the earthquakes. In the frames rehabilitated by PSRM, due to increasing in ductility, stiffness and lateral load strength capacity of frames, the damage indices have small values that unlike the original cases of frames which experience the significant structural damages.

REFERENCES

- [1] Badoux M, Jirsa JO., 1990. Steel bracing of RC frames for seismic retrofitting. *Journal of structural engineering*, 116(1): 55–74.
- [2] Bush TD, Jones EA, Jirsa O., 1991. Behaviour of RC frame strengthened using structural steel bracing. *Journal of structural engineering*, 117(4):1115–26.
- [3] Rodriguez M, Park R., 1991. Repair and strengthening of reinforced concrete buildings for seismic resistance. *Journal of earthquake spectrum*, 7(3): 439– 459.
- [4] Nateghi-Alahi F., 1995. Seismic strengthening of eight-story RC apartment building using steel braces. *Journal of engineering structure*, 6(17): 461-455.
- [5] Masri AC, Goel SC., 1996. Seismic design and testing of an RC slab–column frame strengthened by steel bracing. *Journal of earthquake spectra*, 12(4): 645–666.
- [6] Maheri MR, Sahebi A., 1997. Use of steel bracing in reinforced concrete frames. *Journal of engineering structure*, 19(12): 1018–24.
- [7] Maheri MR, Kousari R, Razazan M., 2003. Pushover tests on steel X-braced and knee-braced RC frames. *Journal of engineering structure*, 25(13): 1697–1705.
- [8] Ferraioli M, Avossa AM, Malangone P., 2006. Performance based assessment of RC buildings strengthened with steel braces. *Proceedings of the 2nd International Congress*, Naples, Italy.
- [9] Dicleli M, Mehta A., 2009. Seismic retrofitting of chevron-braced steel frames based on preventing buckling instability of braces. *Journal of Structural Stability and Dynamics*, 9(2):333-56.
- [10] Ghobarah A, Abou Elfath H., 2001. Rehabilitation of a reinforced concrete frame using eccentric steel bracing. *Journal of engineering structure*, 23:745–755.
- [11] Durucan C, Dicleli M., 2010. Analytical study on seismic retrofitting of reinforced concrete buildings using steel braces with shear link. *Journal of engineering structure*, 32: 2995-3010.
- [12] Sahoo DR, Rai DC., 2010. Seismic strengthening of non-ductile reinforced concrete frames using aluminum shear links as energy-dissipation devices. *Journal of engineering structure*, 32:3548-3557.
- [13] Mazzolani FM., 2008. Innovative metal systems for seismic upgrading of RC structures. *Journal of constructional steel research*, 65(7): 882-895.
- [14] Elfath A, Mohamed H., 1998. *Rehabilitation of non-ductile reinforced concrete buildings using steel systems*. PhD Thesis, University of McMaster, Hamilton.
- [15] Federal Emergency Management Agency (FEMA356). *Prestandard and commentary for the seismic rehabilitation of buildings*. Washington DC, 2000.
- [16] Mazzoni S, McKenna F, Scott MH, Fenves GL. Open system for earthquake engineering simulation (OpenSees). User command language manual, version 1.7.3. Richmond, CA (USA): Pacific Earthquake Engineering Research Center, University of California, Berkeley; 2006.
- [17] American Concrete Institute (ACI 318-63). *Building code requirement for reinforced concrete*. Farmington Hills, MI. 1963.

- [18] Kasai K, Popov EP., 1968. General behaviour of WF steel shear link beams. *Journal of structural engineering*, **112**(2): 362-82.
- [19] American Institute of Steel Construction (AISC 341-10). *Seismic Provisions for Structural Steel Buildings*. Chicago, IL. 2010.
- [20] European Committee for Standardization (EC8). *Design of structures for earthquake resistance*. Brussels, B. 2003.
- [21] Ramadan T, Ghobarah A., 1995. Analytical model for shear-link behaviour. *Journal of structural engineering*, **121**(11):1574-1580.
- [22] Richards PW., 2004. *Cyclic stability and capacity design of steel eccentrically braced frames*. PhD Thesis, Univ. of California, San Diego.
- [23] Vetr MG., 1997. *Seismic behaviour, analysis and design of eccentrically braced frames with vertical shear links*. PhD Thesis, University of Technology Darmstadt, W. Germany.
- [24] Zou XK, Chan CM., 2005. Optimal seismic performance-based design of reinforced concrete buildings using nonlinear pushover analysis. *Journal of structural engineering*, **27**:1289–1302.
- [25] Priestley MJN, Seible F, Calvi GM., 1996. *Seismic design and retrofit of bridges*. John Wiley & Sons, ISBN: 978-0-471-57998-4, New York.
- [26] American Society of Civil Engineers (ASCE/SEI 7). *Minimum Design Loads for Buildings and Other Structures*. Reston, VA. 2010.

NUMERICAL STUDY OF THE WIND TURBINE WAKE FLOW AND EFFECTS OF THE INFLOW TURBULENCE

Xiaoyu Luo¹, Shengyu Lu²

1. *Electric Power Research Institute of Guangdong Power Grid Co., Ltd., Guangzhou, Guangdong, China; liuzhenqing@hust.edu.cn*
2. *Huazhong University of Science and Technology, Hubei Wuhan, 430074, China*

ABSTRACT

Considering the fact that wind turbines operate at the bottom of the atmospheric boundary layer (ABL) where the turbulence is at a high level, and the difficulty of mesh generation in the fully modelled numerical simulation. It is necessary to carry out researches to study the wake flow of wind turbines with consideration of the inflow turbulence. Therefore, a numerical method generating turbulence was proposed and the results show good agreement with those in experiment, based on which the flow fields in the wake of a wind turbine at two tip speed ratios were examined in detail through three actuator methods, namely, ADM, ADM-R and ALM. The performances of these methods were studied and the error sources for each method are clarified. Moreover, the computational efficiency was revealed and the influencing factor for the efficiency is concluded. Besides, the equilibrium relation of the N-S equation in the wake is revealed, which provides a theoretical basis for the optimal arrangement of the wind turbine. It shows that the mean velocity and fluctuating velocity vary greatly near the wind turbine, and become stable gradually away from the wind turbine. The results of ALM method show the best agreement with the experiment. At near wake region, the turbulent stress term, pressure gradient term and convection term mainly contribute to the equation equilibrium, and convection term is in equilibrium with the turbulent stress term at far wake. The results of ALM method are the most accurate and the most time consuming.

KEYWORDS

Actuator disk, Actuating line, Wind turbines wake, CFD, Numerical simulation

INTRODUCTION

With the increasing demand for clean, safe and cheap energy, wind power has been expanding globally in recent years and it has become a dominant renewable energy source, with over 280 GW installed worldwide by the end of 2012. In general, wind turbines are installed in wind farms along several rows and columns. Because wind turbines generate wakes that propagate downwind, the wakes from turbines in upwind rows can negatively impact the performance of downwind rows. Understanding wake losses is therefore an increasingly important topic as wind farms grow in size and in number of turbine rows. The energy loss caused by wake has a great effect on the economic benefit of a wind farm. Therefore, the study of wind turbine wakes plays an important role in improving the efficiency of wind turbine power generation.

The wind tunnel test and CFD numerical simulation are the main research methods of wind turbine wakes. It is controllable and predictable for the experimental environment, which is the unique advantage of a wind tunnel test. The disadvantage of wind tunnel test is that there is a certain difference between the experimental flow field conditions and the actual flow field. In

addition, it is difficult to collect experimental data. Because of the limited number of sensors, the data can only be collected in the part of the flow field of the wind turbine, and the whole flow field information cannot be obtained better. Due to the limitation of the wind tunnel laboratory site, the wind turbine wind tunnel test is based on the actual wind turbine scale model machine, so the obtained data cannot represent the actual wind field information. When scaling model wind turbine test is carried out, the similarity between the actual wind turbine and the model should be considered, the influence of the wind tunnel size on the experiment should be considered as well. Of course, the most valuable wind tunnel test should be the measurement of the full scale prototype wind turbine at all times, which requires that wind tunnel test site is large enough. At the same time, the test technology is difficult and costly. So at the moment, there is only one full scale wind turbine test record. In 2001, the experimental research of wind turbine was carried out by the Renewable Energy Laboratory of the United States [1-2]. However, this experiment focused on the aerodynamic performance of the blade of the wind turbine, such as the pressure distribution on the blade element, and there was no experimental observation of the tail flow field of the wind turbine. In 1979, by using a hot wire anemometer to study the wind speed distribution in the wind turbine tail, Alfredsson calculated the ratio of wind turbine output [3], and the influence of wake on wind turbine output was revealed. Around 1997, Ebert et al. also used this technique to carry out a large number of wind turbine tail flow characteristics research experiments [4], which include tip vortex and velocity flow field. However, the experimental results show that the anemometer is unable to obtain the global instantaneous flow field information. J. Wha et al. used Particle Image Velocimetry (PIV) technology to measure the wake flow of the three-blade wind turbine model in the water tank [5], and compared the results with the data obtained from the real wind turbine. A new method for the study of wind turbine wake was provided, but the experimental data and the actual data were quite different, and the research was mainly focused on the near wake flow field.

With the development of computer technology, computational fluid dynamics (CFD) is also widely used in numerical simulation of wind turbine wake [6-15]. Based on the RNG turbulence model, Yan Haijin had carried out a simple full model numerical simulation of a single wind turbine [6]. In his study, the results of wind velocity distribution, pressure distribution and flow separation in the whole flow field were obtained. However, the effects of blade rotation, surface and wind speed gradient on the convection field were not taken into account. And it was also difficult to divide the mesh of blade body fitting when the full model numerical simulation was carried out. Combining CFD numerical simulation method with a wind turbine wake model, Li Shaohua studied the wind turbine power and the wake distribution of two wind turbines under the condition of serialiation [7], juxtaposition and misalignment. He qualitatively analysed that under the condition of serial arrangement, the wake from turbines in upwind rows can negatively impact the performance of downwind rows. However, the full model body-fitted grid was also used, the number of grids was large. Yang Rui used actuating disk instead of wind wheel to carry out the numerical simulation of wind turbine tail flow [8]. This method can simplify the mesh, and does not need to mesh the complicated fan blades. The aerodynamic drag of the wind turbines can be simulated by applying the pressure step on the actuating plate, and the power loss between the upwind direction and downwind direction wind turbine can be well simulated. However, the method only considered the axial induced force and the tangential induced force was ignored, so the information of near wake field could not be captured. Ren Huilai used ADM-R to simulate the wind turbine tail flow [9], and qualitatively analysed the characteristics of the wake flow field and its development process. But Ren did not compare the calculated results with the experimental data and was unable to analyse the accuracy of the method. Li Pengfei used the ALM method to carry out the numerical simulation of the wind turbines wake [10], and analysed the wake field information under different tip velocity ratio conditions. But the actual situation of turbulence flow was not taken into account. There were many other scholars who did similar research, such as Han Xingxing, ZHAO Feng, Zhu Chong, Tian Linlin, Hou Yali and so on [11~15].

Although a modern wind turbine can be very large in size, e.g. >100 m in both diameter and hub height, it still operates in the lower part of the atmospheric boundary layer (ABL), where the wind is highly turbulent. In this paper, three actuating methods are developed to study wind turbine wakes. Besides, the author will analyse the flow field information under the conditions of turbulent flow, tip wind speed ratio = 5.52, 9.69, and compare the numerical simulation results with the experimental results [16] to study the respective calculation characteristics. It provides the theoretical basis for the optimal arrangement of the wind turbine.

GOVERNING EQUATIONS

Based on large eddy simulation (LES), the horizontal axis wind turbine tail flow is simulated by three kinds of actuation methods in this paper. Subgrid-scale model is adopted to simulate the effects of small-scale turbulence on large-scale turbulence. The N-S equation is averaged in a small space domain so that small-scale vortex flows are removed from the flow field and the equations satisfied by the large eddy are derived. The filtered incompressible Navier–Stokes equations are as follows:

$$\frac{\partial \rho}{\partial t} + \frac{\partial}{\partial x_i} (\rho \bar{u}_i) = 0 \quad (1)$$

$$\frac{\partial \bar{u}_i}{\partial t} + \frac{\partial (\bar{u}_i \bar{u}_j)}{\partial x_j} = -\frac{1}{\rho} \frac{\partial \bar{p}}{\partial x_i} + \nu \frac{\partial}{\partial x_j} \left(\frac{\partial \bar{u}_i}{\partial x_j} \right) + \frac{\partial \bar{\tau}_{ij}}{\partial x_j} + f_i \quad (2)$$

In the upper formula:

$$\bar{\tau}_{ij} = -\overline{u'_i u'_j} = \overline{u_i u_j} - \overline{u_i u_j} \quad (3)$$

The standard Smagorinsky–Lilly model is used to calculate the subgrid-scale (SGS) stresses. Based on the isotropic turbulence, it is considered that the subgrid-scale turbulence has a mixed length vortex viscosity coefficient. The specific expression is as follows:

$$\tau_{ij} - \frac{1}{3} \tau_{kk} \delta_{ij} = \mu_t \left(\frac{\partial \bar{u}_i}{\partial x_j} + \frac{\partial \bar{u}_j}{\partial x_i} \right) = 2\mu_t \bar{S}_{ij} \quad (4)$$

where \bar{S}_{ij} is a part of the subgrid scale isotropy, μ_t denotes the SGS turbulent viscosity force defined as follows:

$$\mu_t = C_s^2 \rho \Delta^2 \left(2\bar{S}_{ij} \bar{S}_{ij} \right)^{\frac{1}{2}} = C_s^2 \rho \Delta^2 |\bar{S}| \quad (5)$$

where C_s is the Smagorinsky constant and chosen as 0.032 to reduce the diffusion of subgrid stress.

Actuating disk model (ADM)

The method only calculates the axial induced force and assumes that the axial induced force is uniformly distributed in the plane of wind wheel. According to thrust coefficient expression.

Then if the thrust coefficient C_T is known, the axial induced force T can be obtained. The dynamic source term of volume force can be solved as:

$$f_x = \frac{C_T \cdot \rho U_\infty^2 A_D}{2A_D \Delta x} = \frac{C_T \cdot \rho U_\infty^2}{2\Delta x} \quad (6)$$

Actuator disk model with rotation (ADM-R)

Based on the theory of blade element momentum (BEM), this method divides the blade into several blade elements along the radial direction, as shown in Figure 1, then, the lift and drag on each blade element can be calculated as:

$$dL = \frac{1}{2} C_l(\alpha) \rho V_{rel}^2 c dr \quad (7)$$

$$dD = \frac{1}{2} C_d(\alpha) \rho V_{rel}^2 c dr \quad (8)$$

where C_l and C_d are lift coefficient and drag coefficient, respectively. They can be interpolated from the local wind attack angle according to the characteristic curve of air foil coefficient changing with the wind attack angle. The V_{rel} is the air velocity relative to the blade and can be solved by the local velocity vector triangle shown in Figure 1(b), and calculated as follows:

$$V_{rel} = \sqrt{U_\infty^2 (1-a)^2 + r^2 \Omega^2 (1+a')^2} \quad (9)$$

where a is the axial induced factor, and a' is the tangential induction factor. Then, the thrust and moment acting on the blade element can be calculated as:

$$dT = dL \cos \varphi + dD \sin \varphi = \frac{1}{2} \rho V^2 B c (C_l \cos \varphi + C_d \sin \varphi) dr \quad (10)$$

$$dQ = (dL \sin \varphi - dD \cos \varphi) r = \frac{1}{2} \rho V^2 B c (C_l \sin \varphi - C_d \cos \varphi) r dr \quad (11)$$

According to the momentum theorem and angular momentum theorem, the reaction force and moment of the airflow acting on the blade element can be obtained as follows:

$$dT = 2\pi r dr \cdot \rho U_\infty (1-a) 2a U_\infty \quad (12)$$

$$dQ = 2\pi r dr \cdot \rho U_\infty (1-a) 2a' r^2 \Omega \quad (13)$$

After simultaneous solving of formula (10), (11), (12), (13), the a and a' can be obtained iteratively. Since the BEM theory assumes that the wingspan direction is infinitely large and the momentum theory is only applicable to the case where the axial induction factor is relatively small, the Prandtl loss factor and the Grawert loss factor [17] are introduced to modify the induction factor in this paper.

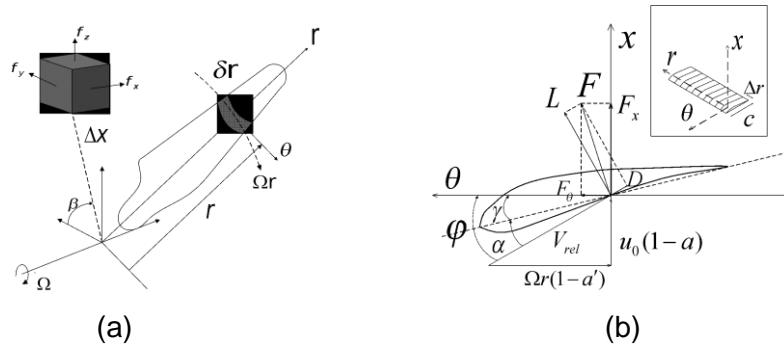


Fig. 1 - BEM theoretical analysis diagram: (a) Blade appearance (b) Blade element force diagram
 Decomposing lift and drag into axial forces dF_x and tangential forces dF_θ , as shown in Figure 1. Then the axial and tangential inductive forces on the three blades are averaged along the radial micro ring, and the dynamic source term of the volume force is calculated as:

$$f_x = -\frac{B}{2\pi r} \frac{dF_x}{\Delta x \delta r} \quad (14)$$

$$f_\theta = -\frac{B}{2\pi r} \frac{dF_\theta}{\Delta x \delta r} \quad (15)$$

Actuator line model (ALM)

The ADM-R method assumes that induced force is uniformly distributed in the radial micro ring of the wind turbine. ALM method gives up such assumption. For a given tip velocity ratio, ALM method can be used to calculate the rotating angular velocity of the wind wheel. Thus, ALM method can determine the grid swept by each blade at any time, and then the volume force term is applied to the corresponding grid. The solution of induced force is the same as ADM-R method, which is based on BEM theory. Dynamic source term of the volume force is calculated as:

$$f_x = dF_x \mathcal{N}, \quad f_\theta = dF_\theta \mathcal{N} \quad (16)$$

where V represents the volume of the blade sweeping through the grid.

NUMERICAL MODEL

Object of study and boundary conditions

The 1 / 100 scaled model wind turbine of MWt-1000[10] is used in this study. The radius of the model is 0.285m and the hub height is 0.7m. The size of model is shown in Figure 2(a). The longitudinal length of the computational domain is 13.5m, the height is 1.8m and the transverse length is 1.5m. The wind turbine is located 8.5m downstream from the inlet. The downstream area of the wind turbine extends to 5m in the longitudinal direction. At a distance of 6m away from the wind turbine, three wedges are arranged to simulate the atmospheric boundary layer conditions with turbulence, as shown in Figure 2(b). At the inlet, a uniform wind speed, 10m/s, is provided, i.e. $u=10\text{m/s}$, $\partial p / \partial n=0$. The pressure-outlet condition is specified at the outlet, i.e. $p=0$, $\partial u / \partial n=\partial v / \partial n=\partial w / \partial n=0$. The symmetry conditions are used at the top and side of the computational domain, i.e. $\partial u / \partial n=\partial v / \partial n=\partial w / \partial n=\partial p / \partial n=0$. And at other boundaries, the wall boundary conditions are used, i.e. $u=v=w=0$, $\partial p / \partial n=0$.

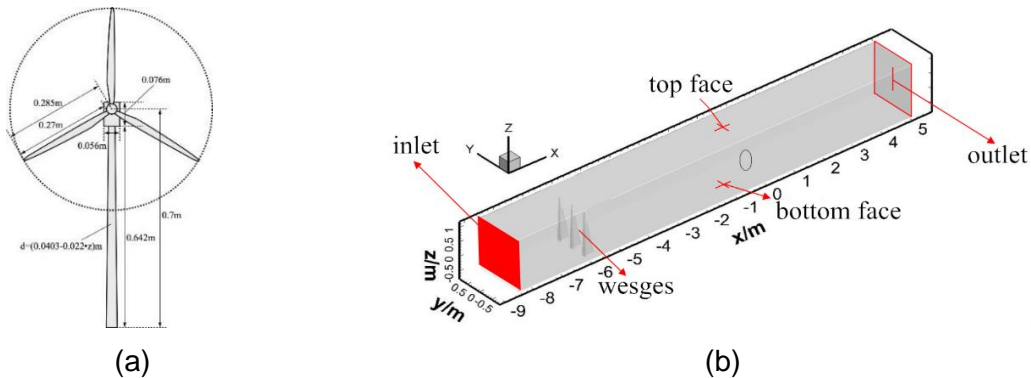


Fig. 2 - Numerical model: (a) The wind turbine model (b) Schematic of the computational domain

Grid system and conditions

In this study, total mesh number of the global calculation domain is 2.5×10^6 , the minimum grid size is 3mm and the maximum grid size is 25mm, the grid system is shown in Figure 3. Considering the large change gradient of velocity, smaller mesh is needed near the bottom of the calculation domain, the wind turbine and the wedges, in order to capture the characteristics of the flow field, so local refinement is done. The vertical size of grids in the bottom of the calculation domain is 5mm, and the vertical grid growing ratio is 1.2. In longitudinal direction, the size of the grids near the wind turbine is 5mm, and the grid growing ratio is 1.1. On the wedges surface, the minimum grid size is 3mm and the maximum grid size is 15mm.

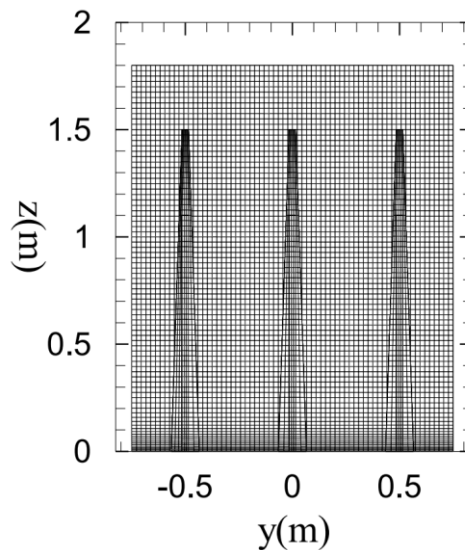


Fig. 3 - Lateral view of the mesh system of the numerical model

In this study, two conditions are carried out. The first one is that the blade tip velocity ratio λ is valued 5.52 when the wind turbines work with rated power, and the other is $\lambda=9.69$ when the maximum generating efficiency of the wind turbine is reached. The wind velocity of inlet is 10m/s, as shown in Table 1.

Tab. 1 - Calculation cases

Case name	λ	wind velocity (m/s)
Case1	5.52	10
Case2	9.69	10

NUMERICAL RESULTS

Accuracy verification of grid system

To ensure that the turbulent wind farm was in accordance with the experimental conditions, numerical simulation was firstly done with the absence of the wind turbine to verify the accuracy of the grid system. The distribution of velocity simulated by LES was used to show the characteristics of the flow field. The computation time step was set to 0.0001s, the maximum number of iterations was 20 times in each time step, and the statistical time was about 7s. At the centre of the wind turbine, the mean velocity of numerical result was 10.55m/s, which matches well with it (10.58m/s) in the experiment. The axial mean velocity and fluctuating velocity were extracted from the section of $y=0$, and dimensionless processing was done by dividing the mean velocity at centre of the wind turbine. The mean velocity contour and the non-dimensional mean velocity profile as well as the fluctuating velocity contour and the non-dimensional fluctuating velocity profile are shown in the Figure 4. The location of mean velocity profile and the fluctuating velocity profile are $x = 0, 2D, 4D, 6D$.

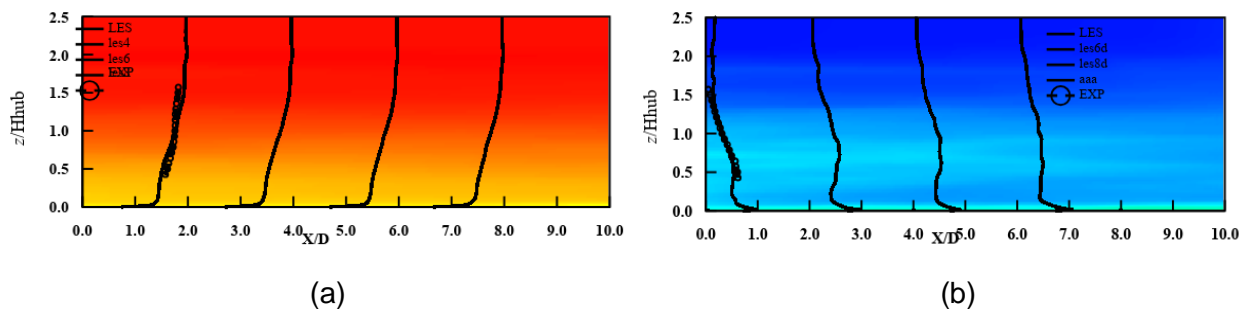


Fig. 4 - The wind field distribution: (a) Axial mean velocity contour (b) Fluctuating velocity contour

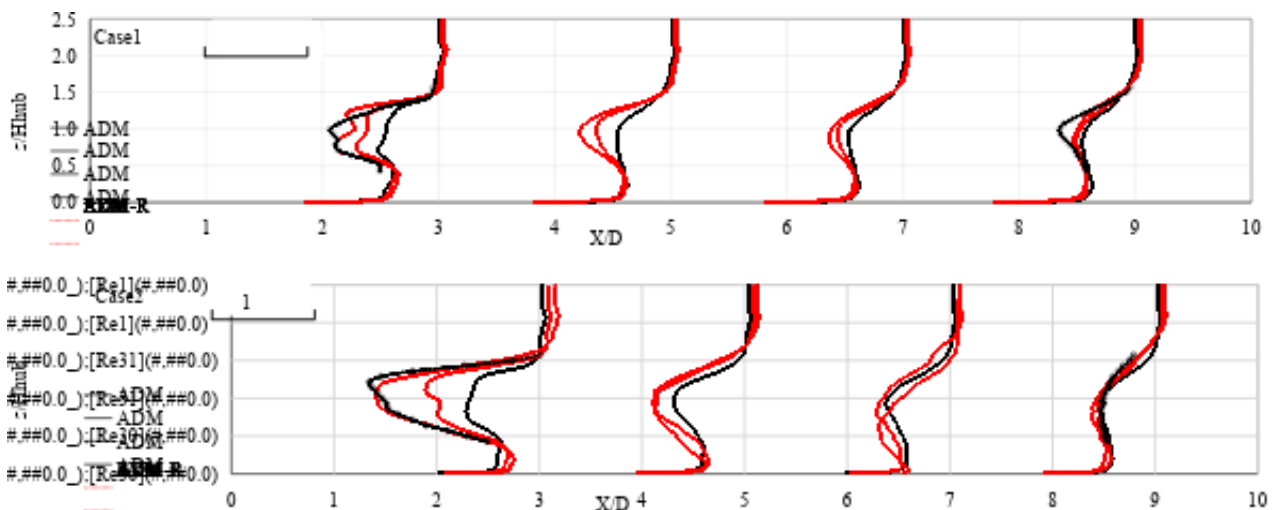


Fig. 5 - The axial wind profile

Flow field analysis of three actuation methods

The results of three actuation methods are compared in this part. The axial mean wind velocity and fluctuating wind velocity are extracted at profile($y=0$). The non-dimensional mean wind velocity profile is shown in Figure 5, and the non-dimensional fluctuating velocity is in Figure 6. The sections of profile are at $x=2D, 4D, 6D, 8D$, respectively. According to Figure 5, the wind speed decreases rapidly after the wind passes through the plane of the wind turbine. And the farther away from the wind turbine, the weaker the disturbance effect of the wind turbine to the wind field will be. At the centre of the wind turbine, the wind speed is the smallest and gradually increases

upward and downward, which is consistent with the experimental trend. The numerical result of ADM and experimental values vary greatly in near wake area. In the meanwhile, ADM-R results match better with experimental data than ADM, and ALM matches the best. In the far wake region, the results of three methods are similar and are in good agreement with the experimental data. That is because that ADM assumes uniform distribution of axial induced force on wind turbine plane and ignore tangential induction force, which means the rotation effect is neglected. Therefore, the near wake flow field error is large, and it cannot capture near wake flow information. Although tangential induction is considered in ADM-R method, it assumes that induction force is uniformly distributed in the radial micro ring of the wind turbine, which is not consistent with the actual situation. So the results of ADM-R have large error near the wake. Different from the former two assumptions, ALM method directly exerts axial and tangential inductive forces on the grid swept by the blade of the wind turbine, so the calculated results are closer to the experimental values.

Figure 6 shows that after the wind passed through the plane of the wind turbine, the fluctuating velocity increases. At the place farther away from the fan, the disturbance effect of fans on wind field is weakened and the fluctuating velocity decreases. The maximum of the fluctuating velocity occurs at blade tip, and the fluctuating velocity gradually decreases upward and downward, which shows good agreement with experiment. The larger the blade tip velocity ratio is, the more obvious the disturbance effect of wind turbine on flow field can be, and the higher fluctuating velocity will be. In general, ADM method has the biggest error compared with experiment and the error of ADM-R method is between the other two methods, ALM shows the best agreement with experiment.

Under the two conditions, the axial mean velocity contours calculated by three methods in several sections ($x=D, 2D, 4D, 6D$) are plotted in Figure 7. As shown in Figure 7, the influence region of the wind turbine in the original flow field is similar to the cylindrical flow tube with the same diameter as the wind turbine. After flow passing through the wind turbine, the velocity of the airflow decreases rapidly and then recovers gradually. The wind speed is basically stable at $x = 6D$. Because of the different assumptions of the three methods, the axial mean velocity calculated by ADM method shows circular uniform distribution, which is in sake of that ADM does not take the effect of the wind wheel rotation into account. Unlike the results of ADM, the axial velocity obtained by ADM-R and ALM is basically circular distribution. Due to the influence of wind shear, the axial velocity is not completely symmetrical distribution. The axial velocity calculated by ADM is smallest among the three methods. And it has great difference with that of the other two methods. However, the calculated values of the three methods show little difference in the region of the far wake (about $x > 6D$).

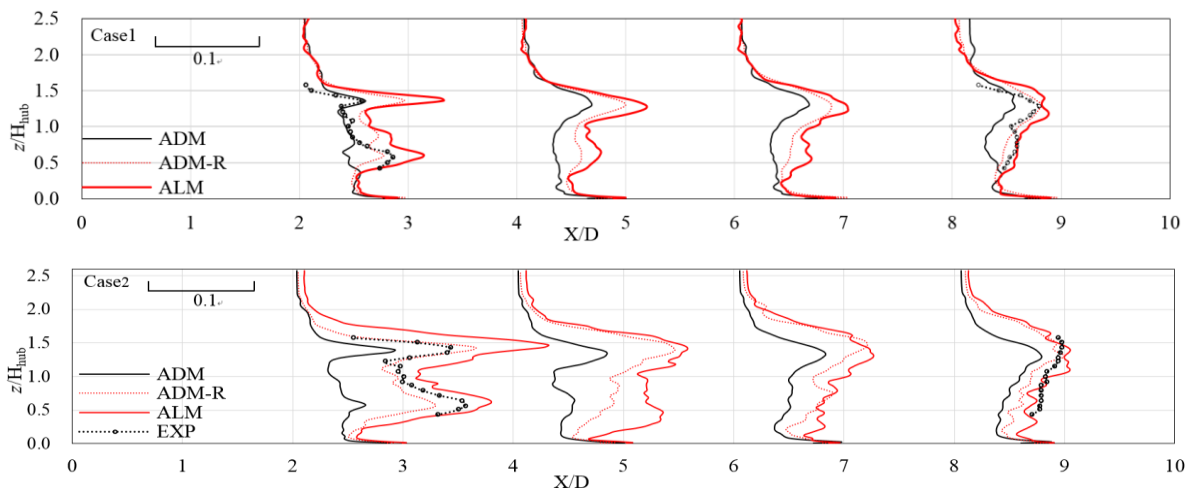


Fig. 6 - The fluctuating velocity profile

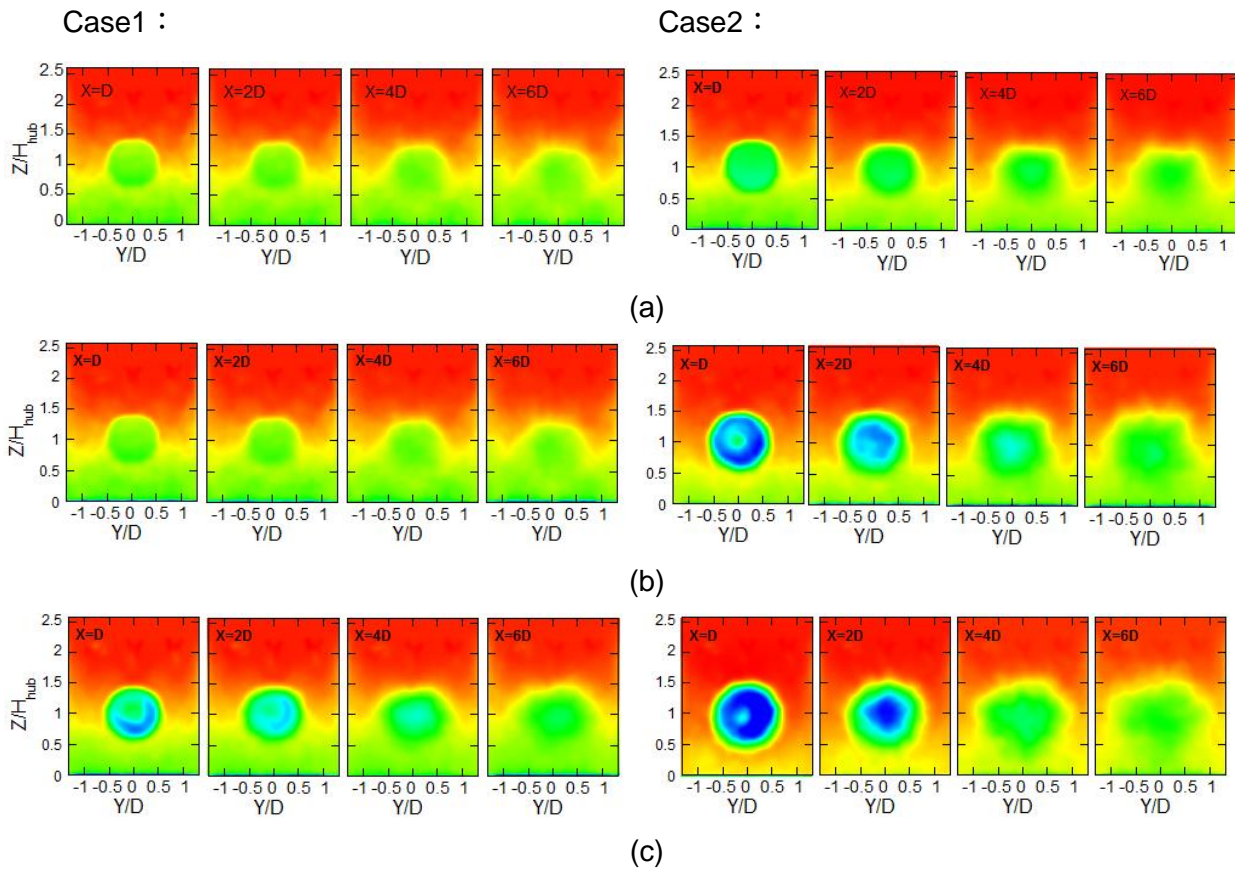


Fig. 7 - The contour of mean velocity in several sections:(a)ADM (b)ADM-R (c)ALM

N-S equation equilibrium analysis of ALM

By time averaged data process of N-S equation, the time-averaged momentum equation in the downwind direction is shown in formula (17):

$$\bar{u}_i \frac{\partial \bar{u}}{\partial x_i} = -\frac{1}{\rho} \frac{\partial \bar{p}}{\partial x} - \frac{\partial u'u'_i}{\partial x_i} + D_u \quad (17)$$

where $\bar{u}_i \frac{\partial \bar{u}}{\partial x_i} = \bar{u} \frac{\partial \bar{u}}{\partial x} + \bar{v} \frac{\partial \bar{u}}{\partial y} + \bar{w} \frac{\partial \bar{u}}{\partial z}$ is the convection term, $\frac{\partial u'u'_i}{\partial x_i} = \frac{\partial u'u'}{\partial x} + \frac{\partial u'v'}{\partial y} + \frac{\partial u'w'}{\partial z}$ is the turbulent stress term, D_u is the diffusion term.

At the center of wind turbine, the distribution along the downwind direction of each terms of N-S equation are plotted in Figure 8 and the distribution curves of each sub item are shown in Figure 9. According to the curves in Figure 8, the turbulent stress term, pressure gradient term and convection term mainly contribute to the equation equilibrium at near wake, and the diffusion term is very small. As the distance away from the wind turbine increases, the pressure gradient term decreases gradually, and the pressure become stable at about $3D$. In the far wake region, the convection term is in equilibrium with the turbulent stress term. It shows that the larger the wind speed ratio of blade tip is, the larger each item of turbulence stress is in the region of near wake flow field ($x < 6D$). But the values of each term are almost identical in the far wake region. In Figure

10, the main action of the convection term is in the x direction, and the other two are basically zero. In the range of $x < 2D$ for turbulent stress term, the turbulence stress in all three directions is relatively large, and the turbulent stress in the x direction is basically zero in the range of $x > 2D$.

In profile of $z=0$, N-S equation equilibrium relation in several sections are plotted in Figure 11, i.e. $x=2D,4D,6D,8D$. In Figure 10(a), with the wind turbine not placed, in the area $x>0$, the pressure gradient term is basically zero, the convection term and the turbulent stress term remain basically unchanged, and both are very small. The convection term and the turbulent stress term mainly contribute to the equation equilibrium. However, when the wind turbine is placed, the values of the three terms increase sharply. At low blade tip velocity ratio ($\lambda=5.52$), the pressure gradient term is very small, and the equilibrium is mainly provided by the turbulent stress term and convection term. For the high blade tip velocity ratio ($\lambda=9.69$), the pressure gradient only works in the near wake, and is very small in the far wake. With the blade tip wind speed ratio increases, the value of three terms increase in the near wake region ($x < 4D$), but in the region of the far wake, i.e. $x > 4D$, the difference of each terms is not significant.

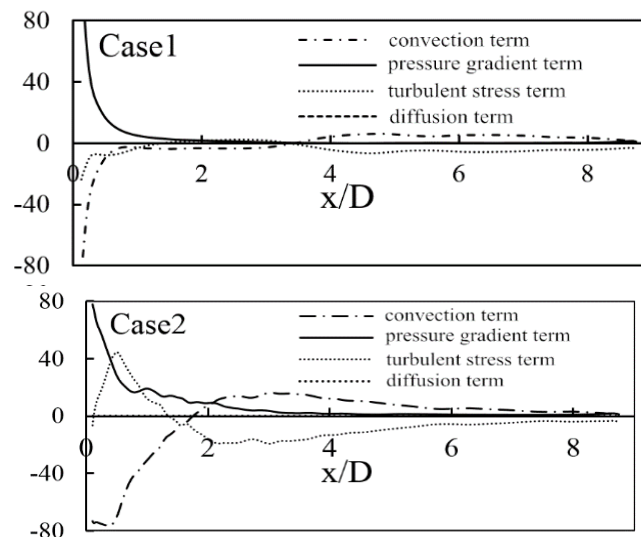


Fig. 8: N-S equation equilibrium curves

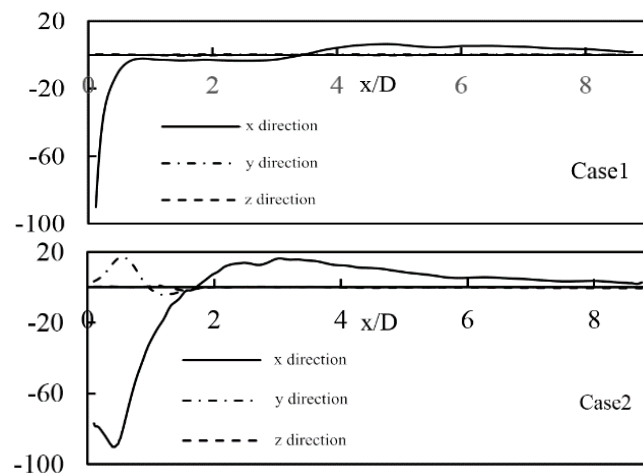


Fig. 9 - Distribution curves of each term: (a) Distribution curve of convection terms

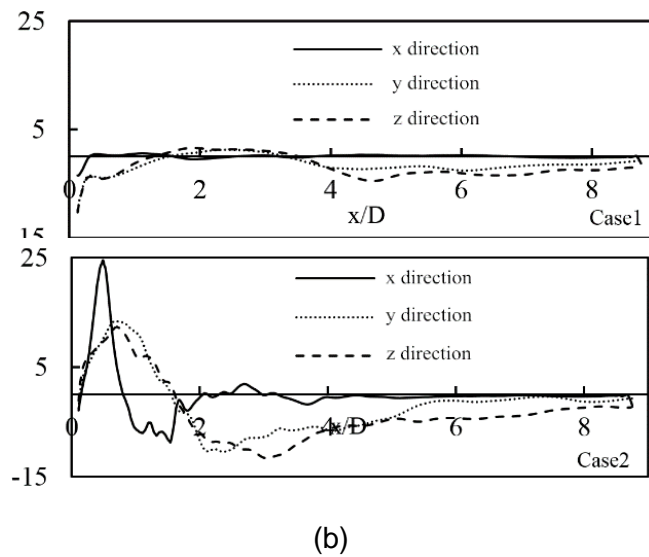


Fig. 9 - Distribution curves of each term: (b) Turbulence curve of convection terms

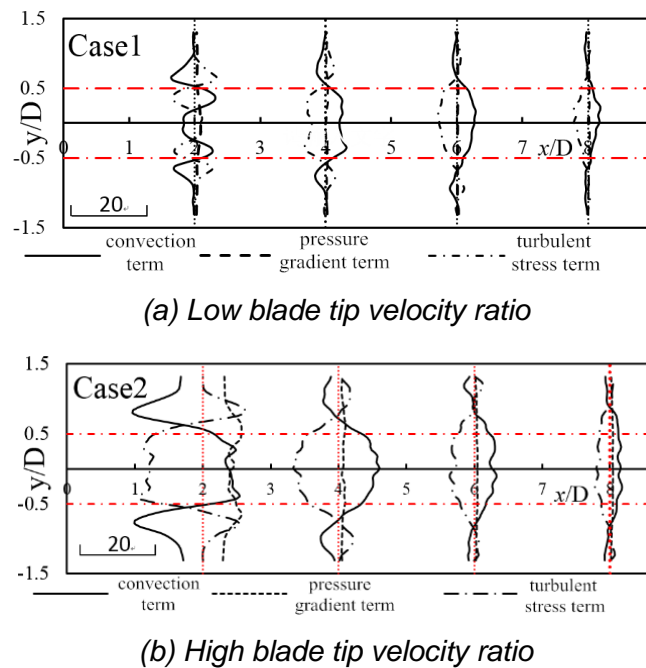


Fig. 10 - Equilibrium curves of N-S equation in several sections

Computing resources

The large eddy simulation (LES) method takes a lot of computing resources. It will take about 120 hours to accomplish the numerical simulation of entire flow field without effects of wind turbine under the parallel computing condition of 16-core I7-5960X CPU. The computing time will increase when considering the effects of wind turbine on flow field. Table 2 lists the computing time of iterating 100 time steps with the same grid system and same computer configuration, in which the time step is set to 0.0001s. It is obvious that ADM method takes the shortest time, which is 3.86% higher than that without the wind turbine, ADM-R method is the second, increasing by

10.45%, and ALM method takes the longest time, increasing by 25.70%. ADM method assumes that the axial inductive force is uniformly distributed, and ADM-R method assumes that inductive force is uniformly distributed in a micro radial ring. In the process of computation, dynamic source term of volumetric force applied by these two methods remains constant. But volume force applied by ALM method varies with time, and the obtained fluctuating velocity is larger, the flow field is more disordered, so the calculation speed is slower.

Tab. 2 - Computing conditions

Case name	Without wind turbine	ADM	ADM-R	ALM
Time-consuming	1934	2018	2146	2431
Increasing ratio	-	4.34%	10.96%	25.70%

CONCLUSION

In this paper, three methods combined with LES model are used to simulate the wind turbine wakes flow field in the presence of turbulent inflow. The results of numerical simulation and experiment are compared, and the computing characteristics of these methods are researched. The following conclusions were drawn:

- (1) Sharp wedges are placed in front of wind turbine to simulate flow turbulence conditions and to reproduce the distribution of average velocity and fluctuating velocity of the boundary layer in low turbulence intensity. The results of numerical simulation are in good agreement with the experimental results, which verifies the accuracy of the numerical model adopted in this study.
- (2) The distribution characteristics of wind turbine wakes flow field in the presence of turbulent inflow are investigated. After the flow encounters the wind turbine, the mean wind velocity decreases rapidly while the fluctuating wind velocity increases. With the increase of the distance away from wind turbine, the initial state is restored, the mean wind speed increases and the fluctuating wind speed decreases. Besides, the wind speed is basically stable at about $x=6D$. It is found that the larger the blade tip wind speed ratio is, the stronger the disturbance of the wind turbine to the original flow field will be, so the average wind speed become smaller and the fluctuating wind speed become larger at the wake.
- (3) The simulation accuracy of three actuation methods under different blade tip wind speed ratios is proved. In the region of near wake flow field, both ADM-R and ADM methods have great error with the experimental data, and cannot capture the information of near wake flow field. However, ALM method is in good agreement with the experimental data. The three methods are all in good agreement with the experimental results in the region of far wake field. Because the influence of cabin on the wind field is not considered, the wind speed calculated by the three methods is slightly larger than the experimental value near the center of the wind turbine. Under the condition of high blade tip velocity ratio, the disturbance effect of fan on flow field is more obvious and the calculation result is more accurate.
- (4) The equilibrium relations of each terms in N-S equation of wind turbine wake are revealed. The turbulent stress term, pressure gradient term and convection term mainly contribute to the equation equilibrium at near wake area. In the far wake region, the convection term is in equilibrium with the turbulent stress term.
- (5) The computational efficiency of the wake simulation method and the factors affecting the computational efficiency are analysed. Because in the ALM method, the volume source term changes with time, the flow field is more disorder and the ALM method takes the longest time,

but the calculation results are the most accurate. In the optimal arrangement of wind turbines, different calculation methods should be comprehensively chosen according to the calculation conditions.

ACKNOWLEDGEMENT

The authors thank for the support from the Guangdong Power Grid Company Limited R&D project (No.GDKJQQ20161150).

REFERENCES

- [1] Hand M M, Simms D A, Fingersh L J, et al.,2001. Unsteady aerodynamics experiment phase VI: wind tunnel test configurations and available data campaigns. National Renewable Energy Laboratory, Golden, CO, Report No. NREL/TP-500-29955
- [2] Schreck S., 2002. The NREL full- scale wind tunnel experiment Introduction to the special issue. *Wind Energy*, 5(2-3): 77-84.
- [3] Alfredsson, P.H. and J.A. Dahlberg.,1979. A preliminary wind tunnel study of windmill wake dispersion in various flow conditions. Part 7.
- [4] Ebert, P.R. and D.H. Wood.,1999. The near wake of a model horizontal-axis wind turbine—II. General features of the three-dimensional flow field. *Renewable Energy*, 8(4): p. 513-534.
- [5] Simms, D., et al.,2013. Wind tunnel testing of NREL's unsteady aerodynamics experiment. In 2001 ASME Wind Energy Symposium.
- [6] Yan Haijin, Hu Danmei, Li Jia.,2010. Numerical simulation of flow field in impeller of horizontal axis wind turbine. *Journal of Shanghai University of Electric Power*, 26 (2): 123-126.
- [7] Li Shaohua, Yue Weipeng, Kuang Qingfeng, et al.,2011. Numerical simulation of double turbine wake interaction and array. *Chinese Journal of Electrical Engineering*, 31 (5): 101-107.
- [8] Yang Rui, Xia Wei, Wang Tingting, et al.,2016. Application of actuating disk model in wind farm. *Journal of Lanzhou University of Technology*, 42 (1): 66-69.
- [9] Ren Huilai, Zhang Xiaodong, Kang Shun, et al.,2017. Simulation analysis of wind turbine tail flow based on non-uniform actuation disk. *Hydroelectric Energy Science*, (2): 193-195.
- [10] Li Pengfei, Liu Jiancheng.,2016. Numerical simulation of wake field of wind turbine based on actuation line model. *Research and Progress of Hydrodynamics*, (2):127-134.
- [11] Han Xingxing, Xu Chang, Liu Deyou, et al.,2016. An actuated disk model for wind farm based on average wind speed of wind turbine. *Journal of Engineering Thermophysics*, V37 (3): 501-506.
- [12] Zhao Feng, Duan Wei.,2010. Parameter Analysis and Strength Calculation of Wind Turbine Blades Based on Element-Momentum Theory and Finite Element Method. *Journal of Mechanical Design and Manufacturing*, (8): 42-44.
- [13] Zhu Chong.,2012. Numerical simulation of wake flow field of wind turbine. *Nanjing University of Aeronautics and Astronautics*.
- [14] Tian Linlin, Zhao Ning, Zhong Wei, et al.,2011. Study on the calculation of the long wake of wind turbine. *Air Dynamics*, 29 (6): 805-809.
- [15] Hou Yali, et al.,2016. Study on the effect of wind shear on turbulence characteristics of wind turbine wake. *Chinese Journal of Mechanical Engineering*, 52 (16): 149-155.
- [16] Ishihara Meng, Qian Qiwei.,2016. Numerical prediction of wind turbine wake and proposal of analytical model. *Symposium on Wind Engineering Symposium Proceedings of 24th Wind Engineering Symposium The Japan Wind Cooperation Association*, 151-156.
- [17] Martin O L H.,2009. *Aerodynamics of Wind Turbines*. Xiao Jinsong, translated. Beijing: China Electric Power Press.
- [18] Masaya Yamauchi, Meng Ishihara, Yozo Fujino.,2016. Proposal of a new analytical model for finding the windmill late flow. *58th Annual Scientific Lecture of JSCE*, I-132.

INFLUENCE OF PVD-ENHANCING SOFT SOIL GROUND ON THE ADJACENT BRIDGE PILES – A 3D FEM ANALYSIS

Hong-quan Li¹, Li-min Wei¹, Sheng-yang Feng^{1,2}, Zhi Chen²

1. School of Civil Engineering, Central South University, Changsha 410075, China; lhq113@csu.edu.cn
2. School of Environment and Safety Engineering, University of South China, Hengyang 421001, China; 14100044@usc.edu.cn

ABSTRACT

The influence of prefabricated vertical drain (PVD)-enhancing soft soil on the adjacent bridge pile foundation is not sufficiently clear. The related studies are scarce and far behind the requirement of engineering practice. Three-dimensional finite element model (3D FEM) is established to investigate this important issue. Plastic drainage boards in the PVD are modelled by a user-defined element, which considers the axial force and permeability of the plastic drainage board, whereas its weight, shear, and torsion are not considered. The elastoplastic-consolidation coupled model is used for the soils. Field measured results of pore water pressure, ground settlement, and pile cap displacement are used to validate the 3D FEM with good accuracy. A number of useful conclusions can provide guidelines for similar projects and inform designers of the adverse effects of PVD-enhancing soft soil ground on the adjacent bridge pile foundation.

KEYWORDS

PVD, Soft soil, Bridge pile foundation, FEM

INTRODUCTION

In the past three decades, with the rapid development of China, land resources for municipal and civil projects became increasingly scarce, especially in the developed coastal areas of China. However, because of the widespread distribution of soft soil in these areas, ground treatment techniques are widely used for soft soil foundation to provide a foundation that satisfies requirements of bearing capacity and strength. These techniques include the use of lightweight materials [1], stone columns [2], deep mixed (DM) columns [3], vertical drains [4], and prefabricated vertical drains (PVDs) [5-7], the latter being one of the most cost-efficient method and has been widely used in practice [8]. PVDs can greatly accelerate the consolidation and drainage process of soft soil ground and effectively increase the bearing capacity of soft soil foundation [9-13]. Recently, this technique has been widely used in the construction of urbanization in the world. Lam et al. [14] studied the performance of improved soft clay with PVDs combined with embankment preloading and vacuum preloading for the 2D FEM and field tests. Indraratna et al. [15] proposed an equivalent 2D numerical modelling to analyse PVD-assisted soft ground consolidation, and the performance of the model provided a good agreement between the numerical and analytical predictions, as well as the field measurements. Ya et al. [16] proposed a method to calculate the ground settlement and the lateral displacement induced by vacuum preloading and analysed two well-documented field cases in China. Ye et al. [8] used the field test and numerical analysis method to study the performance of PVD-reinforced soft soil with surcharge preloading and vacuum preloading.

Most of the consolidation deformation of soft soil ground can be completed in a short time owing to the PVD [17] and rapidly break the pile–soil interaction balance of the adjacent pile foundation, which result in excessive post-construction deformation of the adjacent pile foundation. This excessive post-construction deformation may lead to the collapse of the superstructure. A PVD-enhancing soft soil ground is unfavourable to an adjacent bridge pile foundation. However, if inappropriately implemented, would seriously endanger the safety of the superstructure. However, at present, the influence of the PVD-enhancing soft soil on the pile foundation of adjacent bridge is not evident. The related studies are scarce and far behind the requirement of engineering practice.

The PVD-enhancing soft soil ground is located in Guangzhou City, Guangdong Province, China. The settlement of the adjacent bridge pile foundation and the pore water pressure in soft soil ground are monitored in the site to validate the three-dimensional finite element model (3D FEM). The influence of the PVD-enhancing soft soil on the adjacent bridge pile foundation is studied systematically by using the verified 3D FEM.

PROJECT DESCRIPTION

The site of the PVD-enhancing soft soil ground is located in Guangzhou City, Guangdong Province, China. In terms of thickness, the subsoil of this site is composed of 2.4 m miscellaneous fill, 13.1 m very soft soil (also called mucky clay in China), 2.2 m medium sand, 5.7 m fine sand, 4.3 m soft silt clay, and medium sand. The groundwater level is 0.5 m below the ground surface. The typical properties along with the soil parameters are depicted in Figure 1.

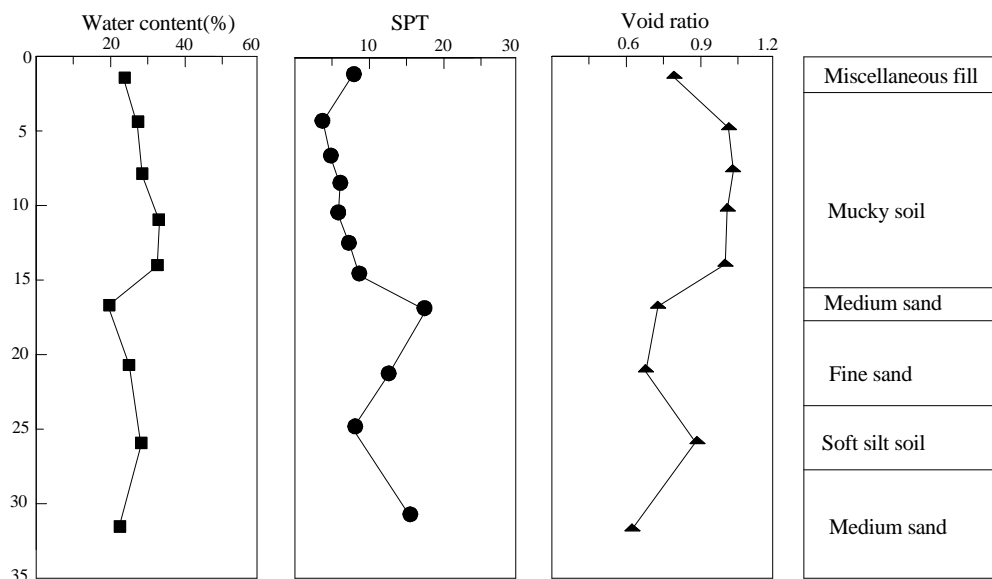


Fig. 1 – Soil profile and properties at the site

The site of PVD-enhancing soft soil ground is an irregular quadrangle, 106.59-m long, 91.62-m wide, and an area of 8555 m². A highway bridge pile foundation exists at approximately 43 m away from the site. The plane view of the site is shown in Figure 2. The settlement, pore water pressure of the PVD-enhancing soft soil ground, and the deformation of the adjacent pile foundation are monitored synchronously in the process of construction. The location of the monitoring components is also shown in Figure 2. The pore water pressure monitoring point is located in the very soft soil layer at 8 m below the T1 and T2 monitoring points; XS-186 pore water pressure gauge is used to measure the pore water pressure. The settlement and deformation

monitoring points are designated at the T1–T2 and T3–T4 monitoring points (i.e., two corners of the bridge pile cap) by using a high-precision monitoring station. The plastic drainage boards with an area of 0.007 m² and a length of 16 m are punched through the very soft soil layer and embedded in the middle sand layer at a spacing of 1 m. Gravelly soils with the height of 2 m are used as surcharge fill material for 56 d.

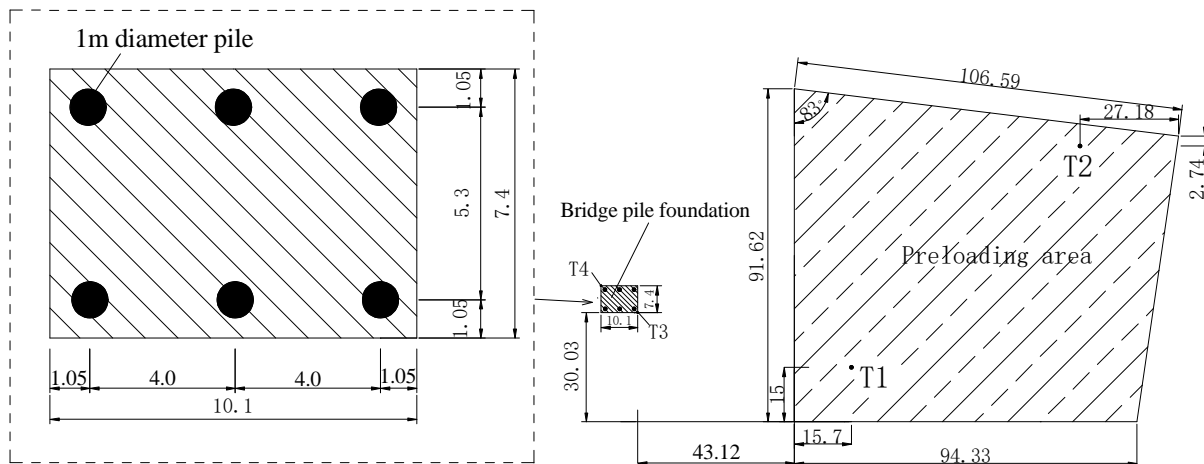
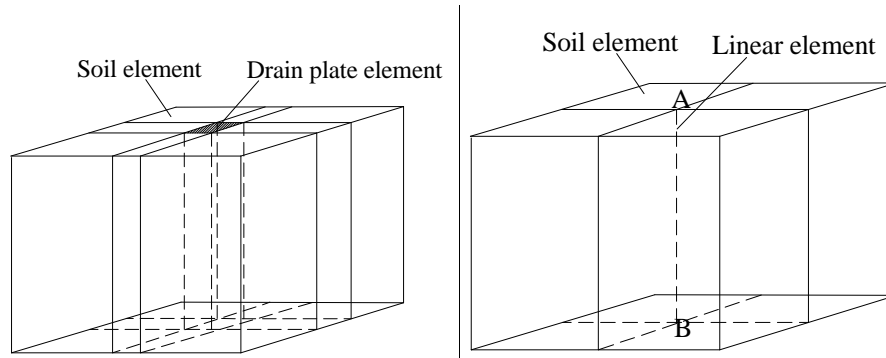


Fig. 2 – Plane view of the test site and location of the monitoring components

NUMERICAL MODELLING

At present, the conventional numerical modelling for PVD-enhancing soft soil ground are simplified to axisymmetric single well or plane strain [18-20]. Axisymmetric single well can effectively model one type of sand, but they cannot analyse ground lateral deformation and load distribution. In the plane strain method, the equivalent transformation is required to convert the three-dimensional PVD-enhancing soft soil ground into the two-dimensional drainage plate wall for plane strain modelling. However, after the equivalent transformation, the geometric position of each point of the ground cannot correspond to the prototype one by one. Thus, the method is evidently unsuitable for complex engineering problems, such as those similar to this study. The ideal method is to use 3D FEM. However, if the plastic drainage plate is divided as a solid element, then the computing scale of the numerical model becomes extremely large.

Increasing the permeability of the soil is the main function of the plastic drainage board, while improving the corresponding mechanical properties is only secondary. We used a user-defined element (called UEL subroutine in ABAQUS), a one-dimensional two-node linear element proposed by Fei [21], to model the plastic drainage board. If the drain plate is considered a solid element, then its mesh is rough (Figure 3a). If the drain plate element is a line element and shares nodes A and B (Figure 3b) with the soil element, then the number of elements and nodes are reduced to avoid inaccurate simulation results caused by the difference between the size of the drainage plate element and the surrounding soil element. The weight, shear, and torsion properties of the plastic drain board are not considered in the simulation, only the axial force and its influence on overall permeability.



(a) Mesh of drainage plate with solid element (b) Mesh of drainage plate with linear element
 Fig. 3 – Schematic of the drainage plate element

Then, we used the ABAQUS software to establish a 3D FEM of the PVD-enhancing soft soil ground, as shown in Figure 4. The transverse, longitudinal and vertical directions of the model are 400, 200, and 96 m. The pile foundation of the adjacent bridge is composed of 3×2 concrete cast-in-place piles with 1.0 m diameter. The thicknesses of the pile length, longitudinal pile spacing, transverse pile spacing, and pile cap are 32, 4, 5.3, and 1.5 m, respectively. The elastoplastic-consolidation coupled model is used for the soils, and the model parameters of each soil layer are shown in Table 1. The elastic model is applied to the bridge pile foundation. The density, elastic modulus, and Poisson's ratio of the pile foundation are 2500 kg/m³, 32 GPa, and 0.17, respectively. The plastic drainage boards are modelled by the UEL element with the elastic modulus of 1.5 GPa and the permeability coefficient of 1×10⁻² m/s. The contact element is arranged on the pile–soil interface and the pile cap–soil interface, in which the Coulomb friction model is used for the pile-side interface. The non-friction hard contact model is used for the pile-bottom soil and the pile cap–soil interface. The friction coefficient of the pile-side interface μ can be calculated by the internal friction angle φ , written as $\mu = \tan 0.75\varphi$. The eight-node hexahedron pore pressure element (called C3D8P in ABAQUS) is used for the soils, and the eight-node hexahedron element (C3D8) is used for the piles. In the 3D FEM, the horizontal direction of the side surface and the vertical displacement of the bottom surface are fixed, and the top surface is set to drainage boundary. The PVD surcharge load is equal to 40 kPa that lasts for 56 d. The total load on the bridge pile foundation is 13287 kN.

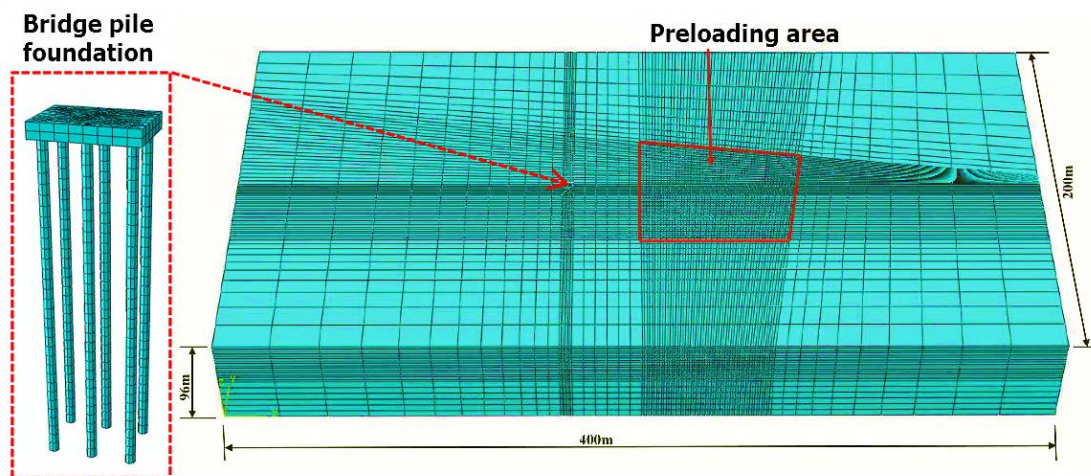


Fig. 4 – 3D FEM of preloading

Tab. 1 - Parameters of soil physical mechanics

Soil Layer	Thickness /m	Density /(g/cm ³)	Young modulus /MPa	Permeability coefficient /(cm/s)	Cohesion /kPa	Internal friction angle /°	Void ratio
Miscellaneous fill	2.4	1.8	6.2	6e-5	14.2	15.8	0.82
Mucky clay	13.1	1.68	3.7	1.54e-6	8.4	6	1.03
Medium sand	2.2	1.95	36.2	6e-4	0.1	21.4	0.72
Fine sand	5.7	1.8	22.1	3.4e-4	0.1	12.9	0.68
Soft silt clay	4.3	1.75	7.8	1.3e-5	12.4	7.8	0.92
Medium sand	5.4	1.9	61.8	7.8e-4	0.1	23.7	0.66

DISCUSSION OF RESULTS

Figure 5 presents the field measured pore water pressure along with the calculated results from the numerical analysis in the mucky clay layer of 8 m below monitoring points T1 and T2. The calculated results of pore water pressure in soft soil ground are close to the measured results. The pore water pressure increased rapidly in the early stage (0–0.5 d) of PVD-enhancing soft soil ground, and then decreased slowly with time. The process of pore water pressure dissipation is completed on the 56th day.

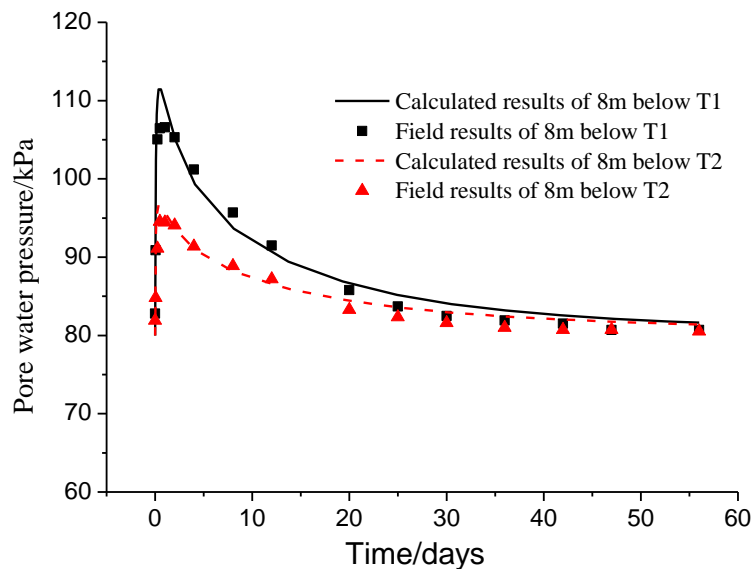


Fig. 5 – Calculated and measured pore water pressure in the mucky clay layer of 8 m below T1 and T2

Figure 6 shows the field measured ground settlement along with the calculated results from numerical analyses at monitoring points T1 and T2. The calculated ground settlement is close to the measured result. Most of the ground consolidation settlement is completed in a short time given that the plastic drainage plate accelerated the dissipation of pore water pressure in the soil. The ground settlement has gradually become stable after 56 d, which indicates that the soft soil ground has been strengthened.

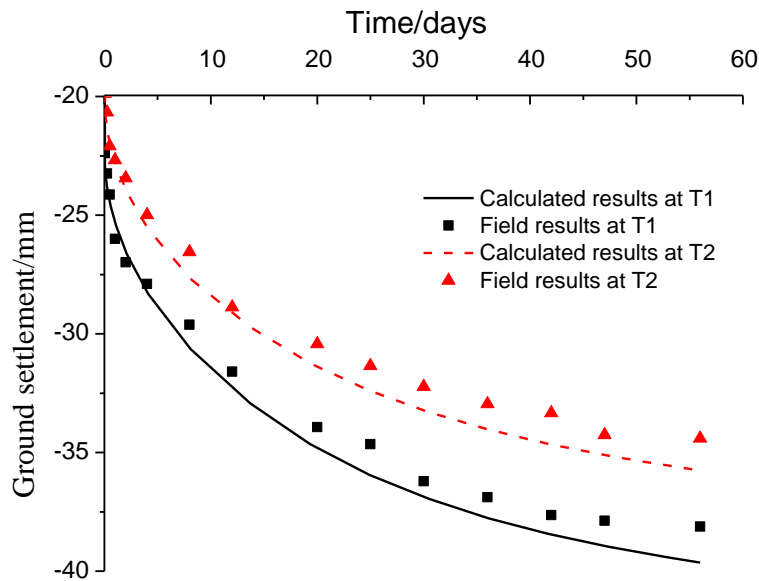
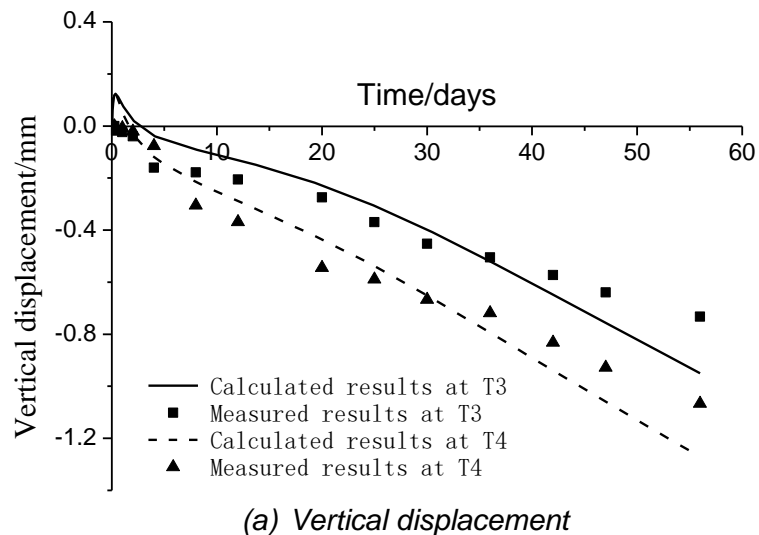


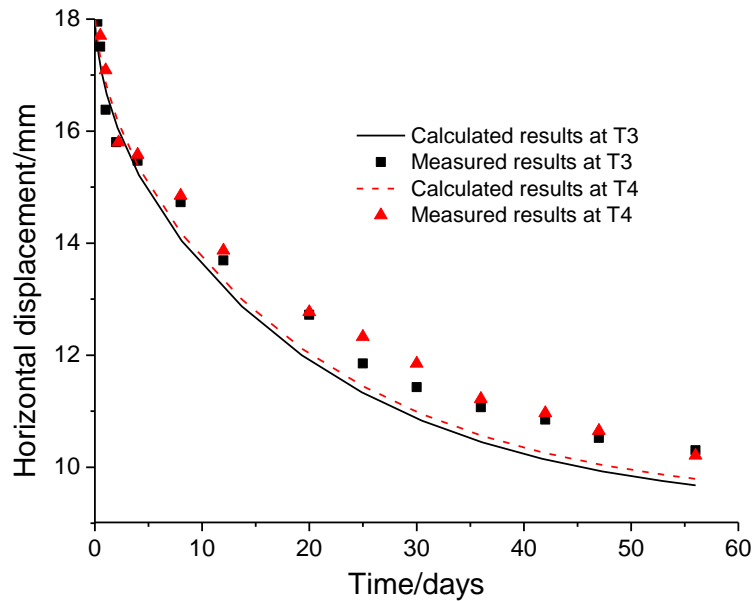
Fig. 6 – Calculated and measured ground settlement at T1 and T2

Figure 7 presents the measured vertical displacement and horizontal displacement along with the FEM results at monitoring points T3 and T4 on the pile cap corner of the adjacent bridge. The calculated vertical displacement and horizontal displacement are close to the measured results. Figure 7(a) shows that in the early stage (0–3 d), the lateral displacement occurs in the upper soil under the PVD-enhancing soft soil ground, which squeezed the adjacent pile foundation and caused the pile cap to appear slightly uplifted. The pile cap is restored to its initial position and gradually subsided with the dissipation of pore water pressure. Figure 7(b) shows that under the influence of PVD-enhancing soft soil ground, a large horizontal displacement appears in the pile cap, and the maximum is up to 18.5 mm at the initial stage. The horizontal displacement of the pile cap gradually decreased with the dissipation of pore water pressure and is approximately 9.3 mm.



(a) Vertical displacement

Fig. 7 – Calculated and measured vertical displacement and horizontal displacement at T3 and T4



(b) Horizontal displacement

Fig. 7 – Calculated and measured vertical displacement and horizontal displacement at T3 and T4

Figure 8 presents the horizontal displacement of the pile shaft at different PVD preloading times calculated by numerical simulation. The horizontal displacement of the pile shaft decreased with the dissipation of pore water pressure. The pile horizontal displacement decreased along the pile depth at the early stage and increased at the later stage because the pore water in the deep soil has gradually discharged along the plastic drainage board. Moreover, the effective stress of the deep soil increased gradually, which resulted in the increase in passive earth pressure on the pile side. As a result, the horizontal displacement of the bottom section of the pile widened increasingly.

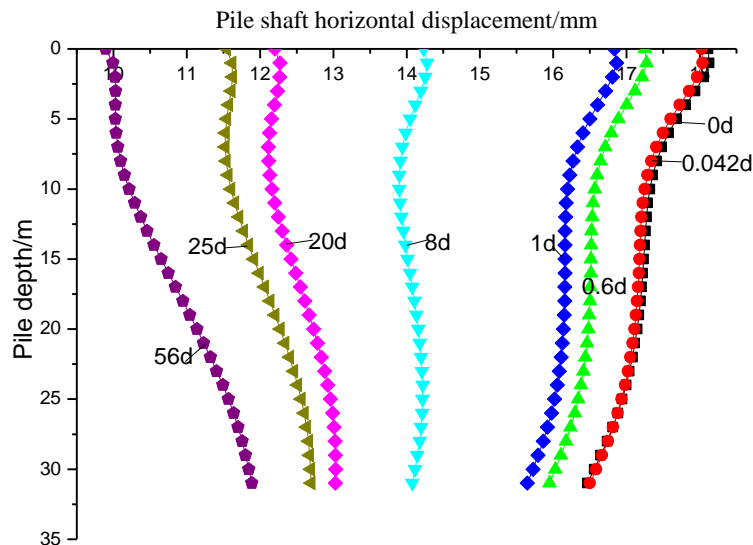


Fig. 8 – Calculated horizontal displacement of the pile shaft at different PVD preloading times

Figure 9 shows the calculated passive earth pressure on the pile side at different PVD preloading times, where the negative value indicates that the passive earth pressure comes from

the opposite side of the surcharge and the positive value comes from the same side of the surcharge. The passive earth pressure gradually decreased with time, and the distribution of the passive earth pressure along the pile shaft tends to be increasingly uniform with the dissipation of pore water pressure. Thus, the adverse effect of PVD-enhancing soft soil ground on the adjacent pile foundation mainly occurs in the early stage, when the passive earth pressure on the pile side is the largest.

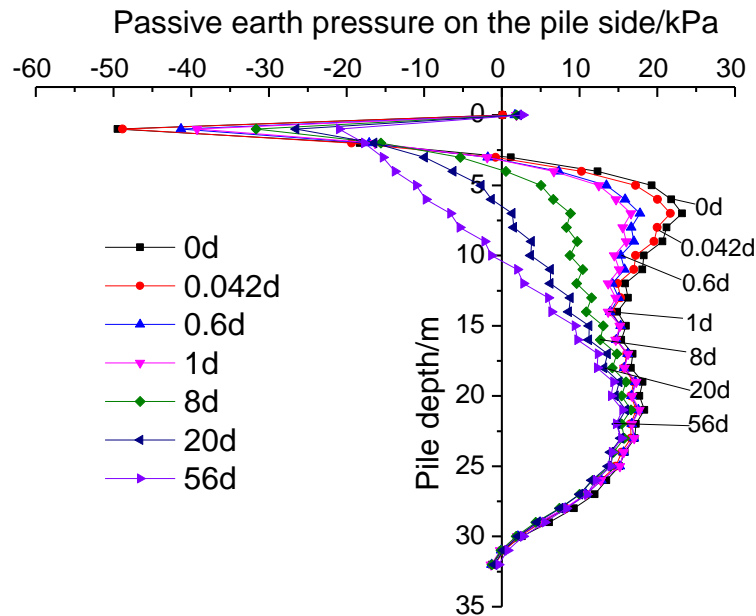


Fig. 9 – Calculated passive earth pressure on the pile side at different PVD preloading times

Figure 10 presents the calculated bending moment of the pile shaft at different PVD preloading times. All the maximum bending moments of the pile shaft at different times are located at the interface between the pile top and the pile cap, where the maximum is 247.3 kN.m at the beginning. After PVD preloading for 56 d, the maximum bending moment of the pile shaft decreased to 190.9 kN.m.

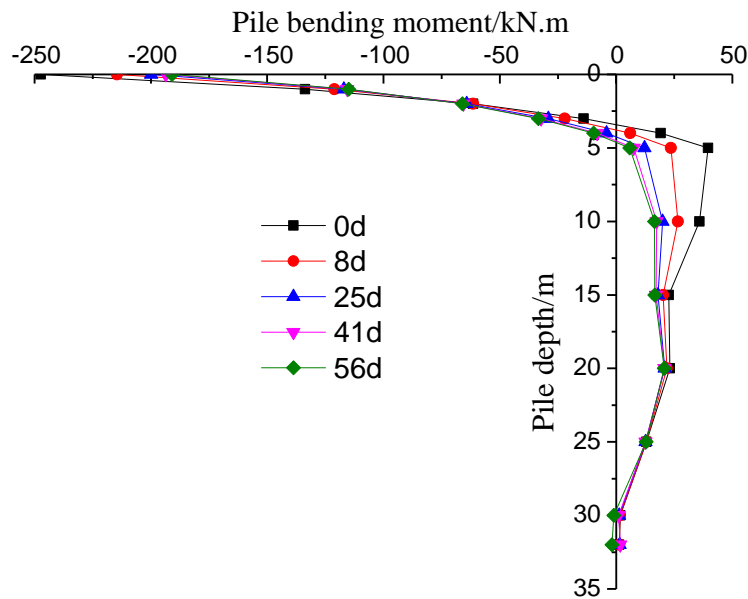


Fig. 10 – Calculated bending moment of the pile shaft at different preloading times

We studied the influence of the PVD fill surcharge distance on the adjacent bridge pile foundation by using 3D FEM. The PVD fill surcharge distance of 2B, 3B, 4.3B, 6B, and 10B are used in the 3D FEM, where B is the width of the pile cap of the adjacent pile foundation ($B = 10.1$ m) and 4.3B is the actual distance. Figure 11 presents the relationship between the maximum horizontal displacement of the pile shaft and the PVD fill surcharge distance at 56 d. Figure 12 depicts the relationship between the maximum bending moment of the pile shaft and the PVD fill surcharge distance at 56 d. The maximum horizontal displacement and bending moment of the pile shaft decreased sharply with the increase in the PVD fill surcharge distance. When the PVD fill surcharge distance is 2B, the maximum horizontal displacement and bending moment are 29.28 mm and 592 kN.m, respectively. This PVD fill surcharge distance greatly harms the adjacent pile foundation. When the PVD fill surcharge distance reached 10B, the maximum horizontal displacement and bending moment are 0.58 mm and 13.8 kN.m, respectively. The influence of this PVD fill surcharge distance on the adjacent pile foundation can be neglected.

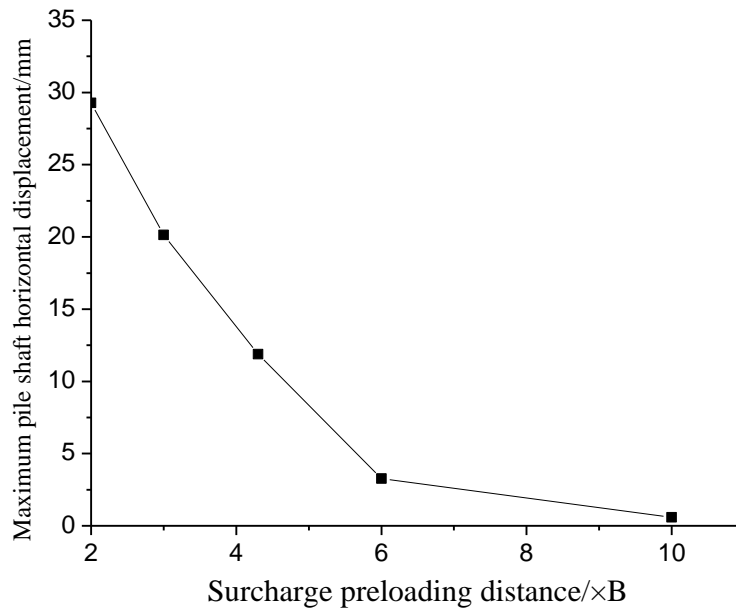


Fig. 11 – Relation between the maximum pile horizontal displacement and the fill surcharge distance at 56 d

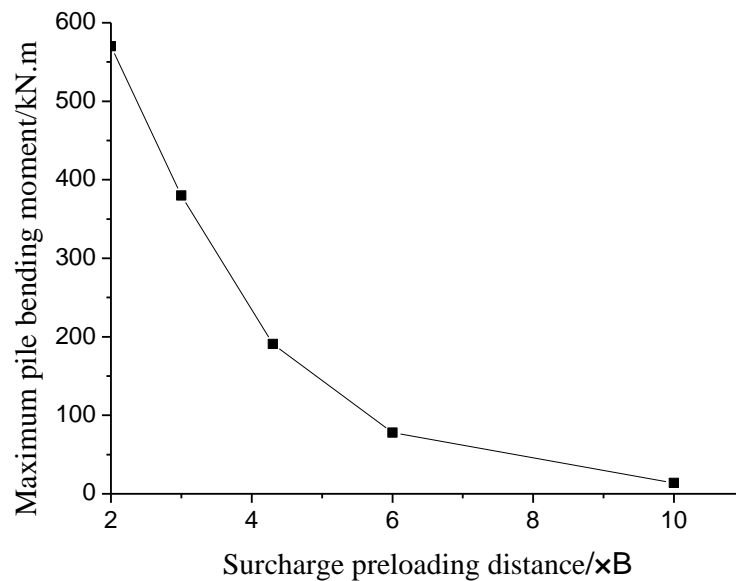


Fig. 12 – Relation between the maximum pile bending moment and the fill surcharge distance at 56 d

CONCLUSION

Field tests and numerical analyses are conducted to evaluate the influence of PVD-enhancing soft soil on the adjacent bridge pile foundation. The following conclusions can be drawn:

(1) The 3D FEM established in this study can accurately simulate the influence of PVD-enhancing soft soil ground on the adjacent bridge pile foundation. A good match exists between the calculated and measured pore water pressure, ground settlement, and pile cap displacement.

(2) The pore water pressure increased sharply in the early stage of PVD fill surcharge, then decreased with time, and the pore water pressure dissipated rapidly in the early stage and decreased gradually in the later stage.

(3) Under the influence of the PVD fill surcharge, the deformation of the adjacent pile foundation is mainly horizontal, and the vertical displacement is small. The pile horizontal displacement decreased gradually with time with the dissipation of pore water pressure.

(4) The adverse effects of PVD-enhancing soft soil ground on the adjacent pile foundation mainly occur in the early stage of PVD fill surcharge when the passive earth pressure on the pile side and pile bending moment, which are located at the top of the pile, are the largest. With the dissipation of pore water pressure, the passive earth pressure and bending moment gradually decreased with time.

(5) The maximum horizontal displacement and bending moment of the pile decreased sharply with the increase in the PVD fill surcharge distance. Therefore, the appropriate PVD fill surcharge distance should be maintained to ensure the safety of the adjacent bridge pile foundation. The safe PVD fill surcharge distance should also be comprehensively assessed on the basis of the actual situation of the site, and the relevant assessment methods should be further studied.

ACKNOWLEDGMENTS

This work was supported by Scientific Research Project of Shanghai Railway Bureau (No. 2013144) and National Natural Science Foundation of China (No.11705083).

REFERENCES

- [1] Kim, Y.T., Kang, H.S. 2011. Engineering Characteristics of Rubber-Added Lightweight Soil as a Flowable Backfill. *Material Journal of Materials in Civil Engineering*. Vol. 23: 1289-1294.
- [2] Adalier, K., Elgamal, A. 2004. Mitigation of liquefaction and associated ground deformations by stone columns. *Engineering Geology*. Vol. 72: 275-291.
- [3] Ye, G.B., Zhang, Z., Han, J. 2013. Performance Evaluation of an Embankment on Soft Soil Improved by Deep Mixed Columns and Prefabricated Vertical Drains. *Journal of Performance of Constructed Facilities*. Vol. 27: 614-623.
- [4] Rujikiatkamjorn, C., Indraratna, B. 2009. Design procedure for vertical drains considering a linear variation of lateral permeability within the smear zone. *Canadian Geotechnical Journal*. Vol. 46: 270-280.
- [5] Bergado, D.T., Balasubramaniam, A.S., Fannin, R.J., Holtz RD. 2002. Prefabricated vertical drains (PVDs) in soft Bangkok clay: a case study of the new Bangkok International Airport project. *Canadian Geotechnical Journal*. Vol. 39: 304-315.
- [6] Li, A.L., Rowe, R.K. 2001. Combined effects of reinforcement and prefabricated vertical drains on embankment performance. *Canadian Geotechnical Journal* 38: 1266-1282.
- [7] Ghandeharioon, A., Indraratna, B., Rujikiatkamjorn, C. 2010. Analysis of soil disturbance associated with mandrel-driven prefabricated vertical drains using an elliptical cavity expansion theory. *International Journal of Geomechanics*. Vol. 10: 53-64.
- [8] Ye, G.B., Xu, Y., Zhang, Z. 2017. Performance Evaluation of PVD-Reinforced Soft Soil with Surcharge and Vacuum Preloading. *International Journal of Civil Engineering*, Vol. 4: 1-13.
- [9] Chai, J.C., Carter, J.P., Hayashi, S. 2005. Ground Deformation Induced by Vacuum Consolidation. *Journal of Geotechnical & Geoenvironmental Engineering*. Vol. 131:1552-1561.
- [10] Saowapakpiboon, J., Bergado, D.T., Voottipruex, P., et al. 2011. PVD improvement combined with surcharge and vacuum preloading including simulations. *Geotextiles & Geomembranes*. Vol. 29: 74-82.
- [11] Indraratna, B., Rujikiatkamjorn, C., Balasubramaniam, A.S., et al. 2012. Soft ground improvement via vertical drains and vacuum assisted preloading. *Geotextiles & Geomembranes*. Vol. 30: 16-23.

- [12] Le, G.L., Bergado, D.T., Hino, T. 2015. PVD improvement of soft Bangkok clay with and without vacuum preloading using analytical and numerical analyses. *Geotextiles & Geomembranes*. Vol. 43: 547-557.
- [13] Chai, J., Rondonuwu, S.G. 2015. Surcharge loading rate for minimizing lateral displacement of PVD improved deposit with vacuum pressure. *Geotextiles & Geomembranes*. Vol. 43: 558-566.
- [14] Lam, L.G., Bergado, D.T., Hino, T. 2015. PVD improvement of soft Bangkok clay with and without vacuum preloading using analytical and numerical analyses. *Geotextiles & Geomembranes*. Vol. 43: 547-557.
- [15] Indraratna, B., Zhong, R., Rujikiatkamjorn, C. 2016. An Analytical Model of PVD-assisted Soft Ground. *Consolidation Procedia Engineering*. Vol. 143: 1376-1383.
- [16] Wu, Y., Xu, F., Yuan, M., Sun, D. 2016. Ground deformation induced by vacuum loading–unloading. *Environmental Earth Sciences*, Vol. 75: 1-8.
- [17] Indraratna, B., Sathanathan, L., Rujikiatkamjorn, C., et al. 2005. Analytical and Numerical Modeling of Soft Soil Stabilized by Prefabricated Vertical Drains Incorporating Vacuum Preloading. *International Journal of Geomechanics*. Vol. 5: 114-124.
- [18] Yildiz, A. 2009. Numerical analyses of embankments on PVD improved soft clays. *Advances in Engineering Software*. Vol. 40: 1047-1055.
- [19] Rujikiatkamjorn, C., Indraratna, B., Chu, J. 2007. Numerical modelling of soft soil stabilized by vertical drains, combin. *Canadian Geotechnical Journal*. Vol. 44: 326-342 .
- [20] Karim, M.R. 2013. Behaviour of piles subjected to passive subsoil movement due to embankment construction – A simplified 3D analysis. *Computers & Geotechnics*. Vol. 53: 1-8.
- [21] Fei, K., Zhang, J. 2010. Application of ABAQUS in geotechnical engineering, 243-249 (The Publishing House of Water Conservancy and Hydropower Engineering Beijing) 412 pp.

NUMERICAL INVESTIGATION OF THE PERFORMANCE OF INSULATED FRP-STRENGTHENED REINFORCED CONCRETE BEAMS IN FIRE

Osama El-Mahdy¹, Gehan Hamdy² and Moustafa Abdullah²

1. *Department of Civil Engineering, Faculty of Engineering at Shoubra, Benha University, Shoubra, Cairo, Egypt; osama.alhenawy@feng.bu.edu.eg, os8294@hotmail.com*
2. *Department of Civil Engineering, Faculty of Engineering at Shoubra, Benha University, Shoubra, Cairo, Egypt*

ABSTRACT

Fiber reinforced polymers (FRP) have been widely used in retrofitting and strengthening of deteriorated or deficient reinforced concrete (RC) elements. A major concern about those systems is their performance under elevated temperature which limits the application of FRP for strengthening requirements. Fire protection of the strengthening FRP system can be made by applying an external coating layer of a thermal resisting material. In order to predict the fire performance of such insulated FRP-strengthened members and their efficiency, experimental investigations are required to be carried out for such elements under realistic fire conditions, which requires time and cost.

This paper presents numerical modelling of RC beams strengthened with externally bonded FRP and insulated by a fire protection layer under elevated temperature specified by standard fire tests. The nonlinear time domain transient thermal-stress finite element analysis is performed using the general purpose software ANSYS 12.1 in order to study the heat transfer mechanism and deformation within the beam for fire conditions initiating at the bottom side of the beam. The finite element model accounts for the variation in thermal and mechanical parameters of the constituent materials such as concrete, steel reinforcement bars, FRP and insulation material with temperature. Application is made on an FRP-strengthened and insulated RC T-beam which has been experimentally tested in the published literature in order to verify the adopted modelling procedure. The obtained numerical results are in good agreement with the experimental results regarding the temperature distribution across the beam and mid-span deflection. The presented procedure thus provides an economical and effective tool to investigate the effectiveness of fire insulation layers when subjected to high temperatures and to design thermal protection layers for FRP strengthening systems that satisfy fire resistance requirements specified in building codes and standards.

KEYWORDS

Fiber reinforced polymers, Flexural strengthening, Elevated temperature, Fire, Thermal insulation, Finite element, Nonlinear analysis

INTRODUCTION

Fiber reinforced polymers (FRP) have been used for retrofitting and strengthening of deteriorated concrete structures due to their advantageous properties such as light weight, corrosion resistance and high strength. Externally bonded FRP sheets or laminates have been demonstrated to successfully enhance the flexural and shear capacity of reinforced concrete (RC) beams [1]. However, there are increasing concerns about their performance in the case of fire. Polymer materials undergo change in mechanical properties and loss of stiffness and bond strength when exposed to temperatures higher than the glass transition temperature (T_g) which is about 60 – 82 °C for the common polymers and adhesives [2]. When the temperature rises to this level, such as likely to happen in the case of fire, damage will occur to the bond between the FRP and the concrete surface and consequently the effectiveness of the FRP strengthening is severely threatened and may be totally lost [2, 3]. Fire performance is pointed out as a critical factor that requires more research before FRP can be used with confidence in strengthening applications [2]. Specifications and design guidelines limit the use, increase the load factor or limit the desired strength enhancement in order to meet fire hazard [4, 5]. Higher values of strengthening limits are allowed only if it can be proved through testing and technical assessments that such fire protection systems can increase fire endurance of FRP systems to exceed the fire resistance rating of building codes [4, 5]. There are still no design guidelines available for FRP-reinforced or strengthened concrete structures under fire conditions regarded as one of the major threats to buildings and other structures.

Experimental studies were carried out for FRP-strengthened RC members under elevated temperatures or fire by several researchers [6- 10]. To provide protection of carbon fiber reinforced polymer (CFRP) from direct fire exposure, a coating layer of a thermal insulating material, typically gypsum products, was placed around the beam cross-section [11, 12]. A fire test program was conducted by Blontrock et al. [6] in which ten CFRP-strengthened RC beams protected with calcium silicate boards were subjected to the design service loads of Eurocode [13]. The best fire resistance was provided by fire insulation layer applied as U-shape over the bottom and sides of the beams [6]. Using a 50 mm thick layer of Perlite mortar has protected CFRP strengthening system against 500 °C for three hours with only 4 - 12% loss in its capacity [11]. Different coating layers of Perlite, Vermiculite and Portland Cement mortars in addition to clay and ceramic fiber were studied and experimentally demonstrated to give protection and maintain 90% of the residual flexural capacity of FRP-strengthened beams compared to control beams after a two-hour exposure to 600 °C [12].

Beam-slab assemblies strengthened with FRP laminates and protected with vermiculite-gypsum (VG) cementitious layer were tested by Williams et al. [14] by exposure to standard fire load of ASTM E119 [15]. Efficient thermal protection and three hours fire endurance ratings were achieved by a 25 mm and 38 mm thick layer of the VG insulation [14].

Some studies in the published literature addressed numerical modelling to predict the performance of FRP-strengthened RC members subjected to fire [16 - 18] and the heat transfer through the different insulation layers during fire exposure [19]. However, more research work is needed that addresses modelling the performance of FRP-strengthened structures under elevated temperatures, in order to enable analysts and designers to accurately predict the fire endurance and economically design thermal insulation layers for such structures.

OBJECTIVE

The present research aims at studying numerically the behaviour of RC beams strengthened by externally bonded FRP laminates and thermally protected, under standard fire test

loading, thereby providing an economic tool for design of fire protection for FRP-strengthened RC beams.

To achieve this aim, numerical modelling by finite elements is performed to represent the beam components and account for the variation in thermal and mechanical parameters of the different materials with temperature. Nonlinear time analysis is performed using ANSYS 12.1 [20] in order to study the heat transfer mechanism and deformations within the beam. The numerical results are presented and compared to the previously published experimental and numerical results [14, 19] in order to verify the efficiency of the adopted numerical procedure.

NUMERICAL MODELING AND ANALYSIS

Finite Element Modelling

Modelling is made by finite elements using ANSYS 12.1 [20] for a thermally protected CFRP-strengthened RC beam that has been subjected to fire test in the published literature [14]. The T-beam is simply supported with total length 4000 mm and clear span 3900 mm, has the cross-sectional dimensions of 400 mm depth, 1220 mm flange width, 150 mm flange thickness and 300 mm web thickness, as shown in Figure 1. The T-beam reinforcement details were as follows; the main steel reinforcement was two 20 mm diameter bars. Shear stirrups were 10 mm diameter bars spaced at 150 mm centre to centre. Concrete cover to the web stirrups was 40 mm and concrete cover for flange reinforcement was 25 mm. A CFRP laminate of 1.3 mm thick and 100 mm wide is adhered to the bottom of the beam along the span and stopped at 100 mm from the support. A layer of VG plaster having a thickness of 25 mm is applied on the beam soffit and web and extends for a distance of 125 mm underneath the flange, as shown in Figure 1, along the entire length of the beam.

The element types used for transient thermal and structural finite element analysis are listed in Table 1. Full bond is assumed between concrete and reinforcement bars, CFRP and insulation layer. The details of finite element model are shown in Figure 2.

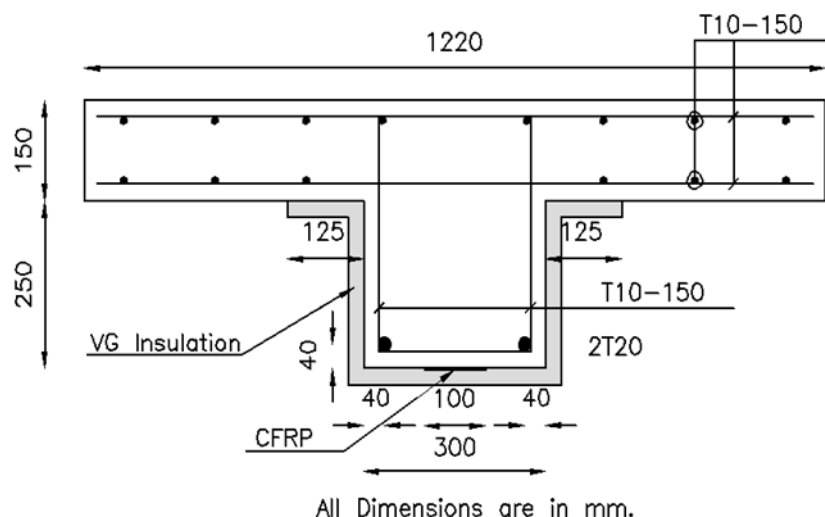


Fig. 1 - Experimentally tested T-beam cross-section [14]

Tab. 1 - Element types used for thermal and structural analyses

Material	Elements for thermal analysis	Elements for structural analysis
Concrete	SOLID70	SOLID65
Steel bars	LINK33	LINK8
CFRP layer	SHELL 57	SHELL 41
VG insulation	SOLID70	SOLID45

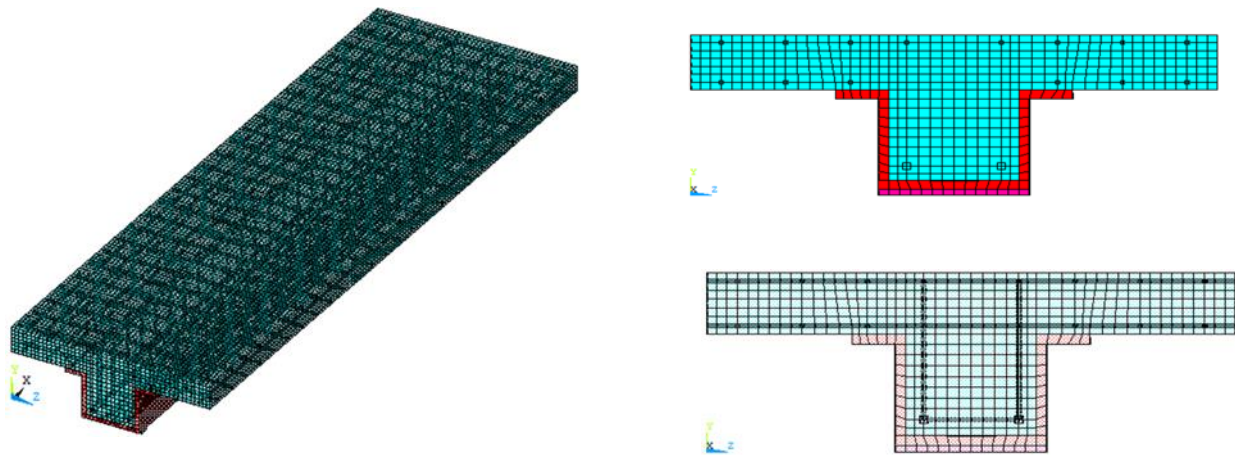


Fig. 2 - Finite Element Mesh of the Studied T-Beam

Material Mechanical and Thermal Properties

The concrete characteristic compressive strength is 41 MPa. The main steel reinforcement has yield and ultimate strengths of 500 and 650 MPa, respectively. The 10mm diameter reinforcement bars of stirrups and slab reinforcement have yield and ultimate strengths of 429 and 611 MPa, respectively. The 1.3 mm-thick CFRP laminate possesses a design tensile strength of 460 MPa in the direction of the fibres and ultimate elongation of 2.2% at failure [14]. Table 2 gives the values for the mechanical and thermal properties for concrete, steel reinforcement, CFRP and insulation materials at room temperature [19, 21].

Tab. 2 - Mechanical and thermal material properties at room temperature [19, 21]

Material	E_o MPa	K_o W/mm.K	C_o J/kg.K	μ	α	ρ_o Kg/m ³
Concrete	30200	2.7×10^{-3}	722.8	0.20	6.08×10^{-6}	2400
Steel bars	210000	5.2×10^{-2}	452.2	0.30	6.00×10^{-6}	7860
CFRP	228000	1.3×10^{-3}	1310	0.28	-0.90×10^{-6}	1600
VG Insulation	2100	2.5×10^{-4}	1654	0.30	1.70×10^{-5}	269

Note: E_o : stiffness modulus, K_o : thermal conductivity, C_o : specific heat, ρ_o : material density, α : coefficient of thermal expansion, and μ : Poisson's ratio.

The thermal and mechanical properties at elevated temperature for concrete and steel are available in the literature and the main equations are mentioned herein [13, 21, 22]. The steel reinforcement density is considered by Eurocode [22] to remain constant under elevated temperature. Density of concrete changes due to elevated temperature according to Equation. (1):

$$\rho(T) = \rho(20^\circ C) \quad \text{for } 20^\circ C \leq T \leq 115^\circ C \quad (1.a)$$

$$\rho(T) = \rho(20^\circ C) \left(1 - \frac{0.02(T - 115)}{85} \right) \quad \text{for } 115^\circ C < T \leq 200^\circ C \quad (1.b)$$

$$\rho(T) = \rho(20^{\circ}\text{C}) \left(0.98 - \frac{0.03(T - 200)}{200} \right) \quad \text{for } 200^{\circ}\text{C} < T \leq 400^{\circ}\text{C} \quad (1.c)$$

$$\rho(T) = \rho(20^{\circ}\text{C}) \left(0.95 - \frac{0.07(T - 400)}{800} \right) \quad \text{for } 400^{\circ}\text{C} < T \leq 1200^{\circ}\text{C} \quad (1.d)$$

Thermal conductivity of concrete changes with temperature according to Equation (2) and the variation in thermal conductivity of steel reinforcement with temperature is given in Equations (3).

$$K(T) = 2 - 0.2451 \left(\frac{T}{100} \right) + 0.0107 \left(\frac{T}{100} \right)^2 \quad \text{in } \left(\frac{\text{W}}{\text{m}} \cdot \text{K} \right) \quad \text{for } 20^{\circ}\text{C} \leq T \leq 1200^{\circ}\text{C} \quad (2)$$

$$K(T) = 54 - 3.33 \times 10^{-2} \quad \text{in } \left(\frac{\text{W}}{\text{m}} \cdot \text{K} \right) \quad \text{for } 20^{\circ}\text{C} \leq T \leq 800^{\circ}\text{C} \quad (3.a)$$

$$K(T) = 27.30 \quad \text{in } \left(\frac{\text{W}}{\text{m}} \cdot \text{K} \right) \quad \text{for } 800^{\circ}\text{C} < T \leq 1200^{\circ}\text{C} \quad (3.b)$$

The specific heat of concrete changes with temperature according to Equations (4). The peak specific heat of concrete depends mainly on the moisture content and occurs between 100°C and 115°C with linear decrease between 115°C and 200°C. For zero moisture content the peak specific heat is 900 J/kg K, while for moisture content 1.5 % and 3% of concrete weight the peak specific heat is 1470 J/kg K and 2020 J/kg K, respectively. For the beam of the present study, moisture content equal to 3 % of concrete weight is adopted throughout the modelling.

$$C(T) = 900 \quad \text{in } \left(\frac{\text{J}}{\text{Kg}} \cdot \text{K} \right) \quad \text{for } 20^{\circ}\text{C} \leq T \leq 100^{\circ}\text{C} \quad (4.a)$$

$$C(T) = 900 + (T - 100) \quad \text{in } \left(\frac{\text{J}}{\text{Kg}} \cdot \text{K} \right) \quad \text{for } 100^{\circ}\text{C} < T \leq 200^{\circ}\text{C} \quad (4.b)$$

$$C(T) = 1000 + \frac{(T - 200)}{2} \quad \text{in } \left(\frac{\text{J}}{\text{Kg}} \cdot \text{K} \right) \quad \text{for } 200^{\circ}\text{C} < T \leq 400^{\circ}\text{C} \quad (4.c)$$

$$C(T) = 1100 \quad \text{in } \left(\frac{\text{J}}{\text{Kg}} \cdot \text{K} \right) \quad \text{for } 400^{\circ}\text{C} < T \leq 1200^{\circ}\text{C} \quad (4.d)$$

Equations (5) show the change in specific heat for steel reinforcement with temperature as given by Eurocode [22], for temperature range between 20 °C to 1200 °C.

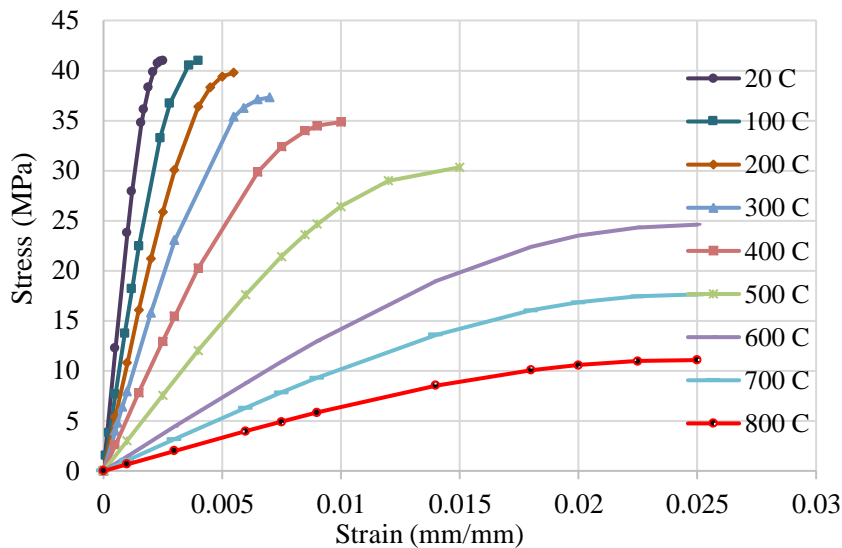
$$C(T) = 425 + 7.73 \times 10^{-1} T - 1.69 \times 10^{-3} T^2 + 2.22 \times 10^{-6} T^3 \quad \text{in } \left(\frac{\text{J}}{\text{Kg}} \cdot \text{K} \right) \quad \text{for } 20^{\circ}\text{C} \leq T \leq 600^{\circ}\text{C} \quad (5.a)$$

$$C(T) = 666 + \left(\frac{13002}{738 - T} \right) \quad \text{in } \left(\frac{\text{J}}{\text{Kg}} \cdot \text{K} \right) \quad \text{for } 600^{\circ}\text{C} < T \leq 735^{\circ}\text{C} \quad (5.b)$$

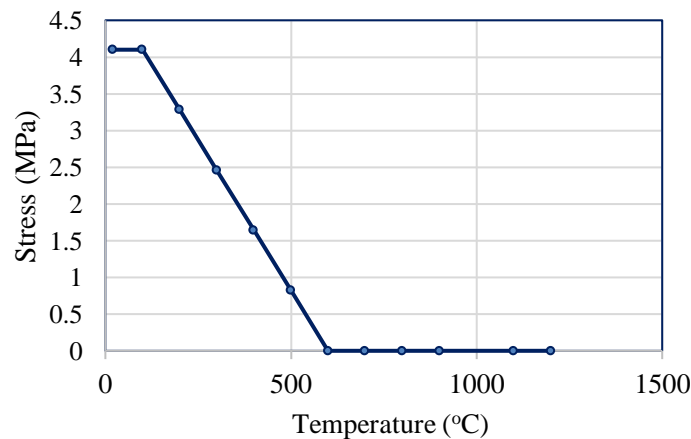
$$C(T) = 545 + \left(\frac{17820}{T - 731} \right) \quad \text{in } \left(\frac{\text{J}}{\text{Kg}} \cdot \text{K} \right) \quad \text{for } 735^{\circ}\text{C} \leq T < 900^{\circ}\text{C} \quad (5.c)$$

$$C(T) = 650 \quad \text{in } \left(\frac{\text{J}}{\text{Kg}} \cdot \text{K} \right) \quad \text{for } 900^{\circ}\text{C} \leq T \leq 1200^{\circ}\text{C} \quad (5.d)$$

The stress-strain curves for concrete in compression under elevated temperature adopted in the present study are shown in Figure 3 (a), and the variation of concrete tensile strength with temperature is shown in Figure 3 (b) [14, 21]. The variation of the mechanical and the thermal properties of FRP and the materials used for thermal insulation is addressed in researches and not quite established. In this study, the thermal and mechanical properties of CFRP and VG insulation and their variation with temperature are based on the findings of other researchers [23 - 25].



(a) Stress-strain curves in compression under elevated temperature



(b) Variation of concrete tensile strength with temperature

Fig. 3 - Concrete mechanical behaviour under elevated temperature

Nonlinear Analysis Parameters, Loading and Boundary Conditions

Concrete is modelled using the standard nonlinear constitutive concrete material model implemented within ANSYS [20]. Based on the formulation by Williams and Warnke [26], a multi-nonlinear compressive stress-strain curve is pointed. When a crack occurs, elastic modulus of the concrete element is set to zero in the direction parallel to the principal tensile stress direction. Crushing occurs when all principal stresses are compressive and are outside the failure surface; then the elastic modulus is set to zero in all directions and the element local stiffness becomes zero causing large displacement and divergence in the solution.

The analysis is carried out as two consecutive load cases. First, in the transient thermal analysis load case, standard temperature-time conditions described by ASTM E119 [15] and shown in Figure 4 are applied as nodal temperature-versus-time to the bottom surface of the T-beam. Equation 6 gives the ASTM E119 time temperature loading applied to the studied beam.

$$T = 20 + 750 \left(1 - e^{-0.49\sqrt{t}}\right) + 22\sqrt{t} \quad (6)$$

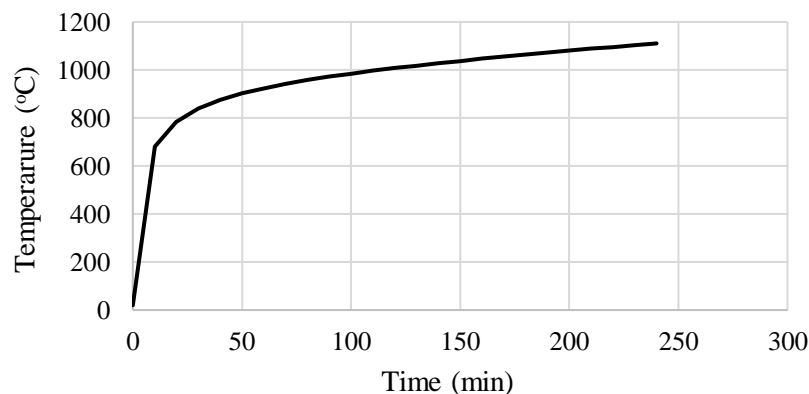


Fig. 4 - Applied temperature conforming to standard fire test curve of ASTM E119

The thermal gradient distribution in the T-beam obtained from the thermal analysis is next applied to the beam as nodal temperatures at several time load steps and sub-steps and structural stress analysis is performed. The experimentally applied sustained uniformly distributed load of 34 KN/m [14] is simulated by applying a pressure of 0.0278 MPa to the top surface of the T-beam flange.

NUMERICAL RESULTS AND DISCUSSION

In order to validate the accuracy of the model developed in this study, the obtained finite elements results are compared to the published experimental and numerical results. The thermal analyses results are evaluated by checking the temperatures at key locations with temperature gradients between the key locations of the beam model. The nodal temperature distribution within the T-beam cross section after one, three and four hours of fire exposure are shown in Figure 5.

The variation with time of the numerically calculated temperatures in VG, CFRP, and concrete at the same points that were measured in the experiment work [14] are plotted in Figure 6. It can be observed from Figure 6 that, there is a good agreement between the presented numerically predicted temperatures and the published experimental and numerical results [14, 19]. The average temperature of the steel reinforcement is less than 270 °C after four hours of fire exposure, which is below the ASTM E119 temperature limit of 593 °C.

Figure 7 shows the numerically predicted and the experimentally measured mid-span deflection at the centreline of the cross section throughout the fire exposure time. It is obvious that the mid-span deflection increases steadily during the fire exposure. The increase in deflection is associated with increase in the total strain on the beam tension side. This behaviour occurred as a result of rise of temperature of the CFRP and reinforcing steel on the tension side of the beam, thus reducing their stiffnesses, which caused further beam deflection. It is observed from Figure 7 that, the predicted mid-span deflection matches very closely the measured experimental one [14]. The deflection continues to increase nonlinearly in the numerical model under the sustained load.

The time until failure in both the finite element model and experiment is more than the fire endurance ratings required by North American standards in typical building applications. Furthermore, the accuracy of the adopted model herein is due to modelling the FRP system using shell elements rather than the solid elements used in the published model [19], in addition to proper description of the constituent materials properties and the refined meshing used in the present model.

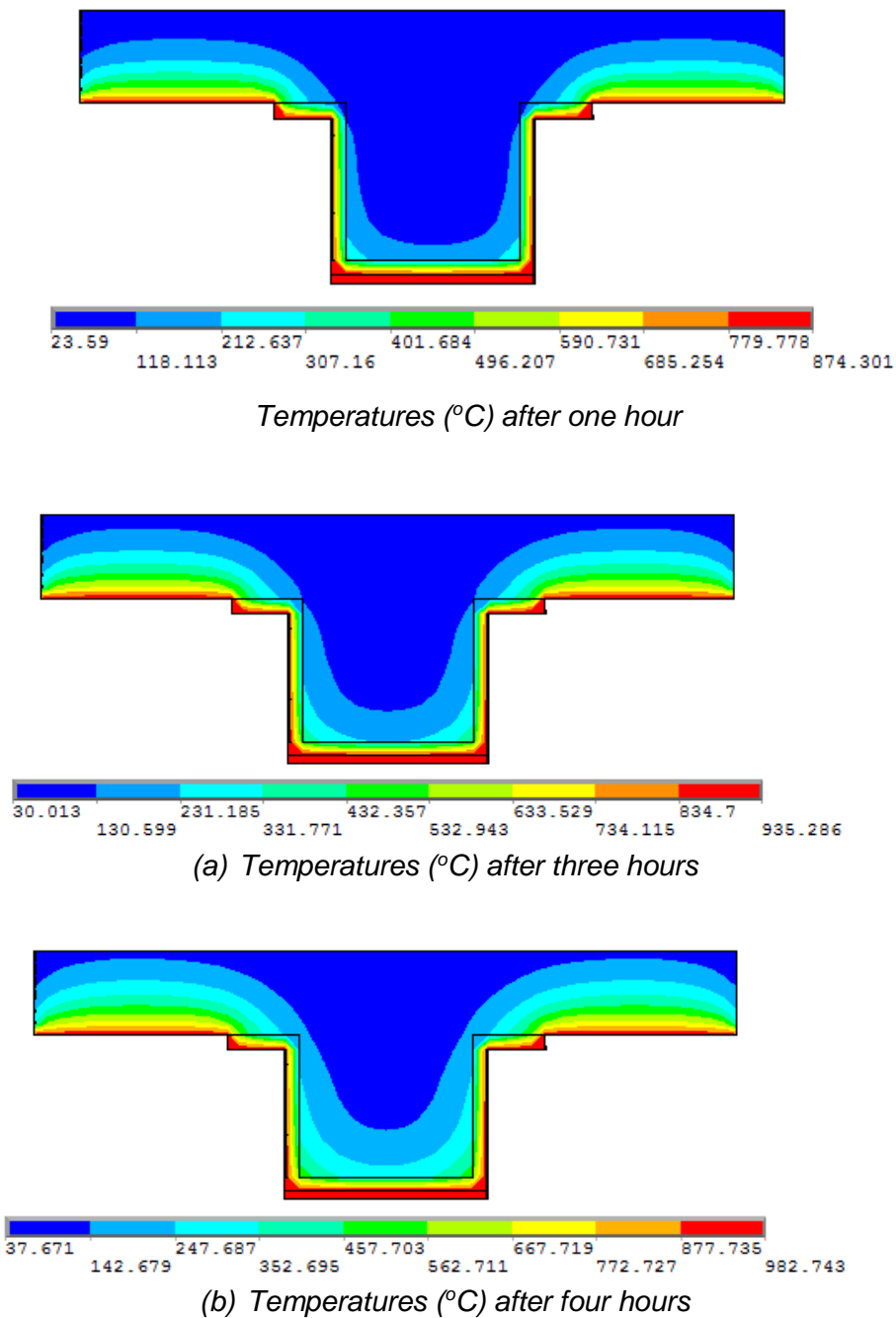


Fig. 5 - Numerically predicted temperature distribution in the beam cross-section

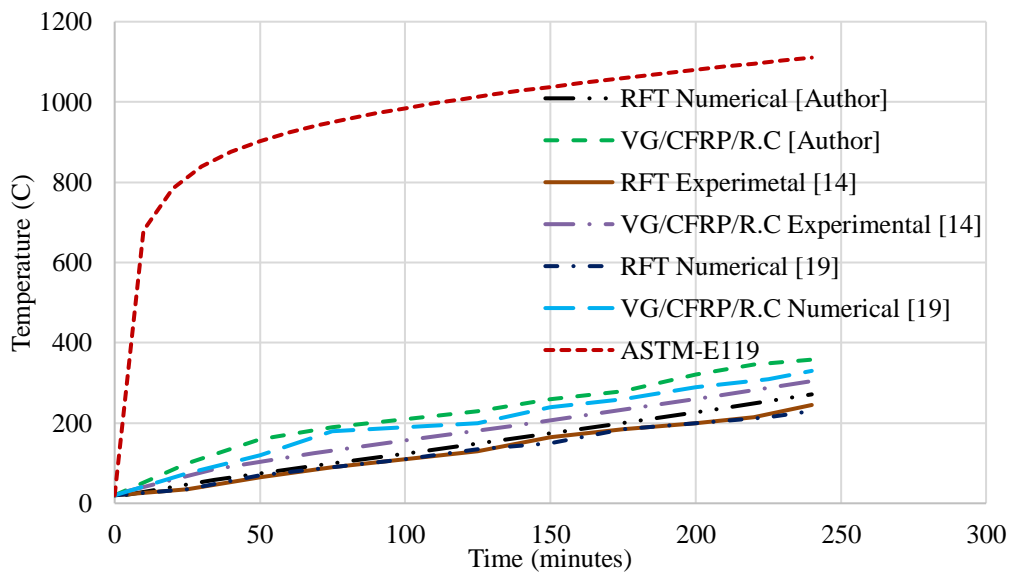


Fig. 6 - Numerical results of temperature versus time compared to experimental results

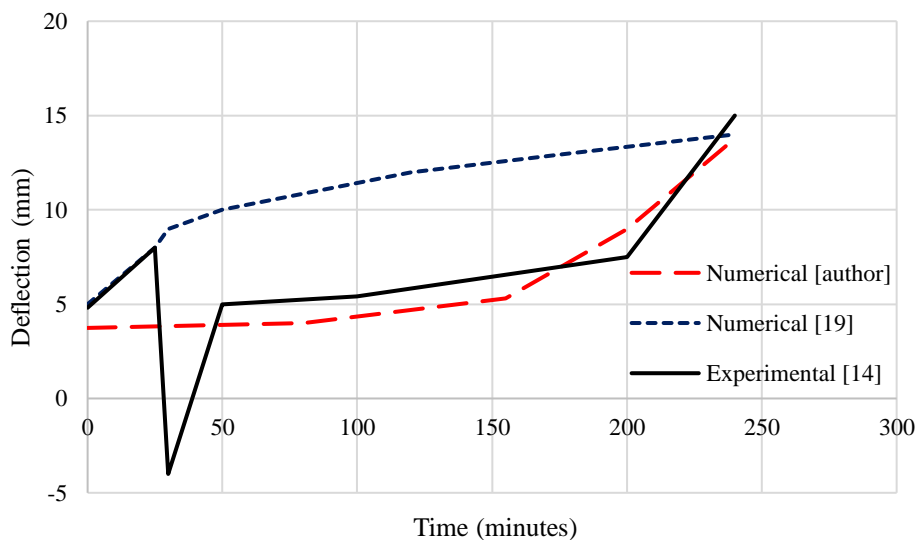
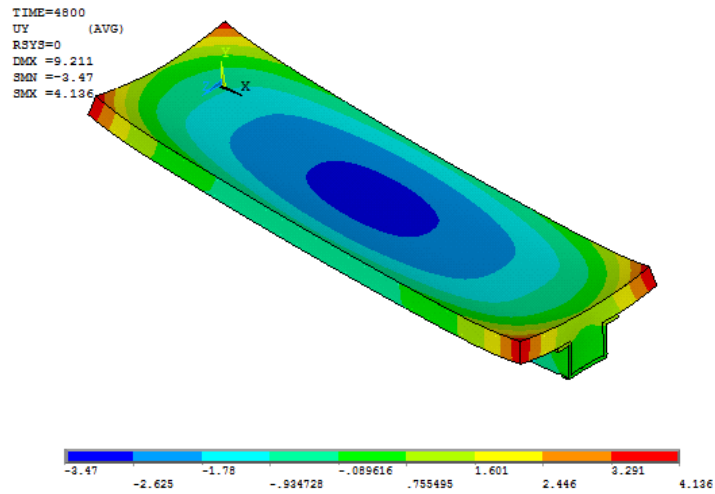
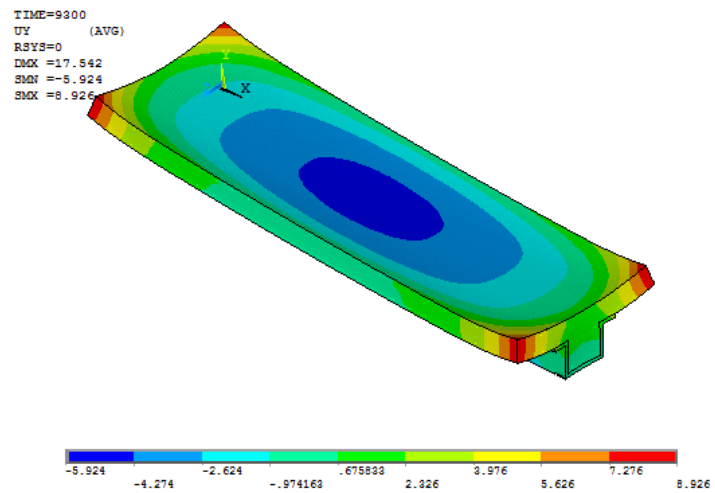


Fig. 7 - Variation of mid-span deflection with exposure time

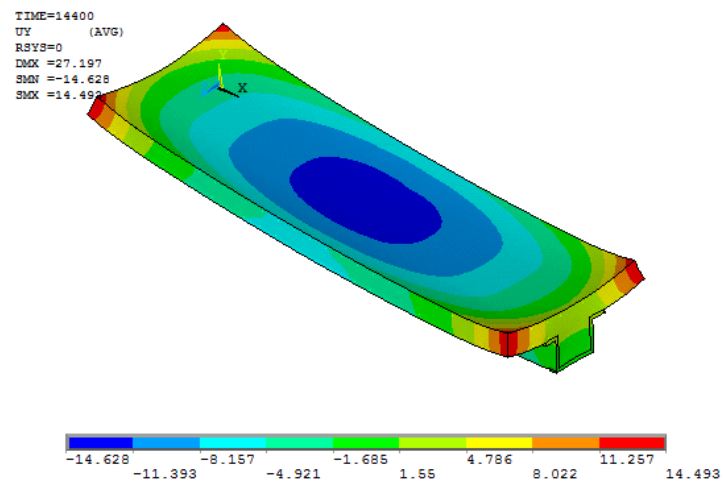
Figure 8 shows the numerically predicated vertical deflection of the studied beam under elevated temperature after one, three and four hours of exposure to standard fire temperature. The mid-span deflection increases with time due to heating the bottom surface of the beam resulting in additional tensile strains which increase the mid-span deflection of the studied beam. Also, Figure 9 shows the numerically predicted cracks in the studied beam cross-section after one, three and four hours of exposure to elevated temperature. The number and width of cracks increases with exposure time due to the increase in the total strain in concrete resulting from both structural and thermal loading conditions Figure 10 shows the 3-D developed crack patterns after four hours. Again, the comparison of crack patterns held between the model results with the experimental work results presented in this paper, shows a good correlation achievement between the numerical and experimental results.



(a) Deflection (mm) after one hour

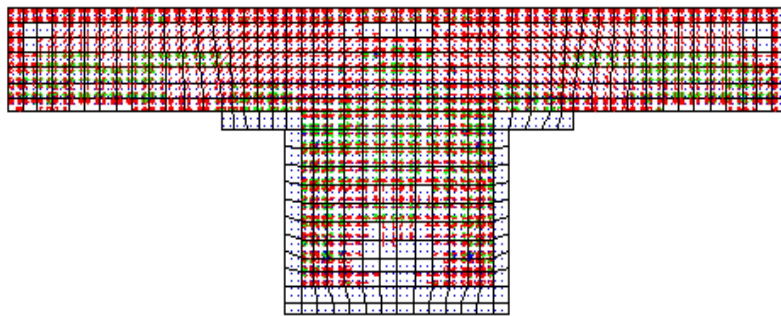


(b) Deflection (mm) after three hours

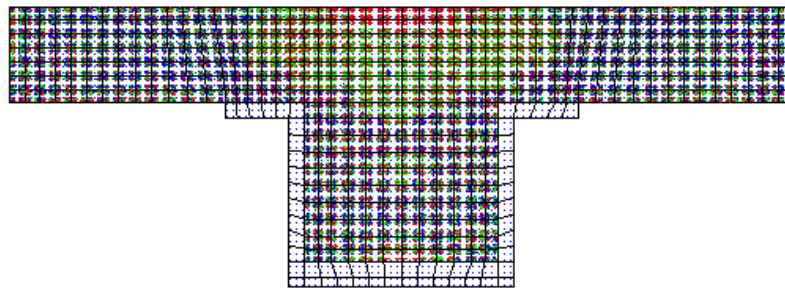


(c) Deflection (mm) after four hours

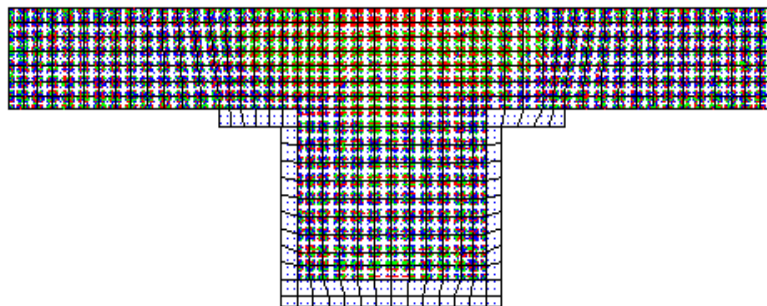
Fig. 8 - Numerically evaluated deflections after exposure to elevated temperature



(a) Cracking after one hour



(b) Cracking after three hours



(c) Cracking after four hours

Fig. 9 - Numerical results of the cracks in the beam cross-section

CRACKS AND CRUSHING
 STEP=1
 SUB =4
 TIME=14400

ANSYS
 OCT 18 2016
 22:21:29

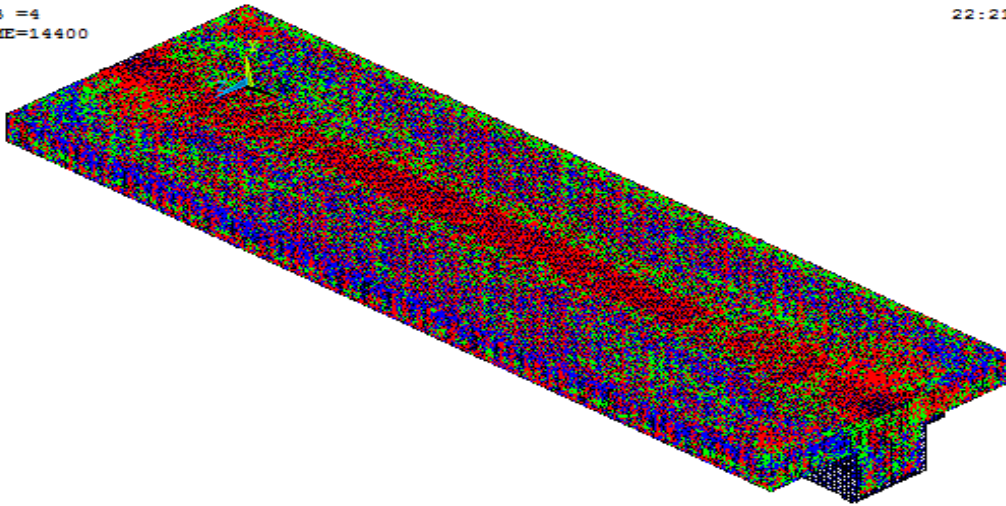


Fig. 10 - Numerical cracking pattern after four hours

CONCLUSION

The paper presents numerical modelling procedure by finite elements that accurately simulate the behaviour of thermally insulated RC beam strengthened in flexure with externally bonded FRP when exposed to standard fire test. Numerical modelling and nonlinear analysis are performed using ANSYS 12.1 [20]. The proposed procedure is verified by comparing the numerical results with experimental results in the published literature. Based on the obtained numerical results, the following conclusions can be drawn:

1. The numerical results of the adopted approach are in good agreement with the published experimental results regarding mid-span deflection and temperature distribution within the cross-section throughout the elevated temperature time history.
2. The proposed model gives more accurate representation for mid-span deflection compared with published numerical results due to using shell elements for FRP, proper representation of the constituent materials used and the refined meshing used in the present model.
3. The presented model managed to predict accurately the full fields of temperatures and deflection in CFRP-strengthened insulated T-beams exposed to underside fire scenario.
4. Numerical results indicate that the mid-span deflection increases nonlinearly throughout the fire exposure time. This is due to the increase in the total strain on the tension side of the beams and due to concrete cracking.
5. The developed finite element model provides reliable coupled thermal-structural results and provides useful information on the fire resistance of insulated strengthened structural member.
6. The developed numerical procedure thereby provides an economic tool to check and design fire protection layers for FRP-strengthened RC beams.

REFERENCES

- [1] Bakis, C.E., Bank, L.C., Brown, V.L, Cosenza, Davalos, J.F., Lesko, J.J, Machida, A., Rizkalla, S.H., and Triantafillou, T.C., "Fiber-reinforced polymer composites for construction—state-of-the-art review", *Proceedings of Journal of Composites for Construction*, 6 (2002) 73 – 87.

- [2] Yu, B., and Kodur, V.K.R., "Effect of temperature on strength and stiffness properties of near-surface mounted FRP reinforcement", *Composites Part B: Eng.* 58 (2014) 510-517.
- [3] Firmo, J.P., Pitta, D., Correia, J.R., Tiago, C., and Arruda, M.R.T., "Experimental characterization of the bond between externally bonded reinforcement (EBR) CFRP strips and concrete at elevated temperatures", *Cement Concrete Composites*, 60 (2015) 44-54.
- [4] American Concrete Institute (ACI). ACI 440.2R-08: "Guide for the design and construction of externally bonded FRP systems for strengthening concrete structures", ACI Committee 440, Farmington Hills, MI, USA, 2008.
- [5] ECP Committee 208, ECP 208-05: "Egyptian code of practice for the use of fiber reinforced polymer in the construction field", ECP Committee 208, Ministry of Housing and Urban Communities, Egypt, 2005.
- [6] Blontrock, H., Taerwe, L., and Vandeveld, P. "Fire tests on concrete beams strengthened with fiber composite laminate", Third Ph.D. Symposium, Vienna, Austria, (2000), 10 pp.
- [7] Williams, B., Kodur, V.K.R., Green, M.F., and Bisby, L.A., "Fire endurance of fiber-reinforced polymer strengthened concrete T-beams", *ACI Structural Journal*, 105(1) (2008) 60-67.
- [8] Klamer, E.L., Hordijk, D.A. and Hermes, M.C.J., "The influence of temperature on RC beams strengthened with externally bonded CFRP reinforcement", *Heron*, 53(3) (2008)157–185.
- [9] Zhu, H., Wu, G., Zhang, L., Zhang, J., and Hui, D., "Experimental study on the fire resistance of RC beams strengthened with near-surface-mounted high-Tg BFRP bars", *Composites Part B: Eng.*, 60 (2014) 680-687.
- [10] Firmo, J.P., and Correia, J.R., "Fire behaviour of thermally insulated RC beams strengthened with EBR-CFRP strips: experimental study", *Composite Structures*, 122 (2015) 144-154.
- [11] Salama, A.E., Ghanem, G.M. Abd-Elnaby, S.F., El-Hefnawy, A.A., and Abd-Elghaffar, M., "Behavior of thermally protected RC beams strengthened with CFRP under dual effect of elevated temperature and loading", *HBRC Journal*, 8(1) (2012) 26–35.
- [12] Kamal, O.A., Hamdy, G.A., and Abou-Atteya, M.A., "Efficiency of coating layers used for thermal protection of FRP strengthened beams", *HBRC Journal*, 10 (2014) 183–190.
- [13] Eurocode 2. EN 1992-1-2: Design of concrete structures. Part 1-2: General rules-Structural fire design, European Committee for Standardization, Brussels, Belgium, 2004.
- [14] Williams, B., Kodur, V.K.R., Green, M.F., and Bisby, L., "Fire endurance of fiber-reinforced polymer strengthened concrete T-beams, *J. ACI Struct*; 105(1) (2008) 60–67.
- [15] American Society for Testing and Materials (ASTM). ASTM E119: Standard Test Methods for Fire Tests of Building Construction and Materials, West Conshohocken, PA, USA, 2007.
- [16] Gao, W.Y., Dai, J.G., Teng, J.G., and Chen, G.M., "Finite element modeling of reinforced concrete beams exposed to fire", *Engineering Structures*, 52 (2013) 488-501.
- [17] Dai, J., Gao, W., and Teng, J., "Finite element modeling of insulated FRP-strengthened RC beams exposed to fire", *Journal of Composites in Construction*, 19(2) (2015)1-15.
- [18] Arruda, M.R.T., Firmo, J.P., Correia, J.R., and Tiago, C., "Numerical modelling of the bond between concrete and CFRP laminates at elevated temperatures", *Engineering Structures*, 110 (2016) 233–243.
- [19] Hawileh, R., A., Naser, M., Zaidan, W., and Rasheed, H. A., "Modeling of insulated CFRP strengthened reinforced concrete T-beam exposed to fire", *Eng. Struct.*, 31 (12) (2009), pp. 3072–3079.
- [20] ANSYS. Finite Element Computer Code. Version 12.1.0. ANSYS Inc., Canonsburg, PA, 2009.
- [21] Harmathy, T.Z., "Fire Safety Design and Concrete, Concrete Design and Construction Series", Longman, UK, 1993.

- [22] Eurocode 3. EN 1993-1-2: Design of steel structures. Part 1-2: General rules- Structural fire design, European Committee for Standardization, Brussels, Belgium, 2005.
- [23] Griffis, C. A., Masmura, R.A., and Chang, C.I., "Thermal response of graphite-epoxy composite subjected to rapid heating", *Journal of Composite Materials.*, Vol. 15 (1981), pp. 427-442.
- [24] Cramer, S.M., Friday, O.M., White, R.H., and Sriprutkiat, G., "Mechanical properties of gypsum board at elevated temperatures", *Fire and Materials* (2003) 33–42.
- [25] Park, S. H., Manzello, S., L., Bentz, D., P., and Mizukami, T., "Determining thermal properties of gypsum board at elevated temperatures", *Fire and Materials*, (2009), pp. 237-250.
- [26] Willam, K.J. and Warnke, E.D., "Constitutive model for the triaxial behavior of concrete", *Proceedings of international association for bridge and structural engineering*", ISMES. 1975. Bergamo, Italy, 1975, pp. 1–30.

INFLUENCE OF VIBRATION ON PERFORMANCE OF RECYCLED CONCRETE

*Ergang Xiong^{*1}, Tian Li¹, Sheliang Wang², Yujiang Fan³*

1. *School of Civil Engineering, Chang'an University, Xi'an 710061, China; xerg@chd.edu.cn*
2. *School of Civil Engineering, Xi'an University of Architecture & Technology, Xi'an 710055, China*
3. *School of Architecture, Chang'an University, Xi'an 710061, China*

ABSTRACT

In this study, the vibration mixing technology is researched, and the effect of the vibration on the performance of recycled concrete is investigated. Through the analysis of the strengthened mechanism on the recycled concrete adopting vibration mixing, the vibration could increase of collision numbers between aggregates so as to purify the surface of recycled aggregates, and improve the interface between the recycled aggregates and cement pastes, and realize the macroscopic and microscopic uniformity of recycled concrete to improve the performance of recycled concrete. The performance of recycled concrete mixed by ordinary forced mixing and vibration mixing respectively, was compared experimentally. And the results indicate that the vibration could increase the air contents of recycled concrete, improve the mechanical performance of the recycled concrete, provide a favorable environment in order to enhance the microscopic structure and strengthen the recycled concrete.

KEYWORDS

Forced mixing, Vibratory, Concrete performance, Recycled concrete

INTRODUCTION

The utilization of recycled concrete is one of the idealized ways to recycle the waste cement concrete. After the waste concrete is subjected to crushing, cleaning, and sieving, the substitute of the resulting recycled aggregates for new sandstone aggregates can realize the concrete preparation and thus realize recycling of such primary materials as sand, stone, etc. Since the recycled aggregate and natural aggregate possess different structures and properties, primarily the residual mortar is attached to the surface of recycled aggregates, and micro-cracks are present in the surface [1]; compared to the ordinary concrete, all these defects will lead to a lower apparent density, a higher porosity, a worse mobility, which results in the inferior mechanical behaviour of recycled concrete and inferior durability including chloride ion permeability, impermeability and freeze-thaw resistance [2].

So far domestic and international researchers launched a lot of investigations on improving the performance of recycled concrete, which were primarily focused on the improvement of material property and material preparation. Aiming at the characteristics of recycled aggregates, some researchers performed plastic processing on the recycled aggregate particles and immersed the aggregates into acid liquor to remove the attached mortar; then they immersed the aggregates into the sodium silicate solution and cement pastes to fill the pores and micro-cracks so as to improve the behaviour of recycled concrete [3]. Some researchers added some additives and mineral during the recycled concrete preparation in order to improve the behaviour; the additives were water reducing agent, which could compensate the quantity of free water absorbed by the residual mortar attached to the recycled aggregate so as to reduce the effect of free water on the behaviour of concrete [4]. The mineral additives are commonly fly ash and silica fume. Researchers found that the beads in the fly ash could fill pores and micro-cracks, and replace the water in the pores and micro-cracks to improve the strength and mobility of recycled concrete; the unique fineness and activity of silica fume could react with Ca(OH)_2 during the early hydration of cement to produce C-S-H gel filling the pore micro-cracks, which could then increase the strength of recycled concrete [5]. Several scholars suggested that according to the characteristics of recycled aggregate, the adjustment of the mix proportion could improve the behaviour recycled concrete [6]. The researches on preparation technologies were centred around the adjustment of the aggregates feeding order, mixing time, mixing velocity, and their combination of various technology parameters in order to improve the properties of recycled concrete. The most common preparation technology is the remixing technology of recycled concrete [7]. The different aggregate feeding orders and phased mixing could realize the full uniform mixture of each constituent; the hydrate covered the aggregates like a protection layer, which could effectively avoid the further contact between water and aggregate, and restrain the thickness of water film; the transitional layer with a low water cement ratio could allow the improvement of strength and behaviour of recycled concrete.

Aiming at the restraints of the recycled aggregate defects on the performance of recycled concrete, in this study, the feasibility to improve the behaviours of recycled concrete by the use of vibration mixing is investigated. The vibration mixing technology to prepare ordinary concrete is an efficient strengthened preparation method. The effect of this technology on the behaviours of recycled concrete is scarcely researched. In combination with the feature of recycled aggregates, the vibration mechanism on recycled concrete is researched; the comparative experiments are performed on the recycled concrete mixed by vibration and on ordinary concrete mixed by forced mixing; from the differences of macro-behaviours and microstructures of recycled concrete, the influence of vibration mixing on behaviours of recycled concrete are analysed.

STRENGTHENED MECHANISM TO IMPROVE THE BEHAVIOURS OF RECYCLED CONCRETE WITH VIBRATION MIXING

After the waste concrete subjected to crushing and sieving, the surfaces of recycled aggregates are present of residual mortar, and the mortar is unevenly distributed along the surface of aggregates. Pores and micro-cracks unavoidably exist in crushed recycled aggregates, as shown in Figure 1.

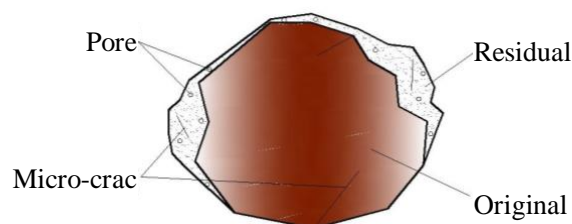


Fig.1 - Schematic diagram of recycled aggregate structure

During the preparation of recycled concrete, recycled aggregates, new aggregates, cement and water are proportionally placed into the vibration mixer, as shown in Figure 2. Under the action of mixing blades, in the 3-D mixing space comprising the axial and radial directions, a strong axial cyclic movement and a counter current movement between shafts will accrue to each constituent in the mixing pan. Each constituent can attain a macroscopic uniform mixing in a short time [8]. At the time of conventional mixing, the mixing shaft and blades exert vibration of a certain frequency to aggregates to force the aggregates in chattering states; the aggregates move in a large cycle and vibrate within a small range; the movements result in the increase of collision numbers between aggregates and contribute to purify the surface of recycled aggregates; during the early mixing, the vibration can immediately break the structures of cement agglomeration and water cluster to form smaller cement particles and water cluster particles, followed by the activation for the activity of cement particles and water, thus accelerating formation of the hydrate. During the later mixing, the vibration pressure wave due to the vibration accelerates the diffusion velocity of liquid-phase hydrate towards the surface of aggregates; meanwhile, the vibration breaks the bond between particles caused by microtubule pressures, and the cement pastes quickly cover the surface of aggregates, subsequently filling the micro-cracks of aggregates, improving the interface between the recycled aggregates and cement pastes and realizing the macroscopic and microscopic uniformity of recycled concrete so as to comprehensively enhance the behaviours of recycled concrete.

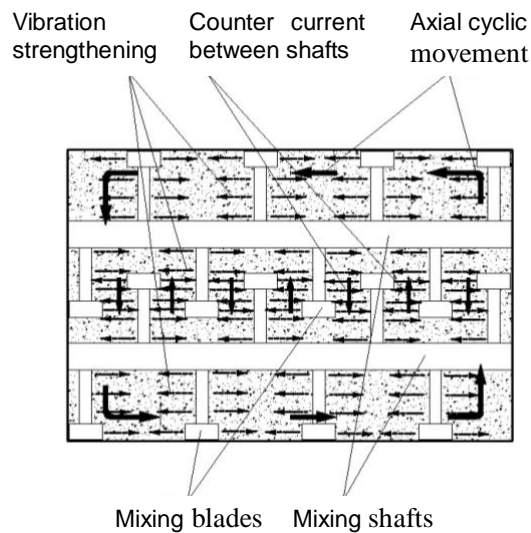


Fig. 2 - Strengthening mechanism of vibratory mixing of recycled concrete

EXPERIMENTAL PRIMARY MATERIALS AND MIX PROPORTION OF RECYCLED CONCRETE

The experimental cement is P.O32.5R Portland cement. The fine aggregate is common medium sand, whose apparent density is 2620kg/m³, and fineness modulus 2.89. The new coarse aggregate is continuously graded limestone with particle sizes of 5-25mm. The recycled aggregates come from waste C20, C30, C40 concrete; the recycled aggregates with particle sizes of 5-25mm are obtained by crushing and sieving the waste concrete as shown in Figure 3. The behaviours of recycled aggregates and new aggregates are given in Table 1. The mixing water is common tap water. No additives are used.



Fig.3 - Recycled aggregates

Tab. 1 - Behaviours comparison between recycled aggregates and new aggregates

Aggregate type	Apparent density/ (kg/m ³)	Packing density/ (kg/m ³)	Porosity/ %	Crushing index/ %	Water absorption/ %
Recycled aggregate	2470.6	1354.6	45.2	17.0	7.1
New aggregate	2800.1	1611.7	42.4	6.1	2.4

The design strength of recycled concrete for tests is C30. Based on the frequently used aggregate contents, the percentages of recycled aggregates are selected as 0%, 25%, 50%, and the design slump is 10-30mm. The new mix proportion is obtained by adopting the actual water gel ratio of recycled concrete, as shown in Table 2.

Tab. 2 - Mix proportion of recycled concrete

Concrete strength	Amount of each constituent/(kg/m ³)					Percentage of recycled aggregates/ %
	Cement	Water	Fine aggregate	New aggregate	Recycled aggregate	
C30	391	180	657	1172	0	0
C30	388	198	651	872	291	25
C30	385	212	647	578	578	50

EXPERIMENTAL SETUP AND EXPERIMENTAL METHODS

Experimental setup

The double horizontal shaft vibration mixer was designed and manufactured by our research team. The mixer utilizes the independent mixing actuation and vibration actuation shown in Figure 4. The mixing actuating device can only drive the mixing shaft and blades to realize common mixing of the concrete; the vibration actuating device can force the mixing shaft and blades to vibrate; the simultaneous utilization of the mixing actuating and vibration actuating devices can realize a vibration mixing. The main parameters of the mixer are shown in Table 3.



Fig. 4 - Test mixer of vibratory mixing

Tab. 3: Main parameters of the mixer

Volume/L	Number of mixing blades (single mixing shaft)	Design amplitude/mm	Vibration angular frequency/(rad/s)	Rotational speed of mixing blades/(r/min)	Linear speed/(m/s)
100	2+5(Return blade+propulsion blade)	1.2	185	50	1.47

Experimental methods

At the same testing conditions, the behaviours of recycled concrete with varying percentage of recycled aggregates are measured respectively by the use of ordinary forced mixing and vibration mixing. When tests prepared, the aggregate feeding order is recycled aggregate, new aggregate, cement, fine aggregate and water; the mixing time is 60s; the behaviour of the newly mixed concrete is obtained; after being cured in the same conditions, the mechanical behaviour of the concrete and micro-structures are also obtained. In accordance with *standard for test method of performance on ordinary fresh concrete* (GB/T 50080-2011), the apparent density, mobility, cohesiveness, water retention and air content are measured for fresh concrete to study the influence of vibration on the behaviours of fresh concrete. On the basis of *standard for test method of mechanical properties on ordinary concrete* (GB/T 50081-2011), the compressive strengths of 7d, 14d and 28d of recycled concrete test blocks, are measured to study the effect of vibration on the behaviours of recycled concrete. After the blocks are cut, scoured, polished, and dried, the processed blocks are then scanned by JSM-6390A, and the SEM diagrams of 500 and 6000 times are obtained to investigate the effect of vibration on the micro-structures of recycled concrete.

EXPERIMENTAL RESULTS

Influence of vibration on the behaviours of fresh recycled concrete

For different percentages of recycled aggregates, through ordinary forced mixing and vibration mixing, the average apparent densities of fresh concrete are shown in Figure 5, the average slumps shown in Figure 6, and air contents shown in Figure 7. From Figure 5, the apparent densities of recycled concrete mixed by the above mixing methods tend to a little decrease with the varying recycled aggregate contents. The apparent density of recycled concrete mixed by forced mixing drops by 3.75% for 0 aggregates and 50% aggregates, and the apparent density mixed by vibration mixing drops by 2.92%; for the same percentage of recycled aggregates, the apparent density mixed by vibration mixing is higher than that by forced mixing; when the percentage of recycled aggregates is 50%, the apparent density is 1.07% higher than that mixed by forced mixing, which indicates that the vibration mixing will bring about an obvious purification of aggregates surface; the vibration can reduce the internal frictions between aggregate particles; the cement pastes can fill the pores, micro-cracks in recycled aggregates and restrain the decrease of the

apparent density for recycled concrete. From Figure 6, the recycled aggregates significantly influence the slump of recycled concrete. By the use of ordinary forced mixing, the slump loss is very fast with the increase of recycled aggregate contents, and the slump loss is 90% when the percentage of recycled aggregates is 50%; the vibration mixing can evidently improve the slump loss of recycled concrete, although the slump of newly mixed recycled concrete is 30% lower than that of ordinary concrete; however the slump of recycled concrete mixed by vibration mixing is the same as that of ordinary concrete mixed by forced mixing; the slump has no visible change when the percentage is 50%; this is because the vibration mixing destroys the structures of cement agglomeration and water cluster thus to form smaller cement particle and water cluster particle and increase the activity the cement particles and water, then leading to a sufficient hydration; the vibration mixing purifies the recycled aggregates surface, peels off some residual mortar, reduces the water absorbing capacities of recycled aggregates, increases the free water, reduces the slump loss of recycled concrete and improves the mobility. From Figure 7, compared to the recycled concrete mixed by ordinary forced mixing, the air contents of recycled concrete mixed by vibration mixing is obviously increased; for different percentages of recycled aggregates, the air contents are respectively increased by 66.7%, 18.2% and 42.9%; the mixing of blades can wrap the big bubble into the aggregates, the vibration can decompose the big bubble into small bubble kept in the recycled concrete, further improving the air contents of recycled concrete, which can easily satisfy the engineering requirements for air contents. The increase of air contents in recycle concrete is a commonly adopted method to improve the durability of concrete [9]. Therefore, the vibration mixing can increase the air contents of fresh recycled concrete and can contribute to the improvement of concrete durability.

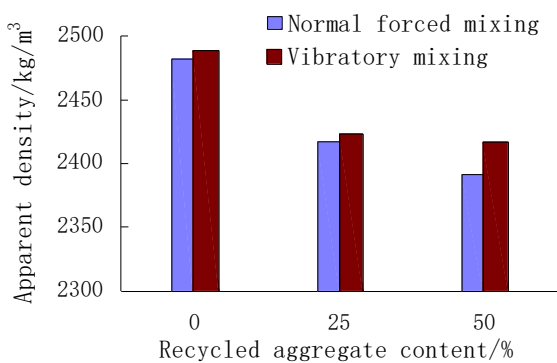


Fig. 5 - Apparent density of with different mixing methods

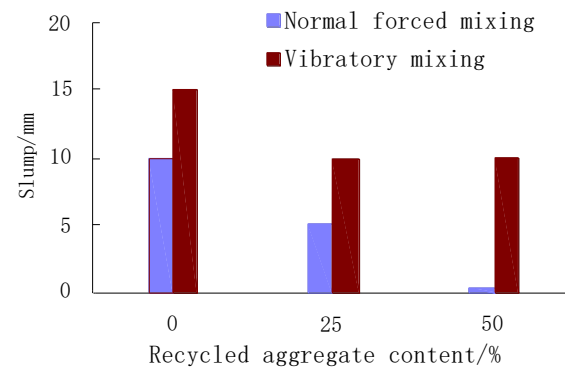


Fig. 6 - Slump with different mixing methods

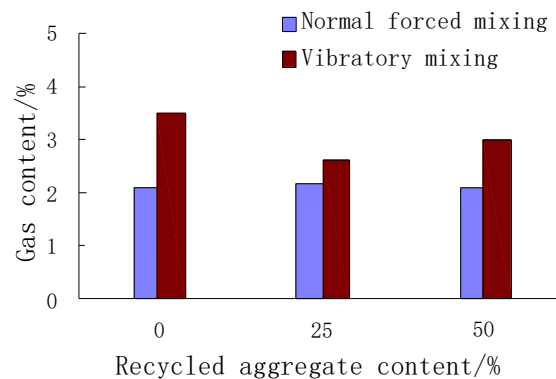


Fig. 7 - Air content with different mixing methods

Influence of vibration on the compressive strength of recycled concrete

For different percentages of recycled aggregates, the compressive strengths of 7d, 14d and 28d for hardened concrete with different mixing methods are shown in Table 4. From Table 4, in contrast to ordinary concrete without recycled aggregates, whether the recycled concrete is mixed by ordinary forced mixing or vibration mixing, the compressive strengths of recycled concrete blocks equally tend to fall; the compressive strength decreases with increasing the percentage of recycled aggregates. For 50% recycled aggregate content, the compressive strength of 28d for recycled concrete mixed by ordinary forced mixing is reduced by 23.4% and the compressive strength by vibration mixing is reduced by 24.2%. The compressive strength depends on the strength of aggregates, the strength of cement stone, and the bond strength of interface between them. Since the aggregate and cement stone have a higher strength, undoubtedly the failures frequently occur at the interface, which is the weakest location [10,11]. For recycled concrete, the interfaces of recycled concrete not only include the interfaces between the old aggregates and old cement paste, but also include the new interface between the new cement paste and old cement paste. With the increase of recycled concrete contents, the weak interfaces are more and more, and thus the recycled concrete is more susceptible to fail, which just illustrates the lower compressive strength of recycled concrete. For the same percentage of recycled aggregates, the compressive strength mixed by vibration mixing is higher than that by forced mixing. At 25% recycled aggregate content, the compressive strength of recycled concrete mixed by vibration mixing is 17.5% higher than that by ordinary forced mixing. At 50% recycled aggregate content, the compressive strength of recycled concrete mixed by vibration mixing is 12.1% higher than that by ordinary forced mixing. The vibration mixing can exert forced mixing and vibration energy to aggregates, the movement velocity of aggregate particles will increase and attain a macroscopic uniformity; in the meanwhile, the aggregates will be in a chattering state so that the collision of aggregate particles will purify the recycled aggregates surface, and spall some residual cement pastes; the vibration energy will destroy the cohesive structures of cement, the area of hydration will increase, the hydration products will increase, the movement velocity of hydration products attached to recycled aggregates surface will accelerate, and fill the pores and micro-cracks, to repair the recycled concrete, the bond strength and the compressive strength will be enhanced.

Tab. 4 - Compressive strength with different mixing methods

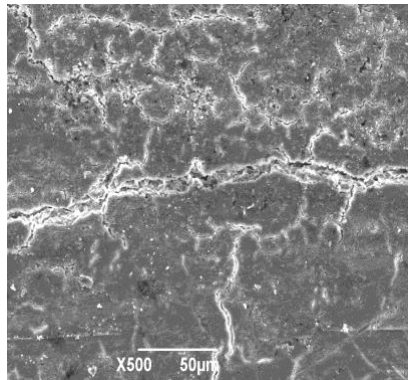
Percentage of recycled aggregate content/%	Ordinary forced mixing			Vibration mixing		
	7d Compressive strength/MPa	14d Compressive strength /MPa	28d Compressive strength /MPa	7d Compressive strength /MPa	14d Compressive strength /MPa	28d Compressive strength /MPa
0	20.77	23.34	28.56	21.85	26.76	32.36
25	18.65	20.35	22.23	19.25	23.98	26.94
50	17.10	19.89	21.88	17.86	21.79	24.53

Influence of vibration on the microstructures of recycled concrete

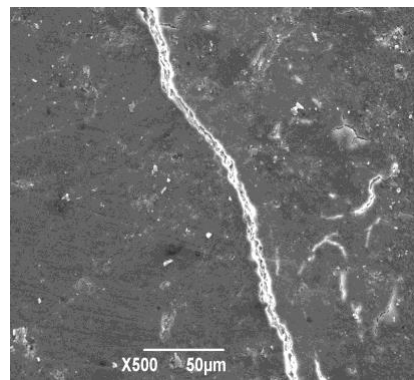
Through different mixing method, the recycled concrete with different recycled aggregate contents is cured for 28d. The SEM specimens of 8 mm×8 mm×5 mm are prepared by cutting apparatus; the specimens are subjected to scouring, polishing, and drying, and the specimens are sprayed with metal to ensure the conductivity. The SEM diagrams of 500 times and 6000 times for specimens are obtained as shown in Figure 8 and Figure 9.

The inherent pore cracks of recycled aggregates and the water absorbability of the residual mortar will give rise to difficult realization of microscopic uniformity of recycled concrete with the water cement ratio used in ordinary forced mixing. From Figure 8(a), in the identical curing conditions the microscopic hydration of recycled concrete specimens is not uniform by ordinary forced mixing method; the pores and cracks of concrete are densely distributed, composing series of big, medium and small cracks which are connected each other like a net, which will affect the strength of recycled concrete. It is indicated that the uniformity of microscopic water cement ratio is bad; under the action of ordinary forced mixing, the cement paste is present of cement agglomeration and water cluster; the water absorbing capacity of recycled concrete is a bit higher, and the water is transferred from cement pastes to recycled aggregates, which further leads to that the hydration reaction around recycled aggregates has a larger water cement ratio, and the region far from recycled aggregates has a smaller water cement ratio; thus the hydration velocities at each region is not uniform when the strength of concrete is initiated, and the inconsistent velocities will induce dense cracks. From Figure 8(b), the phenomenon of densely distributed pore cracks does not occur in the recycled concrete mixed by vibration mixing; the hydration of concrete surface is uniform and compact, which indicates that the vibration can break cement agglomeration and water cluster; the hydration of cement paste is sufficient and the microscopic water cement ratio is of recycled concrete is uniform; during the curing process, the consistent hydration velocity can thus improve the strength of recycled concrete, which can avoid the phenomenon of dense cracks. From Figure 9, the microscopic interface of recycled concrete mixed by vibration mixing is more tight than that by ordinary forced mixing; the granular and cluster C-S-H gels contributing to bond strength are more, the flake and plank crystals with smaller contribution are less, which indicates that the destruction of cement agglomeration and water cluster provides a favourable environment for the

formation of the C-S-H gels, it is favourable for needle-like, stick-like ettringite, and the granular and cluster C-S-H gels to generate, which can improve the microscopic structures and strength of recycled concrete.

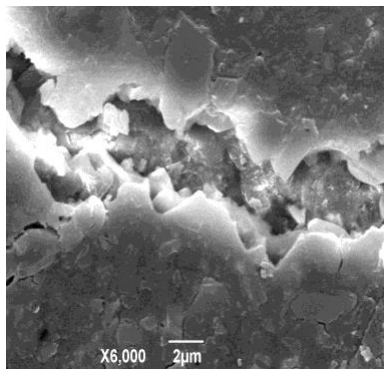


(a) Ordinary forced mixing

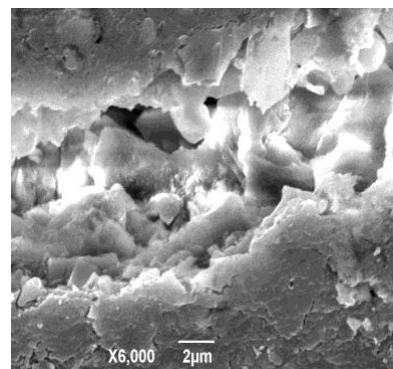


(b) Vibration mixing

Fig. 8 - 500 times SEM diagrams of recycled concrete aggregates



(a) Ordinary forced mixing



(b) Vibration mixing

Fig. 9 - 6000 times SEM diagrams of recycled concrete aggregates

CONCLUSIONS

(1) The influence of vibration mixing on the behaviours of fresh recycled concrete is of great significance; the apparent densities of newly mixed recycled concrete tends to decrease with increasing the recycled aggregate contents; for the same percentage of recycled aggregates, the vibration mixing can improve the reduction phenomenon of apparent density; the vibration mixing can considerably reduce the slump loss of recycled concrete, and improve the mobility of recycled concrete; the vibration mixing can remarkably increase the air contents of recycled concrete and thus improve the durability of recycled concrete.

(2) Whether mixed by ordinary forced mixing or by vibration mixing, with the increase of the recycled aggregate contents, the compressive strengths tend to descend; for the same percentage of recycled aggregates, the compressive strength of recycled concrete mixed by vibration mixing is higher than that by ordinary forced mixing, which indicates that the vibration mixing can improve the mechanical behaviour of recycled concrete.

(3) By the utilization of ordinary forced mixing, the microscopic hydration reaction of recycled concrete specimens is not uniform, and the pore cracks are densely distributed; however, by the utilization of vibration mixing, the hydration of specimens surface is uniform without densely distributed pore cracks, and the structure of the microscopic interface is tight, followed by the formation of needle-like, stick-like ettringite, and the granular and cluster C-S-H gels, which shows that the hydration reaction by vibration mixing is more uniform and provide a favourable condition for C-S-H gels to form and can furthermore improve the microscopic structure and strength of recycled concrete.

ACKNOWLEDGEMENTS

The author would like to acknowledge the financial support from the National Natural Science Foundation of China (Nos. 51678480, 51108035, 51208058, 51178388), the Natural Science Basic Research Plan in Shaanxi Province of China (2017JQ5061, No. 2016JM5007, No. 2013JM7030), the Special Fund for Basic Scientific Research of Central College (No. 310828162017, No. 310828161009, No. 310841171001), and Shaanxi Provincial Postdoctoral Science Foundation funded project (No. SX2014120057).

REFERENCES

- [1] K. Hou. Recycled concrete economic and social benefit analysis. *Sci. Tribune-electron (middle)*, (1): 160-160 (2014).
- [2] J.C. Wang. The application prospect of recycled aggregates and compressive benefit analysis Southwest university of science and technology, 2012.
- [3] Z.W. Wang. Industrialization chain and economy analysis of recycling waste concrete. *Concrete*, (4), 103-106, 2007.
- [4] T. Li. Recycled aggregate defects of recycled concrete research on the effect of mechanical properties, Beijing Jiaotong University, 2013.
- [5] M.Q. Qin. The old and new concrete interface bonding state research. Wuhan university of technology, 2006.
- [6] F. Flora, J. Cristian, B. Marilda, A. Diego, V. Enrick, and P. Carlo, Rheology of fresh concretes with recycled aggregates. *CBM*, 73(30), 407-416, 2014.
- [7] V.W.Y. Tam, X.F. Gao, C.M. Tam. Microstructural analysis of recycled aggregate concrete produced from two-stage mixing approach. *Cement and Concrete Research*. 35(6), 1195-1203, 2005.
- [8] C.H. Fu, Z.X. Feng and L. Zhang. Effects of Mixing Method on Concrete Air Content and Pore

Distribution. Journal of Zhengzhou university, 32(2): 42-45, 2011.

- [9] S.L. Wang, B. Zhang, and X. Zhao, et al. A multivariate mixed renewable fiber reinforced recycled concrete preparation, China, CN 102584135A 2012-07-18.
- [10] B.Z. Zhang, S.L. Wang and B. Zhang, L.P. Jing, S.C. Luo. Experiment analysis of the basic mechanical properties of recycled concrete, concrete, (7): 4-6, 2011.
- [11] Yu-Jiang Fan, Bin-Shan Yu, She-Liang Wang. Analysis and Evaluation of the Stochastic Damage for Recycled Aggregate Concrete Frames Under Seismic Action, International Journal of Civil Engineering, 1-9, 2017. DOI 10.1007/s40999-017-0203-x.

DIFFUSION CHARACTERISTICS OF GROUT IN LAYERED FAULT MEDIUM

Li Peng¹, Zhang Xiao², Wang Qian³ and Zhang Qingsong²

1. *Ocean University of China, Engineering College, Qingdao, Shandong 266100, China; superlipeng021@126.com*
2. *University of ShanDong, Research Center of Geotechnical and Structural Engineering, Jinan, Shandong 250061, China; sduzhangxiao@sdu.edu.cn*
3. *Ji'nan rail transit Group Construction Investment Co., Ltd. Jinan, Shandong 250101, Chin; 352392515@qq.com*

ABSTRACT

The grouting method has been widely adopted to improve the soft and broken ground properties in tunnelling engineering. This paper carries out numerical and experimental investigation to study the diffusion characteristics of grout in layered fault, considering the influence of flowing water and multiple injections. The fault is simplified to consist of (1) fault gouge, (2) fault breccia and (3) mixed area. It can be concluded that the grout shows significantly different diffusion characteristics in fault breccia and mixed area, moreover, due to the scouring effect of flowing water, grout has greater diffusion tendency in the direction of the water. In the case of single injection, the grout diffusion distance in mixed area was between 75.86 % and 88.10 % of that in fault breccia, while it was 59.8 % when multiple injections were carried out. It appeared that, the higher the injection pressure, the grout diffusion priority in fault breccia is greater. It can be also concluded that the pressure dissipated gradually from the injection hole to periphery, and the pressure dissipation in mixed area is faster than that in fault breccia. The results of experiment match reasonably well with numerical simulation, furthermore, the grouting reinforcement mode for layered fault medium are proposed. These conclusions can be used to better understand grouting theory.

KEYWORDS

Grouting, Layered fault medium, Grout diffusion characteristics, Reinforcement mode

INTRODUCTION

With the rapid development of tunnelling and underground engineering in China, weak rock masses such as fault which tends to have complex lithology, rich groundwater and low strength, are commonly encountered by excavation, resulting in susceptibility to groundwater and mud inrush [1,2].

For safety purposes, the grouting method [3,4] has been one of the most popular methods that used to improve the permeability and strength resistance of fault, and to avoid associated negative effects. However, due to its high complexity, our current understanding of grout diffusion theory [5] especially for fault is still limited and therefore, there is a lack of an effective theoretical framework for grouting scheme design.

To our knowledge, by using theoretical, numerical and experimental approaches, current studies on grout diffusion theory have focused on the interaction between grout and medium, description of diffusion mode as well as calculation of diffusion radius, and also the influence of key

factors including injection pressure, injection rate and grout properties on them. For example, Houlsby [6] presented a model to describe the propagation of grout in a single fracture. Gothäll and Stille [7], Eisa [8], and Tirupati [9] investigated the grout diffusion characteristics in porous media by adopting model experiment. Silas and Deborah [10], Adam [11,12] proposed theoretical models for compensation grouting in sand, which can be used to calculate the width-to-length ratio of the fracture induced in the grout injection.

Various researchers and engineers have contributed to further increase our understanding of grout diffusion theory. However, little is known about grout diffusion characteristics in layered fault medium, especially taking into consideration the influence of flowing water and interaction between multiple injections.

This study aims to obtain knowledge on the propagation of grout in layered fault medium, under the influence of flowing water and multiple injections. With the purpose of simplifying complicated geological conditions in engineering, a simplified model for layered fault medium is proposed and adopted in this investigation.

SIMPLIFIED GROUTING MODEL

Engineering situation

Yonglian tunnel [13, 14] with a length of more than 2500 m is located at Lian’hua City, in Jiangxi Province, China, with a lot of faults and secondary faults such as fault-2. With rich groundwater, strong weathered sandstone and shale, the fault-2 tends to have low strength and has induced a large number of groundwater and mud inrush during excavation, seriously threatening the safety of tunnel construction. Therefore, it is very necessary to reinforce weak rock masses by grouting method to meet the requirements of tunnel excavation.

After carrying out geological prospecting by boreholes, it was found that the fault medium was mainly composed of fault breccia and fault gouge, with significant stratification phenomenon. To simplify the complicated geological conditions of fault-2, a simplified model consisting of fault gouge, fault breccia and mixed area, named as the grouting model for layered fault medium, is proposed, as shown in Figure 1. In addition, the conditions including flowing water, single grouting as well as multiple grouting (three holes), are taken into consideration.

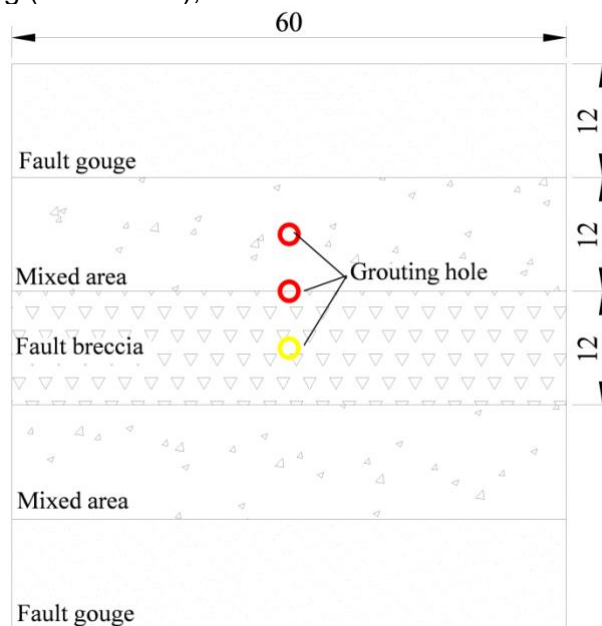


Fig. 1 – Schematic diagram of the grouting model for layered fault medium (unit: cm)

By performing in-situ sampling and laboratory tests, the properties of layered fault medium were measured and are therefore summarized in Table 1.

Tab.1 – Properties of layered fault medium

Medium type	Porosity	Permeability (m ²)	Density (kg/m ³)
Fault breccia	0.5	1e-10	2.2e3
Fault gouge	0.3	2.89e-13	1.85e3
Mixed area	0.4	1e-11	1.95e3

Software selection and control equation

On the basis of finite element method, the COMSOL Multiphysics [15], has been one of the most popular software that used to better calculate, describe and simulate various physical phenomena, by solving partial differential equations under the conditions of multi-physics coupling. This paper selected the porous media and groundwater flow Darcy's law, which belongs to the fluid flow module, to carry out related numerical analysis.

The basic assumptions of two-phase seepage Darcy's law are as follows.

- (1) The injected medium is homogeneous and isotropic, which cannot be compressed.
- (2) The groundwater flow and grout, which are taken as incompressible Newtonian fluid, are assumed to follow the Darcy's law in the seepage process.
- (3) The influence of gravity and capillary water pressure are not taken into consideration.

Equation 1 and Equation 2 [16] show the control equations of two-phase seepage Darcy's law under two-dimensional conditions.

$$-\frac{K_0}{\mu_0} \left[\frac{\partial^2 p}{\partial x^2} + \frac{\partial^2 p}{\partial y^2} \right] = \phi \frac{\partial (S_0)}{\partial t} \quad (1)$$

$$-\frac{K_w}{\mu_w} \left[\frac{\partial^2 p}{\partial x^2} + \frac{\partial^2 p}{\partial y^2} \right] = \phi \frac{\partial (S_w)}{\partial t} \quad (2)$$

Where K_0 = permeability coefficient of grout; K_w = permeability coefficient of water; μ_0 = viscosity coefficient of grout; μ_w = viscosity coefficient of water; p = pressure tensor; S_0 = saturation of grout; S_w = saturation of water, and $S_0 + S_w = 1$; ϕ = porosity of injected medium.

Calculation model and boundary conditions

Generally, the fault in actual engineering tends to have a large size. However, in order to verify the rationality and correctness of numerical simulation results, model experiment should be performed and therefore, the sizes of models that adopted in numerical simulation and model experiment should be consistent.

Taking into account the feasibility of the model experiment, the two-dimensional square calculation model with the dimensions of 60 cm × 60 cm was adopted, as shown in Figure 1 and

Figure 2. The calculation model was equally divided into five parts: (1) fault gouge; (2) mixed area; (3) fault breccia; (4) mixed area and (5) fault gouge.

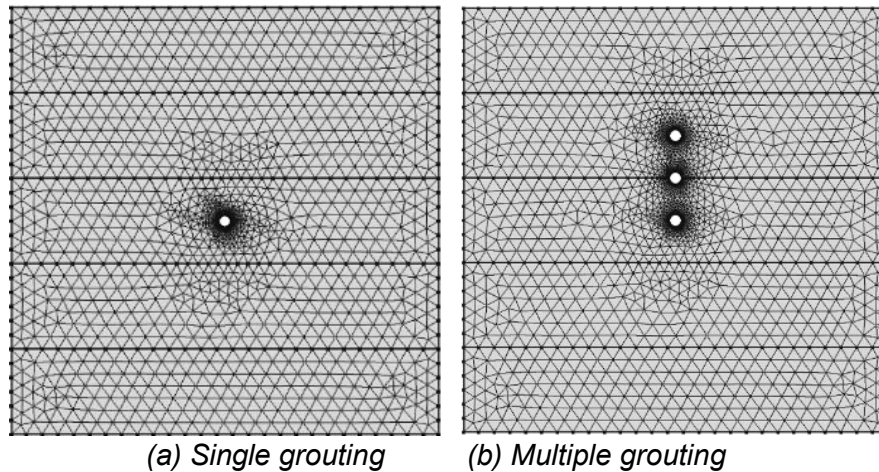


Fig. 2 – Calculation model

In the case of single grouting, the grouting hole with a radius of 1 cm was located at a depth of 30 cm from the upper boundary, and when multiple grouting was performed, the other two grouting holes were located at a depth of 18 cm and 24 cm from the upper boundary, respectively.

The freedom triangular grid was applied, moreover, the grid around the grouting holes was densified to improve calculation accuracy.

Based on the actual conditions of both engineering and experiment, the upper boundary was set for a stable water head with a height of 2 m, and the lower boundary was the exit boundary. In addition, the left and right boundary were impermeable.

Grouting parameters selection

The cement and sodium silicate grout (abbreviated as C-S grout), which is one of the most common grout in engineering, was selected for both numerical simulation and experiment, ignoring the influence of the time-varying characteristics of viscosity. Table 2 shows the properties of water and C-S grout.

Tab.2 – Properties of water and C-S grout

Materials	Density (kg/m ³)	Viscosity (Pa·s)
C-S grout	1500	0.06
Water	1000	0.001

According to the actual engineering conditions and equipment performance, the simulation of grout diffusion characteristics in layered fault medium was carried out at a total of four injection pressure levels ($p = 0.6$ MPa, 0.8 MPa, 1 MPa and 1.2 MPa).

Numerical simulation results and analyses

Results of single grouting

Diffusion mode of grout

By using the volume fraction method to describe the distribution of grout, when $t = 10$ s, 30 s, 50 s, 90 s, 130 s and 200 s, respectively, the diffusion mode of grout is shown in Figure 3.

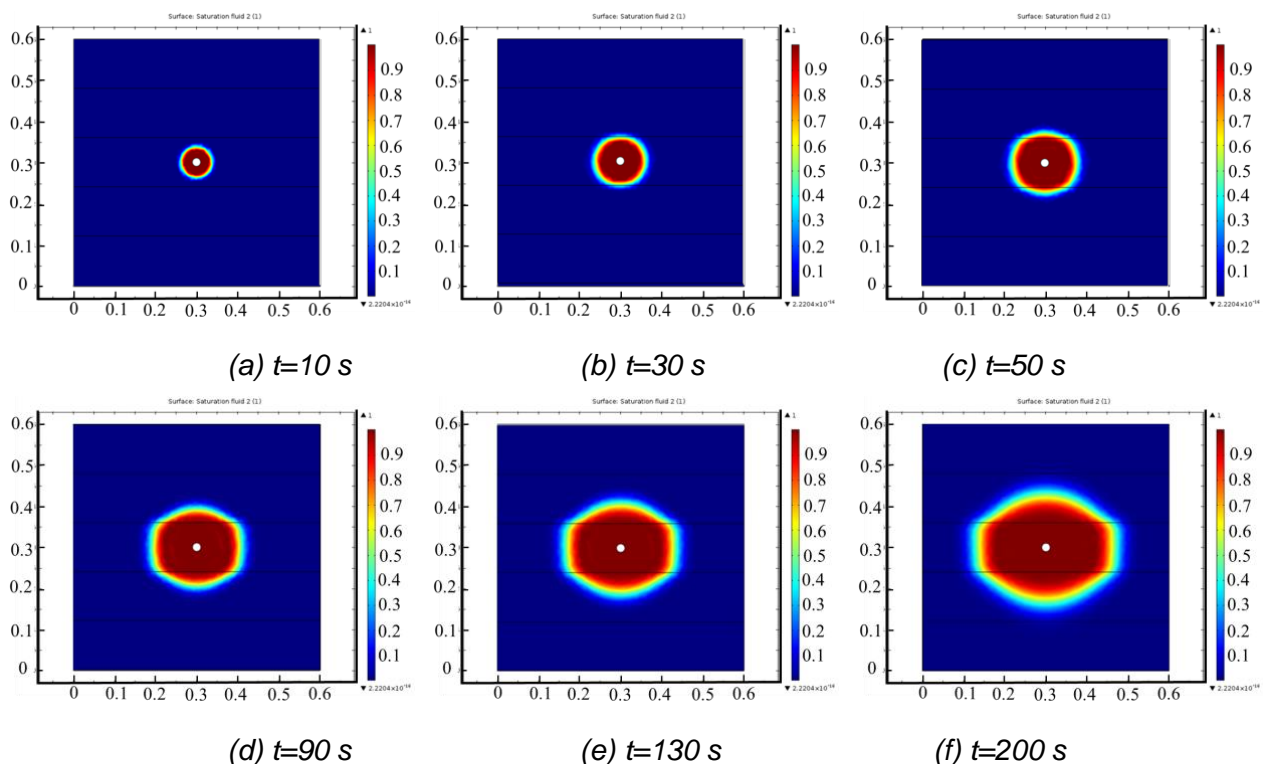


Fig. 3 – Diffusion mode of grout at different times

The grout diffusion characteristics in fault breccia and mixed area is summarized as follows. In the initial stage, the grout propagates in fault breccia with an approximately circular shape and a high velocity (Figure 3a). The boundaries between the fault breccia and mixed area start to play a controlling role for the propagation of grout from 30 s (Figure 3b), resulting in a lower propagation velocity in mixed area. Therefore, due to different propagation tendency and velocity, the grout shows significantly different diffusion characteristics in fault breccia and mixed area from 30 s to 200 s.

The influence of injection pressure on final diffusion mode of grout

Figure 4 shows the final diffusion mode of grout under the conditions of four injection pressure levels ($p = 0.6$ MPa, 0.8 MPa, 1 MPa and 1.2 MPa).

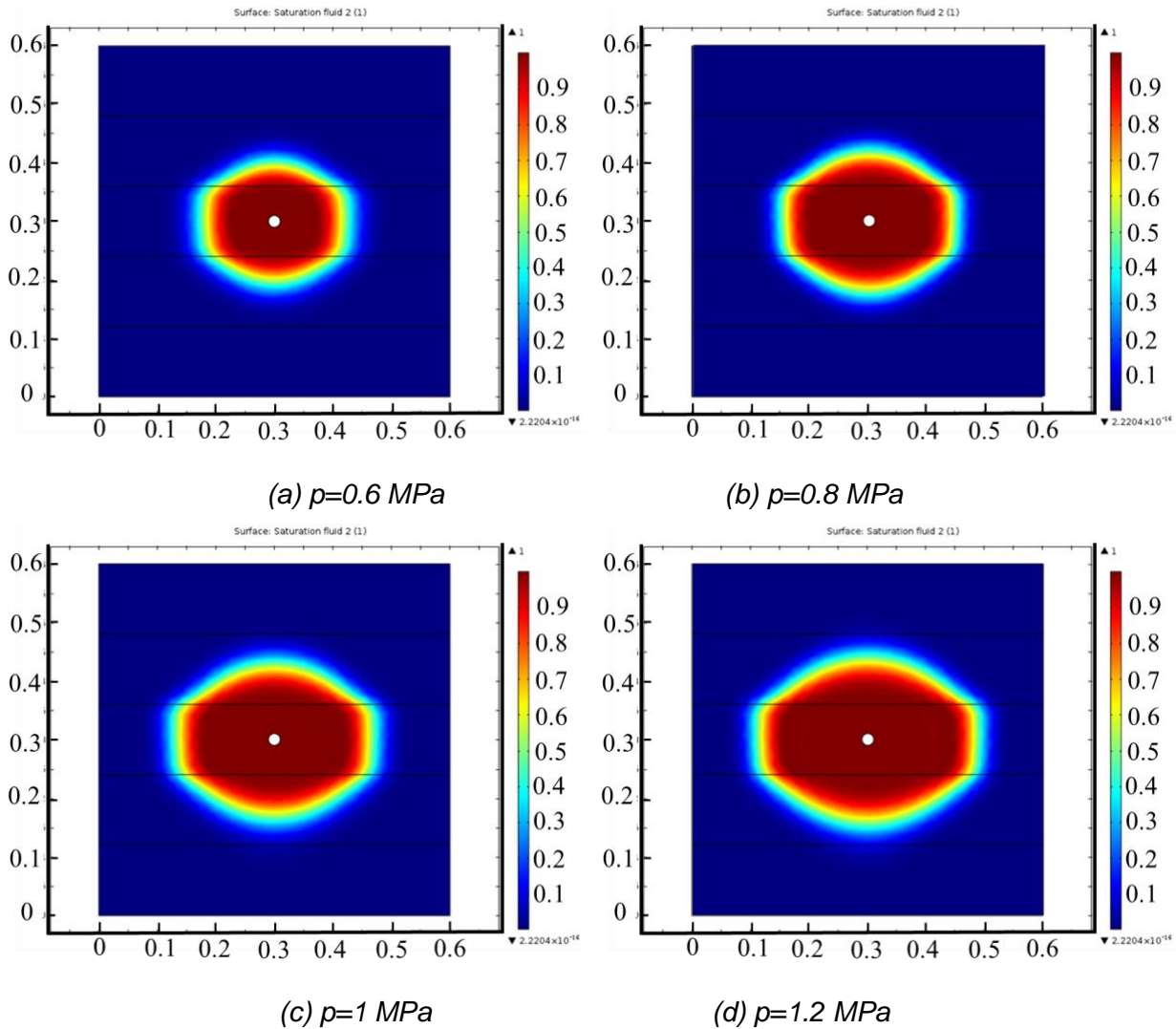


Fig. 4 – Final diffusion mode of grout under four injection pressure levels

It can be concluded from Figure 4 that the grout preferentially propagate in fault breccia, followed by the mixed area. In addition, due to low porosity and injection pressure, as well as far from the grouting hole, the propagation tendency of grout in fault gouge is not obvious. Therefore, in order to characterize this kind of difference of grout propagation, the concepts of (1) diffusion distance in fault breccia (S_b), (2) diffusion distance in mixed area in the reverse direction of the water (S_{m1}), (3) diffusion distance in mixed area in the direction of the water (S_{m2}) and (4) diffusion distance difference (S_d) are proposed, respectively, whose schematic diagram are shown in Figure 5. Moreover, it is noted that S_d refers to the difference between diffusion distance in fault breccia and diffusion distance in mixed area.

The values of S_b , S_{m1} , S_{m2} and S_d versus injection pressure are also shown in Figure 5.

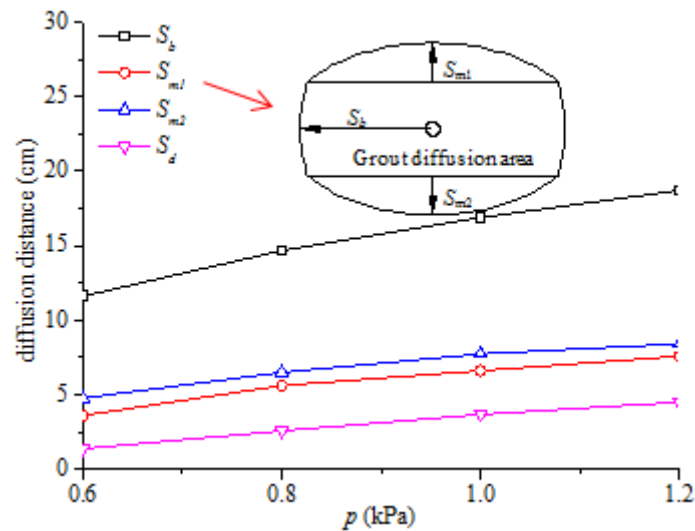


Fig. 5 – The values of S_b , S_{m1} , S_{m2} and S_d with injection pressure varying

It can be found that the values of S_b , S_{m1} and S_{m2} increase gradually with injection pressure increasing. For example, as the injection pressure increases from 0.6 MPa to 1.2 MPa, the values of S_b , S_{m1} and S_{m2} increased by 109.82 %, 76.22 % and 60.98 %, respectively, which is because increasing injection pressure provides greater driving force for grout propagation.

The values of S_b and S_d vary between 11.63 and 18.71 cm, 1.38 and 4.52 cm, respectively, indicating that the higher the injection pressure, the grout diffusion priority in fault breccia is greater. In general, the grout diffusion distance in mixed area is between 75.86 % and 88.10 % of that in fault breccia, and this is because the fault breccia tends to have better inject ability, with higher porosity and permeability.

Besides, under same injection pressure conditions, the value of S_{m1} is less than that of S_{m2} , for example, they are 6.62 cm and 7.75 cm respectively when the injection pressure is taken as 1 MPa, i.e. grout has greater diffusion tendency in the direction of the water, which is caused by the scouring effect of flowing water.

Pressure dissipation in layered fault medium

Figure 6 shows the pressure contours in layered fault medium under the conditions of four injection pressure levels. It is found that the pressure dissipates gradually from the injection hole to periphery, and this is because the grout need to overcome the influence of pore water pressure, viscous resistance, frictional resistance and other factors in the process of propagation. Moreover, in comparison with fault breccia, the pressure contours in mixed area are denser, indicating that the pressure dissipation velocity in mixed area is higher, which is caused by greater resistance.

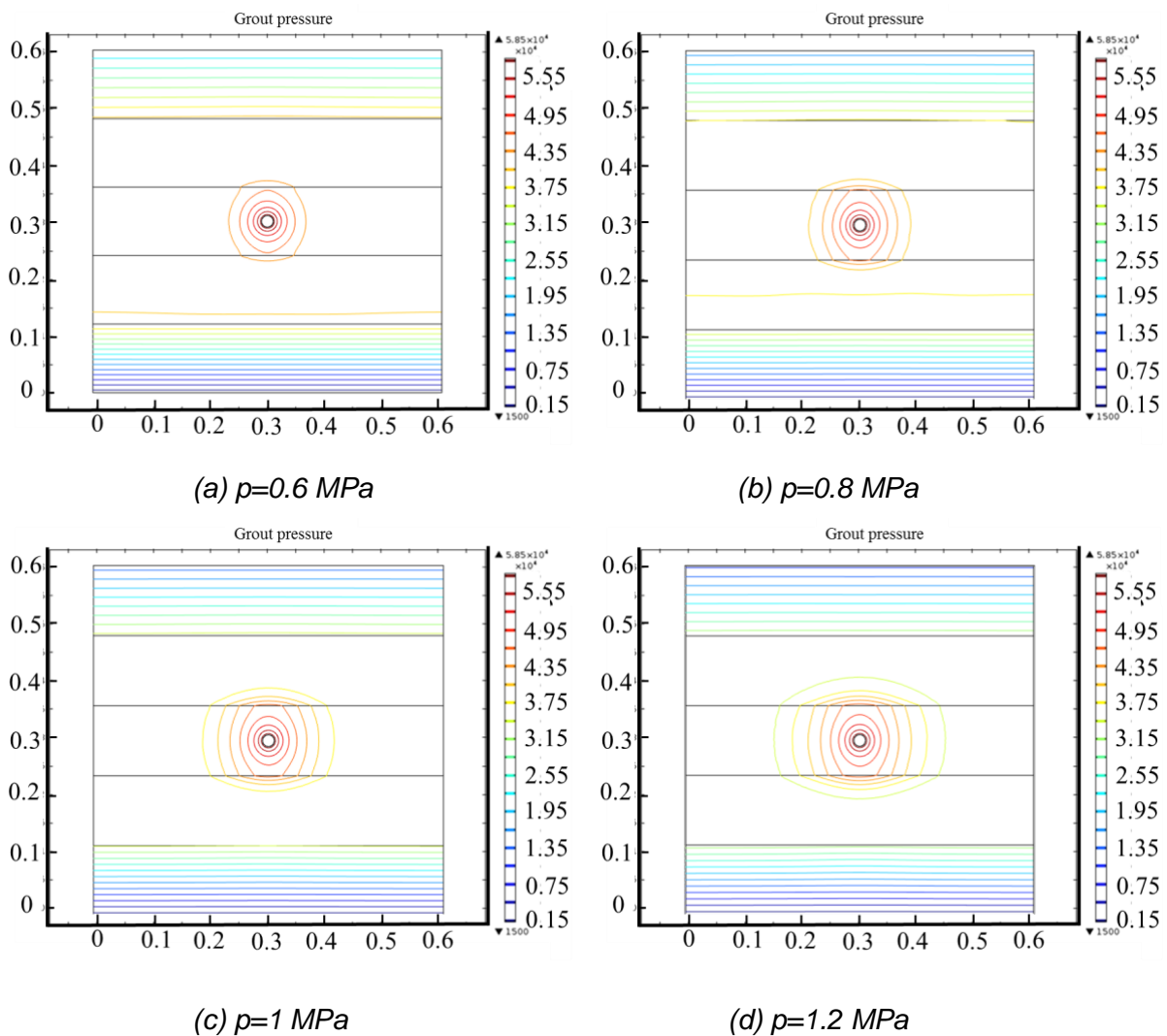


Fig. 6 – The pressure contours in layered fault medium

Results of multiple grouting

In actual engineering, multiple grouting is commonly carried out to get greater reinforcement range and better reinforcement effect. Due to different locations of grouting holes and geological conditions, the grout tends to show different diffusion characteristics. Therefore, simulation is performed to investigate the diffusion characteristics of grout in multiple grouting.

Multiple grouting is carried out synchronously, with the injection pressure set as 1 MPa, also taking into the consideration the effect of flowing water. Figure 7 shows the diffusion mode of grout at different times. It can be found that the grout still showed significantly different diffusion characteristics in fault breccia and mixed area, which is summarized as follows.

Both in fault breccia and mixed area, the grout propagates with an approximately circular shape, whereas the former has a larger diffusion range, e.g. when $t=10 \text{ s}$, their diffusion ranges are 311 cm and 2.29 cm, respectively. The grout from three grouting holes begins to intersect and interact with each other from 50 s, and the grout from boundary hole reaches the range that other two holes cannot cover. Finally, the effective diffusion distance of grout in fault breccia is 13.89 cm, whereas it is 8.31 cm in mixed area.

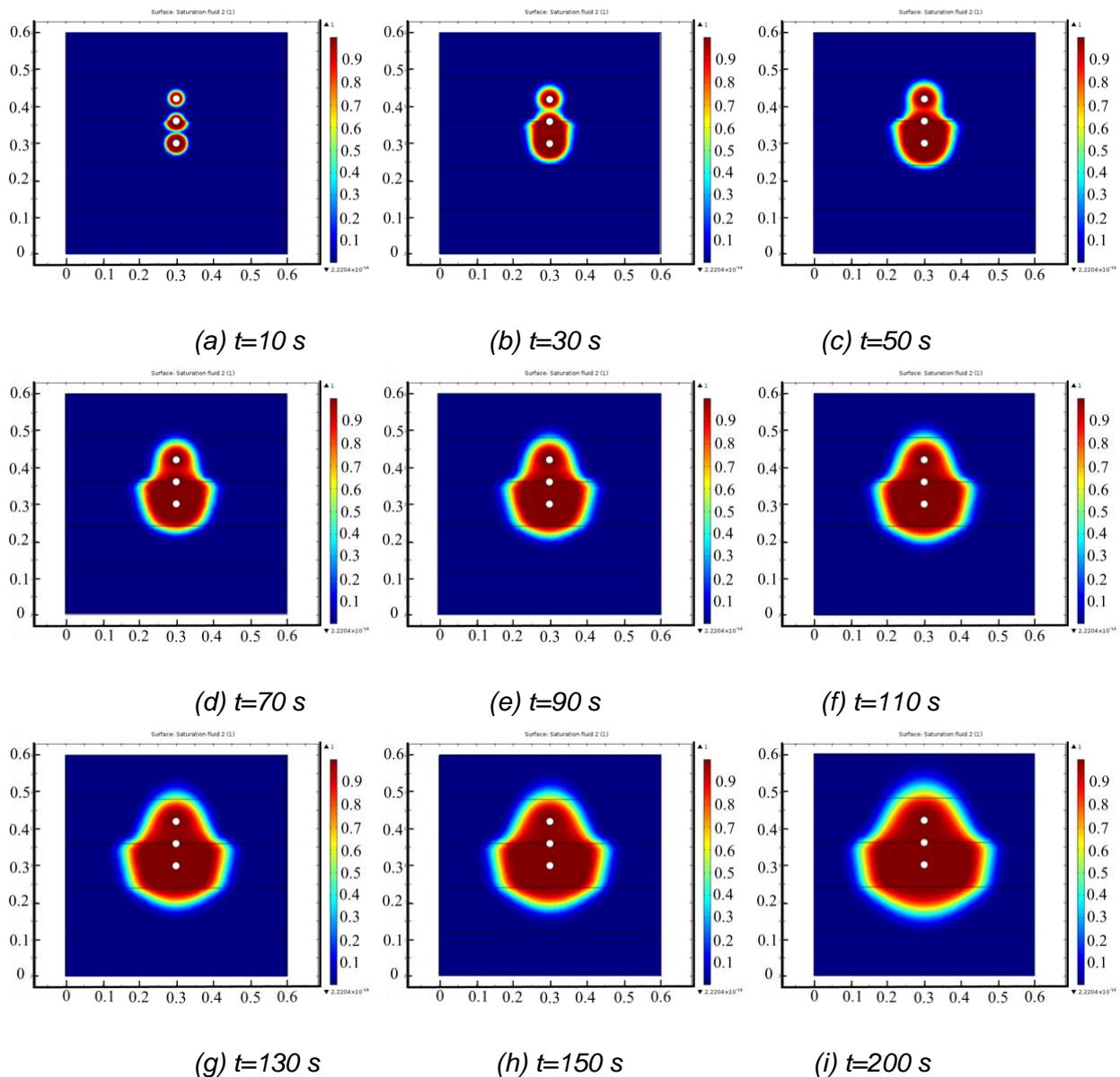


Fig. 7 – Diffusion mode of grout at different times in multiple grouting

EXPERIMENTAL INVESTIGATION

Experimental set-up

Figure 8 shows a picture of the experimental set-up, which is composed by (1) grouting equipment, (2) data acquisition system, (3) layered medium simulation device and (4) water supply device. A manual pump was used to carry out grouting with small velocity and high pressure. Data acquisition system consists of soil pressure transducers, pore pressure transducers and matched data acquisition equipment.



Fig. 8 – Picture of the experimental set-up

For the sake of convenience for assembling, filling medium and excavation after grouting, the layered medium simulation device is composed of three cells (inside dimensions: 60 cm × 60 cm × 20 cm), which is made up of steel plate with a thickness of 1 cm. In addition, to meet the requirements of bearing high pressure, the cells were fixed by high strength bolts and sealed by sealant.

Two reservoirs with a volume of 15 L were positioned above the layered medium simulation device at a height of 2 m, providing stable flowing water conditions.

Experimental design and materials

Materials including fault breccia and fault gouge used to simulate the layered fault medium were obtained from Yonglian tunnel, whose grain composition and properties are shown in Table 3 and Table 4, respectively. The mixed area was made up of fault breccia and fault gouge with a ratio of 1:1.

Tab.3 – Properties of fault gouge [17,18]

Optimum moisture content (%)	Maximum dry density (g · cm ⁻³)	Liquid limit (%)	Plastic limit (%)	Plasticity index
23.1	1.7	48.3	25.6	22.7

Tab.4 – Grain composition of fault breccia

Grain size (mm)	2.5 ~ 5	1.25 ~ 2.5	0.63 ~ 1.25	0.315 ~ 0.63	0.16 ~ 0.315	0.08 ~ 0.16	< 0.08
Content (%)	74.03	69.41	54.70	33.36	13.18	9.03	1.43

The fault gouge, mixed area and fault breccia were filled into the layered medium simulation device in sequence, ranging from (1) 0 ~12 cm, (2) 48~60 cm and 24 ~ 36 cm, (3) 12~24 cm and 36~48 cm.

Consistent with the numerical simulation, C-S grout (1:1) was selected for experimental investigation, which was injected into the container through single grouting hole, with an injection pressure of 1 MPa, as shown in Figure 9.



Fig. 9 – Picture of grouting process

Experimental results

Diffusion mode of grout

Excavation was carried out after curing of 24 hours and therefore, the diffusion mode of grout is shown in Figure 10.



Fig. 10 – Picture of grout diffusion mode

With an injection pressure of 1 MPa, the values of S_b , S_{m1} and S_{m2} are shown in Table 5.

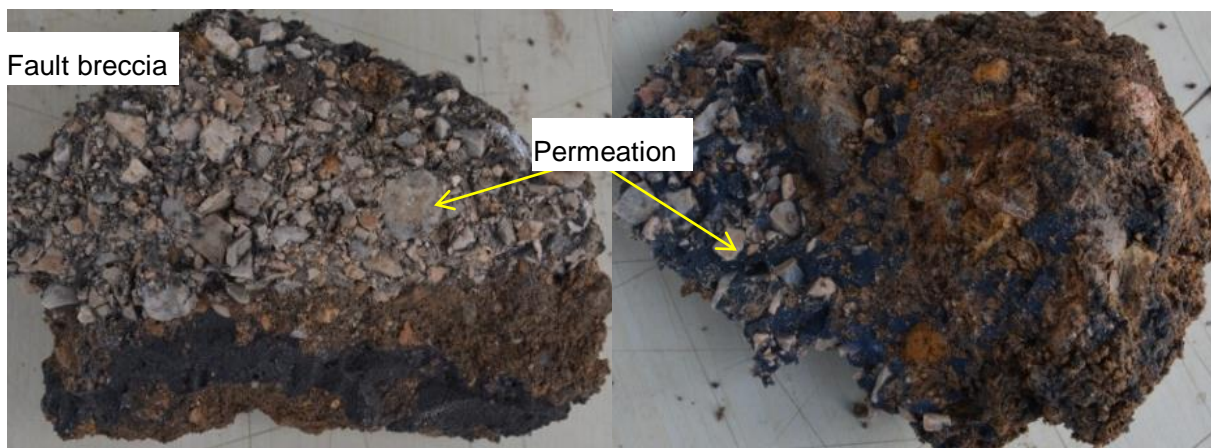
Tab.5 – Comparison of numerical and experimental results

Type	S_b (cm)	S_{m1} (cm)	S_{m2} (cm)
Numerical results	16.89	6.62	7.75
Experimental results	30	7.85	8.38

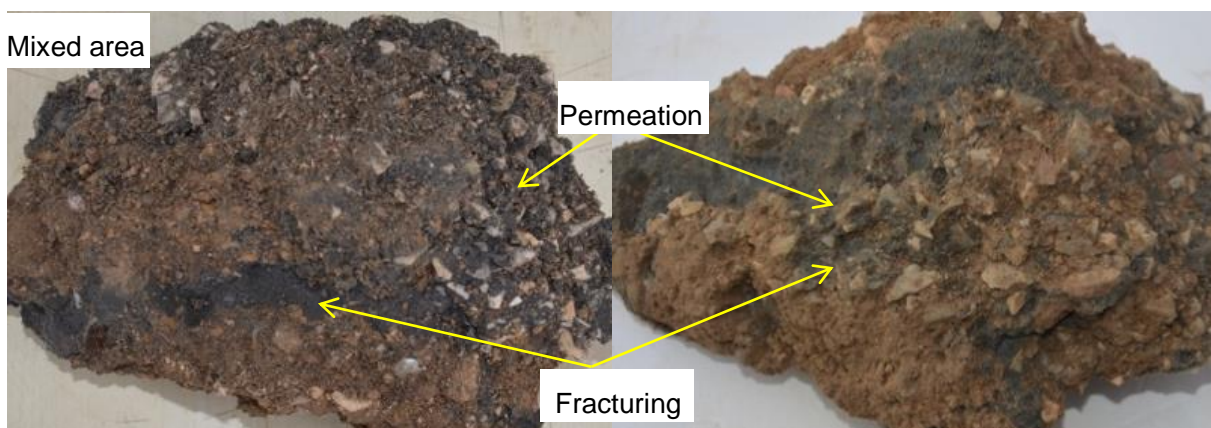
It can be concluded from Table 5 and Figure 10 as follows. In the longitudinal direction, the experimental and numerical results are approximate, with the former 15.7 % and 7.6 % larger than the latter. However, there was an obvious boundary effect in the transverse direction (S_b), with the experimental results significantly larger than the numerical results. This is because it is difficult to ensure the uniformity of materials when filling into the container, resulting in possible weak interface in which grout will preferentially propagate. However, as a whole, the experimental results agree with the numerical results well, i.e. the grout preferentially propagate in fault breccia, followed by the mixed area.

Reinforcement mode of grout

By excavation, it can be also found that grout has different reinforcement mode for fault breccia and mixed area, which has been classified into two types as follows. Due to large porosity, grout penetrates into the fault breccia to cement particles (Figure 11a), whereas the mixed area has small porosity, therefore, in addition to permeation effect, grout tends to fracture the medium and form veins to play a supporting role (Figure 11b).



(a) Permeation effect



(b) Permeation and fracturing effect Fig. 11 – Picture of grout reinforcement mode

CONCLUSION

On basis of the current investigation, conclusions can be drawn as follows.

A simplified grouting model for layered fault medium is proposed, composed of (1) fault gouge, (2) fault breccia and (3) mixed area.

In the case of single grouting, the grout diffusion distance in mixed area was between 75.86 % and 88.10 % of that in fault breccia, while it was 59.8 % for multiple grouting. The concepts of S_b , S_{m1} , S_{m2} and S_d are proposed to characterize propagation difference of grout in layered fault medium, whose relationship with injection pressure is also analysed.

The pressure dissipated gradually from the injection hole to periphery, and the pressure dissipation in mixed area is faster than that in fault breccia.

Experimental investigation was performed, whose results correspond well with what was found in numerical simulation.

ACKNOWLEDGEMENTS

This project was gratefully supported by National Key Research Projects (Grant No. 2016YFC0801604), National Natural Science Foundation of China (Grant No. U1706223) and Shandong Natural Science Foundation (Grant No. ZR2017MEE070). Great appreciation is also extended to the editorial board and the reviewers of this paper.

REFERENCES

- [1] Qian, Q.H. 2012. Challenges faced by underground projects construction safety and counter-measures. *Chin. J. Rock Mech. Eng.* vol. 31: 1945-1956.
- [2] Zhang, Q.S.; Han, W.W. 2012. Comprehensive grouting treatment for water gushing analysis in limestone fault breccias fracture zone. *Chin. J. Rock Mech. Eng.* vol.31: 2412-2419.
- [3] Li S.C., Li M.T., Zhang X. And Zhang Q.S. 2018. *The civil engineering journal*, vol. 364-379: 1945-1956.
- [4] Giuseppe, M.; Joanna, B. 2012. Analysis of Foundations Reinforced with Jet Grouting. *Journal of Geotechnical and Geoenvironmental Engineering.* vol.138: 1442-1454.
- [5] Zong, Y. J. 2013. Mechanical characteristics of confined grouting reinforcement for cracked rock mass. *Journal of Mining & Safety Engineering.* vol. 30: 483-488.
- [6] Houlsby, A.C. 1990. *Construction and design of cement grouting-A guide to grouting in rock formation.* John Wiley&Sons, Inc., NY.
- [7] Gothall, R.; Stille, H. 2010. Fracture-fracture in-teraction during grouting. *Tunnelling and Underground SpaceTechnology.* vol. 25: 199-204.
- [8] Eisa, K. 2010. Compensation grouting in sand[Ph. D. Thesis]. University of Cambridge, London.
- [9] Tirupati, B. 2009. Experimental Investigations of Colloidal Silica Grouting in Porous Media. *Journal of Geotechnical and Geoenvironmental Engineering.* vol. 135: 697-700.
- [10] Silas, C.N.; Deborah, J.G. 2000. Physical model testing of compaction grouting in cohesionless soil. *Journal of Geotechnical and Geoenvironmental Engineering,* vol. 126: 848-852.
- [11] Adam, B. 2010. Compensation Grouting in Sand- Experiments, Field Experiences and Mechanisms[Ph. D. Thesis]. Delft University of Technology.
- [12] Adam, B. 2011. Analytical Model for Fracture Grouting in Sand. *Journal of Geotechnical and Geoenvironmental Engineering.* vol. 137: 611-620.
- [13] Zhang, Q.S; Li, P.; Wang, G. 2015. Parameters optimization of curtain grouting reinforcement cycle in Yonglian tunnel and its application. *Mathematical Problems in Engineering.* vol. 2018: 1-15.

- [14] Li, P.; Zhang, Q.S.; Zhang, X. 2017. Grouting Diffusion Characteristics in Faults Considering the Interaction of Multiple Grouting. *International Journal of Geomechanics*. vol. 5: 1-10.
- [15] Liu, J.; Liu, R.T.; Zhang, X. 2012. Diffusion law model test and numerical simulation of cement fracture grouting. *Chin. J. Rock Mech. Eng.* vol.31: 2445-2552.
- [16] Wang, G. 2014. Study on stability and parameters of curtain grouting reinforcement ring in water-rich strata of tunnel. Shandong University, Jinan.
- [17] Li, P.; Zhang, Q.S.; Zhang, X. 2014. Analysis of fracture grouting mechanism based on model test. *Rock and Soil Mechanics*. vol.35: 3221-3230.
- [18] Zhang, Q.S.; Li, P. 2015. Model test on grouting strengthening mechanism for fault gouge of tunnel. *Chin. J. Rock Mech. Eng.* vol.34: 924-934.

3D DYNAMIC TIME-HISTORY RESPONSE ANALYSIS OF AN ISLAND PLATFORM METRO STATION IN LOESS AREA

Wang Ke^{1,2}, Siyue He^{2*}, Guanglong Zhang³

1. China Railway First Survey and Design Institute Group CoLtd., Xi'an 710043, China
2. School of Highway, Chang'an University, Xi'an 710064, China; hesiyue@chd.edu.cn, 408423231@qq.com
3. Shandong Academy of Building Research, Ji'nan 250031, China

ABSTRACT

Through the years, the seismic resistance of underground structures has attracted more and more attention, and dynamic characteristics of metro station is one of the most important issues. In this article, the 3D numerical model of Zhang Wangqu metro station along Metro Line 5 in Xi'an is established to study on seismic dynamic response of roof, floor, columns and beams in the island platform metro station. Compared with the earthquake damage of Dakai metro station in the Kobe M7.2 Earthquake and the shaking table test of metro station in loess area, results reveal that horizontal acceleration can reflect seismic wave characteristics under the horizontal seismic wave; the maximum relative displacement of roof and floor, the maximum axle force and shear force at transfer node are bigger than the standard section and reduce with the increase of buried depth; the maximum axle force and shear force of columns increases from top to bottom. The island platform metro station should focus on the structural settings of transfer node, and the columns and beams here must select materials with greater strength.

KEYWORDS

Dynamic characteristics, Xi'an Metro, 3D numerical model, Island platform metro station, Transfer node, Dynamic seismic analysis

INTRODUCTION

With the rapid development of China's economy, the ground transportation system can no longer meet the demand of passenger transportation in urban traffic, and the development of Urban Rail Transit System with underground railway as the backbone is the main way to solve the traffic problems in big cities. Due to restrained effect of soil layer, compared with the ground structures, seismic performance of the underground structures is stronger, and its seismic capacity strengthens with the increase of buried depth. Due to the short history of underground constructions, the dynamic response and seismic research of underground structures is not enough. While the Kobe

M7.2 Earthquake of Japan in 1995, the Chi Chi M7.6 Earthquake of Taiwan in 1999, the Wenchuan M8 Earthquake of Wenchuan in 2008, the metro stations were seriously damaged, the ground sank, the columns and beams cracked and collapsed; the study of seismic response and seismic resistance of underground structures is gradually improving. In recent decades, the research on metro station seismic resistance has focused on theoretical research, shaking table test and numerical simulation. For theoretical research, Zhuang [1], Liu [2], and Wang et al. [3] utilized the seismic response displacement method of soil-structure interaction and nonlinear analysis of equivalent inertial force method to correct the calculation theory of FEM and improve the seismic response system of metro station. For shaking table test, Yang [4], Bian [5], Jing [6], Chen [7], Zhuang [8], Chen [9], and Quan et al. [10, 11] carried out shaking table test of metro station on liquefiable foundation and studied the seismic response of three-arch and multi-storey metro station in loess region. For numerical simulation, Parra-Montesinos [12], Du [13], and Liu et al. [14] combined the destruction of Dakai metro station by Kobe M7.2 Earthquake of Japan in 1995 and used FEM to establish numerical model, analysed the mechanism of earthquake damage at different location of the metro station. Liu [15], and Bao et al. [16] used FEM to establish numerical model for metro station in the liquefiable soil layer, and studied the seismic response of metro station under horizontal and vertical seismic waves. Wang [17], Zhuang [18], and Li et al. [19] used FEM to establish numerical model for metro station in soft soil, and analysed the seismic response and failure mechanism of metro station with different depths, layers and structures. For comprehensive analysis, Chen [20, 21] and Moghadam et al. [22] carried out shaking table test and used FEM to establish numerical model for test, compared the results of shaking table test and numerical simulation, and studied the seismic response of metro station deeply. These studies are based on structural dynamics, mainly study the seismic responses of the columns and some structures of metro station, and do not analyse the difference between the seismic response of metro station with different structures, so there is no systematic and comprehensive analysis of the earthquake response of the island platform metro station.

China is between the Eurasian seismic belt and the Pacific seismic belt, the earthquake is frequent, and loess is widely distributed. Loess has the special structure of columnar joints, large pores, weak cementation and special sensitivity to water, which makes the earthquake damage in loess area very serious. Xi'an Metro is the first subway project to build in the loess area, and there have been three earthquakes above magnitude 7 and eleven earthquakes above magnitude 6; the island platform metro station has the advantages of economical use, large capacity, etc., and has been widely adopted, so the seismic response analysis of island platform metro station in Xi'an is of great significance.

BACKGROUND

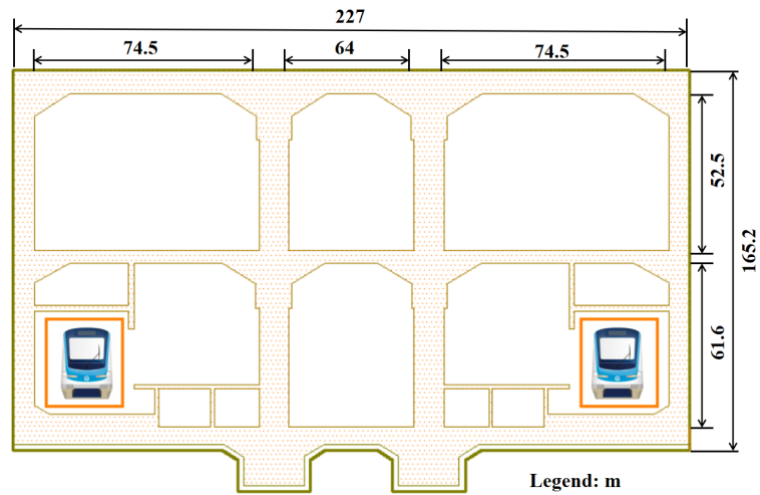
Zhang Wangqu metro station is the ninth station of the Metro Line 5 in Xi'an and located on the east intersection of the Kunming Road and the Feng Jing Avenue [23, 24]. The metro station is two layers excavated island platform station and total floorage is 17,386 m², the main building area is 12,414 m², and the ancillary floor area is 4,972 m². The metro station is provided with four entrances,

two groups of wind pavilions, and a safe entrance. The total length is 245.25m, overall width of standard section is 22.7 m, the depth of metro station is 14.34~16.121 m, and thickness of covering soil is 2~4 m, the main design parameters are shown in Table 1. The reinforced concrete frame structure with double columns and three-span is used in the metro station, the standard section is divided into two layers, as shown in Figure 1(a), and the transfer joint is divided into three layers, as shown in Figure 1(b).

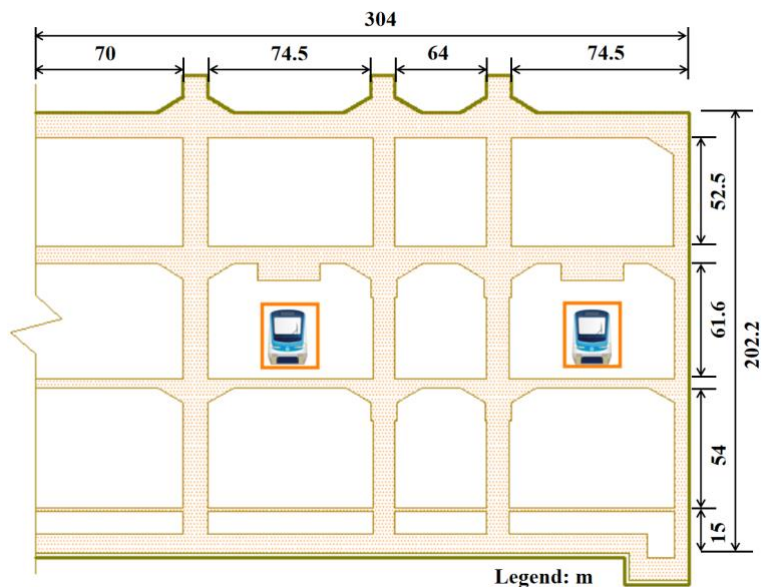
According to geological investigation, landforms along the metro station are divided into the Weihe bench land, the Feng He River bed, and the primary alluvial terrace and residual two stage alluvial terrace. The geological exploration depth is within 50.0 m, and the stratum is mainly quaternary accumulation, new artificial fill (Q^{4ml}), loess, medium sand and silty clay (Q^{4al+pl}), and silty clay (Q^{3pl}). The floor of the metro station is located in the medium sand layer. The thickness of the surface filling layer is about 0.40~1.50 m, the main ingredients are crushed brick and concrete, mainly for the construction waste. The thickness of plain filling layer 0.40~12.80 m, the main components is the silty clay, containing a small amount of ash and slag brick, sand, uneven soil, mainly for road backfill of the Keyuan Road and site backfill of the Qili town in Xi'an.

Tab. 1 - Design parameters of the Zhang Wangqu station

Item	Zhang Wangqu station
Metro station structure	Island platform metro station (Two layers and L type transfer)
Construction method	Open Cut Method
Total length	245.25 m
Total width	22.7 m
Thickness of soil	2~4 m
Depth of metro station	Depth of floor 1 5m (Local depth 22 m)
Main column distance	9.75 m



(a) Cross section of standard structure



(b) Cross section of transfer joint

Fig. 1 - Section of subway station

NUMERICAL MODEL

Based on the Midas-GTS software, numerical analysis is carried out, the rock mass in the numerical model is simulated with solid element, and the constitutive model uses the Mohr-Coulomb to consider nonlinear deformation; the columns and beams are simulated by beam element, the exterior wall and floor are simulated with plate elements, and the constitutive model uses the linear elastic model. The concrete strength grade of roof, floor, the exterior wall is C30; the concrete strength grade of columns and beams is C45; the grade of steel is HRB400. In the

horizontal direction, the distance between the artificial boundary and the underground structure of the numerical model is 3 times the effective width of the metro station; in the vertical direction, the distance between artificial boundary and the numerical model is 3 times the effective height of the metro station. The length of the numerical model is 586 m, width is 253 m, height is 47 m, the soil layers are divided into six layers, from the top to bottom are filling soil, loess soil, silty clay 1, medium sand 1, silty clay 2, and medium sand 2. The unit size is between 1/10 and 1/8 of the maximum wavelength of the input wave [25], the whole numerical model is divided into 133,655 nodes and 123,405 units. The material parameters of the soil layers are shown in Table 2, and the material parameters of the metro station structure are shown in Table 3, the finite element network of the whole system is shown in Figure 2, the detail structure of metro station and measuring points layout are shown in Figure 3(a), the beams, columns and measuring points layout of the metro station are shown in Figure 3(b).

Tab.2 - The material parameters of the soil layers [26]

Soil type	Depth /m	Density/ g·cm ⁻³	Shear wave velocity/m·s ⁻¹	Longitudinal wave velocity/m·s ⁻¹	Dynamic modulus of elasticity/MPa	Dynamic shear modulus/MPa	Poisson's ratio
Filling soil	3.5	1.9	210.3	378.1	293.8	101.3	0.33
Loess soil	4	2	107.5	187.9	162.4	56	0.26
Silty clay 1	4.3	1.9	405.8	763.2	568.1	195.9	0.4
Medium sand 1	8.9	1.9	210.4	374.8	290.9	100.3	0.32
Silty clay 2	6.3	1.9	619.6	1176.3	870.7	290.3	0.3
Medium sand 2	20	1.9	312.5	580.4	416.1	148.6	0.32

Tab. 3 - Material parameters of metro station

Component	Unit weight/kN•m ⁻³	Modulus of elasticity/GPa	Poisson's ratio	Size/m
Exterior wall	24	31	0.2	a
Roof	24	31	0.2	b
Beams	24	31	0.2	0.6*0.6
Columns	24	2.4	0.2	0.7*1.2
First floor	24	31	0.2	c
Second floor	24	31	0.2	d
Third floor	24	31	0.2	e

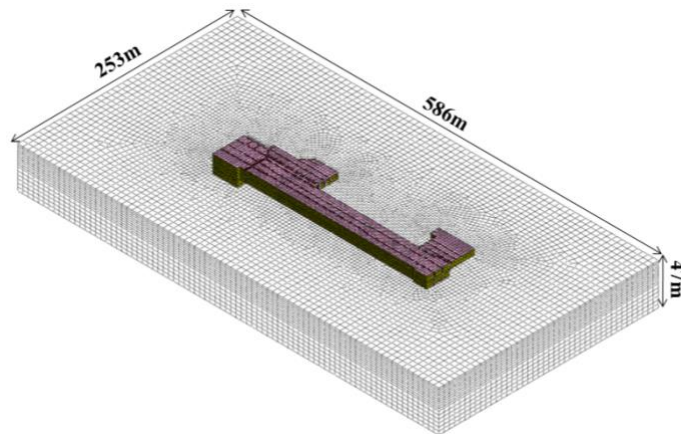
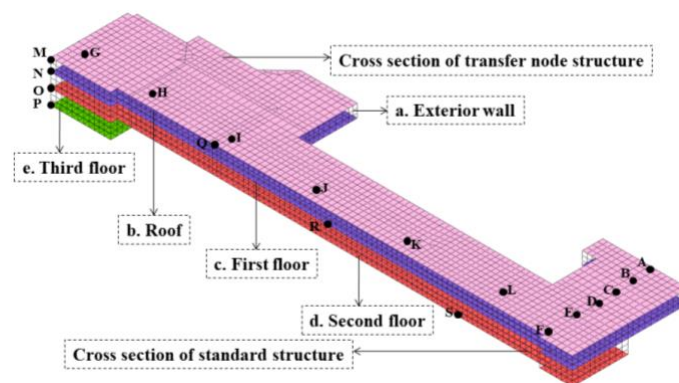
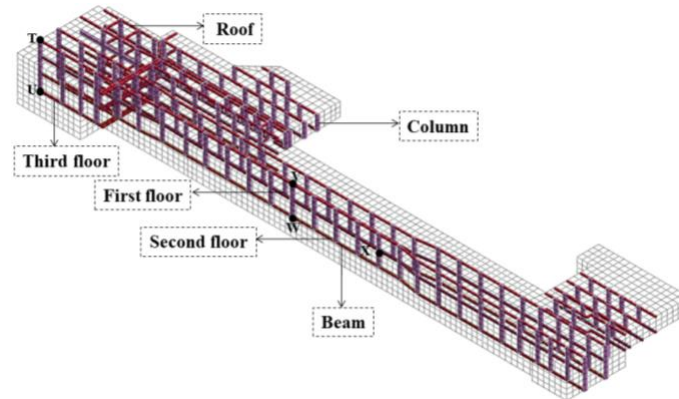


Fig. 2 - The finite element network of the whole system



(a) Measuring points layout of metro station

Fig.3 - Detail structure and measuring points layout and beams and columns of metro station



(b) Beams and columns of metro station

Fig.3 - Detail structure and measuring points layout and beams and columns of metro station

BOUNDARY CONDITIONS AND DAMPING SETTINGS

For the limited range of computing areas, the wave energy will be reflected on the artificially boundary under the action of seismic waves, causing the wave to oscillate, resulting in simulated distortion [27-30]. To solve the problem of wave reflection on the boundary of numerical model, the boundary conditions adopt the viscoelastic absorbing boundary proposed by Deeks et al. [25]. The viscoelastic boundary can not only simulate the radiation damping of the foundation, but also simulate the elastic recovery performance of the earth medium, and it has good low frequency stability, the vertical ground response coefficient and horizontal ground reaction coefficient are as Formula 1 and Formula 2, the reaction coefficient of foundation is 1 [31-32]. In eigenvalue analysis, the first ten order values are taken, among them, the first and second order of mass participation coefficient is highest, the characteristic cycles are 1.059 s and 0.999 s; Rayleigh damping is used in the time-history analysis of the numerical model, the fixed bottom condition is selected, and its damping are calculated as Formula 3 and Formula 4.

$$k_v = k_{v0} \cdot \left(\frac{B_v}{30}\right)^{\frac{3}{4}} \quad (1)$$

$$k_h = k_{h0} \cdot \left(\frac{B_h}{30}\right)^{\frac{3}{4}} \quad (2)$$

Among them:

$$k_{v0} = \frac{1}{30} \cdot \alpha \cdot E_0 = k_{h0}, B_v = \sqrt{A_v}, B_h = \sqrt{A_h}$$

A_v and A_h are the cross sectional area of vertical and horizontal element, respectively. E_0 is the modulus of elasticity of the soil, α is 1.0.

For P waves:

$$C_p = \rho \cdot A \cdot \sqrt{\frac{\lambda + 2G}{\rho}} = W \cdot A \cdot \sqrt{\frac{\lambda + 2G}{W \cdot 9.81}} = c_p \cdot A \quad (3)$$

For S waves:

$$C_s = \rho \cdot A \cdot \sqrt{\frac{G}{\rho}} = W \cdot A \cdot \sqrt{\frac{G}{W \cdot 9.81}} = c_s \cdot A \quad (4)$$

Among them:

$$G = \frac{E}{2(1+\nu)}, \lambda = \frac{\nu E}{(1+\nu)(1-2\nu)}$$

E is the modulus of elasticity of the soil, ν is the Poisson's ratio, A is the boundary area. That is the area of the boundary on both sides of the model.

SEISMIC WAVE

Xi'an is located at the southwest end of the Fen Wei fault depression, belonging to the middle and strong seismic belt. Since the second century BC, there have been 128 earthquakes with magnitude greater than 4, including 25 earthquakes over 5. Zhang Wangqu metro station belongs to the general area of earthquake fortification, the site category is class II field, for non collapsibility ground, collapsibility grade is I, the maximum thickness of the collapsibility of 4.2vm; there is no seismic liquefaction, and there is no bad geological phenomenon like ground fissure, landslide, collapse, etc. In view of seismic safety evaluation report of the Xi'an metro line 5, we simulate the seismic fortification intensity of 8 degree, the peak ground acceleration (PGA) A_g is 0.20 g, the characteristic period is partitioned into II areas, spectrum cycle partition value T_g is 0.40 s, and time-history seismic waveform in the numerical model is shown in Figure 4. The attenuation coefficient of seismic wave is 0.85 at the X boundary, the damping ratio of all vibration modes is 0.05, the loading time is 20 s, the analysis time step is 0.4 s, the output time step is 1, and the output is 50 steps.

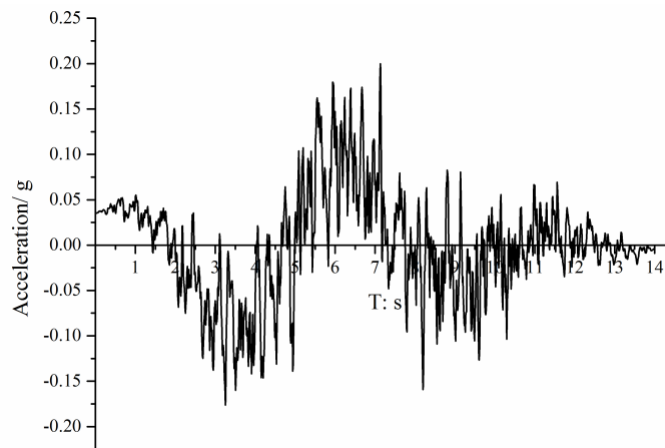


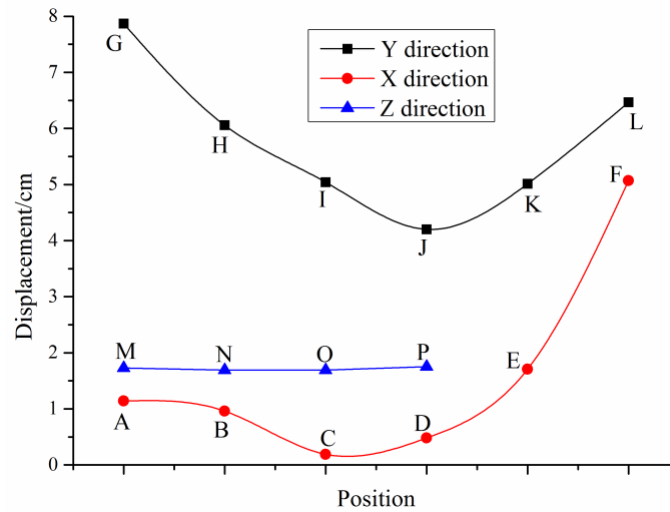
Fig. 4 - Seismic waveform

RESULTS ANALYSIS

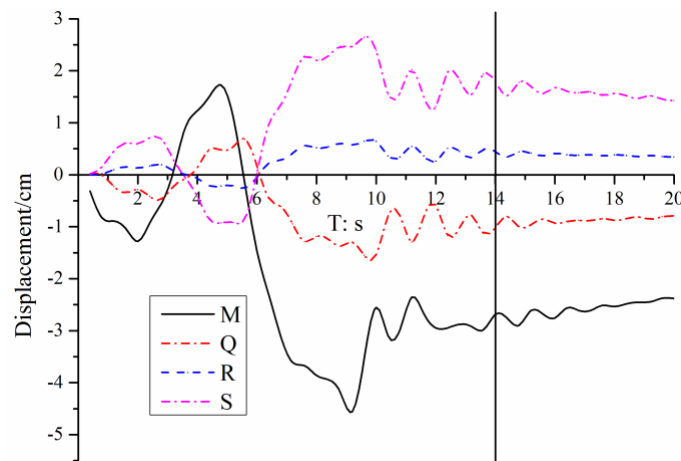
Displacement analysis

Absolute displacement analysis

The displacement measuring points A-E along the Y axis are arranged, and the displacement measuring points G-L along the X axis are arranged, and the displacement measuring points M-P along the Z axis are arranged shown in Figure 3. The vertical displacement of the metro station is positive value, the metro station floats; along the X and Y directions, the maximum vertical displacement shows a depression, the maximum vertical displacement of measuring points C and J is the minimum; along the Z direction, the maximum vertical displacement of the middle is basically unchanged; the maximum vertical displacement in each direction shows that the middle is smaller. The horizontal direction of seismic wave has no effect on the Z axis direction of the maximum vertical displacement. The displacement measuring points M, Q, R and S of roof and floor are shown in Figure 5(a), the vertical displacement time-history curve is shown in Figure 5(b). The vertical displacement of the roof is measuring point M and Q, and the vertical displacement of the first floor is measuring point R, and the vertical displacement of the second floor is the measuring point S. Before 14s, the vertical displacement curve of different plates is similar, and reaches the peak at the same time, with the increase of buried depth, the vertical displacement decreases, but after 14s, the seismic wave unloads, the metro station moves slightly under the action of inertia force, but it is basically in stable state.



(a) Maximum vertical displacement



(b) Time-history of maximum vertical displacement

Fig. 5 - Maximum vertical displacement and time-history of maximum vertical displacement

Relative displacement analysis

The relative displacement measuring points M, R, S, P of the roof and floor are shown in Figure 3, the measuring point M is located in the roof, R is located in the first floor, measuring point S is located in the second floor, and measuring point S is located in the third floor. The horizontal relative displacement time-history curve is shown in Figure 6, the relative horizontal displacement curve of measuring points M, R, S, P is similar to seismic wave fluctuation. Before 14 s, the relative horizontal displacement of the second floor is the maximum, the relative horizontal displacement of the third floor is the minimum. The maximum horizontal relative displacement of crest is smaller, the maximum horizontal relative displacement of trough is larger. After 14 s, the maximum horizontal

relative displacement is almost constant, and the maximum relative displacement between of different floor is a fixed value.

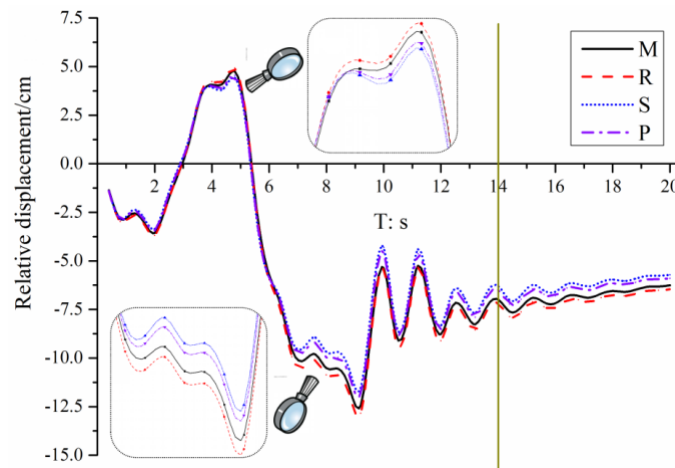
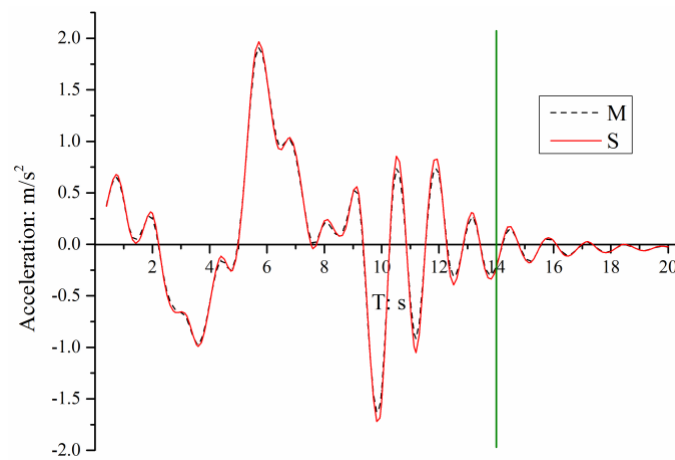


Fig. 6 - Maximum relative horizontal displacement of measuring points

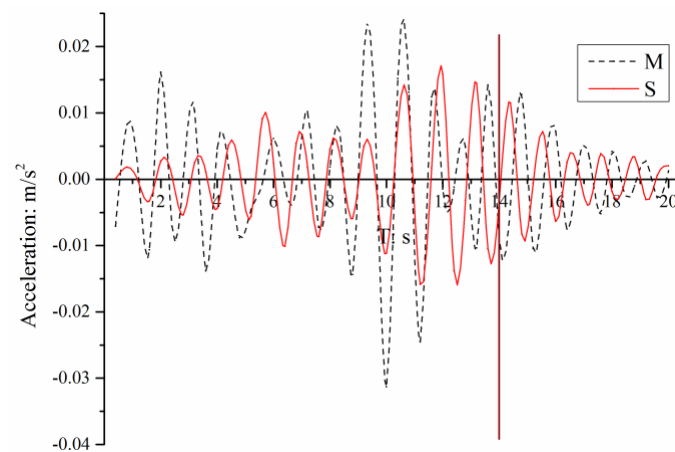
Acceleration analysis

Acceleration analysis of sidewall

The acceleration measuring points M and S of sidewall are shown in Figure 3. The maximum horizontal acceleration in the standard section is the maximum, the maximum horizontal acceleration in the transfer node is the minimum. The maximum vertical acceleration at the transfer node is large, especially in the corner, the vertical acceleration reaches the maximum value; the maximum vertical acceleration in the standard section is small. The horizontal acceleration time-history of the measured points M and S are shown in Figure 7(a), and the vertical acceleration time-history of the measured points M and S are shown in Figure 7(b). Under the action of horizontal seismic wave, the horizontal acceleration time-history curves of the measuring points M and S are almost identical and can reflect the seismic waveform, the role of the stratum is equivalent to the spring, and the seismic wave is reduced after loading on the metro station; the vertical acceleration of measuring points M and S is distorted and cannot reflect the seismic waveform. With the increasing buried depth of metro station, the horizontal and vertical acceleration decreases.



(a) Maximum horizontal acceleration



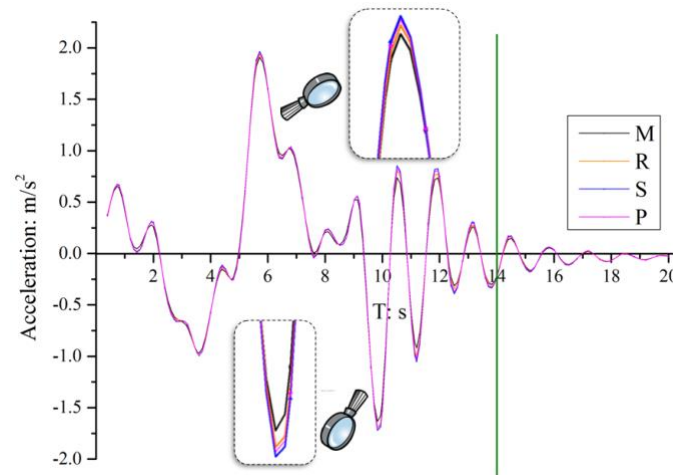
(b) Maximum vertical acceleration

Fig. 7 - Time-history of maximum horizontal and vertical acceleration of measuring points

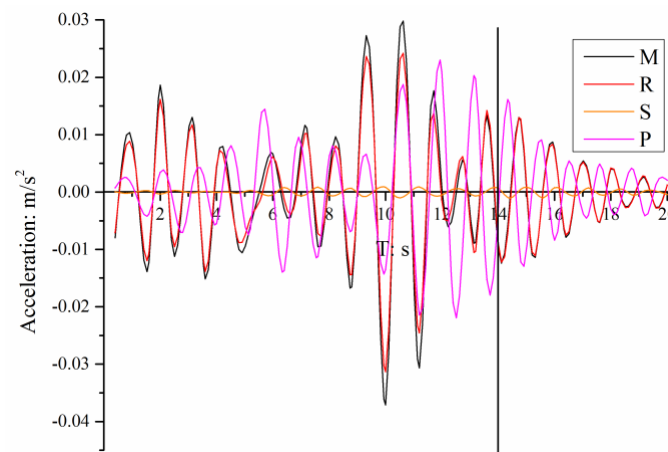
Acceleration analysis of roof and floor

The acceleration measuring points M, R, S and P of roof and floor are shown in Figure 3. The horizontal acceleration of standard section is large, the horizontal acceleration of transfer node is small. The vertical acceleration of transfer node is big, the vertical acceleration of standard section is small. The horizontal acceleration time-history curve of M, R, S and P are shown in Figure 8(a), and the vertical acceleration time-history curve is shown in Figure 8(b). Before 14s, the horizontal acceleration curve of floor and roof is similar and both can reflect seismic waveform, wherein the horizontal acceleration peak value of the first floor is the maximum, the horizontal acceleration peak value of the fourth floor is the minimum, but the difference between the two plates is small. With the increase of the buried depth, the horizontal acceleration at the floor and roof decreases. The vertical acceleration time-history curves of the floor and roof are quite different and cannot reflect the

seismic waveform. After 14s, the vertical acceleration time-history still fluctuates greatly, which indicates that the inertia force has a great influence on the vertical direction of the metro station.



(a) Maximum horizontal acceleration



(b) Maximum vertical acceleration

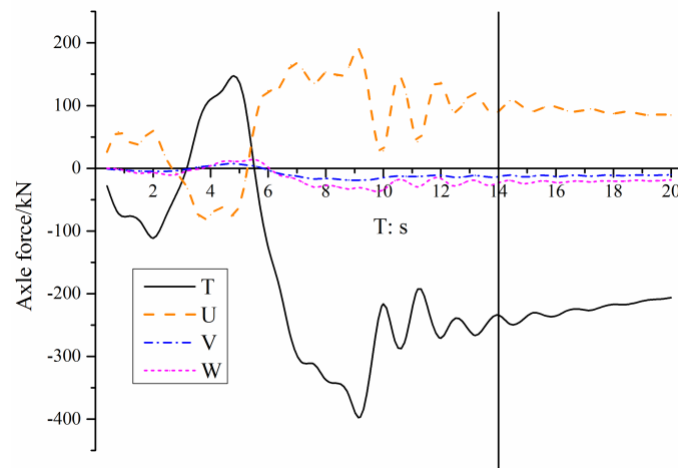
Fig. 8 - Time-history of maximum horizontal and vertical acceleration of measuring points

Internal force analysis

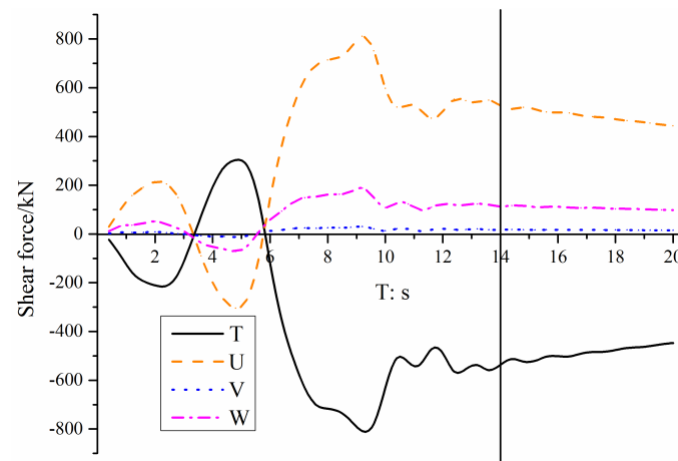
Internal force analysis of columns

There are 123 columns in the metro station. The measuring points T, U, V, W at the top and the bottom of the columns are shown in Figure 3, and the axial force time-history of measuring points is in Figure 9(a). Before 14 s, the axle force at the top and the bottom of the columns in transfer node is large, the fluctuation range is large, and the maximum tension is 198 kN, the maximum pressure of 387kN, while the axle force at the top and the bottom of the columns in transfer node is small, the maximum tensile force is 8kN, the maximum pressure of 42 kN. After 14 s, the seismic wave

unloads, the axle force of the columns decreases and gradually tends to a steady state. The shear force time-history of measuring points is in Figure 9(b). Before 14s, the shear force at the top and the bottom of the columns in transfer node is large, and the fluctuation range is large, while the axle force at the top and the bottom of the columns in transfer node is small, and the volatility is not obvious. The top and bottom of the columns is under the interaction of axial force and shear force in different direction, the "shear compression effect" is more obvious than "shear pull effect", and the two effects exist simultaneously, resulting in the destruction of columns.



(a) Axle force

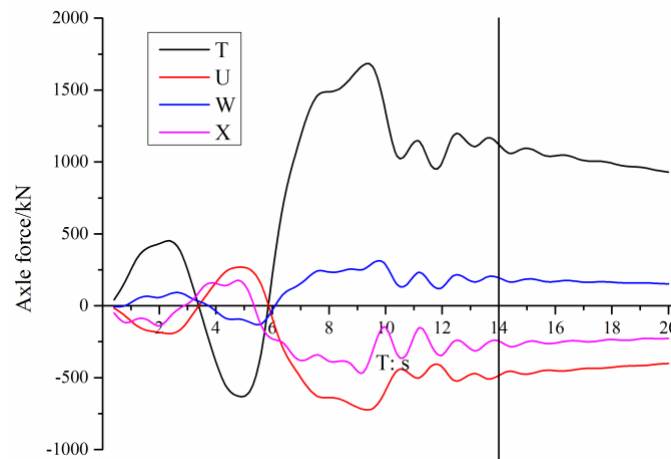


(b) Shear force

Fig. 9 - Time-history of axle force and shear force of measuring points

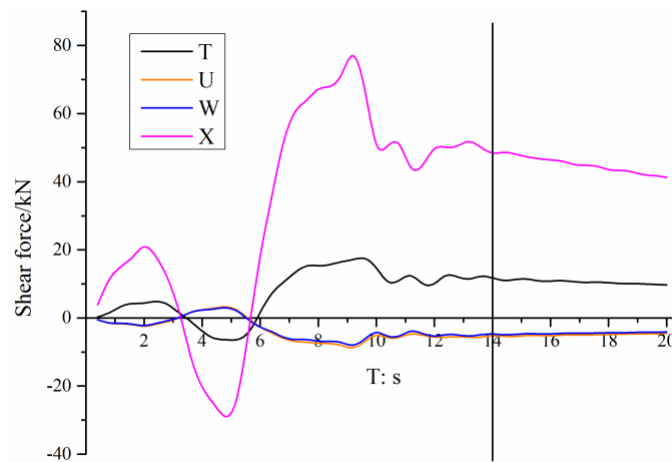
Internal force analysis of beams

The metro station is divided into four layers of beams. The measuring points T, U, W, X of different beams is shown in Figure 3, the axial force time-history of beams is as shown in Figure 10(a). The axial force of measuring point T is the maximum, the maximum tensile force is 1679kN, the maximum pressure is 605kN; the axial force of measuring point X is the minimum, the maximum tensile force is 236kN, the maximum pressure is 498 kN, the axial force of measuring points U and W is between the measuring point X and T. With the increase of buried depth, the axial force of beams reduces, and axial force difference between different layers of the beams increases. Before 14s, the axial force fluctuation of beams is large, the range between crest and trough is also large, on the same floor, the beam may be partly pulled and partly compressed. After 14s, the seismic wave unloads, under the action of inertia, the axial force of beams decreases and gradually tends to be stable. The shear force time-history of measuring points T, U, W, X is shown in Figure 10(b), the shear force of measuring point X is the maximum, the maximum shear force is 78 kN, the minimum shear force is 32 kN; the shear force of measuring points U and W is the minimum, the maximum shear force is 11 kN, the minimum shear force is 4 kN; so shear force at the transfer node beam is small, while the shear force of standard section is small. Before 14 s, the shear force fluctuation of beams is large, the range between crest and trough is also large. The shear force of beams is less than 100 kN, therefore, the beam shear has little effect on the beam strength; the maximum axial force of beams is 1679kN, therefore, the damage of the beams may be caused by the excessive tension.



(a) Axle force

Fig. 10 - Time-history of axle force and shear force of measuring points



(b) Shear force

Fig. 10 - Time-history of axle force and shear force of measuring points

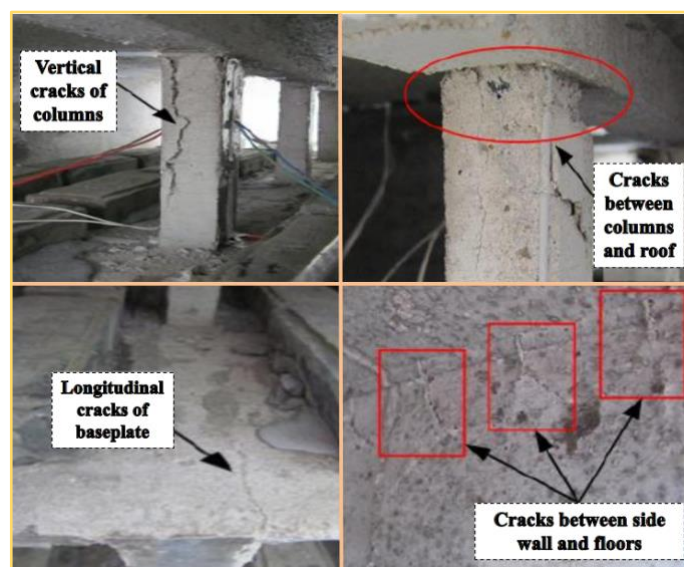
DISCUSSION

Earthquake damage of metro station

The Mexico earthquake in 1985, the subway tunnel was dislocated. The Loma Prieta earthquake in 1989, the Alameda immersed tube tunnel cracked in the Gulf of San Francisco, where water seepage and floating phenomena occurred. The Wenchuan earthquake in 2008, many tunnels in the Dujiangyan-Wenchuan Expressway near the epicenter were seriously damaged, there are lining cracking, floor heave, steel exposed, lining seepage and so on. The Kobe M7.2 Earthquake of Japan in 1995, the destruction of subway structure is the most serious. In the earthquake, a total of 5 metro stations and 3km tunnel were destroyed to varying degrees, the Dakai metro station suffered the most serious damage [13], as shown in Figure 11(a). The columns broke, the roofs collapsed, and the ground subsidence appeared. The destruction of the metro station is almost impossible to repair, which directly aroused the attention of Japan to the earthquake science and the earthquake resistance of underground structures.



(a) Earthquake Damage of Dakai metro station [13]



(b) Destruction of metro station in shaking table test [10, 11]

Fig. 11 - Earthquake damage of Dakai metro station and destruction of metro station in shaking table test [10, 11, 13]

Shaking table test of metro station

Matsui Jun et al. [33] carried out the earliest shaking table test of underground structures. In recent years, the shaking table test has been widely used in the study of soil-pile-superstructure interaction. Some scholars have gradually applied the shaking table test to the seismic research of metro station, as shown in Table 4. Based on the analysis of the stratum of Shanghai Metro, Yang et

al. [4] established the shaking table test of double-deck and three-span metro station, and obtained the time-history of acceleration, structural stress, and soil surface deformation of the model; Chen et al. [7, 20, 21] conducted a large shaking table test on liquefiable sand foundation in Nanjing, the reaction law of pore water pressure and acceleration response of the model were analysed; Bian et al. [5] carried out shaking table test of geological conditions in Beijing area, analyzed the time-history of dynamic stress, and studied the acceleration and stress distribution in different positions of the metro station; Cheng et al. [34] conducted the shaking table test of three-layer metro station, obtained the conclusion that failure of multi-layer metro station was controlled by displacement and improving the ductility of the structure was an effective method to improve the seismic performance of the underground structure.

For earthquake resistance of metro station in loess area, Quan et al. [10, 11] took the metro station of Xi'an Metro Line 4 as the prototype structure, and used the loess, granular concrete and galvanized steel wire to carry out shaking table test of the rectangular double-deck and two-span metro station. He found there was serious structural damage in metro station model. The upper columns occurred typical "shear compression failure" and appeared serious vertical cracks. The concrete in the columns peeled off, the longitudinal steel bar exposed, and destruction of the joint between the upper columns and the roof and the connection between the columns and the roof was the most serious. Cracks occurred at the joint between the side wall and the floor, in addition to the connection between the components, the roof, floor and other parts of the side wall had not obvious damage. Under the action of horizontal seismic wave, columns in frame-type metro station bear the vertical pressure and horizontal shear force; and compared with the side wall, floor, the section and integral stiffness of the columns are smaller, thus serious damage. The typical earthquake damage of metro station in loess area is as shown in Figure 11(b). The Zhang Wangqu metro station along Xi'an Metro Line 5 is similar to it.

Tab. - 4 Material parameters of metro station

Scholar	Examination Contents	Model box	Soil and similar materials	Performance of shaking table
Yang Linde [4]	Shaking table test of metro station in soft soil in Shanghai (Double-deck and double-span structure)	Rigid model box	Raw soil, silty clay, particulate concrete, galvanized steel wire	Platform size: 4m*4m Maximum load: 15t
Chen Guoxing [7, 20, 21]	Shaking table test of metro station in liquefied fine sand in Nanjing (Double-deck and double-span structure)	Rigid model box	Raw soil, fine sand, undisturbed soil, galvanized steel wire	Platform size: 6m*6m Maximum load: 80t
Bian Jin [5]	Shaking table test of metro station in sandy silt in Beijing (Double-deck and double-span structure)	Rigid model box	Raw soil, sandy silt, fine grained concrete, barbed wire	Platform size: 12.3m*18.7m Maximum load: 10t
Cheng Xinjun [34]	Shaking table test of metro station in Harbin (Three-deck and three-span structure)	Cascade shear box	Raw soil, fine particle concrete, fine steel wire	Model proportion: 1:30
Quan Dengzhou [10, 11]	Shaking table test of metro station in loess in Xi'an (Double-deck and double-span structure)	Cascade shear box	Raw soil, loess, particle concrete, galvanized steel wire	Platform size: 3.36m*4.86m Maximum load: 25t

CONCLUDING REMARKS

Through the dynamic time-history response analysis of the Zhang Wangqu metro station in the Xi'an Metro Line 5, compared the numerical simulation results with seismic damage of Dakai metro station in Japan and shaking table test of large metro station in loess area, the following conclusions are obtained:

- (1) The relative displacement of roof and floor reaches the maximum at transfer node and reduces with the increase of buried depth. If the earthquake intensity is large enough, it is very possible to dislocate at the transfer node in island platform metro station.
- (2) Under the horizontal seismic wave, the horizontal acceleration time-history of metro station can reflect seismic wave characteristics, but the vertical acceleration is distorted and cannot reflect the seismic waveform.
- (3) The maximum axial force of columns emerges in the corner transfer node, and the axle force of the other columns is small and uniform; the maximum shear force of beams occurs at both

ends of the metro station, and shear force of columns gradually increases from top to bottom, which may be manifested as shear cracking.

(4) With the increase of buried depth, the maximum axial force of different layer beams reduces and becomes more uneven, so the fatigue failure is easy to occur; the maximum shear force is generated at the end of the beams and is larger at the transfer joint than the standard section of the metro station, which may cause cracks.

(5) For island platform metro station, the columns and at the transfer node have bigger internal force than other positions, so the strength of the columns here needs to be increased; the internal force of beams increases with the increase of buried depth, so the beams in the depth requires greater intensity.

COMPETING INTERESTS

The authors declare that there is no conflict of interests regarding the publication of this paper.

ACKNOWLEDGEMENTS

This work is financially supported by the Brainstorm Project on Social Development of Shaanxi Provincial Science and Technology Department (No. 2016SF-412) and the Special Fund for Basic Scientific Research of Central Colleges of Chang'an University (No. 310821172004, No. 310821153312, No. 310821165011) and the National Key R&D problem of China (No. 2017YFC0805306). We also acknowledge the editor for the valuable suggestion.

REFERENCES

- [1] H. Y. Zhuang, H. Long, G. X. Chen, "Analysis of the nonlinear earthquake responses of a large complicated subway underground station", *Journal of Earthquake Engineering and Engineering Vibration*, Vol. 33, no. 2, pp. 192-199, 2013. (in Chinese)
- [2] J. B. Liu, W. H. Wang, G. Dasgupta, "Pushover analysis of underground structures: Method and application", *Science China Technological Sciences*, Vol. 57, no 2, pp. 423-437, 2014.
- [3] G. F. Wang, X. F. Shang, X. F. Ma, X. Y. Xu, "Equivalent Inertial Force Method of Seismic Calculation for Subway Station in Soft Site", *Shock and Vibration*, Vol. 2016, Article ID 4751071, 9p. doi: [10.1155/2016/4751071](https://doi.org/10.1155/2016/4751071).
- [4] L. D. Yang, Q. Q. Ji, Y. L. Zheng, C. Yang, D. L. Zhang, "Design of a shaking table test box for a subway station structure in soft soil", *Frontiers of Architecture and Civil Engineering in China*, Vol. 1, no 2, pp. 194-197, 2007.
- [5] J. Bian, L. J. Tao, W. P. Zhang, B. Zhang, "Shaking Table Test on Dynamic Soil Stress of the metro station Structure", *Chinese Journal of Underground Space and Engineering*, Vol. 7, no 4, pp. 687-690, 2011. (in Chinese)
- [6] L. P. Jing, X. C. Meng, H. F. Sun, Y. Zou, B. D. Lu, "Shaking table test analysis of three-story subway station", *Journal of Earthquake Engineering and Engineering Vibration*, Vol. 31, no 6, pp. 159-166, 2011.
- [7] G. X. Chen, Z. H. Wang, X. Zuo, X. L. Du, H. M. Gao, "Shaking table test on the seismic failure

- characteristics of a metro station structure on liquefiable ground”, *Earthquake Engineering and Structural Dynamics*, Vol. 42, no 10, pp. 1489-1507, 2013.
- [8] H. Y. Zhuang, Z. H. Hu, X. J. Wang, G. X. Chen, “Seismic responses of a large underground structure in liquefied soils by FEM numerical modeling”, *Bulletin of Earthquake Engineering*, Vol. 13, no 12, pp. 3645–3668, 2015.
- [9] Z. Y. Chen, W. Chen, X. Y. Li, Y. Yuan, “Shaking table test of a multi-story subway station under pulse-like ground motions”, *Soil Dynamics and Earthquake Engineering*, Vol. 82, pp. 111-122, 2016.
- [10] D. Z. Quan, Y. H. Wang, D. Ye, Y. L. Jing, S. Chen, “Shaking table test study on subway station built in loess area”, *China Civil Engineering Journal*, Vol. 49, no 11, pp. 79-90, 2016. (in Chinese)
- [11] D. Z. Quan, “Seismic Response Characteristic and Calculation Method of metro station in Loess”, Xi’an, 2016, Chang’an University. (in Chinese)
- [12] G. J. Parra-Montesinos, A. Bobet, J. A. Ramirez, “Evaluation of soil-structure interaction and structural collapse in Daikai subway station during Kobe earthquake”, *ACI Structural Journal*, Vol. 103, no 1, pp. 113-122, 2006.
- [13] X. L. Du, C. Ma, D. C. Lu, C. S. Xu, Z. G. Xu, “Collapse simulation and failure mechanism analysis of the Daikai subway station under seismic loads”, *China Civil Engineering Journal*, Vol. 50, no 1, pp. 53-62, 2017. (in Chinese)
- [14] T. Liu, Z. Y. Chen, Y. Yuan, X. Y. Shao, “Fragility analysis of a metro station structure by incremental dynamic analysis”, *Advances in Structural Engineering*, Vol. 20, no 7, pp. 1111-1124, 2017.
- [15] H. B. Liu, E. Song, “Seismic response of large underground structures in liquefiable soils subjected to horizontal and vertical earthquake excitations”, *Computers and Geotechnics*, Vol. 32, no 4, pp. 223-244, 2005.
- [16] X. H. Bao, Z. F. Xia, G. L. Ye, Y. B. Fu, D. Su, “Numerical analysis on the seismic behavior of a large metro subway tunnel in liquefiable ground”, *Tunnelling and Underground Space Technology*, Vol. 66, pp. 91-106, 2017.
- [17] C. J. Wang, “Seismic racking of a dual-wall metro station box embedded in soft soil strata”, *Tunnelling and Underground Space Technology*, Vol. 26, no 1, pp. 83-91, 2011.
- [18] H. Y. Zhuang, G. X. Chen, Z. H. Hu, C. Z. Qi, “Influence of soil liquefaction on the seismic response of a subway station in model tests”, *Bulletin of Engineering Geology and the Environment*, Vol. 75, no 3, pp. 1169-1182, 2016.
- [19] X. Y. Li, X. G. Jin, Y. S. Feng, W. Luo, “Effect of soft layer on seismic response of subway station in layered stratum”, *Journal of Vibroengineering*, Vol. 18, no 3, pp. 1602-1616, 2016.
- [20] G. X. Chen, S. Shen, C. Z. Qi, X. L. Du, Z. H. Wang, W. Y. Chen, “Shaking table tests on a three-arch type metro station structure in a liquefiable soil”, *Bulletin of Earthquake Engineering*, Vol. 13, no 6, pp. 1675-1701, 2015.
- [21] G. X. Chen, S. Chen, X. Zuo, X. L. Du, C. Z. Qi, Z. H. Wang, “Shaking-table tests and numerical simulations on a subway structure in soft soil”, *Soil Dynamics and Earthquake Engineering*, Vol. 76, pp. 13-28, 2015.
- [22] M. R. Moghadam, M. H. Baziar, “Seismic ground motion amplification pattern induced by a subway tunnel: Shaking table testing and numerical simulation”, *Soil Dynamics and Earthquake Engineering*, Vol. 83, pp. 81-97, 2016.

- [23] W. Li, W. Zhu, "A dynamic simulation model of passenger flow distribution on schedule-based rail transit networks with train delays", *Journal of Traffic and Transportation Engineering (English Edition)*, Vol. 3, no 4, pp. 364-373, 2015.
- [24] W. H. Zhou, H. Y. Qin, J. L. Qiu, H. B. Fan, J. X. Lai, K. Wang, L. X. Wang, "Building information modelling review with potential applications in tunnel engineering of China", *Royal Society Open Science*, 2017, doi: [10.1098/rsos.170174](https://doi.org/10.1098/rsos.170174).
- [25] A. J. Deeks, M. F. Randolph, "Axisymmetric time domain transmitting boundaries", *Journal of Engineering Mechanics*, Vol. 120, no 8, pp. 25-42, 1994.
- [26] J. X. Lai, F. Y. Niu, K. Wang, J. X. Chen, Q. L. Qiu, H. B. Fao, Z. N. Hu, "Dynamic effect of metro-induced vibration on the rammed earth base of the Bell Tower", *Springplus*, Vol. 2016, Article ID 935, doi: [10.1186/s40064-016-2627-1](https://doi.org/10.1186/s40064-016-2627-1).
- [27] Z. Y. Chen, C. Shi, T. B. Li, Y. Yuan, "Damage characteristics and influence factors of mountain tunnels under strong earthquakes", *Natural Hazards*, Vol. 61, no 2, pp. 387-401, 2012.
- [28] Z. Y. Chen, J. S. Wei, "Correlation between ground motion parameters and lining damage indices for mountain tunnels", *Natural Hazards*, Vol. 65, no 3, pp. 1683-1702, 2013.
- [29] Z. Y. Chen, H. T. Yu, Y. Yuan, "Full 3D seismic analysis of a long-distance water conveyance tunnel", *Structure and Infrastructure Engineering*, Vol. 10, no 1, pp. 128-140, 2014.
- [30] J. X. Lai, H. B. Fan, J. X. Chen, J. L. Qiu, K. Wang, "Blasting vibration monitoring of undercrossing railway tunnel using wireless sensor network", *International Journal of Distributed Sensor Networks*, Vol. 2015, Article ID 703980, doi: [10.1155/2015/703980](https://doi.org/10.1155/2015/703980).
- [31] Z. F. Wang, S. L. Shen, C. Ho, Y. H. Kim, "Investigation of Field Installation Effects of Horizontal Twin-Jet Grouting in Shanghai Soft Soil Deposits", *Canadian Geotechnical Journal*, Vol. 50, no 3, pp. 288-297, 2013.
- [32] Z. F. Wang, S. L. Shen, Z. Y. Yin, Y. S. Xu, "Rapid field evaluation of the strength of cement-stabilized clayey soil", *Bulletin of Engineering Geology and the Environment*, Vol. 74, no 3, pp. 991-999, 2015.
- [33] J. Matsui, K. Ohtomo, K. Kanaya, "Development and Validation of Nonlinear Dynamic Analysis in Seismic Performance Verification of Underground RC Structures", *Journal of Advanced Concrete Technology*, Vol. 2, no 1, pp. 25-35, 2004.
- [34] X. J. Cheng, L. P. Jing, J. Cui, Y. Q. Li, R. Dong, "Shaking-Table Tests for Immersed Tunnels at Different Sites", *Shock and Vibration*, Vol. 2017, Article ID 2546318, doi: [10.1155/2017/2546318](https://doi.org/10.1155/2017/2546318).